

INVESTIGATING SELECTED MECHANISMS OF MODULATION OF BECN1-MEDIATED
AUTOPHAGY

A Dissertation
Submitted to the Graduate Faculty
of the
North Dakota State University
of Agriculture and Applied Science

By
Yue Li

In Partial Fulfillment of the Requirements
for the Degree of
DOCTOR OF PHILOSOPHY

Major Department:
Chemistry and Biochemistry

May 2019

Fargo, North Dakota

North Dakota State University
Graduate School

Title

INVESTIGATING SELECTED MECHANISMS OF MODULATION OF
BECN1-MEDIATED AUTOPHAGY

By

Yue Li

The Supervisory Committee certifies that this *disquisition* complies with North Dakota
State University's regulations and meets the accepted standards for the degree of

DOCTOR OF PHILOSOPHY

SUPERVISORY COMMITTEE:

Dr. Sangita Sinha

Chair

Dr. Christopher Colbert

Dr. Pinjing Zhao

Dr. Changhui Yan

Approved:

7/5/2019

Date

Dr. Gregory Cook

Department Chair

ABSTRACT

Autophagy is a lysosomal degradation pathway wherein cytoplasmic components not needed by or harmful to the cell are degraded and recycled. BECN homologs are key autophagy proteins consisting of an intrinsically disordered region (IDR), flexible helical domain (FHD), coiled-coil domain (CCD) and β - α repeated, autophagy-specific domain (BARAD). Diverse proteins modulate autophagy by binding BECN1. Understanding the mechanisms by which these proteins regulate BECN1-mediated autophagy is important for developing therapeutics targeting these proteins. Toward this goal, we have developed purification protocols for multi-domain BECN1 fragments to explore the conformational flexibility and interactions.

We show that a BECN1 helix transitions between mutually exclusive packing states, wherein it either forms part of the CCD homodimer or packs against the BARAD, but predominantly packs against the BARAD. The same set of residues on this helix contribute to the CCD homodimer or packing with the BARAD, and mutation of these residues abrogates starvation-induced up-regulation of autophagy.

Next, we show the equatorial groove of GAPR-1 may be responsible for binding BECN1. The five conserved residues lining the GAPR-1 equatorial groove are essential for the interaction, as mutation of these residues disrupts GAPR-1:BECN1 interaction. We also solved the structure of this pentad mutant, which indicates the changes in the equatorial groove and the improved dimerization of pentad mutant likely abrogates BECN1-binding.

We then show that BH3D is not required for BECN1 to up-regulate autophagy, though it is required for binding BCL2 homologs. Therefore, we investigated the interactions between BH3D-containing BECN1 fragments and the BCL2 homolog, M11. BECN1 regions outside the BH3D increase binding to M11 by 5-10 fold. In addition, M11-binding increases flexibility of

the nuclear export sequence (NES). Further, homodimerization and thermostability of BECN1 BH3D-FHD-CCD increases upon M11-binding. Lastly, the M11:BECN1-BH3D-FHD-CCD complex appears to fluctuate between two major types of conformations, which may be mediated by the increased flexibility of BECN1 NES upon binding M11.

Lastly, we investigated the interactions between BH3D-containing BECN1 fragments and Bcl-X_L. Our results indicate that BECN1 regions outside the BH3D do not affect BECN1 interaction with Bcl-X_L.

Together, these studies are important for better understanding how proteins down-regulate BECN1-mediated autophagy.

ACKNOWLEDGEMENTS

I am deeply grateful to my adviser Dr. Sangita Sinha for her role in my doctoral work. First, many thanks to her for giving me the opportunity to join the lab. She allowed me to join the lab as a volunteer at the beginning even though I did not have any biochemistry background. Second, I thank her for being supportive of my doctoral work. Sangita gave me the freedom to do whatever I wanted to try for my project, and meanwhile continued to provide me valuable feedbacks and encouragement. Last, I am deeply grateful for her setting a high standard for not only me but also all members of our lab. It was not easy to reach the standard, and I have struggled to reach such a high standard, but when I look back this may be one of the best things I learned from the lab, which makes me a better person and a more qualified PhD candidate. I know that with all the high standards imbedded in my mind and all the strict training I received, I will be confident and courageous in my future career.

I also would like to thank my committee members: Dr. Christopher Colbert, Dr. Pinjing Zhao, and Dr. Changhui Yan. Dr. Christopher Colbert is also the collaborator of our lab, who has given me constructive advice on my projects, shared his knowledge and expertise in many aspects, such as protein purification and crystallography, and shown us the importance of critical thinking. Thank Dr. Pinjing Zhao and Dr. Changhui Yan for their time, valuable advice, and encouragement on my PhD project.

I extend thanks to our current and former members of the Sinha group, including Dr. Minfei Su, Dr. Yang Mei, Dr. Karen Glover, Shreya Mukhopadhyay, Srinivas Dasanna, Elizabeth Bueno, and Samuel Wyatt; and the Colbert group including Dr. Jaime Jensen, Shane Wyborny, Benjamin LeVahn, Beau Jernberg, and Tajnin Sultana. Thank you for contributing to the labs and giving the lab a joyful, lively, and friendly atmosphere. Thank you for your constant

support, advice, assistance and encouragement. I feel so fortunate to have worked with all of you in the past several years.

I also thank our collaborators, especially Dr. Srinivas Chakravarthy at Bio-CAT, APS, Argonne.

This research was funded by NIH grants RO3 NS090939, R15 GM122035 (S. S.), P20 RR015566 (S S.), R21 AI078198 (S. S.), and R15 GM113227 (C. C.); an NSF grant MCB-1413525 (S. S.). Work performed at Bio-CAT was supported by NIH NIGMS 9P41 GM103622 and use of the Pilatus 3 1M detector funded by NIH NIGMS 1S10OD018090-01. Work performed at NE-CAT was supported by NIH NIGMS P41 GM103403. This research used resources of the APS, a US DOE Office of Science User Facility operated for the DOE office of Science by Argonne National Laboratory under contract No. DE-AC0206CH11357.

DEDICATION

For my parents, whose roles in my life are immense, and who support and love me

unconditionally all the time

For my husband, who always makes me laugh and inspires me to be more dedicated to my dream

For my parents in law, who support and love our newly established small family

For my brother and sister in law, who always support me and take good care of our parents

For my grandparents, whom I miss the most

TABLE OF CONTENTS

ABSTRACT.....	iii
ACKNOWLEDGEMENTS.....	v
DEDICATION.....	vii
LIST OF TABLES.....	xvi
LIST OF FIGURES.....	xviii
LIST OF ABBREVIATIONS.....	xxv
CHAPTER 1. INTRODUCTION.....	1
1.1. Introduction to Autophagy.....	1
1.2. BECN1 in Autophagy.....	6
1.3. BCL2 Homologs and Their Interactions with BECN1.....	10
1.4. Potential Therapeutic Molecules Targeting Autophagy.....	11
1.5. Overview of Methods Used in This Study.....	12
1.5.1. X-ray crystallography.....	12
1.5.2. Small angle X-ray scattering (SAXS).....	17
1.5.3. Isothermal titration calorimetry (ITC).....	25
1.5.4. Circular dichroism (CD).....	26
1.5.5. Hydrogen/deuterium exchange mass spectrometry (HDX-MS).....	28
1.6. Specific Aims of This Study.....	32
CHAPTER 2. DETERMINING WHETHER THE INVARIANT CXXC MOTIFS IN THE BECN1 IDR BIND Zn^{2+}	33
2.1. Introduction.....	33
2.2. Materials and Methods.....	34
2.2.1. Creation of protein expression constructs.....	34
2.2.2. Protein expression and purification.....	35
2.2.3. ICP-MS.....	36

2.3. Results	37
2.3.1. Expression and purification results of BECN1 constructs	37
2.3.2. CXXC motifs of BECN1 are responsible for binding Zn ²⁺	40
2.4. Conclusions and Discussion.....	40
CHAPTER 3. STRUCTURAL TRANSITIONS IN CONSERVED, ORDERED BECN1 DOMAINS ESSENTIAL TO REGULATING AUTOPHAGY.....	42
3.1. Introduction	42
3.2. Materials and Methods.....	45
3.2.1. Plasmid preparation.....	45
3.2.2. Protein expression and purification.....	46
3.2.3. ITC.....	48
3.2.4. CD spectroscopy, SAXS data collection and analysis, and autophagy assay	48
3.2.5. Continuous wave electron paramagnetic resonance (CW-EPR).....	49
3.2.6. Crystallization and data collection for BECN1 CCD-BARAD ^{AFM,C353S/C391S}	49
3.3. Results	50
3.3.1. Expression and purification of WT and mutant BECN1 CCDs	50
3.3.2. Aromatic Finger may decrease solubility of BARAD-containing BECN1 fragments	51
3.3.3. Expression and purification of BARAD-containing BECN1 fragments.....	52
3.3.4. AFM increases solubility of BARAD-containing BECN1 fragments, but does not impact BARAD secondary and tertiary structure.....	58
3.3.5. BECN1 CCD structure is destabilized by the OH Tetrad mutation	60
3.3.6. The OH Tetrad mutation impacts the BECN1 OH+BARAD structure less than that of the CCD.....	62
3.3.7. The OH preferentially packs against the BARAD rather than with the CCD homodimer, but transiently samples both conformations.....	62
3.3.8. SAXS indicates the OH packs against the BARAD in the CCD-BARAD protein fragment	64

3.3.9. The Tetrad Mutant decreases starvation-induced autophagy	64
3.3.10. Preparation of BECN1 CCD-BARAD mutants for continuous wavelength electron paramagnetic resonance (CW-EPR).....	65
3.3.11. The CW-EPR result does not provide enough information for determining the orientation of BECN1 CCD-BARAD homodimer.....	69
3.3.12. Crystallization of BECN1 CCD-BARAD.....	70
3.4. Conclusions and Discussion.....	72
CHAPTER 4. INVESTIGATING THE STRUCTURE OF BECN2 AND ITS INTERACTION WITH ANTI-APOPTOTIC BCL2 PROTEINS.....	77
4.1. Introduction	77
4.2. Materials and Methods	79
4.2.1. Delineating BECN2 domain architecture.....	79
4.2.2. Creation of constructs to express different BECN2 fragments	79
4.2.3. Expression and purification of selected BECN2 fragments and mutants.....	84
4.2.4. Over-expression and purification of BECN2 CCD E173L and R243L mutants.....	86
4.2.5. Crystallization and diffraction data collection	86
4.2.6. BECN2 BH3D peptide synthesis.....	87
4.2.7. ITC for BECN2 interactions with M11 and Bcl-X _L	87
4.3. Results	88
4.3.1. Domain architecture of BECN2	88
4.3.2. Purification of BECN2 fragments	89
4.3.3. ITC for MBP-BECN2 BH3D-FHD-CCD interactions with M11 and Bcl-X _L	91
4.4. Conclusions and Discussion.....	94
CHAPTER 5. STRUCTURAL INSIGHTS INTO THE INTERACTION OF CONSERVED MAMMALIAN PROTEINS GAPR-1 AND BECN1	96
5.1. Introduction	96

5.1.1. GAPR-1 belongs to CAP superfamily, the members of which play diverse roles via diverse mechanisms in organisms.....	96
5.1.2. Structure and functions of GAPR-1	99
5.1.3. GAPR-1 down-regulates autophagy by interaction with BECN1	100
5.1.4. The goal of this study	101
5.2. Materials and Methods	102
5.2.1. Constructing a model of the complex of GAPR-1:BEEN1 residues 267-284	102
5.2.2. Creation of cellular protein expression constructs	102
5.2.3. Pull-down assays and western blot.....	103
5.2.4. Large-scale expression and purification of WT and pentad mutant GAPR-1.....	103
5.2.5. Large-scale expression and purification of MBP-BEEN1 CCD-BARAD and BEEN1 ^{Δ31-104}	105
5.2.6. Tat-BEEN1 peptide	106
5.2.7. ITC for GAPR-1-BEEN1 interactions	107
5.2.8. Crystallization, data collection and structure solution	107
5.2.9. Protein structure analysis.....	109
5.2.10. Analytical SEC	109
5.2.11. ITC for GAPR-1 homodimer dissociation	109
5.2.12. SEC-SAXS data collection and analysis	110
5.3. Results	111
5.3.1. Expression and purification results of GAPR-1 and BEEN1.....	111
5.3.2. GAPR-1 BEEN1 interaction was not detected by ITC	113
5.3.3. BEEN1 residues 267-284 are predicted to bind to the conserved equatorial groove of the GAPR-1 CAP domain.....	114
5.3.4. Conserved GAPR-1 residues lining the equatorial binding groove are important for binding to BEEN1	117
5.3.5. The pentad mutation does not impact GAPR-1 tertiary structure	118

5.3.6. The pentad mutation alters GAPR-1 quaternary structure	121
5.3.7. The pentad mutation impacts characteristics of the equatorial groove	124
5.3.8. The pentad mutation shifts the GAPR-1 monomer-dimer equilibrium toward dimerization.....	129
5.3.9. SEC-SAXS confirms that WT GAPR-1 is a monomer in solution.....	133
5.3.10. The pentad mutant GAPR-1 transitions between monomer and dimer states in solution	136
5.4. Conclusions and Discussion.....	144
CHAPTER 6. INVESTIGATING THE INTERACTION BETWEEN THE BECN1 BH3D AND VMP1 ATGD.....	147
6.1. Introduction	147
6.2. Materials and Methods	148
6.2.1. Preparation of BECN1 residues 1-135, BECN1 BH3D and VMP1 ATGD.....	148
6.2.2. CD Spectroscopy	149
6.2.3. ITC.....	149
6.3. Results	151
6.3.1. ITC for BECN1 BH3D and VMP1 ATGD interaction	151
6.3.2. Secondary structure of BECN1 BH3D, VMP1 ATGD, and their 1:1 mixture were investigated by CD spectra	152
6.4. Conclusions and Discussion.....	154
CHAPTER 7. INVESTIGATING THE MECHANISM BY WHICH THE γHV68 BCL2, M11, DOWN-REGULATES BECN1-MEDIATED AUTOPHAGY	155
7.1. Introduction	155
7.2. Materials and Methods	156
7.2.1. Sequence alignment.....	156
7.2.2. Autophagy assay.....	156
7.2.3. Protein overexpression and purification.....	157

7.2.4. Isolation of complexes of M11 and different BECN fragments.....	159
7.2.5. ITC.....	160
7.2.6. CD spectroscopy.....	160
7.2.7. HDX sample preparation and deuterium exchange measurement	161
7.2.8. SEC-SAXS data collection and analysis	162
7.3. Results	163
7.3.1. The BECN1 BH3D is not conserved amongst eukaryotes	163
7.3.2. The BECN1 BH3D is not required for starvation-induced autophagy.....	164
7.3.3. Expression and purification results of BECN1 constructs	166
7.3.4. BECN1 regions outside the BH3D increase binding to M11	172
7.3.5. BECN1 domains besides the BH3D undergo significant conformational changes upon M11-binding	174
7.3.6. M11-binding alters secondary structure of BECN1 domains besides BH3D	176
7.3.7. Thermostability of BECN1 increases marginally upon binding to M11.....	180
7.3.8. Binding to M11 increases homodimerization of the BECN1 BH3D-FHD-CCD	183
7.3.9. The BECN1 BH3D-FHD-CCD has a flexible, elongated conformation	185
7.3.10. The M11:BECN1 BH3D-FHD-CCD transitions between two distinct conformations with a predominant elongated conformation.....	189
7.3.11. The BECN1 BH3D-FHD-CCD-BARAD ^{AFM} adopts a flexible, elongated conformation, with the OH either flexible or preferentially packed against the CCD.....	193
7.3.12. The M11:BECN1 BH3D-FHD-CCD-BARAD ^{AFM} complex adopts a flexible, elongated conformation, with the OH preferably packing in the CCD or being flexible.....	198
7.4. Conclusions and Discussion.....	202
CHAPTER 8. INVESTIGATING M11 INTERACTIONS WITH BECN1 FL AND BECN1^{Δ31-104}	206
8.1. Introduction	206
8.2. Materials and Methods	206

8.2.1. Creation of protein expression constructs	206
8.2.2. Protein expression and purification	208
8.2.3. ITC.....	209
8.2.4. SEC–SAXS data collection and analysis	209
8.2.5. Cryo-negative staining.....	210
8.3. Results	210
8.3.1. Expression and purification of BECN1 constructs and their complexes with M11.....	210
8.3.2. M11-binding affinity is not impacted by BECN1 homodimerization.....	217
8.3.3. BECN1 ^{Δ31-104} and its complex with M11 adopt a flexible, elongated conformation.....	218
8.3.4. BECN1 FL and its complex with M11 adopt a flexible, elongated conformation.....	222
8.3.5. Our current BECN1 and M11:BECN1 complex samples are not suitable for EM.....	224
8.4. Conclusions and Discussion.....	226
CHAPTER 9. INVESTIGATION OF BCL-X _L INTERACTION WITH BECN1.....	228
9.1. Introduction	228
9.2. Materials and Methods	228
9.2.1. Protein overexpression and purification.....	228
9.2.2. ITC, CD, and SAXS experiments and analyses were performed as described in Chapter 7	229
9.3. Results	229
9.3.1. Expression and purification results of Bcl-X _L :BECN1	229
9.3.2. Bcl-X _L -binding affinity is not increased by BECN1 domains other the BH3D.....	231
9.3.3. CD cannot be used to evaluate changes in secondary structure content upon Bcl-X _L binding to the BECN1 BH3D-FHD-CCD	233

9.3.4. The Bcl-X _L :BECN1 BH3D-FHD-CCD complex has a flexible, elongated conformation.....	234
9.3.5. Bcl-X _L :BECN1 BH3D-FHD-CCD-BARAD ^{AFM} adopts flexible and elongated conformation, with OH preferably packing against CCD or being flexible.....	238
9.4. Conclusions and Discussion.....	242
CHAPTER 10. CONCLUSIONS AND FUTURE DIRECTIONS	244
REFERENCES	252

LIST OF TABLES

<u>Table</u>	<u>Page</u>
2.1. BECN1 constructs used in Chapter 2.....	35
3.1. BECN1 constructs used in Chapter 3.....	46
3.2. Purification of BARAD-BECN1 fragments.	52
3.3. Average estimated secondary structure content in MBP-BECN1 CCD- BARAD Proteins.	58
3.4. Summary of SEC-SAXS data for MBP-BECN1 CCD-BARAD proteins.	59
3.5. Thermodynamics of self-dissociation of CCD-containing proteins.	61
3.6. Crystallization conditions (all from MSCG-1) that produce crystal hits.....	71
3.7. X-ray data collection statistics of BECN1 CCD-BARAD ^{AFM,C353S/C391S}	72
4.1. Summary of primers used for creating BECN2 expression constructs.....	81
4.2. Gibson Assembly Master Mix composition.	81
4.3. 5 × isothermal reaction buffer composition	81
4.4. Summary of primers used for creation of BECN2 mutants used for cellular assay.	84
4.5. Summary of x-ray data collection of BECN2 CCD N187L mutant.	87
4.6. Thermodynamics of binding of M11 or Bcl-X _L to MBP-tagged BH3D-FHD-CCD fragments of BECN2 and BECN1.	93
5.1. Summary of proteins containing CAP domains and their interaction with metal, lipids, or peptides.	98
5.2. X-ray data collection and structure refinement statistics.....	108
5.3. Concentrations of eluate fractions from SEC.	132
6.1. Thermodynamics of binding of BECN1 and VMP1 ATGD.	152
6.2. Secondary structure contents analysis of CD spectra for VMP1 ATGD, BECH1 BH3D, and their complexes of Table.	153
7.1. Samples used in Chapter 7.....	158
7.2. Thermodynamics of binding of M11 and to BECN1 fragments.....	172

7.3.	Comparison of secondary structure content of M11, BECN1 fragments and their complexes from protein structure and CD.	177
7.4.	Comparison of single Boltzmann and double Boltzmann models fitting to the denaturing curve of BECN1 BH3D-FHD-CCD.	182
7.5.	Thermodynamics of self-dissociation of BECN1 BH3D-FHD-CCD and its complex with M11.	185
7.6.	Structural parameters from data analysis and EOM modeling.	187
8.1.	Samples used in this chapter.	207
8.2.	Thermodynamics of binding of M11 to dimeric and monomeric BECN1 fragments.....	218
8.3.	Structural parameters from SAXS data analysis.....	219
9.1.	Thermodynamics of binding of Bcl-X _L to BECN1 fragments.	232
9.2.	CD analysis: Estimated secondary structure content.	233
9.3.	Structural parameters from data analysis and EOM modeling.	235

LIST OF FIGURES

<u>Figure</u>	<u>Page</u>
1.1. Upstream signals that modulate autophagy in response to starvation.	2
1.2. Schematic diagram of the steps of autophagy.....	3
1.3. Crystal structure of the VPS34 Complex II.	6
1.4. Domain architecture of BECN1 and selected interactions.	7
1.5. Process of determining protein structure using X-ray crystallography.	14
1.6. SAXS (A) data collection and (B) initial data processing.	18
1.7. Guinier plot of a protein sample.	19
1.8. P(r) plot curves and their corresponding protein shape.	20
1.9. Kratky plots corresponding to different folding states of samples.	21
1.10. <i>Ab initio</i> models of a protein sample.	22
1.11. Fit of high-resolution protein structure to SAXS of the protein in solution using CRY SOL.....	23
1.12. EOM analysis for a BECN1 protein fragment.....	24
1.13. Basic principle of ITC.....	26
1.14. CD spectra of proteins composed of different secondary structure.....	27
1.15. HDX-MS experimental procedure.....	30
1.16. HDX-MS data analysis of an example protein.	31
2.1. Sequence alignment of BECN1 orthologs from diverse organisms.	34
2.2. Size exclusion chromatogram and the corresponding SDS-PAGE of MBP- BECN1 ^{AFM} FL.	37
2.3. Size exclusion chromatogram and the corresponding SDS-PAGE of MBP- BECN1 ^{AFM,CysTetrad} FL.....	38
2.4. Size exclusion chromatogram and the corresponding SDS-PAGE of MBP- BECN1 ^{AFM, C18S/C31S} FL.	39

2.5.	Size exclusion chromatogram and the corresponding SDS-PAGE of MBP-BECN1 ^{AFM, C137S/C140S} FL.....	39
2.6.	ICP-MS results for all the samples in Table 2.1.	40
3.1.	The OH has two different packing states.....	43
3.2.	Sequence alignment of the OH and partner helix in BECN1 orthologs.	45
3.3.	Size exclusion chromatogram and the corresponding SDS-PAGE of BECN1 CCD.....	50
3.4.	Size exclusion chromatogram and the corresponding SDS-PAGE of BECN1 CCD ^{TETRAD}	51
3.5.	The aromatic finger of the OH+BARAD buried in the hydrophobic pocket of another molecule.....	52
3.6.	Size exclusion chromatogram and the corresponding SDS-PAGE of MBP-SL-BECN1 CCD-BARAD.	53
3.7.	Size exclusion chromatogram and the corresponding SDS-PAGE of MBP-SL-BECN1 CCD-BARAD ^{AFM}	53
3.8.	Size exclusion chromatogram and the corresponding SDS-PAGE of MBP-SL-BECN1 CCD-BARAD ^{TETRAD}	54
3.9.	Size exclusion chromatogram and the corresponding SDS-PAGE of MBP-SL-BECN1 CCD- BARAD ^{AFM,TETRAD}	55
3.10.	Size exclusion chromatogram and the corresponding SDS-PAGE of BECN1 OH+BARAD ^{AFM}	55
3.11.	Size exclusion chromatogram and the corresponding SDS-PAGE of BECN1 OH+BARAD ^{AFM,TETRAD}	56
3.12.	Size exclusion chromatogram and the corresponding SDS-PAGE of BECN1 CCD-BARAD ^{AFM}	57
3.13.	Size exclusion chromatogram and the corresponding SDS-PAGE of BECN1 CCD-BARAD ^{AFM,TETRAD}	57
3.14.	The AFM does not alter CD spectra of MBP-BECN1 CCD-BARAD.....	58
3.15.	SEC-SAXS analysis of MBP-BECN1 CCD-BARAD proteins.....	60
3.16.	Homodimer dissociation ITC profiles of the BECN1 CCD and CCD ^{TETRAD}	61
3.17.	Homodimer dissociation ITC profiles of the BECN1 CCD-BARAD and CCD-BARAD ^{TETRAD}	63

3.18.	CW-EPR spin labeling and spectra.....	66
3.19.	Structure of BECN1 BARAD.....	67
3.20.	Sequence alignment of the BARAD in BECN1 orthologs from diverse organisms.	67
3.21.	SDS-PAGE gel image of Amylose affinity purification of (A) BECN CCD-BARAD ^{AFM,C353S/C375S} and (B) BECN1-CCD-BARAD ^{AFM,C375S/C391S}	68
3.22.	Size exclusion chromatogram and the corresponding SDS-PAGE of BECN1 CCD-BARAD ^{AFM,C353S/C391S}	69
3.23.	CW-EPR spectra of spin labeled BECN1 CCD-BARAD ^{AFM,C353S/C391S}	70
3.24.	BECN1 CCD-BARAD ^{AFM,C353S/C391S} crystals.	71
4.1.	Sequence alignment of human BECN1 and BECN2.....	89
4.2.	Size exclusion chromatogram and the corresponding SDS-PAGE of BECN2 CCD mutants.....	90
4.3.	Size exclusion chromatogram and the corresponding SDS-PAGE of MBP-BECN2 BH3D-FHD-CCD.	91
4.4.	Representative ITC profiles of BCL2 homologs binding to BECN2 and BECN1 BH3D-FHD-CCD.	92
5.1.	Electrostatic surface of WT GAPR-1 generated by APBS (Baker et al., 2001).....	100
5.2.	BECN1 residues 269-284 (green) in BECN1 BARAD structure (grey) (PDB ID: 4DDP).	101
5.3.	Size exclusion chromatogram and the corresponding SDS-PAGE of WT GAPR-1.....	111
5.4.	Size exclusion chromatogram and the corresponding SDS-PAGE of pentad mutant GAPR-1.	112
5.5.	Size exclusion chromatogram and the corresponding SDS-PAGE of MBP-BECN1 ^{Δ31-104}	113
5.6.	ITC profiles of (A) Tat-BECN1 titrated into WT GAPR-1, (B) WT GAPR-1 titrated into MBP-BECN1 CCD-BARAD, and (C) WT GAPR-1 titrated into MBP BECN1 ^{Δ31-104}	114
5.7.	GAPR-1 sequence conservation..	116
5.8.	Location of mutated, conserved residues within the equatorial GAPR-1 binding groove.	116

5.9.	Computational model of BECN1 (residues 267-284) docked onto WT GAPR-1 (PDB ID: 1SMB).	117
5.10.	GST-BECN1 pull-downs of WT and mutant GAPR-1.....	118
5.11.	Crystals of pentad mutant GAPR-1.	119
5.12.	GAPR-1 tertiary structure is maintained in the pentad mutant.	119
5.13.	2F _o -F _c electron density displayed at contour levels of 1.0 σ around the mutated residues of pentad mutant GAPR-1.	120
5.14.	The pentad mutation impacts GAPR-1 dimerization.....	121
5.15.	The dimer interface varies in the different GAPR-1 dimers.....	122
5.16.	Pentad mutant GAPR-1 dimerization occludes the equatorial groove.	126
5.17.	WT GAPR-1 dimerization occludes the equatorial groove.	127
5.18.	WTinIP6 GAPR-1 dimerization occludes the equatorial groove.	128
5.19.	Analytical SEC profile of GAPR-1.....	130
5.20.	ITC quantification of GAPR-1 self-dissociation.	132
5.21.	I ₀ distribution across the GAPR-1 scattering peak.	133
5.22.	WT GAPR-1 SEC-SAXS data showing R _g distribution across the scattering peak and SVD analysis.....	133
5.23.	SAXS analysis of WT GAPR-1.....	135
5.24.	R _g distribution across the SEC-SAXS elution peak.....	137
5.25.	SVD analysis of SEC-SAXS from pentad mutant GAPR-1.....	139
5.26.	Analysis of the ~20 Å R _g peak part of pentad mutant GAPR-1 SAXS.	141
5.27.	Analysis of the ~16 Å R _g peak part of pentad mutant GAPR-1 SAXS.	143
6.1.	ITC data of BECN1 BH3D peptide titrated into VMP1 ATGD peptide.	152
6.2.	CD spectra of VMP1 ATGD, BECN1 BH3D, and their complexes.	153
7.1.	The BECN1 BH3D is not conserved.	164
7.2.	The BECN1 BH3D is not required for autophagy.....	166

7.3.	Size exclusion chromatogram and the corresponding SDS-PAGE of MBP-BECN1 IDR.....	167
7.4.	Size exclusion chromatogram and the corresponding SDS-PAGE of BECN1 BH3D-FHD.....	167
7.5.	Size exclusion chromatogram and the corresponding SDS-PAGE of BECN1 FHD-CCD.....	168
7.6.	Size exclusion chromatogram and the corresponding SDS-PAGE of BECN1 BH3D-FHD-CCD.....	169
7.7.	Size exclusion chromatogram and the corresponding SDS-PAGE of BECN1 BH3D-FHD-CCD-BARAD ^{AFM}	169
7.8.	Size exclusion chromatogram and the corresponding SDS-PAGE of BECN1 ^{AFM} FL.....	170
7.9.	Size exclusion chromatogram and the corresponding SDS-PAGE of M11:BEHN3D-FHD-CCD.....	171
7.10.	Size exclusion chromatogram and the corresponding SDS-PAGE of M11:BEHN3D-FHD-CCD-BARAD ^{AFM}	172
7.11.	Representative ITC results for M11:BEHN3D-FHD-CCD fragment interactions.....	173
7.12.	HDX heat maps of BECN1 BH3D-FHD-CCD for: (A) Unbound (B) In complex with M11.....	175
7.13.	CD spectra of BECN1 fragments and their complexes with M11.....	176
7.14.	Melting curve of BECN1 fragments and their complexes with M11.....	181
7.15.	Representative ITC raw data of dilution of MBP-BECN1 1-135 into buffer.....	184
7.16.	Determining K _d of homodimerization for: (A) unbound BECN1 BH3D-FHD-CCD and (B) M11:BEHN3D-FHD-CCD complex (B).....	185
7.17.	SAXS analysis of BECN1 BH3D-FHD-CCD.....	186
7.18.	EOM fits for BECN1 BH3D-FHD-CCD.....	188
7.19.	SAXS analysis of M11:BEHN3D-FHD-CCD.....	190
7.20.	EOM fits (1) for M11:BEHN3D-FHD-CCD complex.....	191
7.21.	EOM fits (2) for M11:BEHN3D-FHD-CCD complex.....	192
7.22.	SAXS analysis of BECN1 BH3D-FHD-CCD-BARAD ^{AFM}	194

7.23.	EOM fits (1) for BECN1 BH3D-FHD-CCD-BARAD ^{AFM}	195
7.24.	EOM fits (2) for BECN1 BH3D-FHD-CCD-BARAD ^{AFM}	196
7.25.	EOM fits (3) for BECN1 BH3D-FHD-CCD-BARAD ^{AFM}	197
7.26.	SAXS analysis of M11:BEHN3D-FHD-CCD-BARAD ^{AFM}	199
7.27.	EOM fits (1) for M11:BEHN3D-FHD-CCD-BARAD ^{AFM} complex.	200
7.28.	EOM fits (3) for M11:BEHN3D-FHD-CCD-BARAD ^{AFM} complex.	201
8.1.	Strep-SUMO-BECN1 sequence in pET vector.....	208
8.2.	SEC and the corresponding SDS-PAGE of SUMO-BECN1 ^{Δ31-104}	211
8.3.	SEC and the corresponding SDS-PAGE of M11:SUMO-BECN1 ^{Δ31-104}	212
8.4.	SEC and the corresponding SDS-PAGE of SUMO-BECN1 ^{Δ31-104,AFM}	212
8.5.	SEC and the corresponding SDS-PAGE of M11:SUMO-BECN1 ^{Δ31-104,AFM}	213
8.6.	SEC and the corresponding SDS-PAGE of SUMO-BECN1 ^{AFM} FL.	214
8.7.	SEC and the corresponding SDS-PAGE of M11:SUMO-BECN1 ^{AFM} FL.	215
8.8.	SEC and the corresponding SDS-PAGE of MBP-BECN1 ^{Δ31-104,AFM}	215
8.9.	SEC and the corresponding SDS-PAGE of M11:MBP-BECN1 ^{Δ31-104,AFM}	216
8.10.	SEC and the corresponding SDS-PAGE of SUMO-BECN1 ^{AFM,CCDPentad}	217
8.11.	Representative plots of ITC for M11:BEHN1 interactions.....	218
8.12.	SEC–SAXS results for SUMO- BECN1 ^{Δ31-104,AFM}	219
8.13.	SEC–SAXS results for M11:SUMO- BECN1 ^{Δ31-104,AFM}	220
8.14.	EOM modeling for the M11:SUMO-BECN1 ^{Δ31-104,AFM} complex.	221
8.15.	SEC–SAXS results for SUMO-BECN1 ^{AFM} FL.....	223
8.16.	SEC–SAXS results for M11:SUMO-BECN1 ^{AFM} FL.	224
8.17.	Negative-stained images of (A) SUMO-BECN1 ^{AFM} FL (left panel) and M11:SUMO-BECN1 ^{AFM} FL (right panel).	225
8.18.	Cryo-negatively stained images of (A) and (B) MBP-BECN1 ^{Δ31-104,AFM} and (C) and (D) M11:MBP-BECN1 ^{Δ31-104,AFM}	226

9.1.	Size exclusion chromatogram and the corresponding SDS-PAGE of Bcl-X _L :BH3D-FHD-CCD complex.	230
9.2.	Size exclusion chromatogram and the corresponding SDS-PAGE of Bcl-X _L :BECN1 BH3D-FHD-CCD-BARAD ^{AFM} complex.	231
9.3.	Representative plots of ITC for Bcl-X _L :BECN1 interactions.	232
9.4.	SAXS analysis of Bcl-X _L	234
9.5.	SAXS analysis of Bcl-X _L :BECN1 BH3D-FHD-CCD.	236
9.6.	EOM modeling for the Bcl-X _L :BECN1 BH3D-FHD-CCD complex.	238
9.7.	SAXS analysis of Bcl-X _L :BECN1 BH3D-FHD-CCD-BARAD ^{AFM}	239
9.8.	EOM modeling (Pool 1) for the Bcl-X _L :BECN1 BH3D-FHD-CCD-BARAD ^{AFM} complex.	241
9.9.	EOM modeling (Pool 3) for Bcl-X _L :BECN1 BH3D-FHD-CCD-BARAD ^{AFM} complex.	242

LIST OF ABBREVIATIONS

Å.....	Angstrom
AFM.....	Aromatic Finger Mutation
AMBRA1.....	Autophagy And Beclin 1 Regulator 1
AMP.....	Adenosine Monophosphate
AMPK.....	AMP-activated Protein Kinase
ADP.....	Adenosine Diphosphate
ATP.....	Adenosine Triphosphate
ATG.....	Autophagy Related Protein
ATGD.....	Autophagy-Related Domain
BARAD.....	β - α Repeated, Autophagy-Specific Domain
BCL2.....	B Cell Lymphoma 2
BH3D.....	BH Homology 3 Domain
BHRF1.....	BamHI H Fragment Rightward Reading Frame 1
CCD.....	Coiled-Coil Domain
CD.....	Circular Dichroism Spectroscopy
ΔG	Change in Gibbs Free Energy
ΔH	Change in Enthalpy
ΔS	Change in Entropy
D_{\max}	Maximum Particle Size
DTT.....	Dithiothreitol
EBV.....	Epstein-Barr Virus
<i>E. coli</i>	<i>Escherichia coli</i>
EDTA.....	Ethylenediaminetetraacetic Acid
EM.....	Electron Microscopy

EOM.....	Ensemble Optimization Method
EPR	Electron Paramagnetic Resonance
FBS	Fetal Bovine Serum
FHD.....	Flexible Helical Doman
FL.....	Full Length
γ HV68.....	γ Herpes Virus 68
GAPR-1.....	Golgi-Associated Plant Pathogenesis-Related Protein 1
GFP	Green Fluorescent Protein
GST.....	Glutathione S-Transferase
HDX-MS.....	Hydrogen-Deuterium Exchange Mass Spectrometry
His ₆	Hexa-histidine
HIV	Human Immunodeficiency Virus
HSV.....	Herpes Virus
I(0).....	Scattering Intensity at Zero Angle
I(q).....	Scattering Intensity
ICP-MS	Inductively Coupled Mass Spectrometry
IDR.....	Intrinsically Disordered Region
IPTG.....	Isopropyl Thio- β -D-Galactoside
ITC	Isothermal Titration Calorimetry
K _d	Dissociation Constant
KSHV.....	Kaposi's Sarcoma Herpes Virus
LC3	Light Chain 3
MBP	Maltose Binding Protein
MoRF	Molecular Recognition Feature
mTOR	Mammalian Target Of Rapamycin Complex 1

OH.....	Overlap Helix
PAGE.....	Polyacrylamide Gel Electrophoresis
PDB.....	Protein Data Bank
P(r).....	Pairwise-Distance Distribution
PI.....	Phosphatidylinositol
PI3KC3.....	Class III Phosphatidylinositol 3 Kinase
PI3P.....	Phosphatidylinositol 3-Phosphate
R _g	Radius of Gyration
ROS.....	Reactive Oxygen Species
SAXS.....	Small Angle X-ray Scattering
SDS.....	Sodium Dodecyl Sulfate
SEC.....	Size Exclusion Chromatography
SL.....	Short, Triple Alanine, Linker
TAT.....	Transcriptional Activator Protein Transduction Domain
TEV.....	Tobacco Etch Virus
TFE.....	2,2,2-Trifluoroethanol
TM.....	Transmembrane
T _m	Melting Temperature
TORC1.....	Target Of Rapamycin Complex 1
UPLC.....	Ultra Performance Liquid Chromatography
VMP1.....	Vacuole Membrane Protein 1
VPS.....	Vacuolar Protein Sorting
WT.....	Wild Type
θ.....	Molar ellipticity

CHAPTER 1. INTRODUCTION

1.1. Introduction to Autophagy

Most organisms live in substantially harsher natural environments than that encountered by humans living in civilized societies. One of the most primitive and commonly encountered deficiencies in normal environments is the lack of nutrients. Therefore, eukaryotes have evolved mechanisms that enable them to survive starvation conditions. Key amongst these is autophagy, a lysosomal degradation pathway wherein cytoplasmic components not needed by or harmful to the cell are degraded and recycled. The most typical trigger of autophagy is nutrient starvation, and three major starvation related basic factors: cellular energy levels, amino acids, and starvation-induced oxidative stress, impact autophagy levels. These signals are often transduced to vacuolar protein sorting 34 (VPS34) Complexes, also called Class III phosphatidylinositol 3-kinase (PI3KC3) complexes, via serine/threonine kinases such as AMP-activated protein kinase (AMPK), target of rapamycin complex 1 (TORC1) and the Unc-51 like autophagy activating kinase (ULK) 1/2 complexes.

ATP is the major energy-storing molecule in most living organisms and therefore, is often called the energy currency of life. The availability of carbon sources such as glucose directly affects relative cellular concentrations of ATP, ADP, and AMP as the hydrolysis of glucose results in ATP biosynthesis from ADP/AMP. Elevated ADP and AMP levels reflect energetic stress, therefore the ATP:ADP+AMP ratio is a key indicator of cellular energy levels. At high concentrations, ADP and AMP bind to and activate AMP-activated protein kinase (AMPK) (Laderoute *et al.*, 2006). Activated AMPK phosphorylates and activates Unc-51 like autophagy activating kinase 1 (ULK1), and both phosphorylate VPS34 complex proteins as well as VPS34 complex regulators, to up-regulate autophagy (Kim *et al.*, 2011, Kim *et al.*, 2013)

(Figure 1). Activated AMPK also up-regulates autophagy by phosphorylating and inactivating mammalian (m)TORC1, since activated mTORC1 phosphorylates and represses ULK1 (Kimura *et al.*, 2003, Kim *et al.*, 2011) (Figure 1.1).

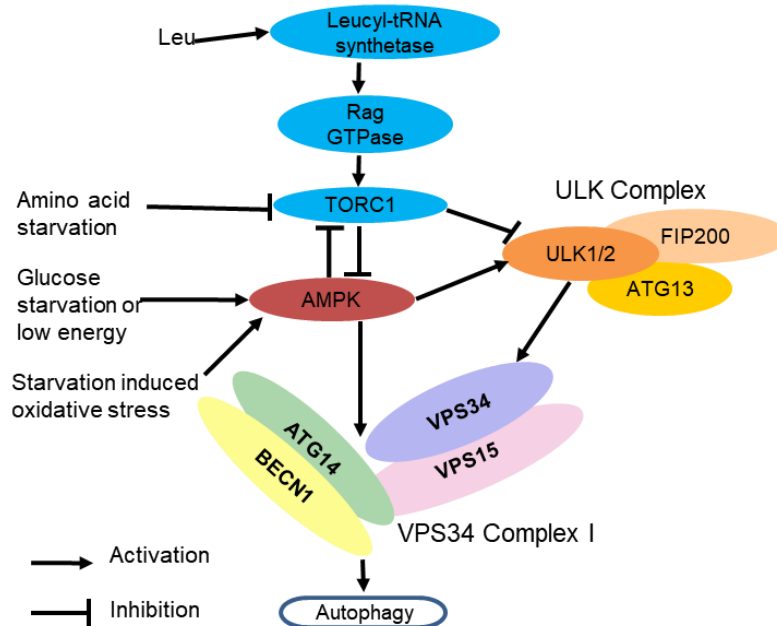


Figure 1.1. Upstream signals that modulate autophagy in response to starvation. Proteins are represented as ovals.

TORC1 activation is also regulated by cellular levels of Leu, Gln, and Arg (Bauchart-Thévret *et al.*, 2010, Duran *et al.*, 2012, Han *et al.*, 2012, Zhu *et al.*, 2015). At high Leu concentrations, leucyl-tRNA synthetase interacts with and activates Rag GTPase which then activates TORC1, leading to suppression of autophagy by phosphorylation of ULK1/2 and AMPK (Han *et al.*, 2012) (Figure 1.1). Gln and Arg are also implicated in mTORC1 activation, but how they are sensed is unknown (Duran *et al.*, 2012, Zhu *et al.*, 2015).

Nutrient depletion leads to malfunction of mitochondrial electron transport. Electrons leak from NADH-Coenzyme Q oxidoreductase and Coenzyme Q-Cytochrome c oxidoreductase, resulting in partial oxygen reduction to superoxide radicals ($O_2^{\bullet-}$), the precursor of most other reactive oxygen species (ROS). These superoxide radicals may be converted to hydrogen

peroxide (H_2O_2) by mitochondrial superoxide dismutase and released from the mitochondrial matrix to the cytoplasm. Starvation-induced H_2O_2 may activate AMPK, which may be redox-sensitive (Shao *et al.*, 2014). Activated AMPK induces autophagy as discussed above (Figure 1.1).

Autophagy pathway involves four distinct stages: (1) vesicle nucleation, (2) vesicle elongation, (3) autophagosome and lysosome docking & fusion, (4) vesicle breakdown & degradation (Melendez & Levine, 2009) (Figure 1.2). Each stage of autophagy is regulated by numerous proteins, and mis-regulation of any stage could lead to failure of autophagy, which has been found to be related to various diseases such as cancer, neurodegenerative diseases, cardiovascular diseases and infectious diseases (Levine & Kroemer, 2008, Mizushima *et al.*, 2008, Jiang & Mizushima, 2014, Mizushima, 2018). Therefore, knowing the molecular mechanisms by which the proteins regulate autophagy is essential for discovery and development of potential drugs targeting those autophagy-regulating proteins.

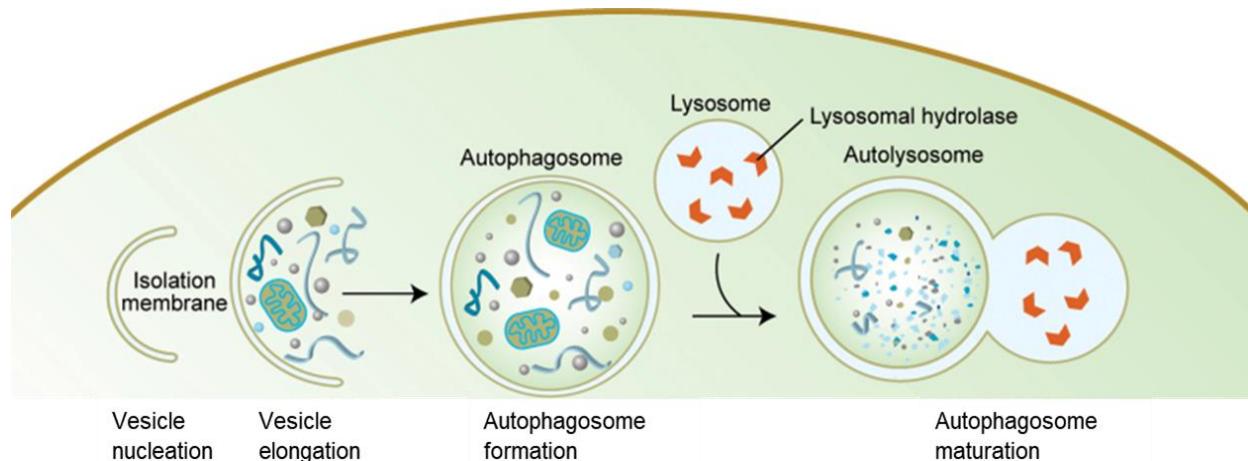


Figure 1.2. Schematic diagram of the steps of autophagy. Figure is adapted from (Meléndez *et al.*, 2005).

In the first stage, vesicle nucleation, bulk cytosol component is captured in a growing double membrane structure named as phagophore. VPS Complex I is activated and recruited to the site of phagophore nucleation (Itakura *et al.*, 2008). VPS34 complex I is comprised of four

core components: VPS34/PI3KC3, VPS15/P150, VPS30/BECN1/ATG6, and ATG14 (Itakura *et al.*, 2008). P150, a myristylated serine/threonine kinase, phosphorylates and activates PI3KC3; activated PI3KC3 catalyzes phosphorylation of phosphatidylinositol to generate phosphatidylinositol-3-phosphate, which is required for the vesicle nucleation (Obara and Ohsumi, 2008); BECN1 and ATG14 are then recruited to the complex to regulate the vesicle nucleation.

The phagophores formed in the first stage then elongate and form autophagosomes. Two ubiquitin-like conjugation systems are involved in regulating this phase (Ohsumi, 2001). One system is called ATG12 system. In this system Atg12, a protein with a ubiquitin-like fold is activated by Atg7, an E1-like enzyme. Subsequently, the Atg12 is transferred to Atg10, an E2-like conjugating enzyme. Finally, the Atg12 is covalently conjugated to Atg5. The Atg12-Atg5 then forms a larger complex with Atg16 (Ohsumi, 2001). The other system is called Atg8 system, wherein Atg8, another ubiquitin-like protein, is first cleaved by Atg4 (a protease) to expose a C-terminal glycine (Ohsumi, 2001). This glycine-exposed form of Atg8 is activated by Atg7, an E1-like enzyme, and transferred to Atg3, a E2-like enzyme. Atg8 forms a conjugate with phosphatidylethanolamine (Ohsumi, 2001, Ichimura *et al.*, 2000).

The autophagosome then fuses with lysosome to form autolysosome. In yeast, this process requires SNARE machinery and several SNARE protein family homologs are involved in the regulation (Darsow *et al.*, 1997, Sato *et al.*, 1998, Mayer & Wickner, 1997). In mammalian cells, the activity of monomeric GTPases such as Rab22 and Rab24 is required for autophagosome maturation (Petiot *et al.*, 2000), and mammalian orthologs of SNARE protein family members may also be involved in the maturation of autophagosome. In addition, UVRAG, Rubicon, valosin-containing protein and syntaxin-5 SNARE complex proteins are also

reported to be involved in regulation of the autophagosome maturation (Liang *et al.*, 2008, Matsunaga *et al.*, 2009, Tresse *et al.*, 2010). VPS34 complex II, which has the same composition of VPS34 complex I, except that the ATG14 is replaced by UVRAG, is also involved in the regulation of autophagosome maturation (Itakura *et al.*, 2008, Itakura & Mizushima, 2009). After the autolysosome is formed, the enclosed components are then degraded and released into the cytosol for recycling.

VPS34 Complex I and II have a very similar V-shaped architecture (Baskaran *et al.*, 2014, Rostislavleva *et al.*, 2015) (Figure 1.3). VPS34 together with VPS15/p150 form one arm of the V-shape (Baskaran *et al.*, 2014, Rostislavleva *et al.*, 2015) (Figure 1.3). The VPS15 kinase domain interacts with the VPS34 activating loop, regulating its activity. The other arm of the V-shape is formed by a parallel heterodimer of VPS30/BECN1 and either ATG14 in Complex I or VPS38/UVRAG in Complex II. The C-terminal domain of each of these proteins, i.e. the VPS30/BECN1 BARAD and VPS38/UVRAG BARA2D are located at the tip of the arm. The base of the 'V' shape is formed by the VPS15/p150 helical domain, the VPS30/BECN1 IDR, and the N-termini of either VPS38 in Complex II or ATG14 in Complex I. The VPS34 C2 domain is buried in the center of the 'V' shaped complex (Figure 1.3), unlike the C2 domains of class I PI3Ks that pack between the helical and kinase domains and bind to membranes through Ca^{2+} .

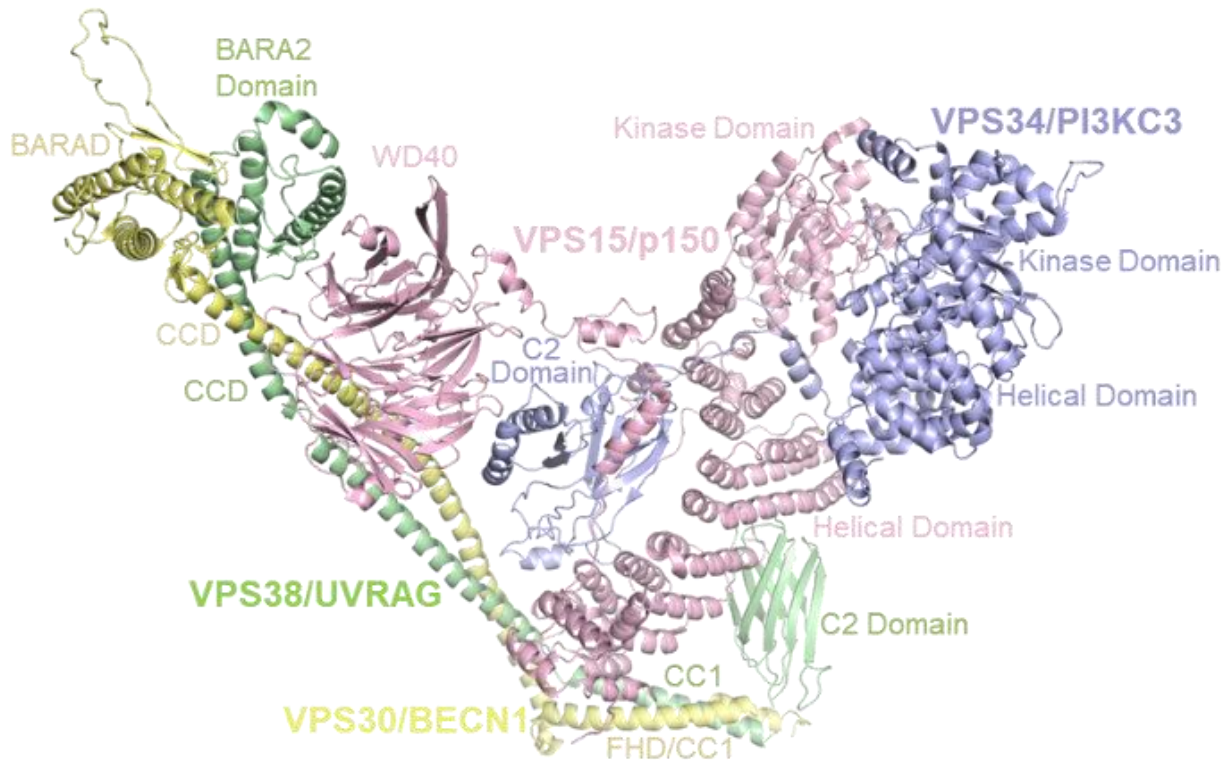


Figure 1.3. Crystal structure of the VPS34 Complex II. (PDB ID: 5DFZ). In VPS34 Complex I, the UVRAG is substituted by ATG14.

1.2. BECN1 in Autophagy

BECN1 as a core component protein of the VPS34 complexes appears to be an interaction hub of autophagy. The conformational flexibility of BECN1 likely plays a key role in facilitating diverse protein interactions (Mei, Glover, *et al.*, 2016). Human BECN1 is composed of 450 amino acids that includes at least four domains/regions (Mei, Glover, *et al.*, 2016) (Figure 1.4): an intrinsically disordered region (IDR), a flexible helical domain (FHD), a coiled coil domain (CCD), and a β - α repeated, autophagy specific domain (BARAD). Different domains of BECN1 are involved in multiple interactions with other proteins, which up- or down-regulate autophagy.

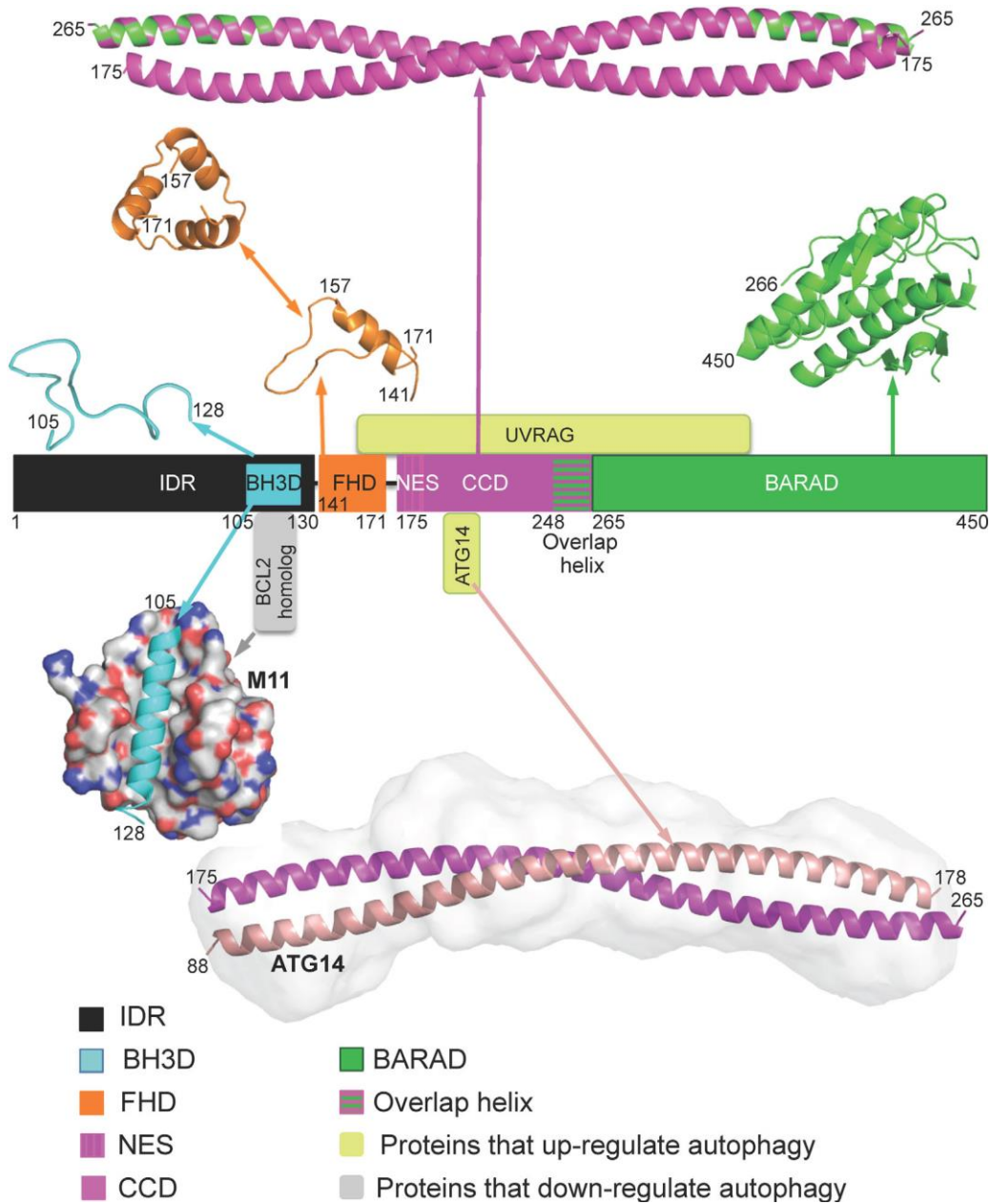


Figure 1.4. Domain architecture of BECN1 and selected interactions. Domains structures are displayed in ribbon above the schematic. Two structurally characterized interactions are displayed below the schematic: (i) The BECN1 BH3D (cyan ribbon) bound to M11 (grey molecular surface) and (ii) The BECN1 CCD (magenta ribbon):ATG14 CCD (salmon ribbon) heterodimer is shown modelled into its SAXS-derived molecular envelope. Yellow-green boxes represent interacting proteins that up-regulate autophagy while grey boxes represent interacting proteins that down-regulate autophagy (Mei, Glover, *et al.*, 2016). The PDB IDs for FHD, CCD, BARAD, and M11:BECN1 complex structures are: 5EFM, 5HHE, 4DDP, and 3DVU).

BECN1 residues 1-140 is defined as an IDR (Figure 1.4) that contains several binding motifs including three Anchor regions: residues 13-49, 79-103, and 116-127 (Mei *et al.*, 2014,

Lee *et al.*, 2016). Anchor regions are sequences flanking or overlapping IDRs that are predicted by the program ANCHOR (Dosztanyi *et al.*, 2009) to nucleate binding-associated folding. Two Anchors of the IDR are identified as α -molecular recognition features (α MoRFs), i.e. regions that undergo disorder-to order transitions upon binding to partners. These two α MoRFs encompassing residues 76-105 which involve the second Anchor; and residues 105-130 which are defined to be BH3 domain (Sinha *et al.*, 2008). Various BCL2 homologs bind the BH3D of BECN1 to down-regulate starvation-induced autophagy (Sinha *et al.*, 2008, Pattingre *et al.*, 2005, Maiuri *et al.*, 2007, Oberstein *et al.*, 2007, Ku *et al.*, 2008). High mobility group box 1 protein, a chromatin-associated nuclear protein, also interacts with this region of BECN1 and competitively prevents BCL2 proteins from interacting with BECN1, thereby up-regulating autophagy (Tang & Da, 2010). Additionally, vacuole membrane protein 1 (VMP1) has also been reported to interact with BECN1 BH3D to up-regulate autophagy (Molejon *et al.*, 2013).

The FHD is comprised of residues 141-171 (Mei, Ramanathan, *et al.*, 2016) (Figure 1.4), containing 2 Anchors: one comprising residues 137-145 that overlaps both the IDR and FHD; the other comprising residues 162-169. Like the BH3D, FHD helicity increases when treated with TFE, indicating that the FHD could potentially undergo disorder-to-order transition upon binding to certain partners (Mei, Ramanathan, *et al.*, 2016). In yeast VPS34 complex II, VPS30 CC1 (equivalent to human FHD) forms an eight-turn helix and packs against VPS38 CC1 (equivalent to human UVRAG FHD) (Rostislavleva *et al.*, 2015). Additionally, the FHD is required for interaction with AMBRA1, an up-regulator of BECN1-mediated autophagy (Fimia *et al.*, 2007, Strappazzon *et al.*, 2011).

The CCD, comprising residues 175-265, forms an anti-parallel homodimer (Li *et al.*, 2012, Mei, Su, *et al.*, 2016) (Figure 1.4), which leads to the homodimerization of BECN1.

BECN1 CCD also interacts either with ATG14 or UVRAG CCD to form parallel heterodimers (Baskaran *et al.*, 2014, Rostislavleva *et al.*, 2015, Li *et al.*, 2012), which potentially recruits other core components, VPS34 and VPS15, to form VPS34 Complex I or II. Residues 250-265 of CCD have been crystallized in two mutually exclusive states: either in CCD or BARAD (Huang *et al.*, 2012, Li *et al.*, 2012, Mei, Glover, *et al.*, 2016, Mei, Su, *et al.*, 2016). This overlap helix (OH) transitions between these two different packing states, with the predominant state comprising the OH packed against the BARAD (Glover *et al.*, 2017). The CCD N-terminal residues (180-190) which pack against the OH, appear to constitute a nuclear export sequence (NES) that is required for nuclear export of BECN1 via the chromosome region maintenance 1 protein (CRM-1) (Liang *et al.*, 2001).

The BARAD, encompassing residues 266-450, is a strong membrane-binding domain (Huang *et al.*, 2012) (Figure 1.4). An aromatic finger, comprising BARAD residues F350, F360, and W361, is found to be responsible for interaction with lipid membranes enriched with cardiolipin (Huang *et al.*, 2012, Rostislavleva *et al.*, 2015). Golgi-Associated Plant Pathogenesis-Related protein 1 (GAPR-1) down-regulates autophagy by interacting with the BECN1 BARAD, and residues 267-284 of the BARAD were required and sufficient for this interaction (Shoji-Kawata *et al.*, 2013).

Mammals have a second BECN1 homolog, BECN2, that also functions in starvation-induced autophagy (He *et al.*, 2013). BECN2 shares 56.6% sequence similarity with BECN1 and is predicted to have similar structure and domain architecture to BECN1. Besides its role in autophagy, BECN2 regulates nutrient intake and ligand-induced endolysosomal degradation of several GPCRs. In the absence of BECN2, the cannabinoid 1 receptor is overexpressed, increasing nutrient intake resulting in weight gain and insulin resistance in cells (He *et al.*, 2013).

1.3. BCL2 Homologs and Their Interactions with BECN1

BCL2 homologs were first discovered as proteins that prevent programmed cell death, apoptosis (Yang *et al.*, 1997, Boise *et al.*, 1993), but have since been found to function in diverse cellular pathways, including autophagy, cell cycle progression, unfolded protein response, calcineurin signaling, glucose homeostasis, mitochondrial dynamics, and transcription regulation (Reed, 1998, Danial *et al.*, 2010). BCL2 homologs are characterized by the presence of BCL2 homology (BH) domains, and there are pro-apoptotic BCL2 proteins and anti-apoptotic BCL2 proteins (Reed, 1998). Pro-apoptotic BCL2 proteins, which promote apoptosis, include BH3-only proteins such as BIM, BAD, Noxa, and PUMA (O'Connor *et al.*, 1998, Yang *et al.*, 1995, Yu *et al.*, 2001, Oda *et al.*, 2000); as well as three-BH (BH1, BH3, BH2) domain proteins: BAX, BAK, and BOK (Reed, 1998, Oltvai *et al.*, 1993, Chittenden, Flemington, *et al.*, 1995, Chittenden, Harrington, *et al.*, 1995, Hsu *et al.*, 1997). Anti-apoptotic BCL2 proteins, which inhibit apoptosis, contain four BH domains, BH4, BH1, BH3, and BH2 (Reed, 1998, Han *et al.*, 2001). Humans encode at least six anti-apoptotic proteins: Bcl-2, Bcl-X_L, Mcl-1, Bcl-w, A1, and Bcl-B (Boise *et al.*, 1993, Yang *et al.*, 1997, Kozopas *et al.*, 1993, Lin *et al.*, 1993, Gibson *et al.*, 1996, Ke *et al.*, 2001). As mentioned above, anti-apoptotic BCL2 homologs are discovered to down-regulate autophagy by binding to the BH3 domain of BECN1 (Patingre *et al.*, 2005, Maiuri *et al.*, 2007).

Numerous herpesvirus also encode anti-apoptotic proteins to hijack apoptosis or autophagy for their benefits, including the BHRF1 and BALF1 of Epstein-Barr virus (EBV) (Henderson *et al.*, 1993, Marshall *et al.*, 1999), M11 of murine γ herpesvirus 68 (MHV-68) (Virgin *et al.*, 1997, Wang *et al.*, 1999, Sinha *et al.*, 2008, Ku *et al.*, 2008, Loh *et al.*, 2005), and the viral Bcl-2 proteins of KSHV (Sarid *et al.*, 1997, Cheng *et al.*, 1997), rhesus rhadinovirus

(RRV) (Alexander *et al.*, 2000), and herpesvirus saimiri (HVS) (Nava *et al.*, 1997).

Many interactions between anti-apoptotic BCL2 proteins and BH3Ds of pro-apoptotic BCL2 proteins or BECN1 have been structurally and thermodynamically characterized. All anti-apoptotic BCL2 homologs adopt similar three-dimensional structures, with a central hydrophobic alpha helix surrounded by six or seven amphipathic helices to form a globular alpha-helical fold known as “Bcl-2 fold” (Kvansakul & Hinds, 2013). Previous structural and mutagenic analyses demonstrated that the BH3 domain of pro-apoptotic BCL2 homologs or the autophagy up-regulator BECN1 binds as an amphipathic helix in the hydrophobic groove of anti-apoptotic BCL2 proteins (Oberstein *et al.*, 2007, Liu *et al.*, 2003, Huang *et al.*, 2002, Petros *et al.*, 2000, Sattler *et al.*, 1997, Sinha *et al.*, 2008, Ku *et al.*, 2008, Su *et al.*, 2014). Different BCL2 homologs have widely varying association affinities for BH3 domains from different pro-apoptotic proteins (Kvansakul & Hinds, 2013). Viral anti-apoptotic BCL2 homologs bind to cellular pro-apoptotic BCL2 homologs with relatively low affinity compared to the binding of the cellular anti-apoptotic proteins (Kvansakul & Hinds, 2013). It is not surprising that different anti-apoptotic BCL2 homologs, either viral or cellular, also bind to BECN1 BH3D differently. Amongst the known interactions, the cellular anti-apoptotic protein Bcl-X_L and the viral anti-apoptotic protein M11 interact with the BECN1 BH3D with the highest affinity.

1.4. Potential Therapeutic Molecules Targeting Autophagy

Many autophagy-regulating proteins, including BECN1 and its interacting proteins, have become major targets for drug discovery and development (Levine *et al.*, 2015, Galluzzi *et al.*, 2017). Rapamycin, a small molecule known to target mTORC1, up-regulates autophagy. Tamoxifen up-regulates BECN1 levels and induces autophagy. 3-Methyladenine and wortmannin target PI3KC3 and inhibit autophagy (Rubinsztein *et al.*, 2012). Bafilomycin A1

activates mTORC1 and inhibits autophagosome fusion with lysosomes as well as induces BECN1 binding to BCL2 (Yuan *et al.*, 2015). Similarly, chloroquine prevents autophagy by blocking autolysosome formation and has been used to target colon cancer, malignant melanoma, hepatocellular carcinoma, low-grade glioma and high grade astrocytoma (Kimura *et al.*, 2013). Small molecules like Verapamil, loperamide and nimodipine up-regulate autophagy, enhancing clearance of soluble mutant huntingtin exon 1-encoded protein and reducing its aggregation and toxicity in neuroblastoma cells (Williams *et al.*, 2008). Cell-permeable peptides or peptide mimetics derived from the BECN1 BH3D, have been shown to selectively disrupt inhibitory interactions between BECN1 and anti-apoptotic BCL2s, activating VPS34 complexes and up-regulating autophagy (Malik *et al.*, 2011, Su *et al.*, 2014). Recently, an all-hydrocarbon stapled peptide that specifically targets the C-terminal region of the BECN1 CCD is shown to prevent BECN1 self-association and promote BECN1–Atg14L/UVRAG interaction, thereby increasing autophagy levels and EGFR degradation (Wu *et al.*, 2018). Another cell-permeable peptide derived from BECN1 residues 267-284 was shown to be a potent autophagy inducer that triggers autophagy to prevent replication of West Nile and Chikungunya viruses and may also target HIV-1 (Shoji-Kawata *et al.*, 2013)

Given the above background, it is essential to understand the molecular mechanisms by which proteins regulate autophagy for discovery and development of potential drugs targeting those autophagy-regulating proteins.

1.5. Overview of Methods Used in This Study

1.5.1. X-ray crystallography

Single protein X-ray crystallography has become the most widely used technique for determining the high-resolution three-dimensional structures of proteins, since the protein

structure of myoglobin was first determined in 1958. To date, more than 148,000 protein or protein:DNA, Protein:RNA complex structures have been deposited in protein databank (<https://www.rcsb.org/>). Amongst them, more than 130,000 structures were solved by x-ray crystallography, suggesting its advantages in studying the structure of biological macromolecules.

The first step of solving protein structure by X-ray crystallography is to obtain crystals with high quality (Figure 1.5). Obtaining single crystals of high-quality is the limiting step to solving a structure using crystallography, and not all protein molecules can grow crystals. Monodisperse protein molecules in solution could increase the chances of growing crystals. However, monodispersity is not a sufficient condition to obtaining crystals; many other conditions impact crystallization. In general, the process of crystallization is to bring the protein solution to supersaturation, which induces aggregation and nucleation that may further grow into larger crystals, wherein individual protein molecules arrange themselves in a repeating unit cells. Good quality crystals need to be single and large enough to generate high-quality diffraction. Conditions such as protein concentration and folding, temperature, buffer type and pH, precipitant type and concentration, and additives all impact crystal formation and growth (Ilari & Savino, 2017, McKee, 1993, Rhodes, 2006). Further, sometimes the protein needs to be modified to make it less flexible for crystallization, and several rounds of screening and optimization of crystallization conditions are usually required to obtain high-quality crystals.

The X-ray diffraction data of high-quality crystals will then be recorded by exposing the crystals to a monochromatic X-ray beam (Figure 1.5). There are two ways to generate X-rays: striking a copper anode by electrons; or from high-energy electrons circulating around the synchrotron (Smyth & Martin, 2000). For protein X-ray crystallography, high-resolution

diffraction data is usually recorded at synchrotrons. The basis of synchrotron is: when accelerating electrons are forced to travel in a curved magnetic path, energy is emitted, including at X-ray wavelengths. The resulting X-ray beams are directed toward a beamline. Regardless of X-ray source, protein crystals are exposed to the X-ray beam while rotating. X-rays are diffracted by the electrons of the atoms in the crystal, and the scattered X-ray is recorded by a detector. When the scattered waves add up, they either become stronger, or weaker, therefore the scattered X-ray as spots of different intensity, called reflections, on the detector (Massa, 2004).

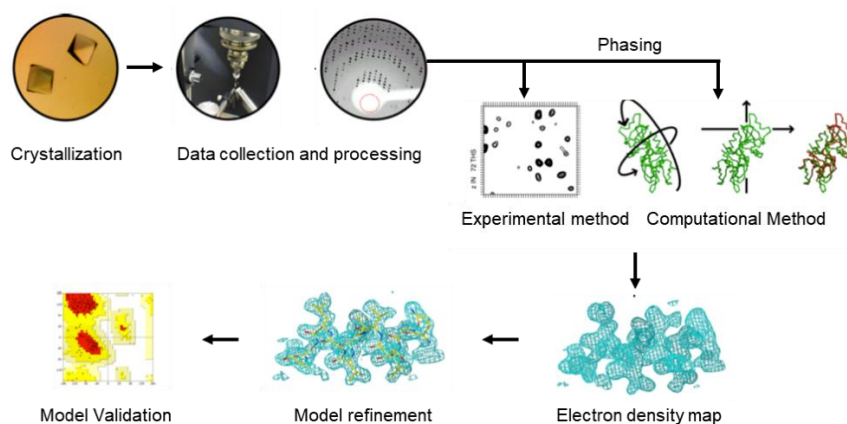


Figure 1.5. Process of determining protein structure using X-ray crystallography. The first step is to obtain high quality protein crystal; the crystal is exposed to X-ray beam and the diffraction data were then recorded and analyzed; phasing problem is then solved by either experimental methods or computational methods to finally generate the electron density map; then the protein structure model is fitted and refined; lastly the model is validated and the final structure is deposited in protein data bank. The figure is adapted from lecture slides of Dr. James Fraser at UCSF.

The reflections of all the diffraction data are indexed, which enables determination of the space group and unit cell dimensions of the crystal. This can often be accomplished using autoindexing programs. The data are then integrated to convert the hundreds of images, each perhaps containing hundreds of reflections, into a single file containing the information of Miller index consisting of three integers h , k , and l , and intensity (the intensity of each spot is a result of both the amplitude of the diffracted waves and their phase relation) of each reflection (Smyth & Martin, 2000). Equivalent diffracted spots from different images are usually merged and scaled.

During scaling, intensities of symmetry-related reflections whose intensities are expected to be identical (within acceptable experimental error) are averaged. All symmetry-related reflections are then merged into a unique set of reflections (Smyth & Martin, 2000). The quality of the data set can be assessed by Pearson correlation coefficient (ρ) between random half-data sets (CC1/2). A CC_{1/2} value of 0.5 or above is acceptable.

Fourier transformation is used to transform the structure factor $F_{(hkl)}$ to electron density map of the protein molecules. The electron density $\rho_{(x,y,z)}$ can be calculated as:

$$\rho_{(xyz)} = \frac{1}{V} \sum_h \sum_k \sum_l F_{(hkl)} \exp[-2\pi i(hx + ky + lz)] \quad (1.1)$$

In this equation, x , y , and z are fractional coordinator of the unit cell; V is the volume of the unit cell. $F_{(hkl)}$ can be expressed as:

$$F_{(hkl)} = \sum_{j=1}^{atoms} f_{(j)} \exp[2\pi i(hx_{(j)} + ky_{(j)} + lz_{(j)})] = |F_{(hkl)}| \exp(i\varphi_{(hkl)}) \quad (1.2)$$

Therefore, equation (1.1) can be rewritten as:

$$\rho_{(xyz)} = \frac{1}{V} \sum_h \sum_k \sum_l |F_{(hkl)}| \exp[-2\pi i(hx + ky + lz) + i\varphi_{(hkl)}] \quad (1.3)$$

In equation (1.2), $f_{(j)}$ is the scattering factor of atom j , which depends on the atom type and the diffraction angle of the corresponding reflection (hkl); in equation (1.2) and (1.3), $|F_{(hkl)}|$ is the magnitude of the structure factor, the square of which is proportional to the reflection intensity; $\varphi_{(hkl)}$ is the phase of the structure factor, which is unknown. Therefore, the phasing problem needs to be solved to generate the electron density map of the protein molecules.

The phasing problem can be solved using either experimental methods or computational methods (Figure 1.5). The experimental methods include: multiple isomorphous replacement,

which requires heavy atom be incorporated into the protein crystals; and multiple anomalous dispersion, which is typically done with SeMet replacement. Combinations / variations of these two experimental methods may also be used such as multiple isomorphous replacement with anomalous signal; and single isomorphous replacement with anomalous signal. The computational methods include molecular replacement (MR), and direct and *ab initio* methods. MR is the most commonly used computational method, and all the structures reported in this study is solved by MR.

In MR, the phasing problem is solved by comparing the theoretical diffraction pattern of a known homologous structure with the experimental structure. All possible permutations of different orientations and positions of a known homologous structure is placed in the experimental crystal unit cell. Theoretical diffraction patterns of each permutation are calculated and compared with the experimental diffraction patterns. The orientation and position of the homologous structure that best matches the experimental diffraction is identified. This MR model with the identified orientation and position is then used to calculate phases for each experimental reflection. These phases and amplitudes are used to calculate the structure factor and to generate the initial electron density map. The atomic structure of the unknown protein is then built into this electron density map.

Refinement is then performed in a cyclic process together with model rebuilding to gradually improve the model by adjusting the atomic coordinates of the model to better fit the experimental diffraction data as well as the established geometric constraints. *R*-factor is used to evaluate the agreement between the built model and the experimental data. The *R*-factor can be calculated by the following equation:

$$R = \frac{\sum ||F_{obs}| - |F_{calc}||}{\sum |F_{obs}|} \quad (1.4)$$

In this equation, $|F_{obs}|$ represents the observed amplitudes of the experimental structure factor and $|F_{calc}|$ represents the calculated amplitude of the model structure factor. The free R -factor (R_{free}) is commonly used as a cross-validation method (Brunger, 1992). R_{free} is calculated the same way but only using ~5% -10% of the reflections that are excluded from the refinement. The remaining reflections used in the refinement are known as working set, and the R factor calculated using the working reflections is called R_{work} . The R_{free} is usually slightly larger than R_{work} , but both R_{free} and R_{work} are expected to decrease during the cycles of successful refinement. The difference between R_{free} and R_{work} for the final model should be smaller than 5%; the model is considered over refined when the difference between R_{free} and R_{work} exceeds 5%. Generally, the final value of R_{free} of a successful refinement should be close to one tenth of the structure resolution.

Lastly, in addition to R_{work} and R_{free} , other criteria are also used to evaluate the quality of the model. These includes deviations from ideality of bond lengths, bond angles, violations of dihedral, and chirality restraints, temperature factors, Ramachandran plot, peptide orientation, rotamer analysis, residue real-space electron-density fit and close contacts, etc.

1.5.2. Small angle X-ray scattering (SAXS)

SAXS is a powerful method to analyze the three-dimensional, low-resolution structure of biological molecules in solution (Mertens & Svergun, 2010), especially if combined with *ab initio* modeling. SAXS can also provide information regarding the oligomeric states of protein or complexes, as well as, the flexibility of the protein or complex, which is complementary to the information obtained from high-resolution structures.

Upon irradiation with X-rays, elastic scattering by the biomolecule solution gives rise to an isotropic scattering intensity (Figure 1.6), which depends on the modulus of the momentum transfer s :

$$s = \frac{4\pi \sin(\theta)}{\lambda} \quad (1.5)$$

In equation 1.5, the 2θ is the angle between the incident and scattered beam (Figure 1.6). The intensity can be written as:

$$I(s) = \langle I(s) \rangle_{\Omega} = \langle A(s)A^*(s) \rangle_{\Omega} \quad (1.6)$$

In equation 1.6, the intensity is averaged over all orientations (Ω). $A(s)$ is the scattering amplitude, which is a Fourier transformation of the excess scattering length density (derived from the electron density difference between solute and solvent molecules). After buffer subtraction, the $I(s)$ is proportional to the scattering of a single particle averaged over all possible orientations.

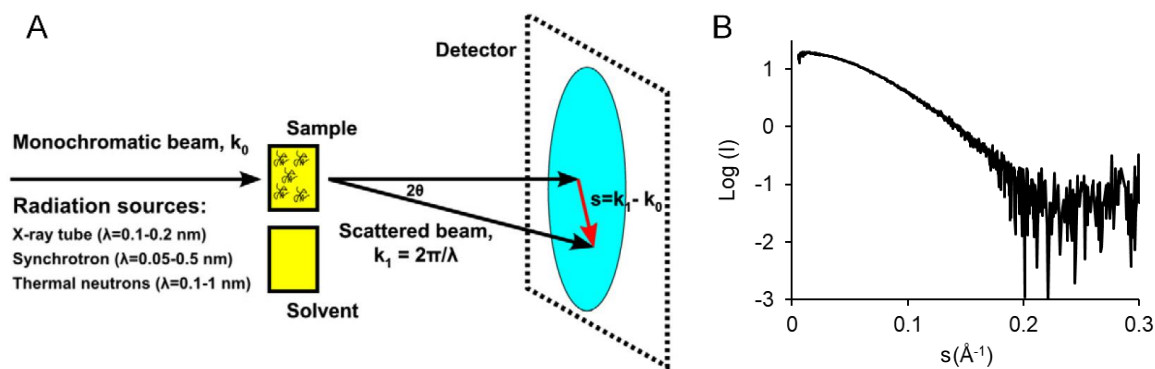


Figure 1.6. SAXS data (A) collection and (B) initial data processing. Figure A is adapted from (Mertens & Svergun, 2010). The solution containing the particle of interest is exposed to monochromatic beam and the scattered X-ray is recorded by a detector. The scattering profile of buffer is subtracted from that of the sample prior to plotting the processed data.

Several overall shape and weight parameters can be extracted directly from the scattering intensity curve, including molecular mass, radius of gyration (R_g), hydrated partial volume (V_p), and maximum particle diameter (D_{max}).

A Guinier analysis (Guinier, 1939) is performed to extract the information of the intensity at 0θ , $I(0)$, and the R_g . The Guinier equation can be written as:

$$I(s) = I(0) \exp\left(-\frac{1}{3}R_g^2 s^2\right) \quad (1.7)$$

In a plot of $\ln[I(s)]$ vs s^2 (Figure 1.7), called a Guinier plot, the y-axis intercept is $I(0)$ and the slope of the linear region is R_g^2 . The lower limit of the s for the linear fit of the Guinier plot is dependent on the experimental set-up, and constitutes the minimum angle at which intensity is recorded. The maximum s for the linear fit is usually $1.3/R_g$ for biomolecules. Besides quantifying $I(0)$ and R_g , the Guinier plot also provides information about sample quality. A non-linear Guinier plot is a strong indicator of sample aggregation or strong inter-particle repulsion.

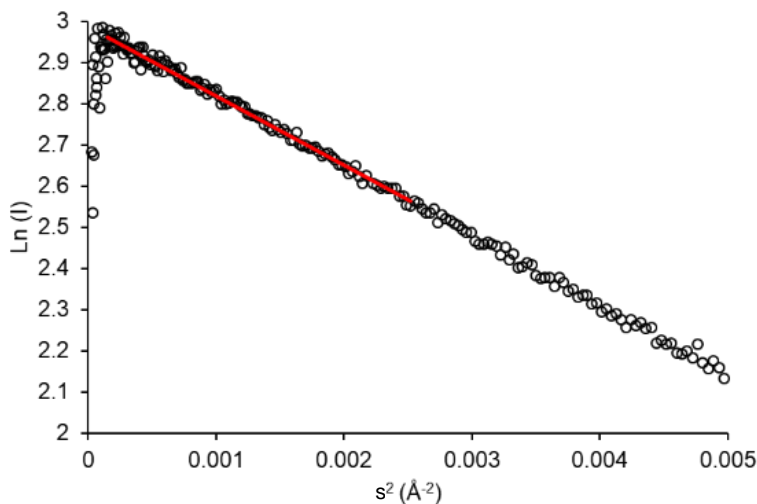


Figure 1.7. Guinier plot of a protein sample. $\ln(I)$ vs s^2 need to be linear at low s range.

The V_p can be estimated by using the Porod's equation (Porod, 1982):

$$V_p = \frac{2\pi^2 I(0)}{Q}, \quad Q = \int_0^\infty s^2 I(s) ds \quad (1.8)$$

V_p allows us to estimate the molecular mass. Typically, for a globular protein, V_p (nm^3) is about 1.5-2 times the molecular mass. Q is the Porod invariant, an empirical small angle scattering value defined for compact folded particles.

The distance distribution function, $P(r)$ can be derived from the Fourier transformation of the scattering data:

$$P(r) = \frac{r^2}{2\pi^2} \int_0^\infty s^2 I(s) \frac{\sin sr}{sr} ds \quad (1.9)$$

The $P(r)$ function provides information about the particle shape (Figure 1.8). Computation of $P(r)$ is not straightforward as the available $I(s)$ is limited from s_{\min} to s_{\max} , and it is not possible to perform a direct Fourier transformation of the scattering curve using these number of points. A solution to this problem is using an indirect method, proposed by Glatter in the 1970s (Glatter, 1977). The indirect transform program GNOM (Svergun, 1992) provides the optimal estimate of D_{\max} . The parameters estimated from this indirect Fourier transform approach also include more accurate estimates of $I(0)$ and R_g , than those obtained from a Guinier analysis as the indirect Fourier transform approach uses the entire scattering curve.

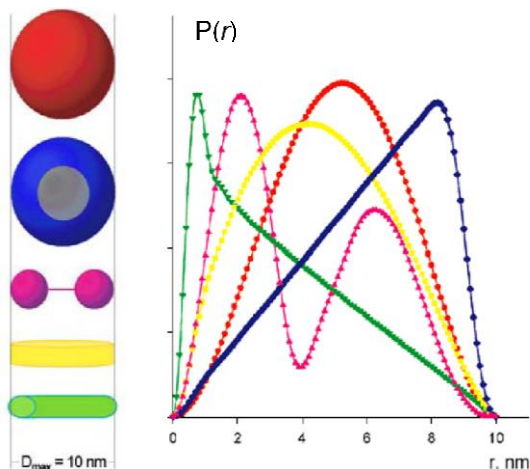


Figure 1.8. $P(r)$ plot curves and their corresponding protein shape. Representative curves for globular (red), hollow sphere (blue), dumbbell (pink), disk shaped (yellow), and elongated molecules. This figure is adapted from (Svergun & Koch, 2003).

The folding of the protein can be evaluated from a Kratky plot ($s^2I(s)$ vs s) (Doniach, 2001) (Figure 1.9). The Kratky plots of a well-folded, globular protein is typically a prominent peak at low s , with the curve returning to 0 at the large s region; the Kratky plot of an unfolded

protein show a continuous increase in $s^2 \times I(s)$ with s , which plateaus at large s ; and for multi-domain proteins connected by flexible linkers, the Kratky plots display a mixture of characteristics of both folded and unfolded proteins.

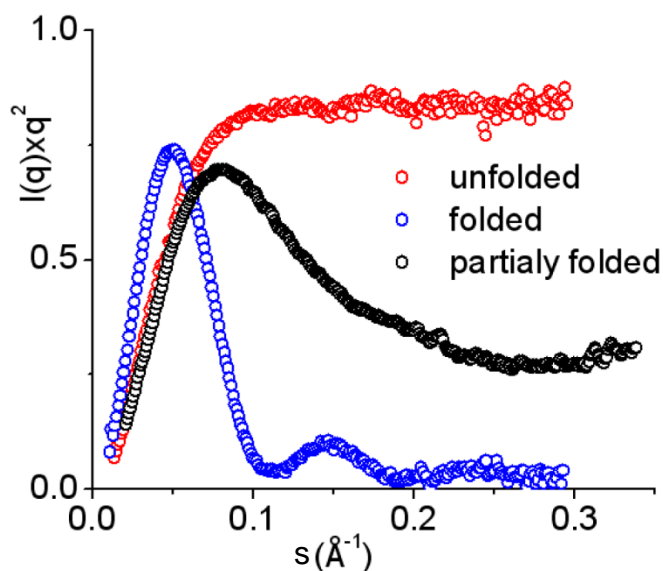


Figure 1.9. Kratky plots corresponding to different folding states of samples. This figure is adapted from a 2012 Bruker lecture: An overview of biological SAXS: instrumentation, techniques, and applications.

Beside this rapid sample characterization from scattering data, a more directed approach is to reconstruct an *ab initio* model from the scattering data, which can estimate overall shape of the particles (Figure 1.10). The most popular *ab initio* bead-modeling programs are DAMMIN (Dummy Atom Model Minimization) (Svergun, 1999), and DAMMIF, a faster *ab initio* bead-modeling program based on DAMMIN (Franke & Svergun, 2009). These programs represent a particle as a collection of many densely packed beads inside a constrained search volume. The method of reconstructing a 3D *ab initio* model from a 1D scattering pattern does not always yield the same model when the program is run multiple times. A comparison of these models from several runs will identify the most persistent features of the model. The programs SUPCOMB (Kozin & Svergun, 2001) and DAMAVER (Volkov & Svergun, 2003) are used to average the models obtained, wherein SUPCOMB is used to superimpose the models to identify the most

probable models; and DAMAVER averages the superimposed models over the ensemble, yielding a smoothed model containing the most persistent features (Figure 1.10). DAMFILT is then used to filter the averaged model created by DAMAVER at a given cut-off volume (Volkov & Svergun, 2003). DAMFILT removes low occupancy and loosely connected atoms according to the frequency map computed by DAMAVER, yielding a more compacted, and also the most probable, model or molecular envelope (Figure 1.10).



Figure 1.10. *Ab initio* models of a protein sample. The outer (sand surface) and inner (grey surface) layers of the model are the output of DAMAVER and DAMFILT respectively.

The *ab initio* analysis of proteins or protein complexes with SAXS is complemented by the high-resolution structural information of the proteins or protein domains. Crystal or NMR structures can be docked into the low-resolution SAXS envelope, and the agreement of the theoretical scattering data calculated from these high-resolution structures to the experimental data can be assessed to determine if it is a good fit. There are several methods used for reconstructing SAXS models by docking high-resolution structures. CRY SOL (Svergun *et al.*, 1995) and Ensemble Optimization Method (EOM) (Tria *et al.*, 2015) were used in this study.

CRY SOL is used to compare the solution scattering of macromolecules to known high-resolution structures (Figure 1.11). In general, a PDB file of the high-resolution structure and the SAXS scattering data file is input, the program calculates the theoretical scattering of the high-resolution structure, and the discrepancy between the calculated theoretical scattering curve of the high-resolution structure and the experimental scattering data is evaluated for the quality of

the fit using the χ^2 test. The limitation of CRY SOL is that a high-resolution structure of the particle is required, and only one PDB file can be input. CRY SOL does not reconstruct models for multi-domain proteins if only individual domain structures are known.

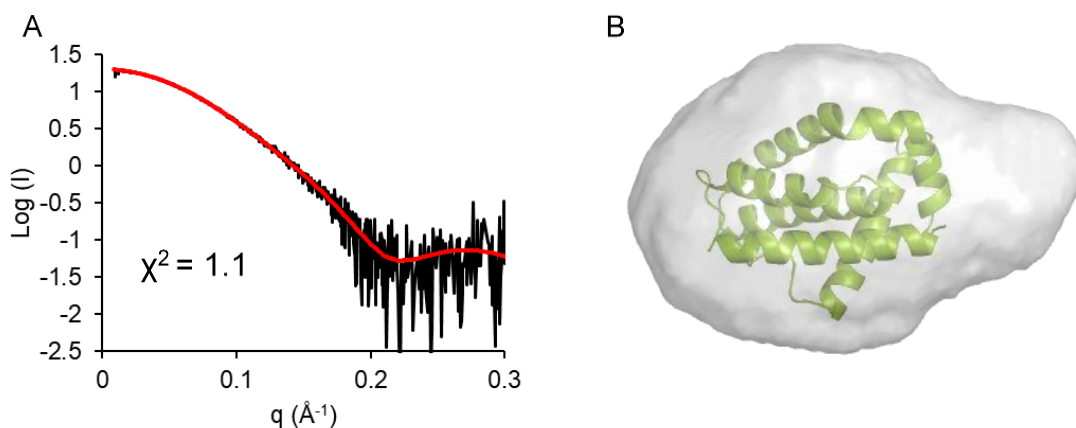


Figure 1.11. Fit of high-resolution protein structure to SAXS of the protein in solution using CRY SOL. (A) Curve fit of experimental data (black) to theoretical scattering (red) calculated from the structure. (B) High-resolution structure (green cartoon) superimposed onto the filtered *ab initio* SAXS envelope (grey surface).

In EOM, a pool of n independent models is generated based on the input sequence and structural information available. Then EOM employs a genetic algorithm to select an ensemble of conformations from the pool that best fits the experimental data (Tria *et al.*, 2015). Genetic algorithm is a search heuristic inspired by the natural evolution theory that select the fittest individuals. The process of genetic algorithm repeats a process of selection of the best fit individuals from the pool, crossover, computing the fitness, and reselection, until the best fit ensemble of individuals are selected. The discrepancy between the theoretical scattering calculated from each conformation and the experimental scattering data is assessed by a χ^2 test to evaluate the quality of fit for each conformer (Figure 1.12A). These R_g and D_{max} distributions of models from the entire initial pool are compared with that of the selected best-fit ensemble of models, to visually delineate overall properties, such as compactness and flexibility, of the sample (Figure 1.12B,C). A narrower R_g or D_{max} distribution of the models in the selected

ensemble indicates these models are less flexible than the models from the initial pool; while a similar R_g and D_{max} distribution of the ensemble models indicate that the selected models are as flexible as those from the pool.

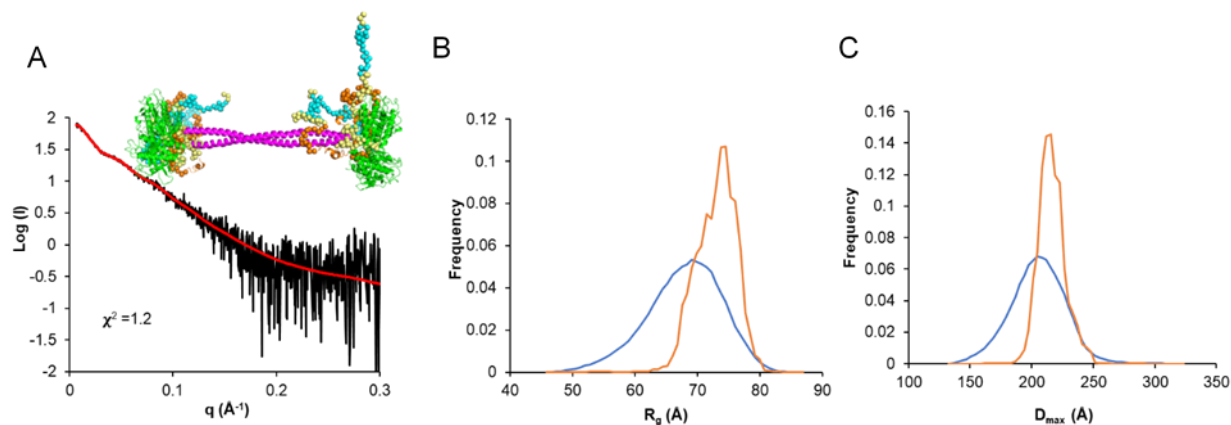


Figure 1.12. EOM analysis for a BECN1 protein fragment. (A) The theoretical scattering curve obtained for an ensemble of models of the BECN1 fragment (red) fit to the experimental SAXS data recorded (black) with a χ^2 value of 1.2. Inset: Structural representations of the 4 models from the ensemble obtained by EOM analysis indicate high flexibility of the N-terminus, shown as spheres. (B) and (C) The initial pool of models with random configurations has a broader distribution of R_g or D_{max} (blue) than that of the selected ensemble (orange).

EOM has many advantages compared to CRY SOL. It can be used to generate disordered regions that are missing from high-resolution structures of a sample (Tria *et al.*, 2015). It allows missing disordered regions to be feasibly modelled without size limitations, using a random or native sequence designation. In addition, EOM can be used to generate oligomeric models. Oligomeric assemblies with flexible regions may be large group of biomolecules, and their analyses involves an extra level of complexity to the ensemble-based modeling. EOM provides an option to input an oligomeric core structure, and use the input complete amino acid sequence and symmetry operators to model in other atomic structures and flexible regions. Further, EOM also generates parameters such as R_{flex} and R_{σ} that can be used to analyze sample flexibility. R_{flex} , is a numerical quantification of the flexibility of the ensemble and the pool. A R_{flex} of 100% indicates maximum flexibility. A comparison of the R_{flex} calculated for the ensemble and pool

can be used to determine if the ensemble is less flexible than the pool. R_σ indicates the difference of the ensemble distribution from that of the original pool. A R_σ value close to 1 is indicative of a fully flexible system. If the R_{flex} of ensemble is smaller than the pool (indicating the ensemble is less flexible than the pool), R_σ should be < 1 . If the ensemble R_{flex} is significantly smaller than that of the pool, but $R_\sigma > 1$, further investigation is required as the results are likely inaccurate.

1.5.3. Isothermal titration calorimetry (ITC)

ITC is used to characterize the thermodynamics of a binding event. Chemical interactions are often associated with a heat exchange with the environment, which can be monitored by ITC. The modern ITC instrument can determine a wide range of dissociation constants, from 10^{-9} M to 10^{-2} M. The measuring unit of the ITC machine is composed of a sample cell and a reference cell that are made of a highly-efficient thermally-conducting and chemically inert material, and sensitive thermopile circuits used to detect temperature differences between the two cells (Figure 1.13). When the ligand or protein is titrated into the sample cell containing its interacting partner, heat is released or absorbed, and the temperature in the sample cell will increase or decrease. Similarly, when a dimeric protein is titrated into the sample cell containing buffer, the dissociation of the dimer also releases or absorbs heat. In order to keep the sample cell and reference cell temperature the same, the power supplied to heat the sample cell will be decreased or increased accordingly. The heat change during the time span of each titration is then calculated by integrating the change in power supplied. Therefore, each titration produces a positive or negative heat signal (Freyer and Lewis, 2008).

During data analyses, integration of the heat peaks provides an estimate of the enthalpy of interaction (ΔH). ΔH is represented by the distance between the two asymptotic lines of the binding curve corresponding to the minimal and maximal heat formation (Figure 1.13). Then an

interaction model or dissociation model is fit into the integrated data, and used to calculate the association constant, K_a ($K_a = 1/K_d$, where K_d is the dissociation constant) and stoichiometry, n (Figure 1.13). The slope at the inflection point of the binding curve reflects K_a . The molar ratio at the inflection point of the binding curve is the stoichiometry. The change in the Gibbs free energy (ΔG) and change in entropy (ΔS) of the reaction can be calculated from ΔH , K_a and reaction temperature. To accurately determine these binding parameters, it is important to obtain a sigmoidal binding curve. Therefore, optimization of sample concentration is required if the binding curve is not sigmoidal.

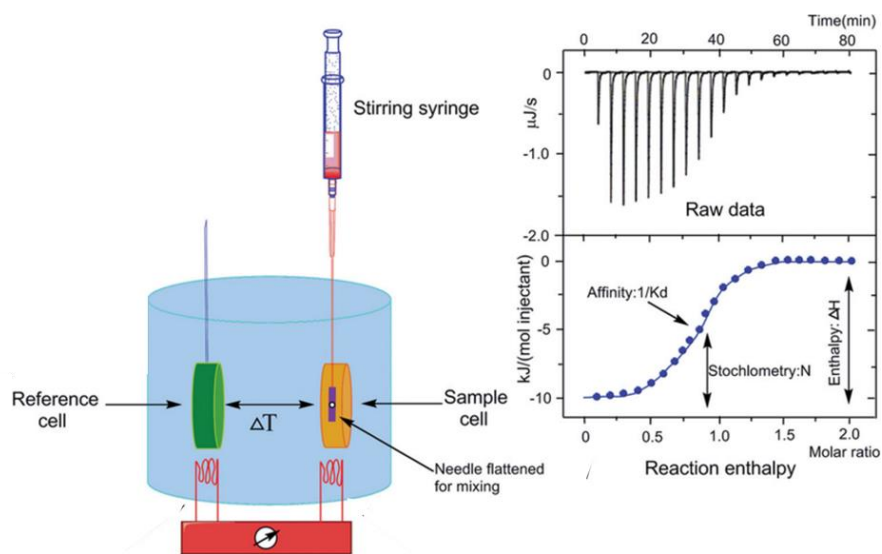


Figure 1.13. Basic principle of ITC. Left: schematic representation of the ITC instrument; right: the raw data (represented as heat per second released for each titration) of a characteristic titration experiment (top) and the fit to an independent interaction model (bottom). Figure is adapted from (Song *et al.*, 2015).

1.5.4. Circular dichroism (CD)

CD was used to investigate the secondary structure composition of proteins in this study. CD detects the difference in the absorption of left-handed and right-handed circularly polarized light by the sample (Greenfield, 2006b). Proteins are chiral molecules, and therefore absorb left-handed and right-handed circularly polarized light differently. In the far UV range (below 250 nm) of CD, the geometric relation between the amide groups of the protein backbone determines the characteristic

CD spectra (Sreerama & Woody, 2004). Therefore, each type of protein secondary structure has a specific CD signature, which makes CD a powerful method to characterize the secondary structure of proteins. CD spectra of proteins is mainly composed of α -helices that have two negative peaks at 208 nm and 222 nm respectively, and a positive peak at 193 nm (Figure 1.14); CD spectra of proteins consisting of β -strands have a positive peak at 195 nm and a negative peak at 218 nm (Figure 1.14); CD spectra of completely disordered proteins have a negative peak near 195 nm and very low ellipticity at wavelengths above 210 nm (Figure 1.14).

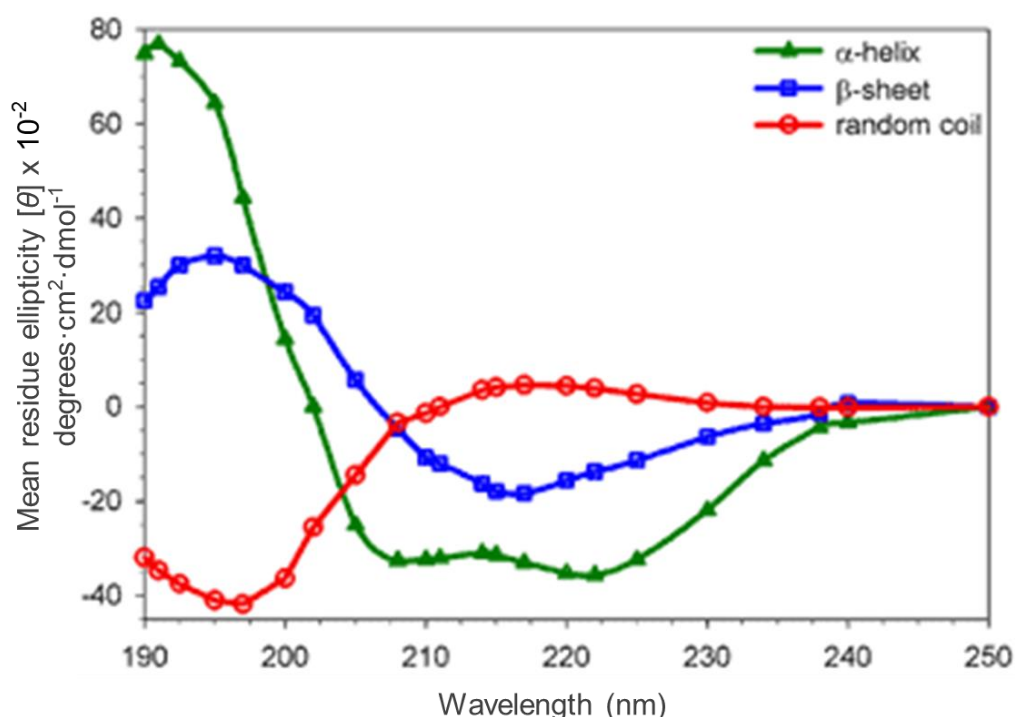


Figure 1.14. CD spectra of proteins composed of different secondary structure. This figure is adopted from “Experimental methods to study protein structure and folding” published by Louise McBride at SlidePlayer.

The CD spectra of a protein is reported as a plot with wavelength as x-axis and mean residue ellipticity ($[\theta]$) as the y-axis with the unit of degrees $\cdot \text{cm}^2 \cdot \text{dmol}^{-1}$. The equation, $[\theta] = \theta \times 10^6 / (C \times l)$, is used to calculate the mean residue ellipticity. In this equation, θ is the dichroism in millidegrees that is read directly from the result output from the CD instrument; C is the sample concentration times the concentration of residues in μM ; l is the pathlength in mm. Further, the

secondary structure content of the protein can be quantitatively estimated by analyzing the CD spectrum using programs in the CDPro program package (Sreerama & Woody, 2000).

CD was also used to study the thermal stability of the proteins in this study. When a protein unfolds upon heating, it loses highly ordered structures such as α -helices, resulting in a change in the CD spectra. Therefore, monitoring the change of the molar ellipticity at a wavelength that is characteristic of the most prevalent secondary structure in that protein, as a function of temperature reflects the unfolding process. Since the CD spectrum for helical proteins has negative peaks at 208 nm and 222 nm (Figure 1.14), whereas proteins mainly comprised of coils have no ellipticity at 208 nm and 222 nm (Figure 1.14), monitoring the change of ellipticity at 222 nm during thermal unfolding of a helical protein enables us to determine the denaturing temperature of this protein by fitting the melting curve with the Boltzmann model. 222 nm is preferred to 208 nm because the signal to noise ratio is larger at 222 nm (Greenfield, 2006a).

1.5.5. Hydrogen/deuterium exchange mass spectrometry (HDX-MS)

HDX-MS is another important technique for examining the structural and dynamic characteristics of proteins in solution. Hydrogen atoms in O-H, N-H, and S-H groups that are not stably hydrogen-bonded, such as in disordered regions, are labile, which means they can rapidly exchange with the surrounding water. Therefore, if the protein is exposed to D₂O instead H₂O, the hydrogen atoms of O-H, N-H, and S-H are exchanged with deuterium from the D₂O, resulting in an increase in the mass of the deuterium-exchanged protein molecules. Although the deuterium exchange also occurs at the side chains, the HDX-MS study is typically focused on the backbone deuterium exchange because the side chain deuterium exchange can be ignored

compared to that of the backbone as every amino acid (except the first amino acid and proline in the polypeptide) in the backbone has a N-H group.

The N-H \rightarrow N-D conversion rate is dependent on the structural characteristics of the protein. Regions with higher order structure have lower conversion rates as the residues from these regions are involved in forming intramolecular N-H \cdots O=C hydrogen bonds. Additionally, for these structured regions, solvent accessibility to the N-H sites is restricted further as they are often buried within the protein. The protection factor P is used to describe the conversion rate relative to that of N-H from disordered, solvent-exposed residues. $P = k_{ch}/k_{HDX}$, wherein k_{ch} is the N-H \rightarrow N-D conversion rate constant of N-H from disordered, solvent-exposed residues; and k_{HDX} is that of the N-H from protected residues. For some well-folded regions of protein, the P could exceed 10^6 . On the other hand, some protected N-H groups may undergo the N-H \rightarrow N-D conversion at a measurable rate due to the conformational fluctuations.

There are several steps for a typical HDX-MS experiments (Figure 1.15). The first step is deuterium exchange, wherein a native protein is exposed to D₂O for different time spans (including a “0” time point or maintained in H₂O), such that the deuterium incorporation can be monitored as a function of exposure time. The time points typically range from minutes to hours. The deuterated samples are then quenched immediately to terminate the deuterium exchange. The quenching buffer usually has a very low pH of 2.5 that substantially decreases the N-H \rightarrow N-D conversion rate. The deuterated proteins are non-specifically proteolyzed by flowing the protein over an immobilized pepsin column. The digested peptides are desalted and separated by reverse phase liquid chromatography (RPLC), and analyzed by ESI-MS. The digestion and LC step need to be performed as rapidly as possible, at 0 °C, in a low pH buffer, to prevent back

exchange of deuterium. Measurements can also be performed at the intact protein level to analyze the overall deuterium incorporation.

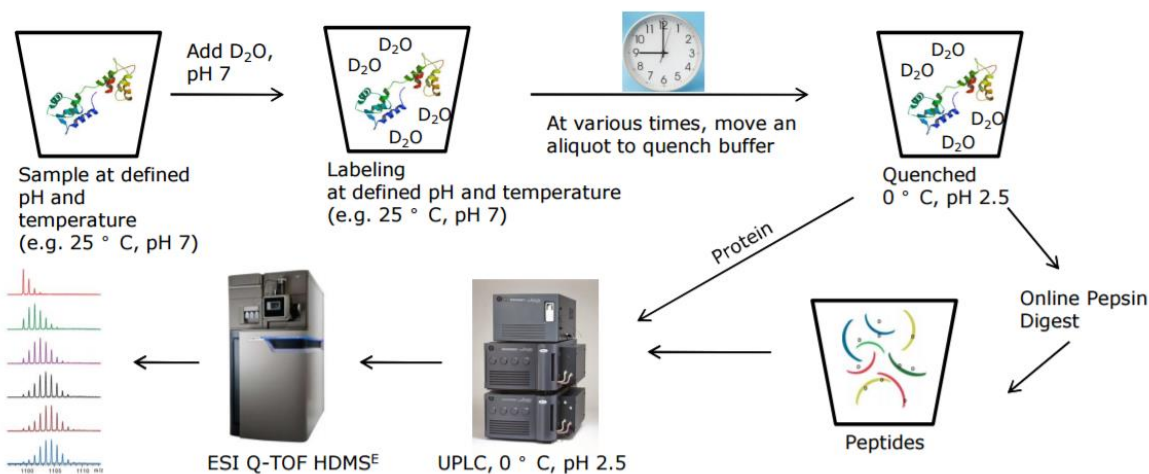


Figure 1.15. HDX-MS experimental procedure. The steps can be summarized as deuteration, quenching, digestion, and MS. Figure is obtained from slides of HDX-MS instruction made by Waters Corporation.

The total ion chromatogram (Figure 1.16A) depicts the HPLC elution profile of digested peptides as detected by the mass spectrometer, which sums up intensities of all mass spectra peaks. A specific m/z ratio that corresponds to a specific peptide is located in the total ion chromatogram and extracted to generate the “extracted ion chromatogram” (Figure 1.16B). The mass spectra contained within the elution peak of this extracted chromatogram are averaged to yield the isotope envelope pattern for the peptide of interest (Figure 1.16C). The isotopic distribution pattern for the peptide of interest shifts to higher mass number as incubation time increases due to increased deuterium incorporation over time (Figure 1.16C, comparison of top and bottom panel).

The area under the peaks (i.e., the centroid) is determined. The number of deuterons (D) incorporated by each peptide at each D₂O time point is calculated using equation 1.10:

$$D(t) = N \frac{m(t) - m_0}{m_{100} - m_0} \quad (1.10)$$

In equation 1.10, N is the number of exchangeable amide hydrogens, $m(t)$ is the centroid mass of the peptide at time t , m_{100} and m_0 are the theoretical mass of the peptide with 100% and 0% deuteration. $D(t)$ can be plotted against time to generate the deuterium uptake plot (Figure 1.16D). The results of the experiment are typically represented in a protein heat map showing the coverage of digested peptides as well as the deuterium exchange rate for amide hydrogens as a function of time, across the entire protein sequence (Figure 1.16E).

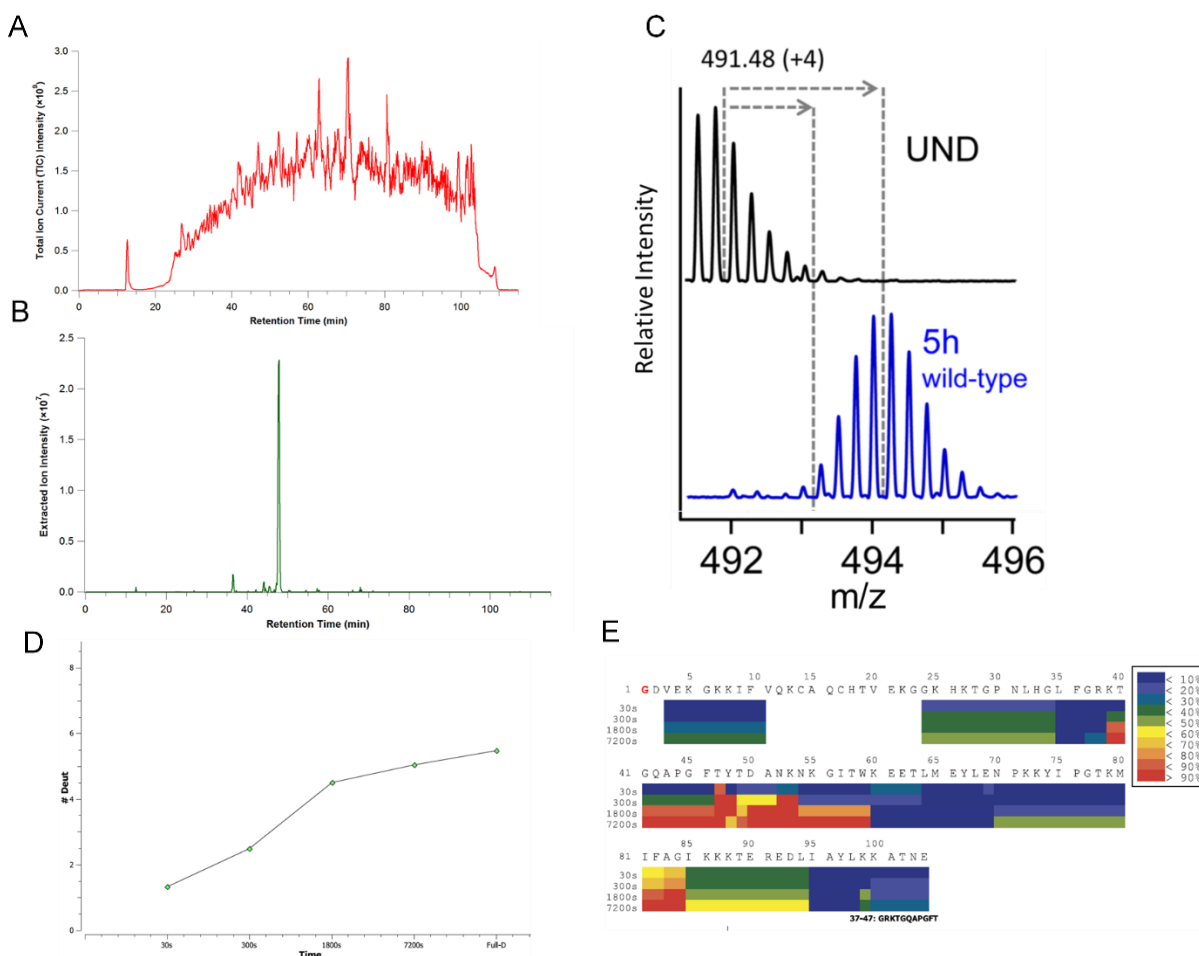


Figure 1.16. HDX-MS data analysis of an example protein. (A) The total ion chromatogram. (B) Extracted ion chromatogram of a specific m/z corresponding to a specific peptide. (C) The isotope envelope of that peptide generated by averaging the peaks under the extracted ion chromatogram. Upper panel: isotope envelope of undeuterated sample; bottom panel: isotope envelope of deuterated sample. (D) Deuterium uptake plot over time. (E) Heat map of the entire protein, colors from blue to red represent different deuterium exchange rates as illustrated by the legend. Figures are adapted from https://en.wikipedia.org/wiki/Mass_chromatogram and (Wales *et al.*, 2013, Campobasso & Huddler, 2015).

1.6. Specific Aims of This Study

BECN1, an interaction hub of proteins, plays an essential role in regulating autophagy, hence, it is important to understand the structure-based mechanism of autophagy proteins that regulate BECN1. The goal of this dissertation is to investigate structures of BECN1 and BECN2, and selected mechanisms by which autophagy regulators regulate BECN1-mediated autophagy.

The specific aims of this research are:

1. To prepare samples of full-length BECN1 wild-type (WT) and invariant cysteine mutants. These samples will be used to assess the role of these cysteines in binding Zn^{2+} and maintaining the structure of the BECN1 IDR.
2. To prepare samples of the BECN1 CCD, BARAD, and CCD-BARAD that are well-behaved in solution and can be used for ITC to assess dimer dissociation of each BECN1 fragment, and for SAXS to investigate structural transitions of the BECN1 Overlap Helix (OH).
3. To prepare protein samples of BECN2 CCD and BECN1 CCD mutants to elucidate the structure of the BECN2 CCD and BECN2 interaction with BCL2 proteins. These proteins samples were used to obtain crystals of BECN2 CCD mutants and to test the interaction of BECN2 with anti-apoptotic BCL2 proteins by ITC.
4. To structurally investigate the mechanism by which the conserved mammalian protein, GAPR-1, down-regulates BECN1-mediated autophagy.
5. To characterize the interactions between the VMP1 ATGD and BECN1 BH3D.
6. To investigate the molecular mechanisms by which the binding of BCL2 homologs to BECN1 down-regulates autophagy.

CHAPTER 2. DETERMINING WHETHER THE INVARIANT CXXC MOTIFS IN THE BECN1 IDR BIND Zn^{2+}

2.1. Introduction

Autophagy is often triggered by various forms of nutrient depletion, with nitrogen and carbon starvation being amongst the best-known triggering signals. Recent reports indicate that Zn^{2+} starvation also triggers autophagy to enable Zn^{2+} homeostasis (Kawamata *et al.*, 2017). Conversely, earlier studies showed that Zn^{2+} up-regulates autophagy, as Zn^{2+} depletion inhibits autophagy, and excessive Zn^{2+} increases tamoxifen, H_2O_2 , ethanol, and dopamine triggered autophagy (Hung *et al.*, 2013, Hwang *et al.*, 2010, Lee & Koh, 2010, Liuzzi & Yoo, 2013). However, the mechanism(s) by which Zn^{2+} regulates autophagy is unknown.

The presence of two or more conserved CXXC motifs in protein sequences is often indicative of metal-, especially Zn^{2+} -binding as summarized in the Metalloprotein Database and Browser (MDB) (Castagnetto *et al.*, 2002). Cys-bound Zn^{2+} has diverse functions in protein structure, catalysis and regulation (Pace & Weerapana, 2014). Zn^{2+} -fingers, perhaps the best-understood examples of cys-bound Zn^{2+} , are structural motifs which function in DNA binding (Klug *et al.* 2011). Cys-bound Zn^{2+} also catalyzes enzymatic transformations in oxidoreductases, transferases, and hydrolases (Pace & Weerapana, 2014). Cys-bound Zn^{2+} also has regulatory functions, such as inhibiting enzyme activity by binding to enzyme inhibitory sites, serves as redox-switches, and stabilizes protein interfaces (Maret, 2013, 2012). Lastly, cys-bound Zn^{2+} regulates cellular Zn^{2+} levels by storing and redistributing Zn^{2+} , as in cys-rich metallothioneins (Maret *et al.*, 1997, Heinz *et al.*, 2005).

BECN1, contains two invariant CXXC motifs, $^{18}CXXC^{21}$ and $^{137}CXXC^{140}$, in its poorly conserved IDR (Figure 2.1), suggesting it might bind Zn^{2+} . Here, we used inductively coupled

mass spectrometry (ICP-MS) to assess and compare Zn²⁺-binding by wild type (WT) BECN1 and BECN1 mutants, wherein the invariant cys were mutated to ser.

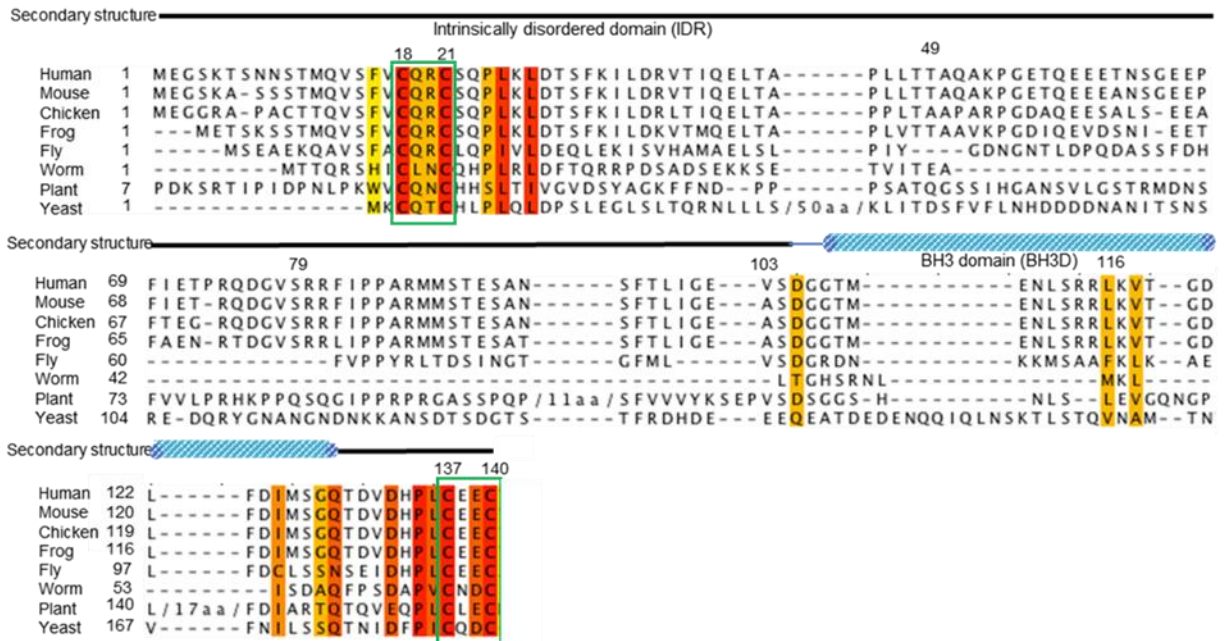


Figure 2.1. Sequence alignment of BECN1 orthologs from diverse organisms. Increasing background color intensity corresponds to increasing residue conservation, with red representing invariant residues. Experimentally determined secondary structure is displayed above the alignment, with cylinders representing helices, and lines representing coils, color-coded by domains as follows: IDR (black), BH3D (cyan). The two CXXC motifs are boxed in green.

2.2. Materials and Methods

2.2.1. Creation of protein expression constructs

Human BECN1 residues 1-450 (FL) was cloned between the *Bam*HI and *Xho*I restriction enzyme sites of the pMBP-Parallel-1 bacterial expression vector and a triad mutation F359D/F360D/W361D made at the aromatic finger of BARAD (the mutant is named as MBP-BECN1^{AFM} FL) using the QuikChange II Site-Directed Mutagenesis Kit (Agilent Technologies) to prevent protein aggregation during purification. Subsequently, the MBP-BECN1^{AFM} FL was used as a template to make cysteine mutants, including MBP-BECN1^{AFM,C18S/C21S} FL, MBP-BECN1^{AFM,C137S/C140S} FL, and MBP-BECN1^{AFM,CysTetrad} FL (C18S/C21S/C137S/C140S) by site-

directed mutagenesis using the QuikChange II Site-Directed Mutagenesis Kit (Agilent Technologies). These BECN1 constructs are summarized in Table 2.1.

Table 2.1. BECN1 constructs used in Chapter 2.

	Label	Description
1	MBP-BECN1 ^{AFM} FL	BECN1 full length (1-450, F359D,F360D,W361D) fusion protein
3	MBP-BECN1 ^{AFM,C18S/C21S} FL	BECN1 full length (1-450, C18S,C21S,F359D,F360D,W361D) fusion protein
4	MBP-BECN1 ^{AFM,C137S/C140S} FL	BECN1 full length (1-450, C137S,C140S,F359D,F360D,W361D) fusion protein
5	MBP-BECN1 ^{AFM,CysTetrad} FL	BECN1 full length (1-450, C18S,C21S,C137S,C140S,F359D,F360D,W361D) fusion protein

2.2.2. Protein expression and purification

Separate aliquots of *E. coli* Arctic Express cells were transformed with expression plasmids for each BECN1 construct (Table 2.1) and grown at 30 °C in LB medium with 100 µg/mL ampicillin to an OD₆₀₀ = 0.6 (log phase). Then the temperature was equilibrated to 13 °C, protein expression induced by addition of 0.5 mM isopropyl thio-β-D-galactoside, and proteins were expressed at 13 °C for 18-20 hours. The cells were harvested via centrifugation at 4000 g for 20 min, then the harvested cells were washed with lysis buffer (50 mM Tris pH 8.0, 300 mM NaCl, 1 mM EDTA, 2 mM DTT), and re-pelleted by centrifugation at 4000 g for 30 min prior to storage at -80 °C. Frozen pellets were thawed and resuspended in 30 ml lysis buffer/L of culture that was pelleted, and a tablet of protease inhibitor cocktail (Bimake) added per 15 ml of resuspended cells, prior to lysis using a NanoDeBEE emulsifier (BEE International) or a sonicator. The lysate was centrifuged at 20,000 g for 30 min to pellet down cell debris and clarify the lysate. At all subsequent stages of purification, the purity of the protein sample was evaluated using SDS-PAGE. The clarified lysate was then passed over 10 mL of amylose affinity resin (GE Healthcare) in a gravity column, then unbound contaminants washed off using 200 ml of lysis buffer. Since EDTA was added to the lysis buffer to inhibit the protease activity, some

Zn²⁺ bound to BECN1 may have been chelated, therefore to replenish any Zn²⁺ that had been lost, three additional washes were performed: 100 ml of Wash Buffer 1 (50 mM Tris pH 8.0; 300 mM NaCl) to wash off residual lysis buffer; 50 ml of Wash Buffer 2 (50 mM Tris pH 8.0; 300 mM NaCl; 0.2 mM ZnAc) to add back chelated Zn²⁺; and 100 ml of Wash Buffer 1 to wash of any unbound Zn²⁺. Finally, the protein was eluted from the amylose resin with Elution Buffer (50 mM Tris pH 8.0; 300 mM NaCl; 2 mM DTT; 25 mM maltose). This protocol was followed for all MBP-BECN1^{AFM} samples, including the Cys mutants, all of which have a theoretical molecular mass of 95.2 kDa. After amylose affinity chromatography, the protein was further purified by SEC using a Superose 6 increase 10/300 GL column (GE Healthcare) in SEC buffer comprising 50 mM Tris pH 8.0; 150 mM NaCl, and the purified protein concentrated in the SEC buffer and stored at -80 °C.

Lastly, an additional MBP-BECN1^{AFM} sample was prepared wherein any Zn²⁺ lost due to chelation by EDTA-containing buffers was not replenished by washing with Wash buffers 1 and 2 and EDTA was included in the SEC buffer as well.

2.2.3. ICP-MS

ICP-MS, performed at Redox Biology Center of University of Nebraska Lincoln, was used to identify and quantify the metal bound to the purified proteins samples. Briefly, the samples were digested by a metal grade 33% v/v HNO₃ for in-solution protein digestion. The acid was used to remove all the attached metal ions in the solution, which was then quantified by MS. The digested protein in solution was screened for 18 metal elements: Li, B, Na, K, S, P, Mg, Ca, Mn, Fe, Ni, Co, Cu, Zn, As, Se, Mo and Cd. Gallium was used as an internal standard. The results were reported as μmol metal/μmol protein sample.

2.3. Results

2.3.1. Expression and purification results of BECN1 constructs

The different constructs (Table 2.1) were over-expressed in *E. coli* Arctic Express cells and purified to homogeneity by amylose affinity chromatography, followed by SEC. Despite the small aggregation shoulder, the major SEC peak on SEC and corresponding single band on SDS-PAGE indicated that each SEC sample was pure and homogenous (Figure 2.2, 2.3, 2.4, and 2.5).

The apparent molecular mass of MBP-BECN1^{AFM} FL, calculated from the elution volume (14.30 ml) of the major SEC peak (Figure 2.2), is 398.1 kD, which is ~2 times larger than the theoretical molecular mass of the MBP-BECN1^{AFM} FL homodimer. This agrees with the fact suggesting that MBP-BECN1^{AFM} FL is an elongated homodimer. The final yield of the purified MBP-BECN1^{AFM} FL was 2 mg / L of bacterial culture.

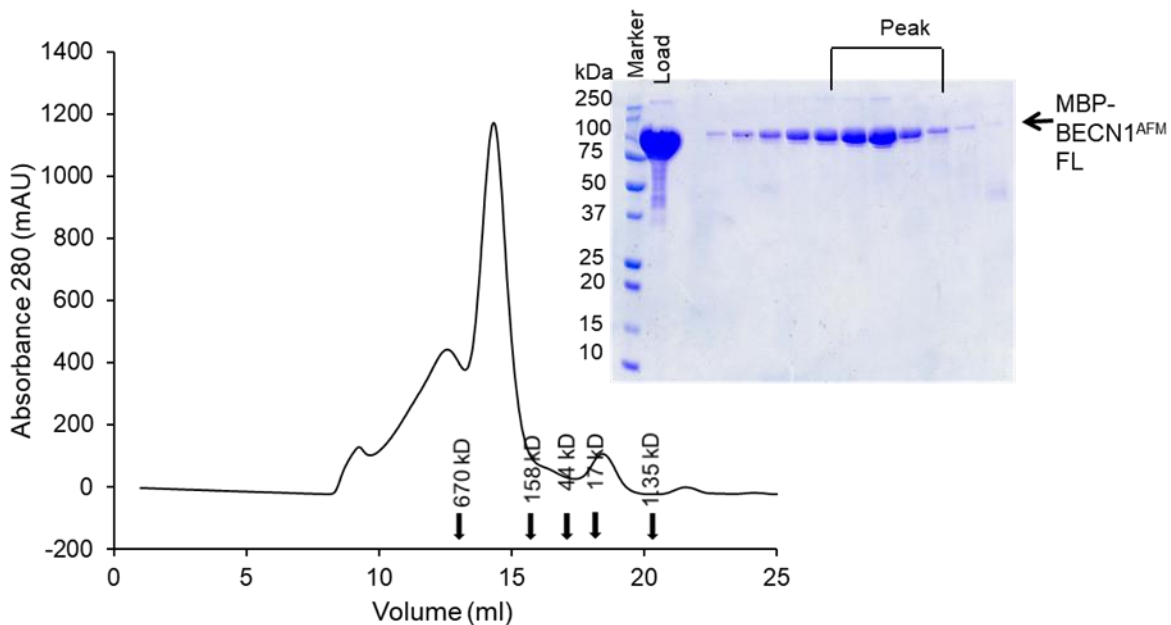


Figure 2.2. Size exclusion chromatogram and the corresponding SDS-PAGE of MBP-BECN1^{AFM} FL. The elution positions of SEC standards are indicated by arrows.

The apparent molecular mass of MBP-BECN1^{AFM,CysTetrad} FL, calculated from the elution volume (13.80 ml) of the major SEC peak (Figure 2.3), is 545.8 kD, which is ~2.9 times larger

than the theoretical molecular mass (Table 2.1), suggesting that MBP-BECN1^{AFM} FL forms an elongated homodimer. The final yield of the purified MBP-BECN1^{AFM,CysTetrad} FL was 3.3 mg / L of bacterial culture.

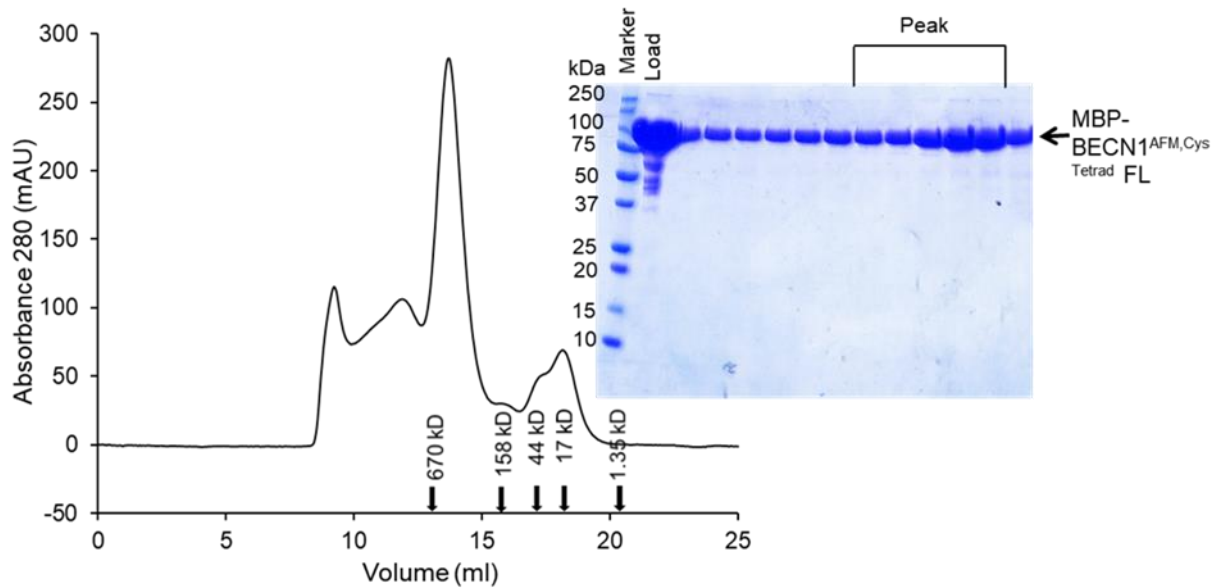


Figure 2.3. Size exclusion chromatogram and the corresponding SDS-PAGE of MBP-BECN1^{AFM,CysTetrad} FL. The elution positions of SEC standards are indicated by arrows.

The apparent molecular mass of MBP-BECN1^{AFM,C18S/C31S} FL, calculated from the elution volume (14.16 ml) of the major SEC peak (Figure 2.4), is 426.6 kD, which is ~2.2 times larger than the theoretical molecular mass (Table 2.1), suggesting that MBP-BECN1^{AFM,C18S/C31S} FL forms an elongated homodimer. The final yield of the purified MBP-BECN1^{AFM,C18S/C31S} FL was 4.4 mg / L of bacterial culture.

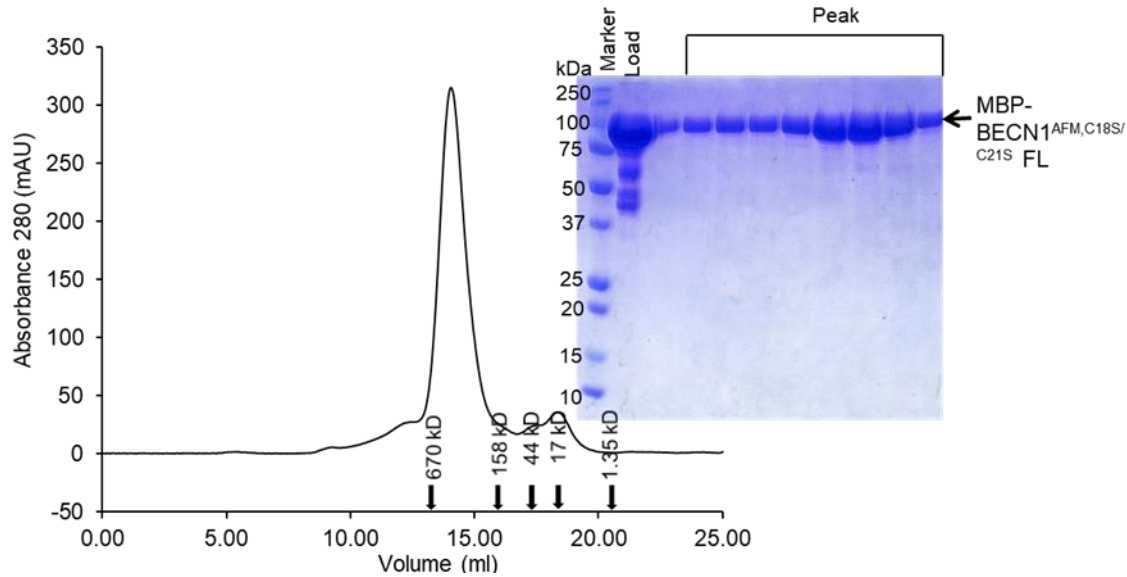


Figure 2.4. Size exclusion chromatogram and the corresponding SDS-PAGE of MBP-BECN1^{AFM, C18S/C31S} FL. The elution positions of SEC standards are indicated by arrows.

The apparent molecular mass of MBP-BECN1^{AFM, C137S/C140S} FL, calculated from the elution volume (13.91 ml) of the major SEC peak (Figure 2.5), is 501.2 kD, which is ~2.2 times larger than the theoretical molecular mass (Table 2.1), suggesting that MBP-BECN1^{AFM, C137SS/C140S} FL forms an elongated homodimer. The final yield of the purified MBP-BECN1^{AFM, C137S/C140S} FL was 2.3 mg/ L of bacterial culture.

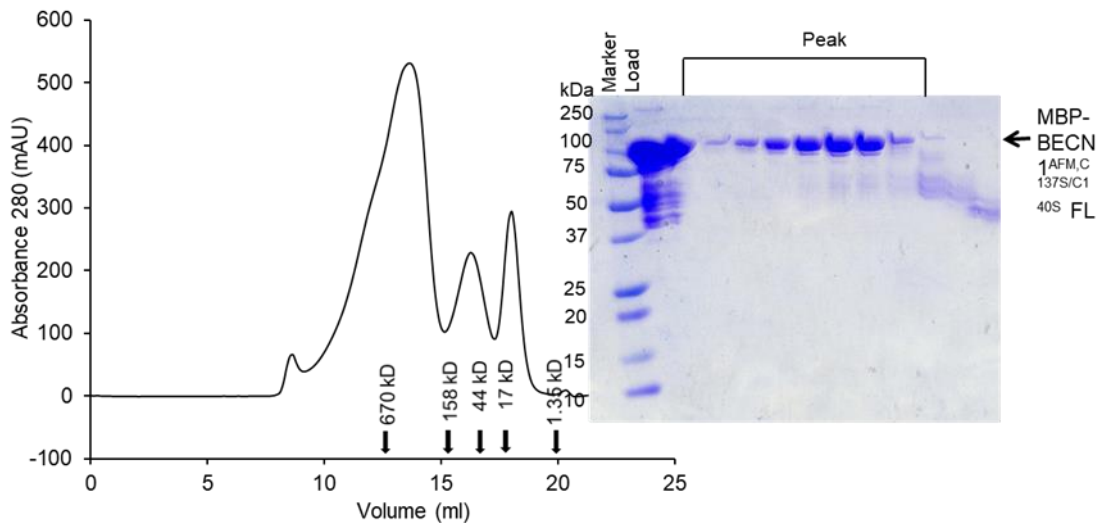


Figure 2.5. Size exclusion chromatogram and the corresponding SDS-PAGE of MBP-BECN1^{AFM, C137S/C140S} FL. The elution positions of SEC standards are indicated by arrows.

2.3.2. CXXC motifs of BECN1 are responsible for binding Zn²⁺

ICP-MS results show that MBP-BECN1^{AFM} FL binds Zn²⁺ in a 1:1 molar ratio, while the MBP-BECN1^{AFM,CysTetrad} FL barely binds Zn²⁺ (Figure 2.6), indicating the CXXC motifs of BECN1 are required for binding Zn²⁺. To determine if both the CXXC motifs are required for Zn²⁺ binding, we also quantified Zn²⁺-binding of MBP-BECN1^{AFM,C18S/C21S} FL and MBP-BECN1^{AFM,C137S/C140} FL. The results show that both MBP-BECN1^{AFM,C18S/C21S} FL and MBP-BECN1^{AFM,C137S/C140} FL bind Zn²⁺ in a ~1:0.5 ratio, suggesting that mutation of either CXXC motifs decreases Zn²⁺-binding by BECN1. We also assessed Zn²⁺-binding by BECN1 in the presence of 1 mM EDTA, and find that MBP-BECN1^{AFM} FL binds Zn²⁺ in a ~1:0.6 molar ratio, suggesting that BECN1 binds Zn²⁺ tightly and EDTA only partially chelates the bound Zn²⁺.

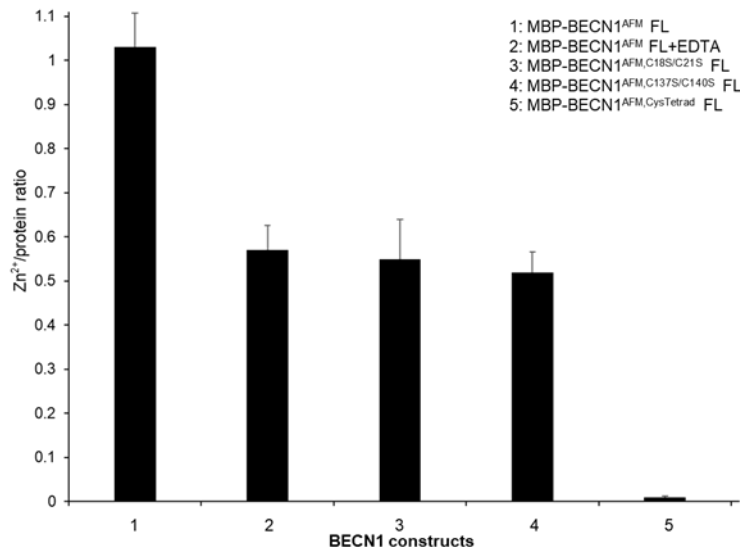


Figure 2.6. ICP-MS results for all the samples in Table 2.1.

2.4. Conclusions and Discussion

Zn²⁺ is essential for cell growth and cells need to maintain Zn²⁺ homeostasis when the availability of Zn²⁺ fluctuates. Transcriptional regulation is a classic way to maintain Zn²⁺ homeostasis, wherein Zap1 activates expression of genes that are responsible for Zn²⁺ uptake from the vacuole when the cells are exposed to Zn²⁺ starvation (Ehrensberger & Bird, 2011).

However, when Zn^{2+} drops to very low levels, other pathways such as autophagy may be induced. Growing evidence shows that Zn^{2+} availability regulates autophagy, though in different ways (Kawamata *et al.*, 2017, Hung *et al.*, 2013, Lee & Koh, 2010, Hwang *et al.*, 2010, Liuzzi & Yoo, 2013). For instance, Zn^{2+} -starvation may trigger autophagy, resulting in the degradation of Zn^{2+} -binding proteins, and the recycling of Zn^{2+} ions for more essential cellular roles. Zn^{2+} starvation has been implicated in inactivating TORC1, thereby up-regulating autophagy (Kawamata *et al.*, 2017). However, TORC1 has no Zn^{2+} -binding site, so this regulation may be indirect. Conversely, Zn^{2+} down-regulates tamoxifen-, H_2O_2 -, ethanol-, and dopamine-mediated autophagy (Hung *et al.*, 2013, Lee & Koh, 2010, Hwang *et al.*, 2010, Liuzzi & Yoo, 2013). Perhaps BECN1, as a critical up-regulator of autophagy, which we have shown has two conserved CXXC motifs that bind Zn^{2+} , may serve as a Zn^{2+} -sensor for autophagy.

Our ICP-MS analysis shows that the CXXC motifs of BECN1 bind Zn^{2+} , and mutation of both CXXC motifs completely abrogates Zn^{2+} -binding by BECN1, while mutation of either CXXC motif decreases the Zn^{2+} -binding, potentially impacting BECN1 conformation, especially of the IDR, and interactions with other autophagy regulators. Therefore, further studies are required to understand how Zn^{2+} -binding by BECN1 impacts autophagy.

CHAPTER 3. STRUCTURAL TRANSITIONS IN CONSERVED, ORDERED BECN1 DOMAINS ESSENTIAL TO REGULATING AUTOPHAGY¹

3.1. Introduction

BECN1 is a conformationally-flexible protein that has at least four domains (Mei, Glover, *et al.*, 2016) as described in Chapter 1. Interestingly, residues 248-264 preceding the BARAD form a helical region that we have named the “overlap helix” (OH), because it has been crystallized in two differently-packed states: (i) as part of the anti-parallel CCD homodimer (Mei, Su, *et al.*, 2016, Li *et al.*, 2012), constituting the C-terminal four turns of each CCD; or (ii) packed against the BARAD (Huang *et al.*, 2012). In the structure of the quaternary complex of yeast VPS34/PI3KC3, VPS15, VPS30/BECN1 and VPS38/UVRAG, VPS30 residues 304-327 (equivalent to residues 248-271 of the human BECN1 OH and BARAD) are part of the VPS30/BECN1 CCD and pack against the CCD of VPS38/UVRAG, stabilizing the parallel CCD heterodimer (Rostislavleva *et al.*, 2015). This led to the assumption that the OH is part of the CCD in the context of full-length BECN1. Notably, mass spectroscopy hydrogen-deuterium exchange experiments indicate that VPS30 residues 312-327 (equivalent to BECN1 residues 256-271), which comprise the latter half of the OH, undergo membrane-binding induced conformational changes, although these residues do not directly bind membranes (Rostislavleva *et al.*, 2015). Thus, different conformational states of the BECN1 OH likely play important roles in regulating protein:membrane or protein:protein interactions.

¹ The material in this chapter was co-authored by Dr. Karen Glover and Yue Li. Dr. Karen Glover prepared protein samples, collected and analyzed CD and SAXS data, performed some of the ITC experiments, and wrote out most of the draft of this chapter. Yue Li prepared some of the mutant constructs and protein samples, the ITC experiments, and contributed in revising the draft written by Dr. Karen Glover. Yue Li also had primary responsibility for the crystallization and EPR experiments for the BECN1 CCD-BARAD.

Co-immunoprecipitation assays show that the BECN1 homodimer exists in cells (Adi-Harel *et al.*, 2010). Inclusion of the OH as part of the anti-parallel CCD homodimer would greatly increase stability of the autophagy-inactive homodimer. However, it is unknown whether the BECN1 OH is part of the CCD or the BARAD when BECN1 is not part of PI3KC3 complexes; nor have the factors that regulate this conformational change been established.

Superimposition of the human BECN1 OH of the OH+BARAD (PDB ID: 4DDP) and one chain of the CCD homodimer (PDB ID: 5HHE) reveals the OH cannot simultaneously be within the CCD and packed against the BARAD, as there are extensive steric conflicts between the BARAD and the partner helix of the CCD (Figure 3.1). Further, the same five OH residues: V250, M254, A257, L261, and L264, involved in the CCD homodimer interface also pack against the BARAD (Figure 3.1). Thus, the OH in the CCD and OH+BARAD crystal structures represent mutually exclusive conformations of BECN1.

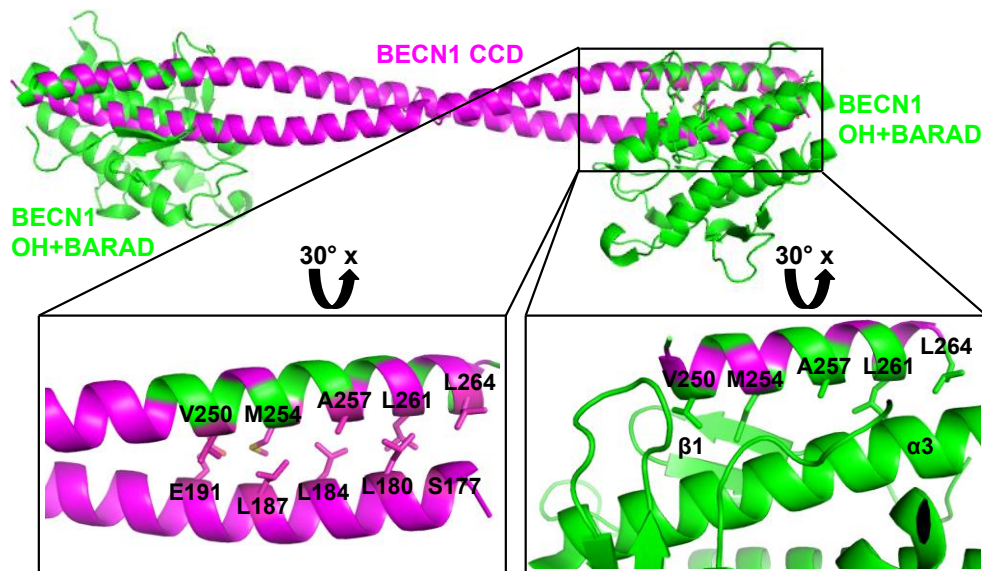


Figure 3.1. The OH has two different packing states. The BECN1 CCD (magenta) and BARAD (green) are shown in ribbon. The OH in the CCD and BARAD structures are superimposed. Boxes indicate regions that are rotated 30° about the x-axis and enlarged to show the mutually exclusive packing arrangement of interacting OH side chains displayed as sticks. The first β -sheet and third helix of the BARAD, against which the OH side chains pack, are labeled $\beta 1$ and $\alpha 3$ respectively. This and other molecular figures were made using PyMOL (v.1.5.0.2; Schrödinger) (Schrodinger, 2015).

Approximately 1359 Å² of surface area are buried upon OH packing against the BARAD, significantly more than the 937 Å² buried when the OH packs within the CCD. Within the CCD, OH residues are only involved in paired interactions. However, OH residues pack against the first β-sheet and third α-helix of the BARAD (Figure 3.1) resulting in more extensive packing.

Each of the OH interface residues are largely conserved from yeast to human (Figure 3.2A). The position equivalent to human M254 is least well conserved, although all examined vertebrates have an M or V at equivalent positions. In comparison to the OH, residues of the partner BECN1 CCD that pack against the OH are not as well conserved (Figure 3.2B). Based on this preliminary analysis, we hypothesized that simultaneous alanine mutagenesis of four of the common OH interface residues; V250A, M254A, L261A, and L264A (Tetrad mutant) would differently impact structure and stability of the CCD and BARAD. Structural and thermodynamic analyses of these differences would allow us to determine whether the OH is part of the CCD, packs against the BARAD, or transitions between the two states.

In order to determine the packing state of the OH in the absence of heterologous binding partners, we investigated the solution structure of BECN1 CCD-BARAD fragment using circular dichroism (CD) spectroscopy and size-exclusion chromatography (SEC) in tandem with small angle X-ray scattering (SAXS). Further, we assessed the impact of mutating OH residues that pack against either the partner helix of the CCD or the BARAD on self-dissociation, using isothermal titration calorimetry (ITC); on structure and stability of the CCD, BARAD and CCD-BARAD by monitoring thermal denaturation by CD and structural changes by SAXS; and lastly on cellular autophagy levels by evaluating the change in the number of autophagosomes per cell.

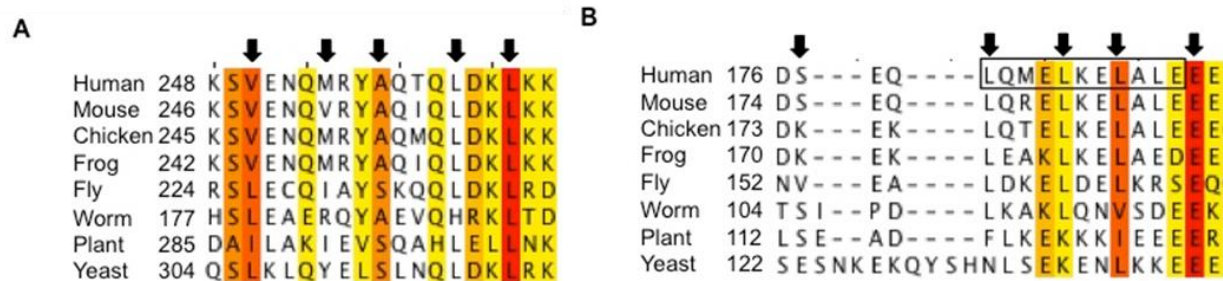


Figure 3.2. Sequence alignment of the OH and partner helix in BECN1 orthologs. Increasing background color intensity corresponds to increasing residue conservation: with red corresponding to invariant residues of the, A) Overlap helix and B) Partner helix with NES boxed. Interface residues are indicated with black arrows.

3.2. Materials and Methods

3.2.1. Plasmid preparation

Human BECN1 residues 175-265 (CCD), residues 175-450 (CCD-BARAD), or residues 248-450 (OH+BARAD) were cloned between the *NcoI* and *NotI* restriction enzyme sites of the pMBP-Parallel-1 bacterial expression vector (Sheffield *et al.*, 1999). BECN1 OH+BARAD was cloned between *XhoI* and *BamHI* restriction enzyme sites into the pET-15b bacterial expression vector encoding an N-terminal His₆ tag (Table 3.1). Site directed mutagenesis was used to generate the aromatic finger mutant (AFM) consisting of F359D, F360D, and W361D mutations; the OH Tetrad mutant consisting of V250A, M254A, L261A, and L264A mutations; and C353S+C391S mutations. The OH Tetrad mutation was also generated by site-directed mutagenesis in the pcDNA3.1 mammalian expression vector encoding full-length human wild-type (WT) BECN1.

For preliminary analyses with maltose binding protein (MBP)-tagged fusion protein, the long, flexible linker between the MBP-tag and N-terminus of the BECN1 domains was replaced with a short, triple alanine linker (SL) via site-directed mutagenesis (primer: 5' GCC CTG AAA GAC GCG CAG ACT AAT GCA GCA GCA CTG TAT TTT CAG GGC GCC 3').

Table 3.1. BECN1 constructs used in Chapter 3.

	Label	Purpose	BECN1 Residues	Theoretical MW of monomer (kDa)
1	CCD	Biophysical assays	175-265	11.2
2	CCD ^{TETRAD}	Biophysical assays	175-265, (V250A,M254A,L261A,L264A)	10.9
3	MBP-SL-CCD-BARAD	To test impact of AFM on structure	175-450	73.6
4	MBP-SL-CCD-BARAD ^{TETRAD}	To test impact of AFM on structure	175-450 (V250A,M254A,L261A,L264A)	73.4
5	MBP-SL-CCD-BARAD ^{AFM}	To test impact of AFM on structure	175-450 (F359D,F360D,W361D)	73.4
6	MBP-SL-BECN1 CCD-BARAD ^{AFM,TETRAD}	To test impact of AFM on structure	175-450 (F359D,F360D,W361D), (V250A,M254A,L261A,L264A)	73.2
7	OH+BARAD ^{AFM}	Biophysical assays	248-450, (F359D,F360D,W361D)	26.0
8	OH+BARAD ^{AFM, TETRAD}	Biophysical assays	241-450, (F359D,F360D,W361D), (V250A,M254A,L261A,L264A)	26.7
9	CCD-BARAD ^{AFM}	Biophysical assays	175-450, (F359D,F360D,W361D)	32.3
10	CCD-BARAD ^{AFM,TETRAD}	Biophysical assays	175-450, (F359D,F360D,W361D), (V250A,M254A,L261A,L264A)	32.4
11	CCD-BARAD ^{AFM,C353S/C391S}	EPR, Crystallization	175-450, (F359D,F360D,W361D), (C353S, C391S)	32.3

3.2.2. Protein expression and purification

E. coli BL21(DE3)·pLysS cells were transformed with plasmids to express either BECN1 CCD and CCD^{TETRAD}, and grown in LB media with 100 µg/mL ampicillin at 37 °C to an OD₆₀₀ of ~0.8 prior to equilibrating the temperature to 20 °C. For WT and mutant, BECN1 CCD-BARAD or His₆-BECN1 OH+BARAD, *E. coli* Arctic Express cells were transformed and grown in LB media with 100 µg/mL ampicillin at 30 °C to an OD₆₀₀ of ~0.6 prior to equilibrating the temperature to 10 °C. In each case, cells were grown to OD₆₀₀ of 0.8-1.2. Expression of CCD and CCD-BARAD was induced by addition of 0.5 mM isopropyl thio-β-D-galactoside (IPTG), and of His₆-OH+BARAD by 0.3 mM IPTG. All constructs were expressed overnight.

Two protease inhibitor tablets (Bimake) were added per pellet from each liter of cell culture during lysis for all protein constructs. At each stage of purification, protein purity was evaluated by SDS-PAGE stained with Coomassie Blue. In each case, the final purified protein

was estimated to be >90% pure by Coomassie Blue stained SDS-PAGE. All purified proteins were flash frozen in liquid nitrogen and stored in -80 °C.

The His₆-BECN1 OH+BARAD fusion protein was purified from clarified crude cell lysate by immobilized nickel ion affinity chromatography using a 3 mL His-select Ni-NTA affinity resin gravity column and wash buffer: 50 mM HEPES acid pH 7.5, 300 mM NaCl, 10% v/v glycerol, 25 mM imidazole, then eluted with Wash Buffer plus 350 mM imidazole. BECN1 OH+BARAD constructs were subsequently purified to homogeneity by size exclusion chromatography (SEC) using a Superdex 200 10/300 GL column (GE Life Sciences) in SEC buffer: 25 mM Tris-HCl pH 7.5, 300 mM NaCl, 2 mM DTT, and concentrated to 5 mg/mL in a 10 kD Amicon Ultra-0.5 centrifugal concentrator (EMD Millipore).

For WT and mutant MBP-BECN1 CCD-BARAD fusion proteins were purified from clarified crude cell lysate by 10 ml amylose affinity resin in gravity column with wash buffer 1: 25 mM Tris-HCl pH 8.0, 300 mM NaCl, 10% v/v glycerol, 1 mM EDTA, 2 mM DTT, then eluted with wash buffer plus 20 mM maltose. Subsequently, the WT protein was purified using anion-exchange chromatography (AEC) using a 5/50 GL MonoQ (GE Healthcare). The protein was loaded onto the column at 50 mM NaCl and eluted at 300 mM NaCl, which concentrated the protein to 7mg/mL. Lastly, the fusion protein was purified to homogeneity by SEC, using a HiLoad 16/60 Superdex 200 or Superdex 200 10/300 GL (GE Life Sciences) column in SEC buffer and concentrated to 5 mg/mL in a 50 kD Amicon Ultra-0.5 centrifugal concentrator (EMD Millipore).

Cleaved BECN1 CCD or BECN1 CCD-BARAD proteins were purified from clarified crude cell lysate by amylose affinity chromatography as above, but instead of elution from the amylose column, they were washed (wash buffer: 25 mM Tris-HCl pH 7.5, 300 mM NaCl, 1

mM EDTA, 2 mM DTT) and subjected to overnight, on-column cleavage by adding glutathione S-transferase – tobacco etch virus (GST-TEV) protease (3 mg GST-TEV protease per L culture was added) at 4 °C to cleave the MBP tag from the. Cleaved protein was washed from the column with wash buffer: 25 mM Tris-HCl pH 7.5, 300 mM NaCl, 1 mM EDTA, 2 mM DTT, and further purified by AEC on a 5/50 GL MonoQ (GE Healthcare) (MonoQ Buffer A: 50mM Tris-HCl pH 7.5, 2mM DTT; MonoQ Buffer B: 50mM Tris-HCl pH 7.5, 2mM DTT, 1M NaCl). BECN1 fragments were purified to homogeneity by SEC as described above and concentrated in a 10 kD Amicon Ultra-0.5 centrifugal concentrator (EMD Millipore) 5 – 8 mg/ml.

3.2.3. ITC

BECN1 CCD, CCD^{TETRAD}, CCD-BARAD^{AFM}, and CCD-BARAD^{AFM,TETRAD} protein samples were dialyzed against 50 mM HEPES base pH 8.0, 150 mM NaCl, and 2 mM β -mercaptoethanol. ITC experiments were performed in triplicate at 20 °C using a Low Volume Gold Nano isothermal titration calorimeter (TA Instruments). 65 μ M CCD-BARAD^{AFM}, 100 μ M CCD-BARAD^{AFM,TETRAD}, 350 μ M CCD, and 100 μ M CCD^{TETRAD} were separately titrated into dialysis buffer using 20 injections of 2.5 μ l each. Data were analyzed with the NanoAnalyze Software (TA Instruments), using a dimer dissociation model to calculate the dimer dissociation constants (K_{ds}).

3.2.4. CD spectroscopy, SAXS data collection and analysis, and autophagy assay

CD spectroscopy and SAXS data collection and analysis were performed by Dr. Karen Glover, and cellular assays were performed by Ms Shreya Mukhopadhyay. These methods were reported in (Glover *et al.*, 2017), as well as in Dr. Karen Glover's dissertation.

3.2.5. Continuous wave electron paramagnetic resonance (CW-EPR)

Purified BECN1 CCD-BARAD^{AFM,C353S/C391S} was dialyzed against buffer comprising of 25 mM Tris pH 8.0 and 50 mM NaCl. The protein was then reacted with a 10-fold molar excess of S-(2,2,5,5-tetramethyl-2,5-dihydro-1H-pyrrol-3-yl) methylmethanesulfono thioate (MTSL, Toronto Research Chemicals, Inc.) at 4°C overnight. Excess MTSL was removed by washing with dialysis buffer using the Amicon spin concentrator (Millipore, 10,000 MWCO, 50 mL). 10 μM of the labeled sample was used for EPR measurements. For the EPR experiments, labeled samples were transferred into a borosilicate capillary tube (0.70 mm i.d./1.00 mm o.d.; Wilmad Labglass, Inc.). A Varian E-109 spectrometer equipped with a cavity resonator was used for the acquisition. All continuous wave (CW) EPR spectra were obtained with an observe power of 200 mW, a modulation frequency of 100 kHz, and a modulation amplitude of 1.0 G.

3.2.6. Crystallization and data collection for BECN1 CCD-BARAD^{AFM,C353S/C391S}

BECN1 CCD-BARAD^{AFM,C353S/C391S} was crystallized at 4 °C by hanging-drop vapor-diffusion, wherein the drop comprised of 3 μl protein stock (5 mg/ml protein in 50 mM Tris pH 8.0, 300 mM NaCl, and 2mM BME) and 1 μl reservoir solution (0.1 M sodium formate; 20% PEG 3350). Crystals grew within a week and were harvested in cryoprotectant comprising of 0.1 M sodium formate, 20% PEG 3350, and 20% glycerol, then flash-cooled in liquid nitrogen. Diffraction data were collected at 100 K at a wavelength of 0.97918 Å in one 360° sweep from a single crystal at the NE-CAT beamline 24ID-C at the Advanced Photon Source (APS), Argonne National Laboratory (ANL), Argonne, IL. Diffraction intensities were recorded on a 4 × 4 tiled MAR mosaic CCD detector (Rayonix) at a crystal to detector distance of 250 mm, over a 1° crystal rotation for 1 second exposure per image. Diffraction data were processed using the RAPD automated processing web server (<https://rapd.nec.aps.anl.gov/rapd/>).

3.3. Results

3.3.1. Expression and purification of WT and mutant BECN1 CCDs

Representative purification results of the BECN1 CCD and CCD^{TETRAD} are reported below. In each case, a single peak on the SEC chromatogram and single band on the corresponding SDS-PAGE indicate that the protein was pure and homogenous, and produced proteins in quantities sufficient for the various biophysical and structural analyses in this study.

The apparent molecular mass of the CCD, calculated from the elution volume (15.10 ml) of the major SEC peak (Figure 3.3), is 39.8 kDa, which is ~1.8 times greater than the theoretical molecular mass of the CCD homodimer calculated from the amino acid sequence (Table 3.1). This is consistent with the CCD forming a rod-shaped dimer. The final yield of purified CCD was 0.83 mg per L of bacterial culture.

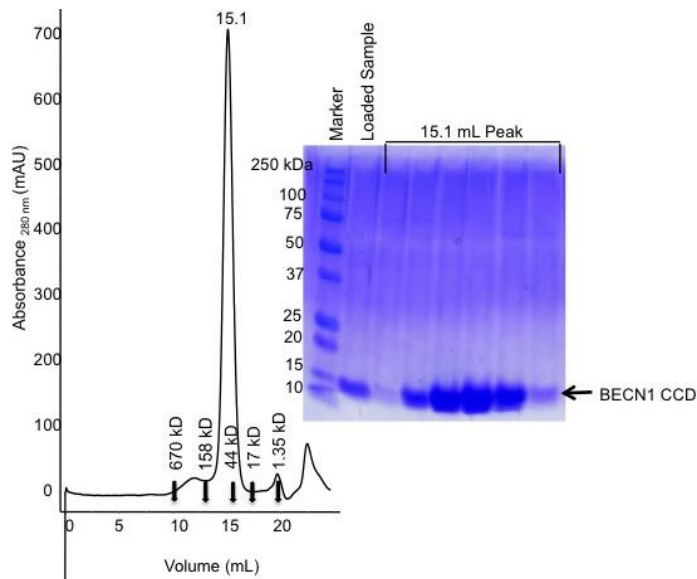


Figure 3.3. Size exclusion chromatogram and the corresponding SDS-PAGE of BECN1 CCD. The elution positions of SEC standards are indicated by arrows.

The apparent molecular mass of the CCD^{TETRAD}, calculated from the elution volume (14.5 ml) of the major SEC peak (Figure 3.4) is 55.4 kDa, which is ~2.5 times greater than the theoretical molecular mass of the CCD^{TETRAD} homodimer calculated from the amino acid

sequence (Table 3.1). This is consistent with the CCD^{TETRAD} forming a rod-shaped dimer. The final yield of purified CCD was 1 mg per L of bacterial culture.

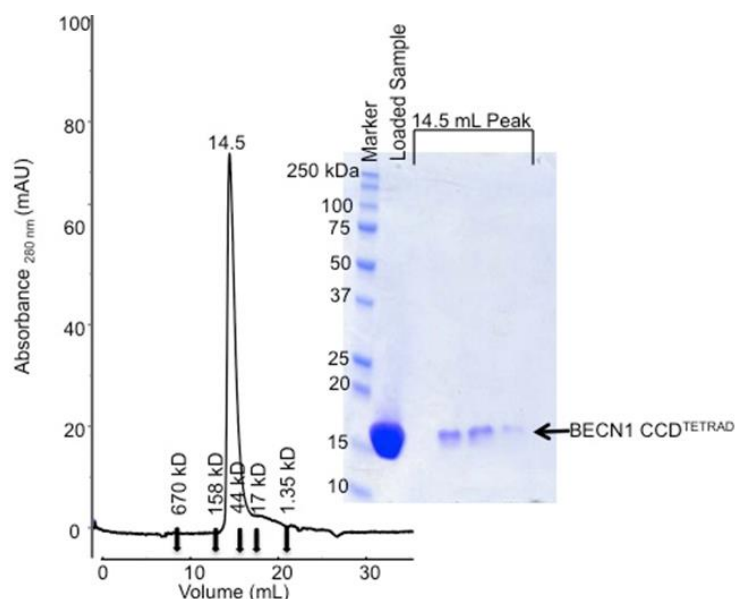


Figure 3.4. Size exclusion chromatogram and the corresponding SDS-PAGE of BECN1 CCD^{TETRAD}. The elution positions of SEC standards are indicated by arrows.

3.3.2. Aromatic Finger may decrease solubility of BARAD-containing BECN1 fragments

We found that the WT OH+BARAD and CCD-BARAD proteins aggregate during purification, especially for the constructs without tag. The purification results of the BARAD and CCD-BARAD are summarized in Table 3.2. Analysis of the OH+BARAD crystal structure (PDB ID: 4DDP) indicates that the OH+BARAD molecules are arranged in a head-to-tail manner in the crystal lattice, stabilized by the aromatic finger, consisting of Phe³⁵⁹, Phe³⁶⁰, and Trp³⁶¹, of one OH+BARAD molecule being buried within a hydrophobic pocket formed partly by the OH in the next OH+BARAD molecule (Huang *et al.*, 2012) (Figure 3.5). We hypothesized that this interaction may be the cause of protein aggregation during purification of WT OH+BARAD-containing constructs. Therefore, for all BARAD-containing constructs described here, an aromatic finger mutant (AFM), wherein the aromatic finger residues, Phe³⁵⁹, Phe³⁶⁰, and Trp³⁶¹, are mutated to Asp, was created.

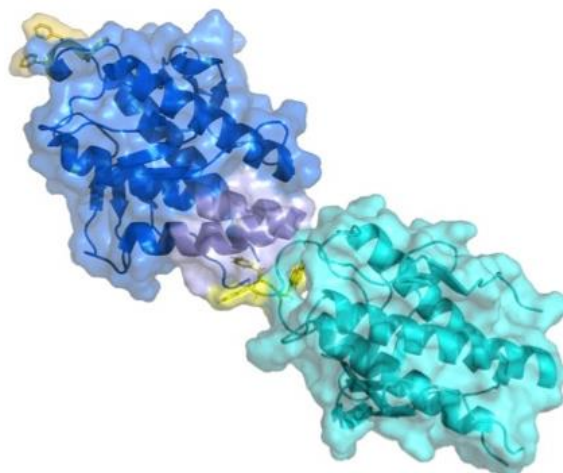


Figure 3.5. The aromatic finger of the OH+BARAD buried in the hydrophobic pocket of another molecule. The aromatic finger is shown in yellow and hydrophobic pocket is shown in grey.

Table 3.2. Purification of BARAD-BECN1 fragments.

BECN1 fragments	Purification Results
His ₆ -BARAD	Protein aggregation (performed by Dr. Glover)
MBP-BARAD	Protein aggregation (performed by Dr. Glover)
BARAD (cleaved MBP tag)	Did not try
MBP-CCD-BARAD	Behaves well (performed by Dr. Glover)
MBP-SL-CCD-BARAD	Behaves well
CCD-BARAD (cleaved MBP tag)	Protein aggregation

3.3.3. Expression and purification of BARAD-containing BECN1 fragments

Representative purification results of the BARAD-containing BECN1 fragments (Table 3.1) are reported below. In each case, a single peak on the SEC chromatogram and single band on the corresponding SDS-PAGE indicate that the protein was pure and homogenous, and produced proteins in quantities sufficient for biophysical and structural analyses.

The MBP-tagged CCD-BARAD fusion proteins were purified for use in biophysical analyses, to verify that the AFM does not impact the biophysical characteristics of the purified BECN1 fragments. The apparent molecular mass of MBP-SL-BECN1 CCD-BARAD and the MBP-SL-BECN1 CCD-BARAD^{AFM}, calculated from the elution volume (11.8 ml) of the major SEC peak (Figure 3.6 and Figure 3.7) is 245.4 kD, which is 1.7-times greater than the theoretical molecular mass of the dimer calculated from the amino acid sequence of the proteins being expressed. This

is consistent with the proteins forming rod-shaped dimers. The final yield of purified protein per L of bacterial culture was 0.3 mg for MBP-SL-BECN1 CCD-BARAD (Figure 3.6) and 2 mg for MBP-SL-BECN1 CCD-BARAD^{AFM} (Figure 3.7).

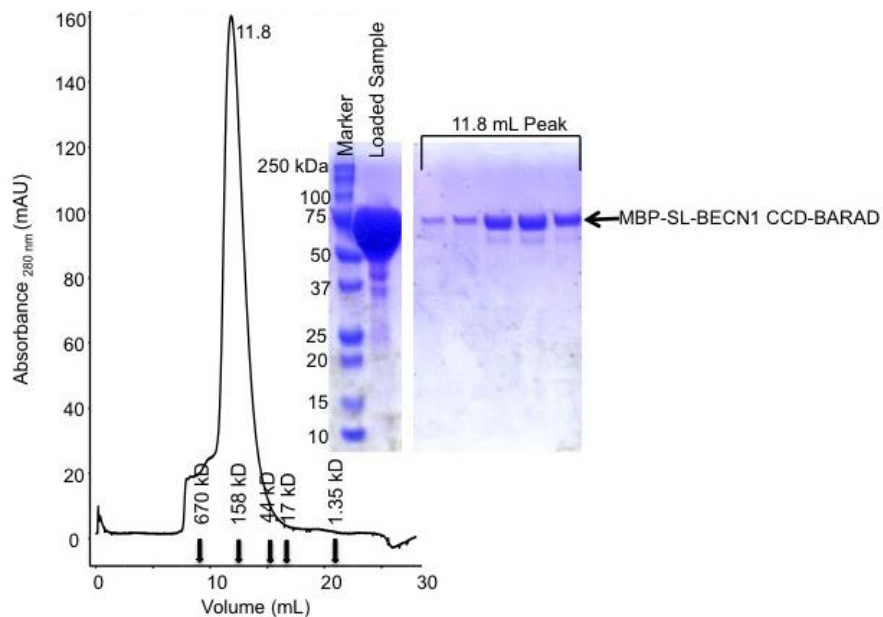


Figure 3.6. Size exclusion chromatogram and the corresponding SDS-PAGE of MBP-SL-BECN1 CCD-BARAD. The elution positions of SEC standards are indicated by arrows.

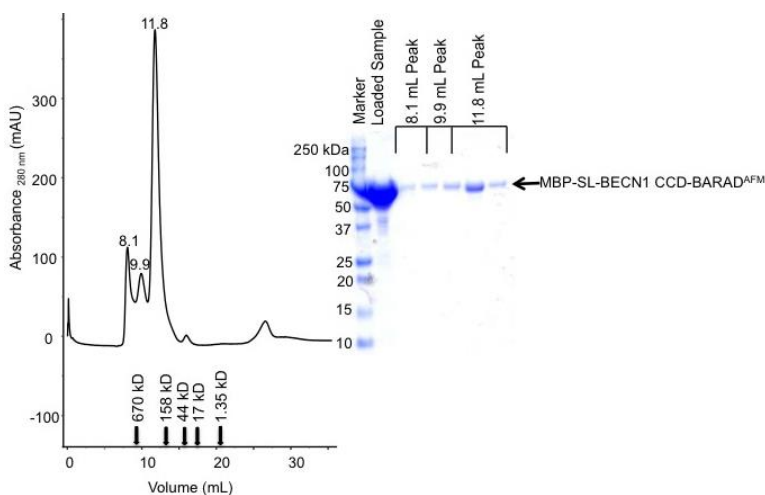


Figure 3.7. Size exclusion chromatogram and the corresponding SDS-PAGE of MBP-SL-BECN1 CCD-BARAD^{AFM}. The elution positions of SEC standards are indicated by arrows.

The apparent molecular mass of MBP-SL-BECN1 CCD-BARAD^{TETRAD}, calculated from the elution volume (13.2 ml) of the major SEC peak (Figure 3.8) is 114.0 kD, which is similar to the theoretical molecular mass of the MBP-SL-BECN1 CCD-BARAD^{TETRAD} dimer calculated

from the amino acid sequence (Table 3.1). This is consistent with the MBP-SL-BECN1 CCD-BARAD^{TETRAD} forming dimers. The final yield of the purified MBP-SL-BECN1 CCD-BARAD^{TETRAD} was 4 mg per L of bacterial culture.

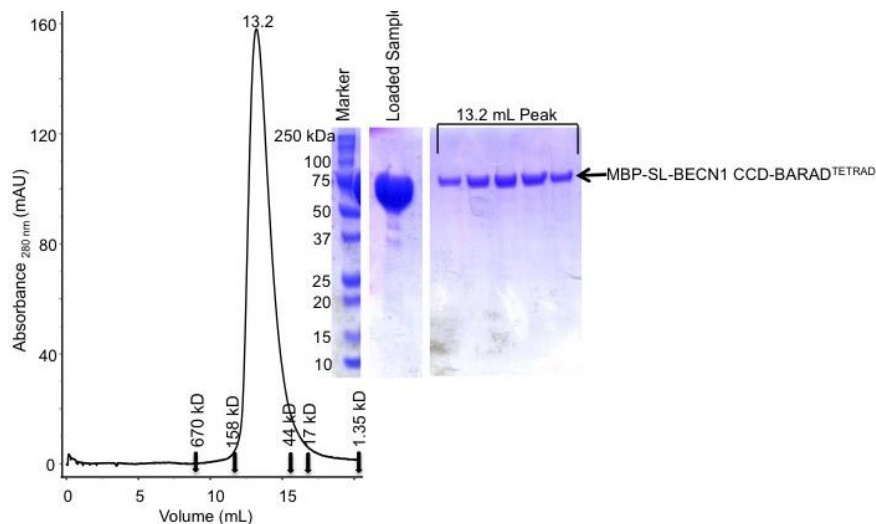


Figure 3.8. Size exclusion chromatogram and the corresponding SDS-PAGE of MBP-SL-BECN1 CCD-BARAD^{TETRAD}. The elution positions of SEC standards are indicated by arrows.

The apparent molecular mass of MBP-SL-BECN1 CCD-BARAD^{TETRAD,AFM}, calculated from the elution volume (15.1 ml) of the major SEC peak (Figure 3.9) is 208.0 kD, which is 1.4-times greater than the theoretical molecular mass of the MBP-SL-BECN1 CCD-BARAD^{TETRAD,AFM} dimer calculated from the amino acid sequence (Table 3.1). This is consistent with the MBP-SL-BECN1 CCD-BARAD^{TETRAD,AFM} forming dimers. The final yield of the purified MBP-SL-BECN1 CCD-BARAD^{TETRAD} was 4 mg per L of bacterial culture.

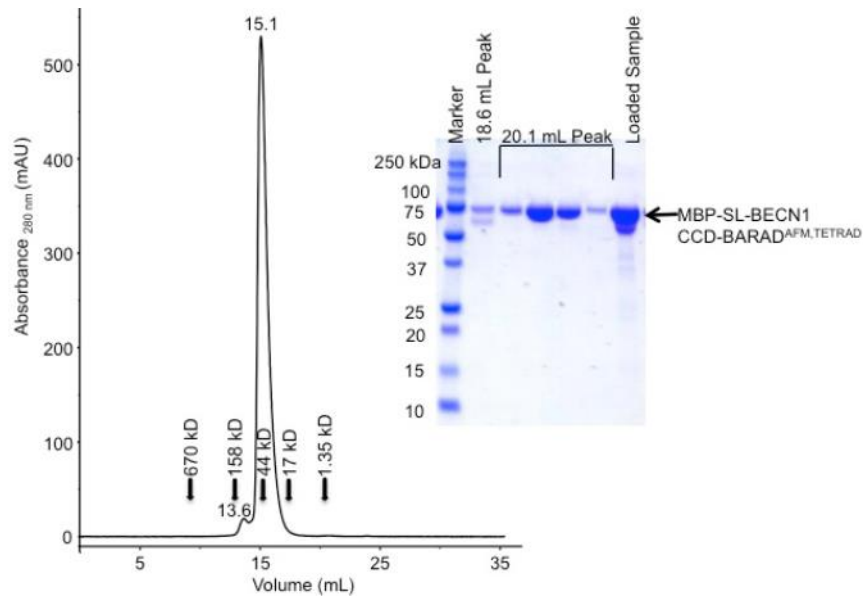


Figure 3.9. Size exclusion chromatogram and the corresponding SDS-PAGE of MBP-SL-BECN1 CCD- BARAD^{AFM, TETRAD}. The elution positions of SEC standards are indicated by arrows.

The apparent molecular mass of OH+BARAD^{AFM}, calculated from the elution volume (16.3 ml) of the major SEC peak (Figure 3.10), is 20.6 kD, which is similar to the theoretical molecular mass of the OH+BARAD^{AFM} monomer calculated from the amino acid sequence (Table 3.1). This is consistent with the OH-BARAD^{AFM} forming a globular monomer. The final yield of purified CCD was 2 mg per L of bacterial culture.

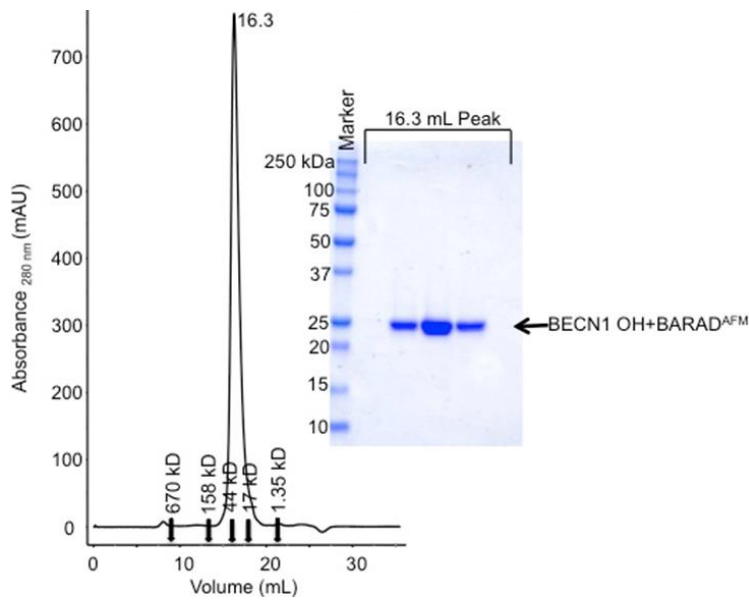


Figure 3.10. Size exclusion chromatogram and the corresponding SDS-PAGE of BECN1 OH+BARAD^{AFM}. The elution positions of SEC standards are indicated by arrows.

The apparent molecular mass of OH+BARAD^{AFM,TETRAD}, calculated from the elution volume (16.4 ml) of the major SEC peak (Figure 3.11), is 19.6 kD, which is ~1.4-times smaller than the theoretical molecular mass of the OH+BARAD^{AFM,TETRAD} monomer calculated from the amino acid sequence (Table 3.1). This is consistent with the OH-BARAD^{AFM,TETRAD} forming a globular monomer. The final yield of purified CCD was 2 mg per L of bacterial culture.

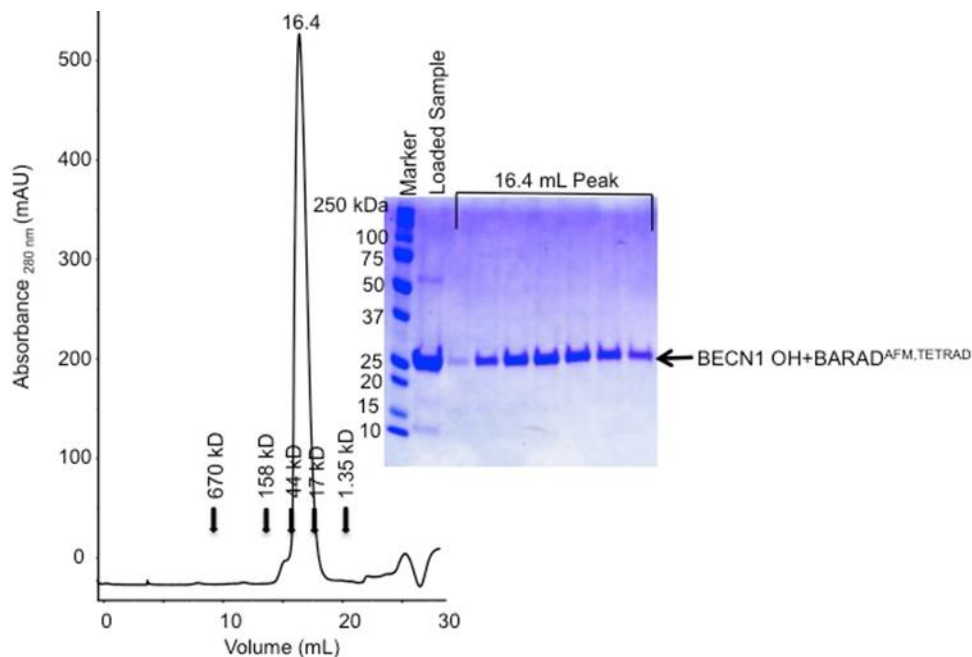


Figure 3.11. Size exclusion chromatogram and the corresponding SDS-PAGE of BECN1 OH+BARAD^{AFM,TETRAD}. The elution positions of SEC standards are indicated by arrows.

The apparent molecular mass of CCD-BARAD^{AFM}, calculated from the elution volume (15.9 ml) of the major SEC peak (Figure 3.12), is 120.0 kD, which is 1.9-times greater than the theoretical molecular mass of the CCD-BARAD^{AFM} homodimer calculated from the amino acid sequence. (Table 3.1). This is consistent with the CCD-BARAD^{AFM} forming a long rod-shaped dimer. The final yield of the purified CCD-BARAD^{AFM} was 2.2 mg per L of bacterial culture.

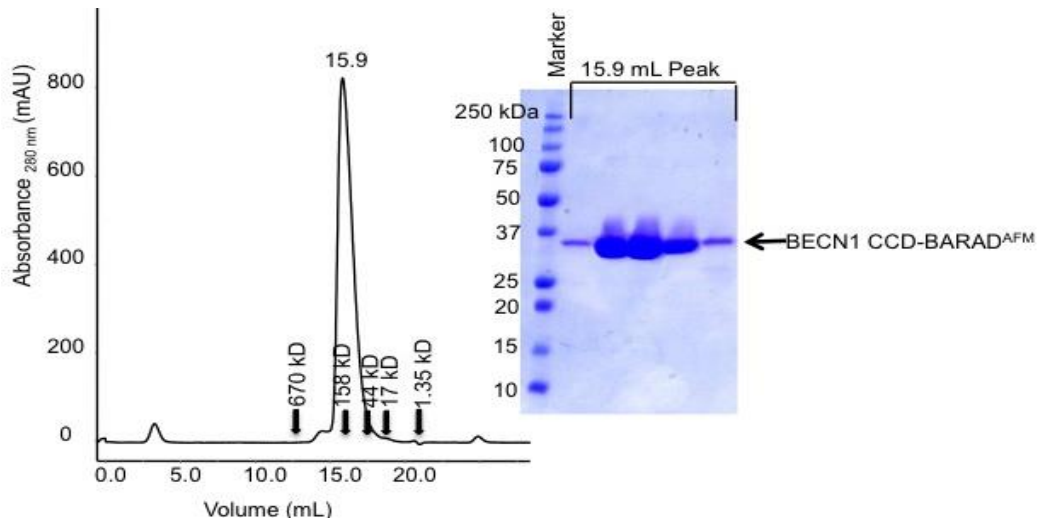


Figure 3.12. Size exclusion chromatogram and the corresponding SDS-PAGE of BECN1 CCD-BARAD^{AFM}. The elution positions of SEC standards are indicated by arrows.

The apparent molecular mass of CCD-BARAD^{AFM,TETRAD}, calculated from the elution volume (15.9 ml) of the major SEC peak (Figure 3.13), is 69 kD, which is similar to the theoretical molecular mass of the CCD-BARAD^{AFM,TETRAD} dimer calculated from the amino acid sequence (Table 3.1). This is consistent with the CCD-BARAD^{AFM,TETRAD} forming a dimer. The final yield of the purified CCD-BARAD^{AFM,TETRAD} was 1.8 mg per L of bacterial culture.

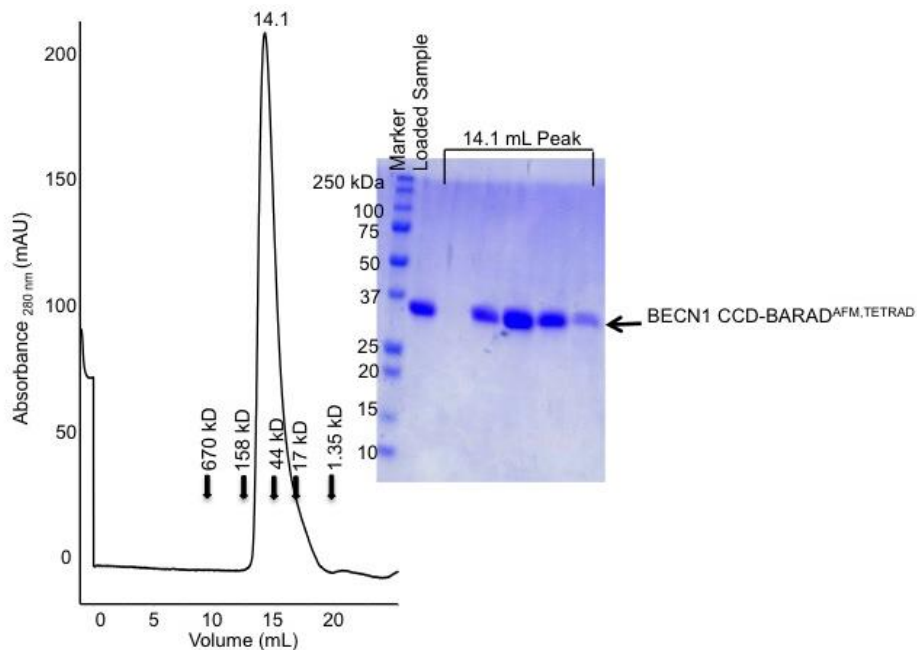


Figure 3.13. Size exclusion chromatogram and the corresponding SDS-PAGE of BECN1 CCD-BARAD^{AFM,TETRAD}. The elution positions of SEC standards are indicated by arrows.

3.3.4. AFM increases solubility of BARAD-containing BECN1 fragments, but does not impact BARAD secondary and tertiary structure

The AFM, wherein the aromatic finger residues in the BARAD, Phe³⁵⁹, Phe³⁶⁰, and Trp³⁶¹, are mutated to Asp, improves solution behavior of purified BARAD-containing fragments, as indicated by the purifications summarized above, but has no effect on the secondary structure content. Secondary structure content estimated by analysis of CD spectra for the MBP-BECN1 CCD-BARAD and the MBP-BECN1 CCD-BARAD^{AFM} indicates that secondary structure content varies less than 10% between MBP-BECN1 CCD-BARAD and MBP-BECN1 CCD-BARAD^{AFM}, regardless of the Tetrad mutation (Figure 3.14, Table 3.3). Therefore, we conclude the AFM does not alter the secondary structure of these proteins.

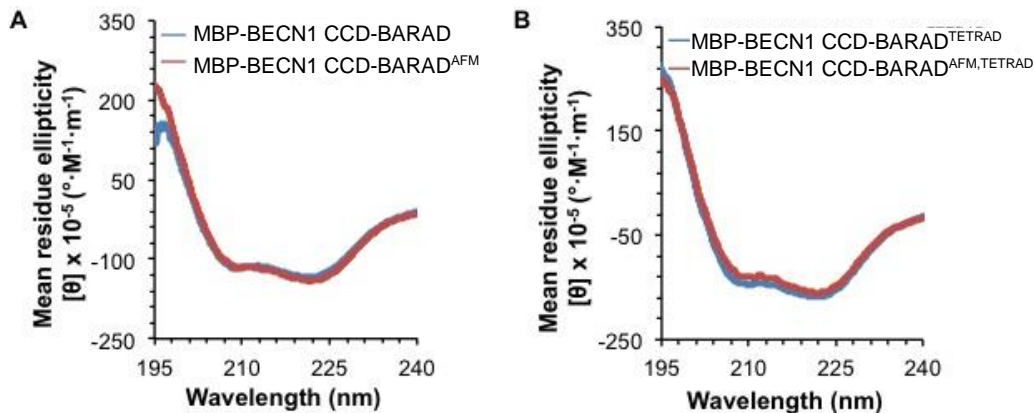


Figure 3.14. The AFM does not alter CD spectra of MBP-BECN1 CCD-BARAD. (A) MBP-BECN1 CCD-BARAD and (B) MBP-BECN1 CCD-BARAD^{TETRAD}.

Table 3.3. Average estimated secondary structure content in MBP-BECN1 CCD-BARAD Proteins

Protein	# Residues	Helix (%)	Beta (%)	Coil %
MBP-BECN1(175-450)	651	41.3 ± 2.9	12.6 ± 1.0	45.5 ± 1.6
MBP-BECN1(175-450) ^{AFM}	651	40.5 ± 1.3	13.7 ± 0.9	46.0 ± 0.9
MBP-BECN1(175-450) ^{TETRAD}	651	46.0 ± 2.9	11.4 ± 0.8	43.3 ± 2.1
MBP-BECN1(175-450) ^{AFM,TETRAD}	651	45.1 ± 2.2	11.2 ± 1.6	44.3 ± 0.6

The AFM, wherein the aromatic finger residues, Phe³⁵⁹, Phe³⁶⁰, and Trp³⁶¹, are mutated to Asp, also has no effect on the SEC-SAXS profile. SEC-SAXS data of the MBP-BECN1 CCD-

BARAD and MBP-BECN1 CCD-BARAD^{AFM} proteins were analyzed. A R_g of 71 Å (Table 3.4) is estimated from the Guinier plots and P(r) plots of MBP-BECN1 CCD-BARAD, as well as of MBP-BECN1 CCD-BARAD^{AFM}. Similarly, a D_{max} of 250 Å is estimated from the P(r) distribution for both samples (Table 3.4). Further, the Kratky plots (Figure 3.15A and C) and the P(r) plots (Figure 3.15B and D) indicate that both the MBP-BECN1 CCD-BARAD and MBP-BECN1 CCD-BARAD^{AFM} are well folded. The P(r) plots (Figure 3.15B and D) also suggest a dumbbell shaped envelope for both samples. This similarity in size and shape of the WT and AFM mutant MBP-BECN1 CCD-BARAD indicates that the tertiary structure of the BARAD is unaffected by the AFM.

Table 3.4. Summary of SEC-SAXS data for MBP-BECN1 CCD-BARAD proteins.

Protein	MW _T (kD)	Guinier	P(r)	
		R_g (Å)	R_g (Å)	D_{max} (Å)
MBP-BECN1(175-450)	147.2 (dimer)	66	71	250
MBP-BECN1(175-450) ^{AFM}	146.9 (dimer)	63	71	250

MW_T: Theoretical molecular mass.

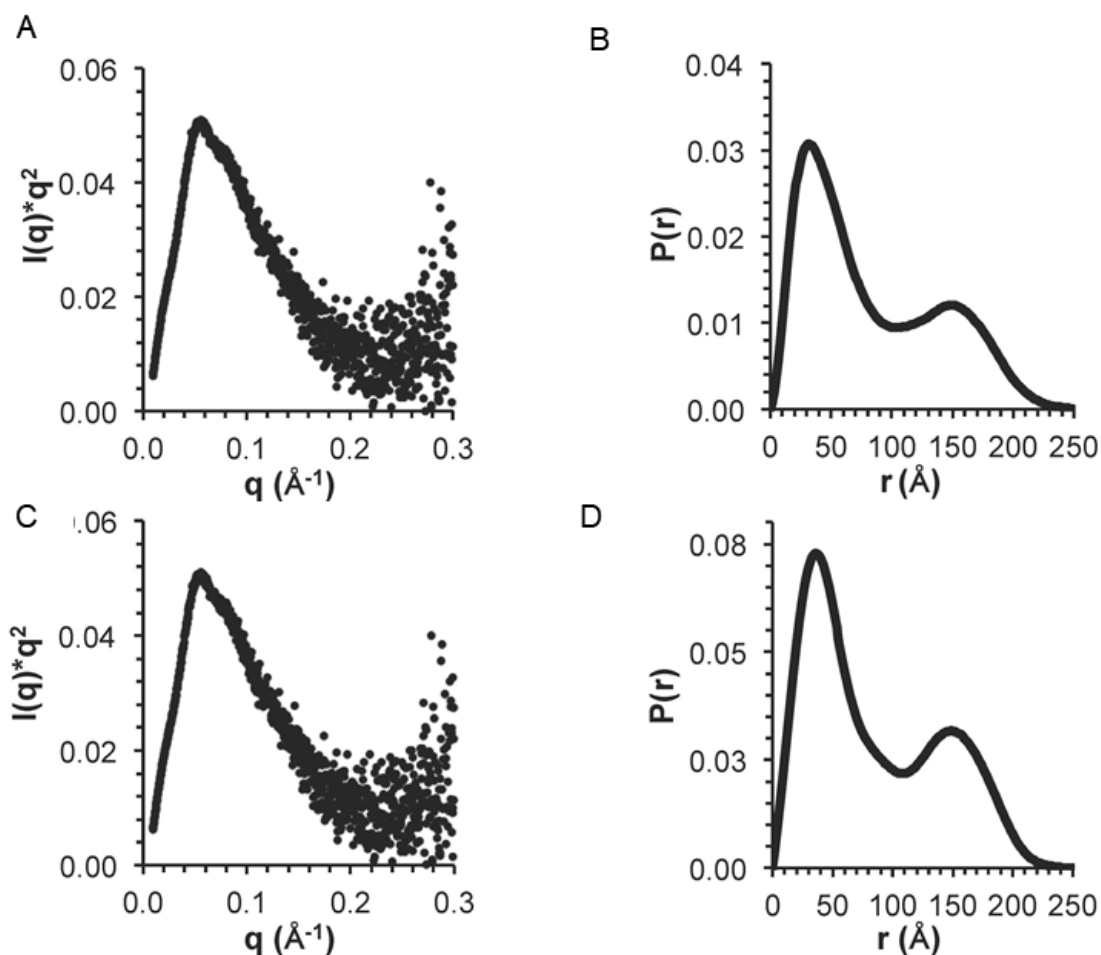


Figure 3.15. SEC-SAXS analysis of MBP-BECN1 CCD-BARAD proteins. For the MBP-BECN1 CCD-BARAD, the (A) Kratky and (B) $P(r)$ pairwise distribution. For the MBP-BECN1 CCD-BARAD^{AFM}, the (C) Kratky, and (D) $P(r)$ pairwise distribution.

3.3.5. BECN1 CCD structure is destabilized by the OH Tetrad mutation

In order to assess the effect of the Tetrad mutation on CCD homodimerization, we quantified dimer self-dissociation constants (K_d) of the CCD and CCD^{TETRAD} by ITC. At 20 °C, self-association of the CCD^{TETRAD} is ~1.5 fold weaker than that of the WT CCD (Figure 3.16, Table 3.5). A comparison of the secondary structure content estimated by analysis of CD spectra for the CCD and CCD^{TETRAD} was performed by Dr. Karen Glover and reported in (Glover *et al.*, 2017), and in her dissertation, which also suggests that Tetrad mutation destabilizes the CCD.

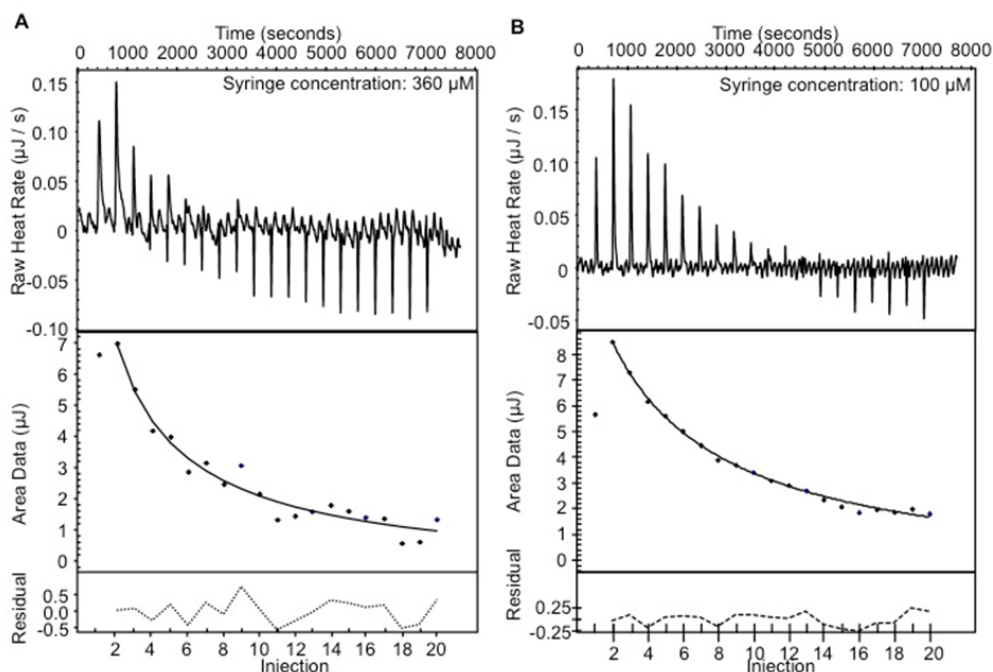


Figure 3.16. Homodimer dissociation ITC profiles of the BECN1 CCD and CCD^{TETRAD}. (A) BECN1 CCD. (B) BECN1 CCD^{TETRAD}.

Table 3.5. Thermodynamics of self-dissociation of CCD-containing proteins

BECN1 Fragment	K _d (μM)	dH ^a (kJ/mol)	dS ^b (J/K mol)
CCD	44.8 ± 2.0	45.0 ± 10.5	236.6 ± 36.2
CCD ^{TETRAD}	70.7 ± 3.1	157.0 ± 8.8	615.1 ± 30.0
CCD-BARAD ^{AFM}	61.0 ± 8.1	207.1 ± 21.5	787.1 ± 73.0
CCD-BARAD ^{AFM,TETRAD}	134.2 ± 4.9	143.0 ± 10.3	561.9 ± 34.9

^adH, change in enthalpy; ^bdS, change in entropy. Performed at 20 °C in 25 mM HEPES salt pH 8.0, 150mM NaCl, 2mM B-me.

We used SEC-SAXS to investigate the impact of the Tetrad mutation on size, shape, and structure of the CCD and CCD^{TETRAD}. The experiments and analysis were performed by Dr. Karen Glover and are reported in (Glover *et al.*, 2017), and in her dissertation. Taken together; the secondary structure and melting temperature estimations by CD, homodimer association affinity quantified by ITC, solution size and shape parameter determinations by SEC-SAXS, and assessment of flexibility by the Kratky plot and EOM, all indicate that CCD secondary, tertiary and quaternary structure stability is significantly disrupted by the OH Tetrad mutation.

3.3.6. The OH Tetrad mutation impacts the BECN1 OH+BARAD structure less than that of the CCD

The crystal structure of the human BARAD (Huang *et al.*, 2012) includes the OH packed against the BARAD, but the OH was not included in the yeast VPS30 BARAD crystal structure (Noda *et al.*, 2012). In each case, the crystal structure as well as solution data indicate that the BARAD is a monomer. Therefore, the OH does not mediate homodimerization of the BARAD, nor does it appear to be required for stability of the BARAD structure in all VPS30/BECN1 homologs.

CD was performed by Dr. Glover to compare the secondary structure content of the OH+BARAD^{AFM} and OH+BARAD^{AFM,TETRAD}, and to compare the denaturing temperature of the OH+BARAD^{AFM} and OH+BARAD^{AFM,TETRAD}. SEC-SAXS was also completed by Dr. Karen Glover to investigate the impact of the Tetrad mutation on size, shape, and structure of the OH+BARAD. The results are reported in (Glover *et al.*, 2017) as well as in Dr. Karen Glover's dissertation. The results of the secondary structure and T_m estimations by CD, solution size and shape parameter determinations by SEC-SAXS analyses, and assessment of flexibility by the Kratky plot and EOM, all demonstrate that the OH Tetrad mutation impacts OH+BARAD structure and stability significantly less than it does the CCD.

3.3.7. The OH preferentially packs against the BARAD rather than with the CCD homodimer, but transiently samples both conformations

A comparison of the secondary structure content estimated from the CD spectra for the BECN1 CCD-BARAD^{AFM} and CCD-BARAD^{AFM,TETRAD} indicates that the Tetrad mutation decreases helical and increases strand and coil content. The experiments were performed by Dr. Karen Glover, and reported in (Glover *et al.*, 2017) and in her dissertation.

In order to determine whether the CCD-BARAD also forms a homodimer like the CCD, we used ITC to quantify the K_d of the dimer. At 20 °C, self-association of the CCD-BARAD^{AFM} is 1.4-fold weaker than that of the WT CCD, but slightly tighter than that of the CCD^{TETRAD} (Figure 3.16, Figure 3.17 A, Table 3.5). Notably, self-association of the CCD-BARAD^{AFM,TETRAD} is approximately 2-fold weaker than the CCD-BARAD^{AFM} (Figure 3.17, Table 3.5). Taken together, these ITC data indicate that the Tetrad mutation destabilizes both the CCD and CCD-BARAD homodimer. Equally importantly, compared to the WT CCD homodimer, the CCD-BARAD homodimer is substantially dissociated, with a K_d comparable to the CCD^{TETRAD} rather than the CCD, suggesting that the OH helix does not stabilize the homodimer as much in the two-domain fragment.

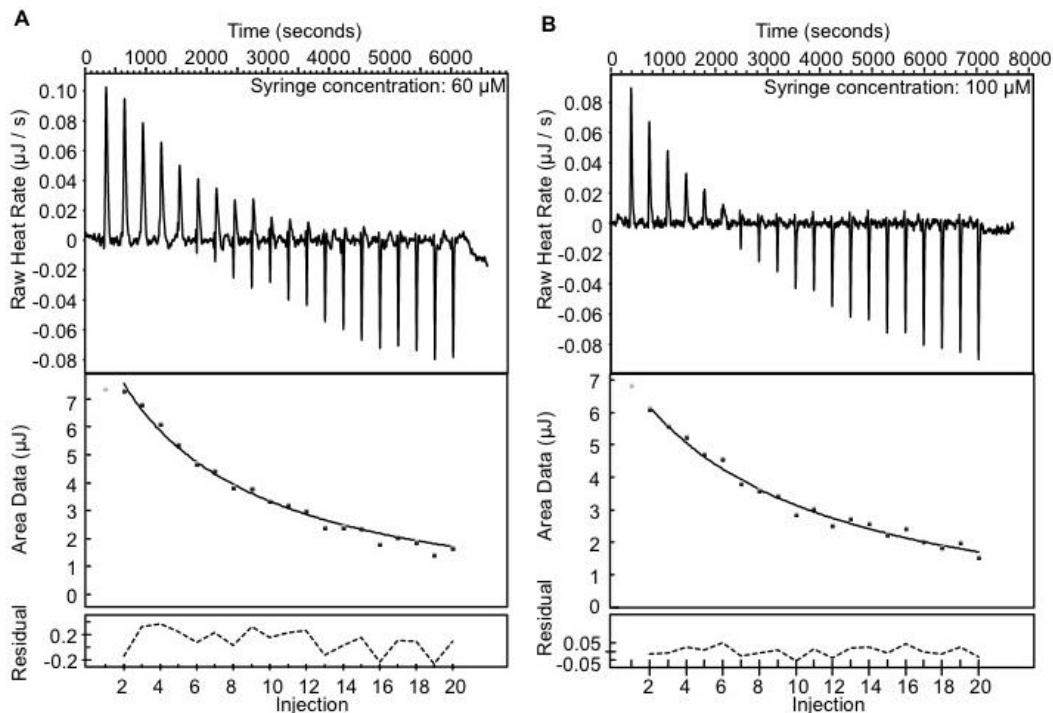


Figure 3.17. Homodimer dissociation ITC profiles of the BECN1 CCD-BARAD and CCD-BARAD^{TETRAD}. (A) CCD-BARAD^{AFM}. (B) CCD-BARAD^{AFM,TETRAD}.

In order to assess the thermostability of the CCD-BARAD and CCD-BARAD^{AFM,TETRAD}, Dr. Karen Glover used CD to monitor denaturation of the two-domain fragment. The results

were reported in (Glover *et al.*, 2017), as well as in Dr. Karen Glover's dissertation. The comparison of the thermostability and T_m of the various fragments suggest that in the CCD-BARAD construct, the OH is not part of the CCD homodimer, but rather packs against the BARAD.

However, self-dissociation measurements by ITC indicate that the CCD-BARAD homodimerizes slightly better than the CCD^{TETRAD} and that disruption of the OH packing interface weakens CCD-mediated homodimerization of the CCD-BARAD, although not as much as in the CCD alone. Taken together, these data suggest that in solution, the OH transitions between packing as part of the CCD or against the BARAD, with the predominant state comprising the OH packed against the BARAD.

3.3.8. SAXS indicates the OH packs against the BARAD in the CCD-BARAD protein fragment

SEC-SAXS was used to further investigate how the Tetrad mutation impacts the conformation of OH in CCD-BARAD^{AFM} and CCD-BARAD^{AFM,TETRAD}. The experiments and analysis were performed by Dr. Karen Glover and reported in (Glover *et al.*, 2017), as well as in her dissertation. These results suggest that different conformations of BECN1 CCD-BARAD homodimer are transiently occupied in solution. The OH preferentially packs against the BARAD rather than within the CCD in the CCD-BARAD homodimer. The Tetrad mutation destabilizes packing of the OH against both CCD and BARAD.

3.3.9. The Tetrad Mutant decreases starvation-induced autophagy

Lastly, we investigated the impact of destabilization of the OH on cellular autophagy levels mediated by exogenously-expressed full-length BECN1, by quantifying and comparing the impact of either WT or the Tetrad mutant (V250A, M254A, L261A, and L264A) BECN1.

The cellular experiments and analysis performed by Ms. Shreya Mukhopadhyay are published (ref) and described in Dr. Karen Glover's dissertation. To briefly summarize, the BECN1 Tetrad mutation does not impact autophagy levels in nutrient rich media; However, the BECN1 Tetrad mutation decreases autophagy levels in starvation media, indicating that these residues are essential for up-regulating starvation-induced autophagy. This is consistent with the established importance of other conserved regions of BECN1 in starvation-triggered autophagy, rather than basal autophagy levels (Mei, Ramanathan, *et al.*, 2016, Mei, Su, *et al.*, 2016).

3.3.10. Preparation of BECN1 CCD-BARAD mutants for continuous wavelength electron paramagnetic resonance (CW-EPR)

We attempted to use CW-EPR to estimate the distance between the BARAD^{AFM} of the CCD-BARAD^{AFM} homodimer. Ideally, samples used for CW-EPR assay should have only two cysteines that can be labeled with sulfhydryl-specific nitroxide reagent, which is called site directed spin labeling (SDSL), to generate a stable spin-labeled side chain (Figure 3.18A). The absorption of microwave radiation corresponding to the energy splitting of an unpaired electron can be measured by EPR spectroscopy when it is placed in a strong magnetic field. Distance information can be obtained from the magnetic dipolar interactions between the unpaired electrons of two cysteine spin labels (Hustedt & Beth, 1999). The energy of the dipolar interaction is inversely proportional to the cube of the distance. When the distance is larger than 20 Å, the CW-EPR spectra has a narrow peak, while at distances smaller than 20 Å, the interaction between the unpaired electrons of the two cysteine spin labels significantly broadens the CW-EPR spectral peak (Hustedt & Beth, 1999, Hustedt *et al.*, 1997, Banham *et al.*, 2008, Altenbach *et al.*, 2001) (Figure 3.18B). Therefore, the distance between the spin labels can be estimated from the degree of peak broadening.

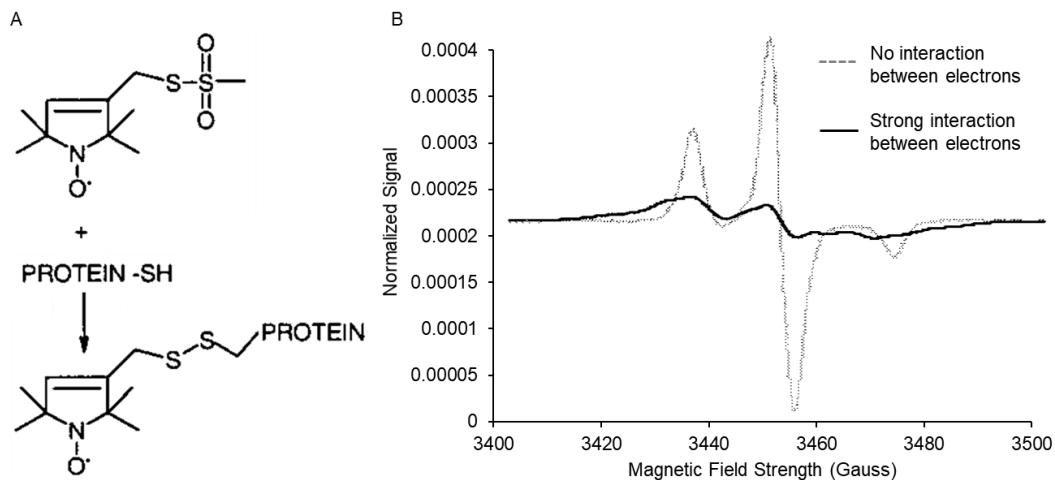


Figure 3.18. CW-EPR spin labeling and spectra. (A) Structure of a representative spin-label reagent and the corresponding side chains produced by reaction with cysteine. (B) CW-EPR spectra of spin labeled sample. Representative spectra of No interaction (Grey curve) or strong interaction (Black solid curve) between the unpaired electrons of the spin labels are shown.

Our experimental design was based on the structural information that an anti-parallel CCD-BARAD homodimer would result in the BARAD domains being positioned farther than 20 Å apart, while they would likely be closer together in a parallel CCD-BARAD homodimer. The BECN1 CCD-BARAD monomer has only three cysteines: C353, C375, and C391; and all are located in the BARAD (Figure 3.19). These cysteines are conserved amongst vertebrates, but not in all eukaryotes (Figure 3.20). Three sets of double mutants: C353S/C391S, C351S/C375S, and C375S/C391S, were made, so each CCD-BARAD would bear only one cysteine, enabling us to record CW-EPR spectra resulting from interaction of spin-labels at the remaining cysteine on each subunit of the homodimer. All the constructs also had the AFM mutation, to prevent aggregation of the expressed proteins. We expected that a narrow and sharp CW-EPR spectral peak would indicate that the CCD-BARAD forms an anti-parallel homodimer, while broadening of the CW-EPR spectral peak would indicate that the BECN1 CCD-BARAD forms a parallel homodimer.

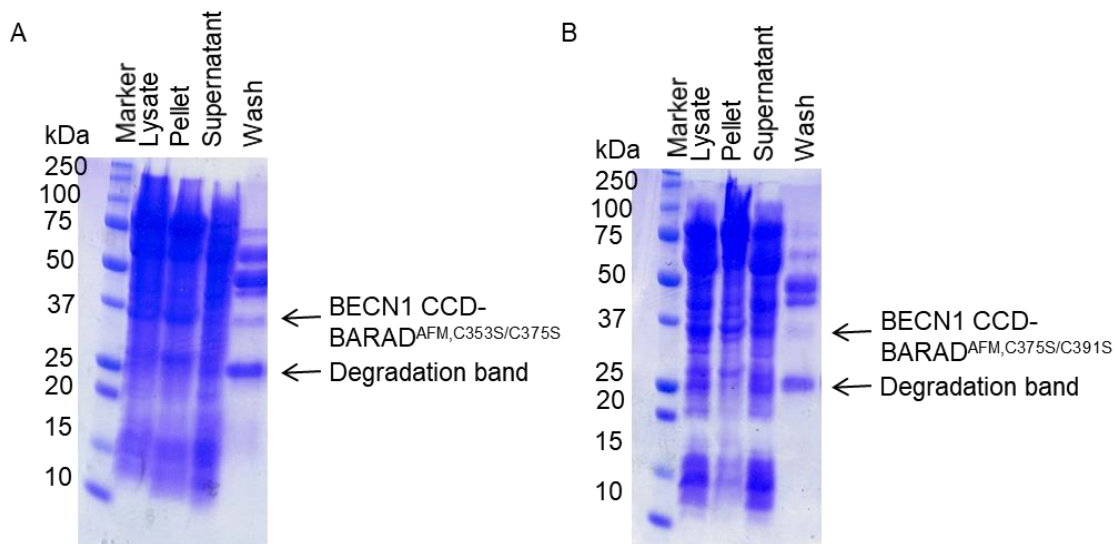


Figure 3.21. SDS-PAGE gel image of Amylose affinity purification of (A) BECN1 CCD-BARAD^{AFM,C353S/C375S} and (B) BECN1-CCD-BARAD^{AFM,C375S/C391S}. The “wash” is the wash after on-column cleavage.

We were able to purify the mutant BECN1 CCD-BARAD^{AFM,C353S/C391S}. The apparent molecular mass of CCD-BARAD^{AFM,C353S/C391S}, calculated from the elution volume (13.1 ml) of the SEC peak (Figure 3.21), is 69.0 kD, which is similar to the theoretical molecular mass of the CCD-BARAD^{AFM,C353S/C391S} dimer calculated from the amino acid sequence (Table 3.1). This is consistent with the CCD-BARAD^{AFM,C353S/C391S} forming a dimer. The final yield of purified CCD was 1.8 mg per L of bacterial culture.

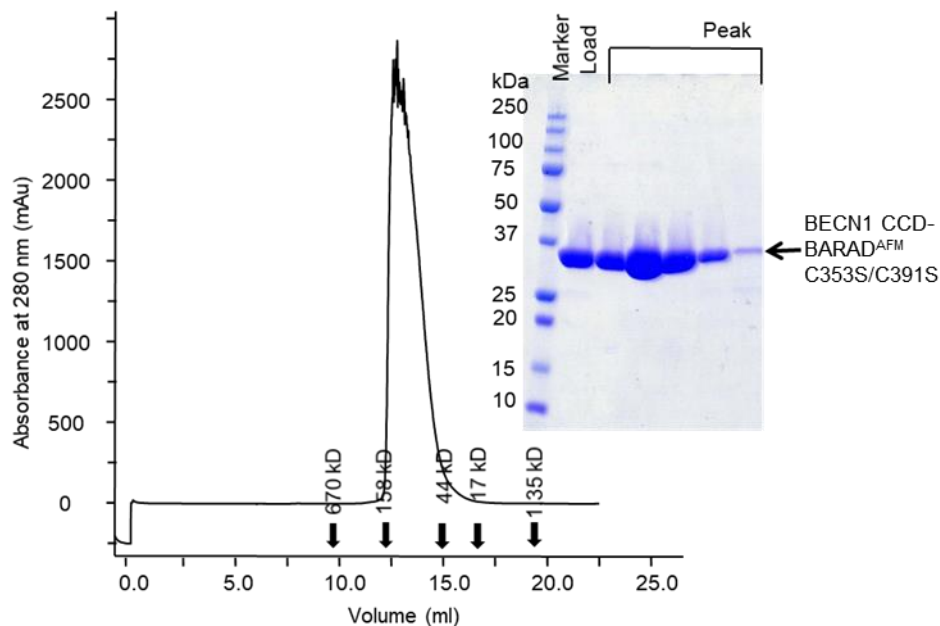


Figure 3.22. Size exclusion chromatogram and the corresponding SDS-PAGE of BECN1 CCD-BARAD^{AFM,C353S/C391S}.

3.3.11. The CW-EPR result does not provide enough information for determining the orientation of BECN1 CCD-BARAD homodimer

The purified BECN1 CCD-BARAD^{AFM,C353S/C391S} was spin-labeled and used for CW-EPR experiments performed with the assistance of Dr. Yanxiong Pan and Dr. Zhongyu Yang from the Department of Chemistry and Biochemistry at NDSU. The result shows that the unpaired electrons of the spin label of BECN1 CCD-BARAD^{AFM,C353S/C391S} do not interact (Figure 3.22), indicating that the distance between the S375 in BECN1 CCD-BARAD^{AFM,C353S/C391S} homodimer is larger than 20 Å. This result indicates that BECN1 CCD-BARAD^{AFM,C353S/C391S} likely forms an anti-parallel homodimer. However, we cannot exclude the possibility of BECN1 CCD-BARAD forming a parallel homodimer as the conformational flexibility of the BECN1 CCD-BARAD arising from the OH transitioning between the CCD and BARAD, may result in the distance between the S375 of each subunit being larger than 20 Å. More evidence is needed to confirm the orientation of BECN1 CCD-BARAD homodimer.

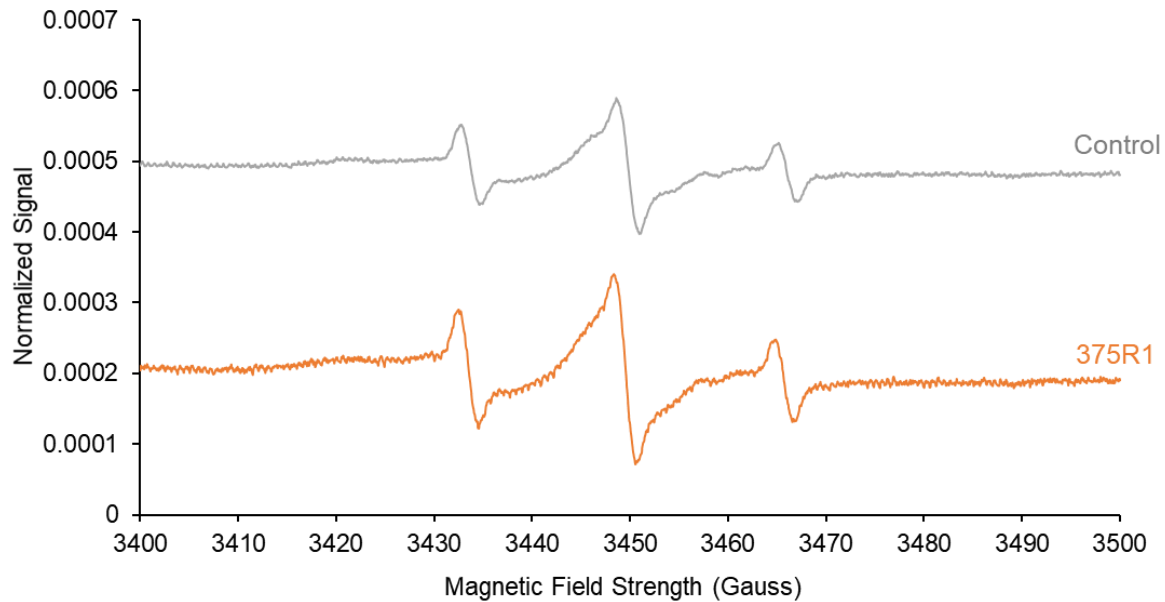

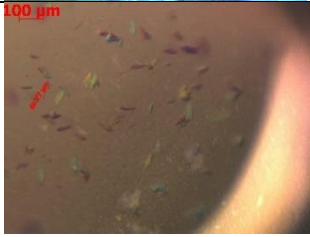

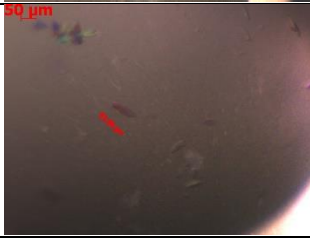


Figure 3.23. CW-EPR spectra of spin labeled BECN1 CCD-BARAD^{AFM,C353S/C391S}. R1 indicates the spin label on the BECN1 CCD-BARAD Cys 375. The grey spectrum corresponds to a control sample wherein there is no interactions between the electron pairs of the spin labels. The spectrum of the BECN1 CCD-BARAD^{AFM,C353S/C391S} with spin label is shown in orange.

3.3.12. Crystallization of BECN1 CCD-BARAD

We had initially tried to crystallize the BECN1 CCD-BARAD^{AFM}, but were not able to identify any potential crystallization conditions. Since the BECN1 CCD-BARAD^{AFM,C353S/C391S} protein is very well behaved in solution, we decided to screen this protein for crystallization using the MSCG-1 crystallization suite (Anatrace). Several crystal hits were identified (Table 3.6).

Table 3.6. Crystallization conditions (all from MSCG-1) that produce crystal hits.

Condition #	Solution	Protein:solution ratio	Temperature	Crystal hits
1	0.1 M HEPES-NaOH pH 7.5; 10% PEG 8000; 8% Ethylene glycol	1:1	20 °C	
2	0.2M LiAc; 20% PEG 3350;	3:1	4 °C	
3	0.2M NaAc; 20% PEG 3350;	3:1	4 °C	
4	0.2M HCOONa; 20% PEG 3350;	3:1	4 °C	

Grid screens were used to vary these conditions to identify optimal crystallization conditions to obtain diffraction-quality BECN1 CCD-BARAD^{AFM,C353S/C391S} crystals (Figure 3.23). Though most of the crystals were clustered, we were able to separate some single crystals with a dimension of $\sim 60 \times 40 \times 3 \mu\text{m}$.

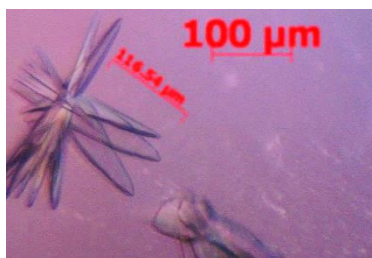


Figure 3.24. BECN1 CCD-BARAD^{AFM,C353S/C391S} crystals.

X-ray diffraction data were collected at the NE-CAT beamline 24ID-C at APS, Argonne National Laboratory, Argonne, IL. Statistics for the best data recorded are shown in Table 3.7. Unfortunately, the poor resolution and quality and low completeness of the diffraction data prevented structure solution.

Table 3.7. X-ray data collection statistics of BECN1 CCD-BARAD^{AFM,C353S/C391S}. Values in parentheses are for the highest resolution shell.

Data Collection statistics	
Space group	P1
Unit Cell Dimension (Å)	65.84, 82.49, 86.90, 73.42, 84.31, 79.13
Resolution (Å)	83.19-4.77
Unique reflections	7897 (2161)
Completeness	92.0 (89.0)
Multiplicity	1.8 (1.8)
I/σ _I	3.1 (1.2)
CC (1/2)	0.871 (0.818)

3.4. Conclusions and Discussion

Based on the biophysical and structural analyses reported here, we conclude that the BECN1 C-terminal domains, the CCD and BARAD, are linked by a conformationally labile helix. Structural superimposition unambiguously demonstrates that the OH residues present in the crystal structure of both the CCD (Mei, Su, *et al.*, 2016, Li *et al.*, 2012) and OH+BARAD (Huang *et al.*, 2012), cannot simultaneously pack as part of the CCD and against the BARAD. Melting temperature measurements by CD spectroscopy and analyses by SEC-SAXS indicate that mutation of OH residues that are key components of the interface with the CCD partner helix and the BARAD, disrupts CCD structure more than the BARAD. Indeed, these mutations substantially diminish CCD homodimer association. Furthermore, the comparative melting temperature analyses, together with the weakened self-association of the CCD-BARAD relative to the CCD, indicate that the OH preferentially packs against the BARAD in the two-domain CCD-BARAD protein fragment. This preference is supported by our buried surface area

calculations, which identify a larger interface between the OH and BARAD than between the OH and the partner helix within the CCD. However, self-dissociation measurements by ITC indicate that the OH also contributes to CCD-BARAD homodimerization. Therefore, contrary to currently established ideas, the OH preferentially packs against the BARAD in the absence of heterologous binding partners, but appears to also transiently sample conformations where it forms part of the CCD.

We further show that the BECN1 homodimer is unstable at physiological temperatures. Our melting temperature analyses show that nearly half the CCD is unfolded in the two-domain CCD-BARAD fragment at 37 °C. Together, the weak self-association and instability of the CCD-BARAD homodimer suggest that BECN1 likely does not exist in a stable homodimeric state at physiological temperatures, unless stabilized in that state by other protein partners such as the BCL2 proteins. BECN1 homodimerization likely serves as an important means of regulating autophagy in cells. Notably, this may be a regulatory mechanism that evolved in higher eukaryotes such as vertebrates, as yeast do not encode BCL2 proteins, and it is unknown whether yeast VPS30 homodimerizes.

This is significant because upregulation of autophagy by BECN1 requires either ATG14 or UVRAG to displace one molecule of the BECN1 homodimer, which would be facilitated by a weak BECN1 homodimer. The 4.4 Å crystal structure (PDB ID: 5DFZ) of full-length yeast VPS30/BECN1 in complex with VPS34/PI3KC3, VPS15/p150, and VPS38/UVRAG (Rostislavleva *et al.*, 2015), shows that the OH is part of a parallel VPS30:VPS38 CCD heterodimer essential for stabilizing this complex. The 28 Å reconstruction of the quaternary complex of human PI3KC3, p150, BECN1 and ATG14 (Baskaran *et al.*, 2014), indicates that BECN1 and ATG14 interact in an analogous manner. A SAXS data-constrained model of the

BECN1:ATG14 heterodimer indicates that four of the OH interface residues identified in the homodimer also contribute to the heterodimer coiled-coil interface (Val²⁵⁰:Ile¹⁶⁵, Met²⁵⁴:Asn¹⁶⁹, Ala²⁵⁷:Leu¹⁷², Leu²⁶¹:Val¹⁷⁶) (Mei, Su, *et al.*, 2016). Notably, these OH residues are largely conserved, especially in vertebrates (Figure 3.2A); and are predicted to pack against ATG14 residues that are also conserved. Indeed amongst these interacting pairs, the least conserved BECN1 residue, Met²⁵⁴, is paired with Asn¹⁶⁹, the least conserved paired residue in ATG14 (Mei, Su, *et al.*, 2016). Thus, the OH contributes critical binding determinants to the parallel CCD heterodimers required for formation of VPS34/PI3KC3 complexes essential for autophagy. Consistent with this, we show that the Tetrad mutation of the OH interface residues abrogates the starvation-induced up-regulation of autophagy, but has no effect on basal levels of autophagy.

Our experimental evidence showing that the OH preferentially packs against the BARAD in the BECN1 homodimer suggests a mechanism wherein homodimerization via the CCD results in BECN1 conformations that prevents the BARAD aromatic finger from associating with membranes, while BECN1 heterodimerization with ATG14 or UVRAG disrupts this inhibitory conformation. The crystal structure and mass spectroscopy hydrogen-deuterium exchange experiments of the yeast PI3KC3:p150:BECN1:UVRAG ternary complex show that the aromatic finger interacts with membranes when the OH participates in the CCD interface of the heterodimer (Rostislavleva *et al.*, 2015). However, formation of a BECN1 homodimer, wherein the OH preferentially packs against the BARAD, would shorten the CCD and involve reorientation of the BARAD relative to that observed in the yeast PI3KC3:p150:BECN1:UVRAG ternary complex. This would reposition the BARAD such that the aromatic finger is no longer able to interact with membranes, thereby inhibiting BECN1-mediated autophagy.

Another important implication of the OH being preferentially packed against the BARAD in the homodimer is that this would release the N-terminal region of the partner helix within the anti-parallel CCD homodimer. The N-terminal region of the human BECN1 CCD (Figure 3.2B) contains a leucine-rich nuclear export signal (NES) that binds the chromosomal protein 1 (CRM1) to enable nuclear export of BECN1 (Liang *et al.*, 2001, Zhang *et al.*, 2014). A functional NES is comprised of the sequence motif: LX₍₂₋₃₎LX₍₂₋₃₎LxL. NES residues L184 and L187 are essential for BECN1 nuclear export, BECN1-mediated autophagy, and tumor suppression (Liang *et al.*, 2001, Zhang *et al.*, 2014). In the CCD homodimer, NES residues L184 and L187 pack against OH interface residues, Ala²⁵⁷ and Met²⁵⁴ respectively (Mei, Su, *et al.*, 2016). Therefore, in order to bind CRM1, the BECN1 NES cannot be packed against the BECN1 OH. Thus, our results showing that the OH preferentially packs against the BARAD in the homodimeric state provide a mechanism of how the NES may be exposed for CRM1-binding to enable nuclear export. Indeed, interaction with CRM1 may stabilize BECN1 conformations wherein the OH is packed against the BARAD. Interestingly, unlike vertebrates, lower eukaryotes do not have a NES located at the N-terminus of the CCD (Figure 3.2B). Therefore, this conformational switch is likely not needed for nuclear export in yeast, as the NES is located between yeast VPS30 residues 12-21 (Liang *et al.*, 2001), which is part of the IDR, rather than the CCD.

Our attempts to crystallize the BECN1 CCD-BARAD^{AFM} fragment were unsuccessful. However, a double C353S/C391S mutation facilitated crystallization, suggesting that the C353S/C391S mutation may help stabilize this fragment. Structural analysis shows that the distance between the C353 sulfhydryl and the carbonyl oxygen of D361 side chain is ~ 3.2 Å (Figure 3.19). The C353S mutation may result in a stronger hydrogen bond formation between

the hydroxyl of the mutated C353S and the carbonyl oxygen of D361 side chain. Similarly, the distance between the C391 sulfhydryl and the carbonyl oxygen of the E384 side chain is ~ 3.1 Å (Figure 3.19), and the C391S mutation may facilitate a stronger hydrogen bond between S391 and E384. These potentially stronger hydrogen bonds may help stabilize the structure of loops bearing S353 and S391 (Figure 3.19). Unfortunately, although the BECN1 CCD-BARAD^{AFM} C353S/C391S mutant crystallized, the crystals did not diffract well, preventing structure solution. Perhaps, the flexibility of the OH, as well as of the NES within the CCD, results in a non-uniform arrangement and/or packing of the molecules in the crystal lattice, preventing high-quality diffraction from these crystals. Since the OH transitions between packing against the BARAD and the NES within the CCD, but preferentially packs against the BARAD, it may be worth trying to crystallize a BECN1 CCD-BARAD fragment without the NES, which may eliminate conformational flexibility of the OH.

In summary, previous studies have established the BECN1 CCD and BARAD as structurally well-defined domains, but here we show that these domains include a region, now termed the overlap helix (OH), that can adopt two distinct, mutually-exclusive packing states, emphasizing overall BECN1 conformational flexibility. Further, in the absence of heterologous partners, the OH transitions between these states with a preference to packing against the BARAD, rather than the CCD as has been commonly assumed. This region likely serves to regulate BECN1 function in autophagy and nuclear transport, and interactions with different partners likely stabilize one packing state or the other to promote these different functions. Understanding how different interactions stabilize different BECN1 conformational states is the next critical step toward understanding the regulation of BECN1-mediated autophagy.

CHAPTER 4. INVESTIGATING THE STRUCTURE OF BECN2 AND ITS INTERACTION WITH ANTIAPOPTOTIC BCL2 PROTEINS²

4.1. Introduction

BEEN2 (Beclin 2), like BECN1, has been shown to interact with various autophagy-regulating proteins by co-immunoprecipitation (He *et al.*, 2013). BECN2 co-immunoprecipitates with other core proteins in the VPS34 complex I and II: Atg14 and UVRAG. For BECN1, CCD is found to be responsible for interacting with the Atg14 CCD and UVRAG CCD (Li *et al.*, 2012, Itakura *et al.*, 2008, Rostislavleva *et al.*, 2015, Baskaran *et al.*, 2014). BECN1 CCD also self-associates and forms an anti-parallel homodimer (Li *et al.*, 2012, Mei, Su, *et al.*, 2016). Since BECN2 CCD has high sequence similarity with BECN1 CCD, BECN2 CCD may also self-associates as well as associates with ATG14 and UVRAG CCD.

Like BECN1, BECN2 also co-immunoprecipitates with Bcl-2, a negative regulator of autophagy (He *et al.*, 2013). Anti-apoptotic BCL2 homologs binds to BECN1 BH3D to down-regulate autophagy, and starvation treatment disrupts BECN1 interactions with these anti-apoptotic BCL2 homologs. However, starvation does not disrupt the BECN2:Bcl-2 interaction (He *et al.*, 2013).

Although BECN2 and BECN1 are broadly similar in sequence and function, the differences in their sequence, detailed structure, interactions and mechanism result in their distinct roles in the cell. An understanding of this difference is necessary to understand the

² The material in this chapter was co-authored by Dr. Minfei Su and Yue Li. Dr. Minfei Su prepared BECN2 samples, collected X-ray diffraction data of BECN2 CCD and its mutants, and wrote out part of the draft of this chapter. Yue Li prepared some of the BECN2 CCD construct and purified and crystallized some of the BECN2 mutant. Yue Li also had primary responsibility for the ITC experiments between BECN2 fragment and BCL2 proteins.

mechanistic bases for the different biological functions of the BECN paralogs and consequently, the reasons why mammals have two paralogs of this protein.

In this study, the domain architecture of BECN2 was delineated based on sequence alignment to BECN1 along with secondary structure predication. Different BECN2 expression constructs, containing full-length, multi-domain and single-domain of BECN2, were designed, cloned, expressed and purified. The BECN2 CCD was successfully crystallized and its X-ray crystal structure was determined, showing that it forms an anti-parallel coiled-coil dimer in which two alpha-helices are coiled around each other. In contrast to the BECN1 CCD homodimer, which has a flat molecular surface, the BECN2 CCD is curved, with a 15 nm radius of curvature. The BECN2 CCD is a metastable dimer with 7 pairs of non-ideal packing interactions, which includes 4 pairs of charged residues and 3 pairs of bulky polar side chains. We use structure-based mutations, CD and ITC to demonstrate that interface mutations that improve homodimerization of the BECN2 CCD also stabilize the homodimer structure, and mutations that adversely impact homodimerization, destabilize CCD structure. We have also solved the X-ray crystal structure of the N187L mutant BECN2 CCD to reveal how it homodimerizes better than WT BECN2. Dr. Minfei Su performed most of the experiments and data analysis. I made the bacteria express constructs, purified BECN2 E173L and R243L mutants, crystallized BECN2 N187L mutant, and made mutant constructs for cellular assay.

In addition of the structural study of BECN2 CCD, we also investigated the BECN2 interactions with anti-apoptotic BCL2 homologs. We used ITC to quantify the interactions between BECN1 constructs (including BECN1 BH3D and MBP-BECN2 BH3D-FHD-CCD (residues 88-250)) and anti-apoptotic BCL2 homologs, M11 and Bcl-X_L.

4.2. Materials and Methods

4.2.1. Delineating BECN2 domain architecture

BECN2 domain architecture was delineated using a combination of bioinformatics tools including the alignment of sequences of human BECN1 and BECN2 using ClustalW2 (Larkin *et al.*, 2007); secondary structure prediction using Jpred (Cole *et al.*, 2008); and sequence analysis using the programs IUPred (Dosztanyi *et al.*, 2009), PrDOS (Ishida & Kinoshita, 2007) and the VSL2B algorithm in the PONDR program suite (Obradovic *et al.*, 2005, Peng *et al.*, 2006) to identify IDRs. These analyses were completed by Dr. Minfei Su from our lab.

4.2.2. Creation of constructs to express different BECN2 fragments

Different recombinant DNA technology methods were used to create plasmids to express the diverse BECN2 fragments as described in detail below. In each case, new expression plasmids were amplified by transforming 50 µl aliquots of chemically competent Top10 cells with 2.5 µl of the final reaction mixture. Transformed cells were plated on LB-agar plates supplemented with 100 µg/ml ampicillin and allowed to grow overnight at 37 °C. Then 5 ml LB medium supplemented with 100 µg/ml ampicillin was inoculated with a single colony of transformed *E. coli* cells and grown overnight at 37 °C. Recombinant plasmid was isolated using E.Z.N.A. Plasmid Mini Kit I (Omega Bio-tek), and DNA sequencing (McLab) used to confirm the sequence of the cloned insert.

Constructs for expression of full-length (FL) BECN2 (residues 1-431), BECN2 FHD-CCD-BARAD (residues 121-431), BECN2 CCD-BARAD (residues 158-431), and BECN1 BH3D-FHD-CCD (residues 88-250) were created using the Gibson Assembly cloning method (Gibson *et al.*, 2009). Briefly, the cDNA corresponding to the BECN2 fragment was inserted between the *EcoRI* and *XhoI* restriction sites of the pMBP parallel vector to express the BECN2

fragment as an MBP-tagged fusion protein. Sense (S) and antisense (A) primers (Table 4.1) were used to amplify corresponding cDNA. 50 μ l of PCR reaction consisted of: 5 μ l of $10 \times$ *Pfu* Ultra AD DNA polymerase reaction buffer, 1 μ l of 10 mM dNTPs mixture, 2 μ l of 20 ng/ μ l template, 1 μ l of each 25 μ M primers, and 1 μ l of 2.5 U/ μ l *Pfu* Ultra AD polymerase and 39 μ l nuclease-free H₂O. PCR was performed on the GeneAmp PCR System 9700 (Life Technologies) for 25 cycles as follows: initial denaturation at 95 °C for 45 sec, denaturation at 95 °C for 30 sec, annealing at 67 °C for 45 sec, extension at 72 °C for 45 sec, final extension at 72 °C for 5 min, and then hold at 4 °C. The PCR amplified DNA was gel purified using E.Z.N.A. Gel Extraction Kits (Omega Bio-tek). The *p*MBP parallel vector was linearized using *EcoRI* and *XhoI*. The reagents used for the 20 μ l restriction digestion reaction were: 1 μ g of vector, 2 μ l of $10 \times$ NEBuffer 2.1, 1 μ l of *EcoRI* (20 U/ μ l), 1 μ l of *XhoI* (20 U/ μ l), and 15 μ l nuclease-free H₂O. The reaction mixture was incubated at 37 °C for 1 hour. The digestion products were gel purified using E.Z.N.A. Gel Extraction Kits (Omega Bio-tek). The 20 μ l assembly reaction consisted of 15 μ l of Gibson Assembly Master Mix (Tables 4.2 and 4.3) to which linearized vector and PCR product were added in a 1:6 molar ratio. The reaction mixture was incubated at 50 °C for 1 hour.

Table 4.1. Summary of primers used for creating BECN2 expression constructs.

Primers	Sequence (5'→3')
FL (S)	CTGTATTTTCAGGGCGCCATGGATCCGGAATTCATGTCTTCCATCCGCTTCCTG
FL (A)	GGCCAGTGCCAAGCTTGGTACCGCATGCCTCGAGCTACTTTTGATACCTTGAGGCAAC
FHD-CCD-BARAD (S)	CTGTATTTTCAGGGCGCCATGGATCCGGAATTCGACCCGACAGTCTTTTAGAG
FHD-CCD-BARAD (A)	GGCCAGTGCCAAGCTTGGTACCGCATGCCTCGAGCTACTTTTGATACCTTGAGGCAAC
CCD-BARAD (S)	CTGTATTTTCAGGGCGCCATGGATCCGGAATTCGAGGCGGCGGGCTGCGGGCG
CCD-BARAD (A)	GGCCAGTGCCAAGCTTGGTACCGCATGCCTCGAGCTACTTTTGATACCTTGAGGCAAC
BH3D-FHD-CCD (S)	CTGTATTTTCAGGGCGCCATGGATCCGGAATTCGCGCCATGCACATGCTCAG
BH3D-FHD-CCD (A)	GGCCAGTGCCAAGCTTGGTACCGCATGCCTCGAGCTAACTGTCAGCTTCTGTGAG
FHD-CCD (S)	GCTGAAGGAAATCAACTAGTGTTCACCGCCACG
FHD-CCD (A)	CGTGGCGGTGAAACACTAGTTGATTTCCCTTCAGC
CCD (S)	GCGGCGGGATCCGGAGGCGGCGGCGTGCAGGCGGAGCTGCGG
CCD (A)	GCGGCGGCGGCCGCCTAGTTGATTTCCCTTCAGCCGGTCCCTCTG
BARAD 1 (residues 230-431) (S)	CTGTATTTTCAGGGCGCCATGGATCCGGAATTCGGAACGTGGAGAAC CAGCTG
BARAD (residues 230-431) (A)	GGCCAGTGCCAAGCTTGGTACCGCATGCCTCGAGCTACTTTTGATACCTTGAGGCAAC
BARAD 1 (residues 223-431) (S)	CATGGATCCGGAATTCCTGGAAGTCTTGATCAGCTGGGGAACGTGGAGAAC
BARAD 1 (residues 223-431) (A)	GTTCTCCACGTTCCCCAGCTGATCAAGCAGTTCAGGAATTCGGATCCATG
BARAD 1 (residues 254-431) (S)	GCCATGGATCCGGAATTCGCCACGTTGAGATCTGG
BARAD 1 (residues 254-431) (S)	CCAGATCTCAAACGTGGCGAATTCGGATCCATGGC

Table 4.2. Gibson Assembly Master Mix composition.

Total mix volume	1.2 ml
5X isothermal reaction buffer	320 μ l
0.2 U / μ l T5 exonuclease ¹	32 μ l
2 U / μ l Phusion DNA polymerase	20 μ l
40 U/ μ l Taq DNA ligase	160 μ l
Nuclease-free water	700 μ l

¹0.2 U/ μ l T5 exonuclease was made by diluting of 10 U/ μ l T5 exoluclease by a buffer comprised of 50% glycerol, 50 mM Tris-HCl pH 7.5, 0.1 mM EDTA, 1 mM DTT, 0.1 M NaCl, 0.1% Triton X-100

Table 4.3. 5 \times isothermal reaction buffer composition.

5 \times isothermal reaction buffer	1 ml
1 M Tris-HCl pH 7.5	0.5 ml
2 M MgCl ₂	50 μ l
100 mM dNTP	10 μ l
1M DTT	50 μ l
PEG-8000	0.25g
100 mM NAD ⁺	50 μ l
Nuclease-free water	340 μ l

The BECN2 CCD expression construct was made by traditional sub-cloning method. The cDNA corresponding to the BECN2 CCD was amplified by PCR using appropriate primers (Table 4.1). 50 μ l of PCR reaction consisted of 5 μ l of $10 \times$ *Taq* DNA polymerase buffer, 1 μ l of 10 mM dNTPs mixture, 2.5 μ l of 20 ng/ μ l template DNA, 5 μ l of 5 μ M both primers, and 0.5 μ l of 5 U/ μ l *Taq* DNA polymerase and 31 μ l nuclease-free water. The PCR was performed on the GeneAmp PCR System 9700 (Life Technologies) as follows: 1) initial denaturation at 94 °C for 3 min; 2) denaturation at 94 °C for 1 min; 3); annealing at 65 °C for 1 min; 4) extension at 72 °C for 1 min; 5) final extension at 72 °C for 5 min and hold at 4 °C. Steps 2-4 are cycled 35 times. The PCR products as well as the pMBP parallel vector were digested by the restriction enzymes *Bam*HI and *Not*I to create overhang ends. The digestion reaction consisted of 2 μ g of DNA, either PCR product or pMBP parallel plasmid; 2 μ l of 10 BSA, 2 μ l of $10 \times$ NEBuffer 3; 1 μ l of *Bam*HI (20 U/ μ l); and 1 μ l of *Not*I (10U/ μ l). Nuclease free water was added to bring the volume to 20 μ l. The reaction mixture was incubated at 37 °C for 2 hours, followed by heat inactivation at 60 °C for 20 min to inactivate the restriction enzymes. The digested products were gel purified using E.Z.N.A. Gel Extraction Kits (Omega Bio-tek). The purified vector and PCR product were ligated in a ligation reaction consisting of 250 ng vector and PCR product in a 1:6 molar ratio, 2 μ l \times T4 DNA ligase reaction buffer, 1 μ l of T4 DNA ligase (400 U/ μ l), and nuclease-free water to bring the volume to 20 μ l. The reaction mixture was incubated at 16 °C for overnight.

The BECN2 FHD-CCD (residues 121-250) expression construct was created by site-directed mutagenesis by inserting a stop codon after the residue 250 of the BECN2 FHD-CCD-BARAD expression construct by PCR, using the the corresponding primers (Table 4.1) and the QuikChange II Site-Directed Mutagenesis Kit (Agilent Technologies). 50 μ l of PCR reaction consisted of: 5 μ l of $10 \times$ reaction buffer, 1 μ l of 10 mM dNTPs mixture, 2 μ l of 10 ng/ μ l

templates, 2.5 μ l of each 50 ng/ μ l primers, and 1 μ l of 2.5 U/ μ l PfuUltra AD DNA polymerase and 37 μ l nuclease-free water. The PCR was performed on the GeneAmp PCR System 9700 (Life Technologies) as follows: 1) initial denaturation at 95 °C for 30 sec; 2) denaturation at 95 °C for 30 sec; 3) annealing at 55 °C for 1 min 4) extension at 68 °C for 6 min; 5) final extension at 68 °C for 7 min and then hold at 4 °C. Steps 2-4 are cycled for 16 times. 1 μ l of *DpnI* was then added to the reaction product to digest the template DNA at 37 °C for 1 hr.

Three different expression constructs with varying N-termini were created for the BECN2 BARAD to identify the most stable BECN2 BARAD construct. A construct comprising BECN2 residues 230-431 was inserted into the pMBP parallel vector was created using the Gibson Assembly method as described above. The corresponding primers were used to amplify the corresponding cDNA. Residues were either added to or removed from the BECN2 BARAD (residues 230-431) construct using site-directed mutagenesis protocol described above to make the BECN2 (residues 223-431) and BECN2 (residues 254-431) respectively. The corresponding primers used are shown in Table 4.1.

The impact of non-ideal packing interactions on the stability of BECN2 CCD dimers was assessed by mutating the seven pairs of non-ideal packing residues to more ideal leucine-leucine or leucine-valine pairs to create stronger hydrophobic interface interactions, with the expectation that this would lead to a more stable homodimer. Five single mutants and two double mutants were created: E173L, N187L, A190L+Y215L, A197L+E208L, H211L, Q222L and R243L.

Table 4.4. Summary of primers used for creation of BECN2 mutants used for cellular assay.

Primers	Sequence (5' → 3')
E173L (S)	CCTGGAGCTGGAGCTGGCCAGGCTGGTGC
E173L (A)	GCACCAGCCTGGCCAGCTCCAGCTCCAGG
N187L (S)	GATGTGGACAGGAACCTGGCAAGAGCAGCGGCG
N187L (A)	CGCCGCTGCTCTTGCCAGGTTCTGTCCACATC
A190L (S)	GGAACAATGCAAGACTGGCGGCGGATCTCCAG
A190L (A)	CTGGAGATCCGCCGCCAGTCTTGCAATTGTTCC
A197L (S)	GCGGATCTCCAGGCACTGCAGGCAGAGGCTGCG
A197L (A)	CGCAGCCTCTGCCTGCAGTGCCTGGAGATCCGC
E208L (S)	GAGCTGGACCAGCAGCTGAGGCAGCACTACAGG
E208L (A)	CCTGTAGTGCTGCCTCAGCTGCTGGTCCAGCTC
H211L (S)	CAGCAGGAGAGGCAGCTGTACAGGGACTACAGTG
H211L (A)	CACTGTAGTCCCTGTACAGCTGCCTCTCCTGCTG
Y215L (S)	CAGCACTACAGGGACCTGAGTGCCTTGAAGCGG
Y215L (A)	CCGCTTCAAGGCACTCAGGTCCTGTAGTGCTG
Q222 (S)	GCCTTGAAGCGGCAGCTGCTGGAAGTCTTGATC
Q222 (A)	GATCAAGCAGTTCAGCAGCTGCCGCTTCAAGGC
R243L (S)	GCCAGGGTCCAGCTGGACCGGCTGAAG
R243L (A)	CTTCAGCCGGTCCAGCTGGACCCTGGC

We also created BECN2 mutants for cellular assays, equivalent to the mutants used for bacterial expression, to investigate how these mutations of the CCD interface residues impact autophagy. The mutants were created by site directed mutagenesis method as described above. pCR3.1 FLAG-BECN2 was used as the template. The corresponding primers used are shown in Table 4.4 The following mutants were created: E173L, N187L, A190L/Y215L, A197L/E208L, H211L, Q222L, and R243L. Unfortunately, cellular assays could not be performed due to technical and expense problems.

4.2.3. Expression and purification of selected BECN2 fragments and mutants

Dr. Minfei Su expressed and purified the WT and most of the mutant BECN2 CCD and the results were reported in her dissertation. I expressed and purified BECN2 CCD E173L and R243L mutants. *E. coli* BL21(DE3)-pLysS cells were transformed with the BECN2 CCD mutant plasmids and grown in LB media with 100 µg/mL ampicillin at 37 °C to an OD₆₀₀ of ~0.8 prior to equilibrating the temperature to 20 °C. The cells were then induced by addition of 0.5 mM

isopropyl thio- β -D-galactoside (IPTG). The cells were harvested via centrifugation at 4,000 g for 20 minutes and the cell pellets were frozen at -80 °C.

Frozen pellets from a 6 L expression were thawed and resuspended in 150 ml lysis buffer (50 mM Tris pH 8.0, 150 mM NaCl, 2 mM DTT) with 0.2 mM AEBSF, and resuspended cells were lysed in a NanoDeBEE emulsifier (BEE International). The lysate was centrifuged at 20,000 g for 40 minutes to pellet cell debris. Soluble MBP-tagged fusion protein was purified from clarified crude cell lysate by amylose affinity chromatography using a 10 mL amylose resin (GE Healthcare) gravity column and washed with 10 column volumes of Wash Buffer: 25 mM Tris-HCl pH 8.0, 150 mM NaCl, 2 mM Dithiothreitol (DTT) prior to overnight, on-column cleavage by 15 mg of glutathione S-transferase – tobacco etch virus (GST-TEV) protease at 4 °C. Cleaved protein was washed from the column with Wash Buffer and further purified by ion exchange chromatography on a 8 ml 5/50 GL MonoQ column (GE Healthcare) (MonoQ Buffer A: 50mM Tris-HCl pH 8.0, 2mM BME; MonoQ Buffer B: 50mM Tris-HCl pH 8.0, 1M NaCl, 2mM BME,). Lastly, the BECN1 CCD mutants were purified to homogeneity by size exclusion chromatography (SEC), using a Superdex 200 10/300 GL and Superdex 75 10/300 GL tandem column (GE Healthcare) column (SEC buffer: 25 mM Tris-HCl pH 8.0, 150 mM NaCl, 2 mM BME). At each stage of purification protein purity was examined by SDS-PAGE. The final purified proteins were concentrated using a 3 kD Amicon Ultra-0.5 centrifugal concentrator (EMD Millipore, Billerica, MA, US) and stored at -80 °C

The MBP-BECN2 BH3D-FHD-CCD fragment was expressed and harvested the same way as the BECN2 CCD mutants mentioned above. Soluble fusion protein was purified from clarified crude cell lysate by amylose affinity chromatography (Wash Buffer: 25 mM Tris-HCl pH 8.0, 150 mM NaCl, 2 mM Dithiothreitol (DTT) followed by SEC, using a Superdex 200

10/300 GL and Superdex 75 10/300 GL tandem column (GE Healthcare) (SEC buffer: 25 mM Tris-HCl pH 8.0, 150 mM NaCl, 2 mM BME). At each stage of purification protein purity was examined by SDS-PAGE. The final purified protein was concentrated using a 30 kD Amicon Ultra-0.5 centrifugal concentrator (EMD Millipore, Billerica, MA, US).

4.2.4. Over-expression and purification of BECN2 CCD E173L and R243L mutants

The M11 residues 1-136 were cloned into pET21(d+) vector (Novagen) encoding a C-terminal His₆-tag and purified as described previously (Sinha *et al.*, 2008). The Bcl-X_L (residues 1-208, N52D/N66D) was cloned, along with a C-terminal His₆-tag, into the *NdeI* and *NotI* restriction sites of pET29 and purified as described previously (Su *et al.*, 2014).

4.2.5. Crystallization and diffraction data collection

The N187L mutant BECN2 CCD was crystallized at 20°C by hanging-drop vapor diffusion from a 1:1 mixture of 12.2 mg/ml protein and reservoir solution comprised of 0.1 M MgCl₂ and 19 % PEG3350. Crystals were harvested and cryo-protected in the reservoir solution plus 25 % glycerol, then flash-frozen in liquid nitrogen. Diffraction data were collected at 100 K at the 24-ID NE-CAT beamline at APS, Argonne National Laboratory, Argonne, IL. Data were recorded in a 180° sweep from a single N187L BECN2 crystal, at 1 second exposure per 1° crystal rotation per image, at a crystal-to-detector distance of 310 mm. Diffraction data were processed using RAPD automated processing suite (<https://rapd.nec.aps.anl.gov/rapd>), which incorporates XDS for integration and scaling (Kabsch, 2010). Dr. Minfei Su solved the structure of the N187L mutant CCD by Phaser-MR in PHENIX (Adams *et al.*, 2010), using the WT BECN2 CCD AB homodimer as the search model. Crystallographic data collection and refinement statistics are summarized in Table 4.5. All the analyses of this structure were completed by Dr. Minfei Su and reported in her dissertation as well as in (Su *et al.*, 2017).

Table 4.5. Summary of x-ray data collection of BECN2 CCD N187L mutant.

Wavelength (Å)	0.97918
Data range (Å)	72.09 - 2.52
Unit cell parameters	C2
Unit cell parameters	a= 127.97 Å b= 44.71 Å c= 94.90 Å β = 130.57°
Average Mosaicity (°)	0.18
Unique reflections	13749 (1362)
Avg. multiplicity	3.7 (3.4)
Completeness (%)	97.1 (86.9)
CC1/2	0.991 (0.761)
Rmeas	0.26 (1.43)
I/ σ I	6.1 (1.1)

Values in parentheses pertain to the outermost shell of data.

4.2.6. BECN2 BH3D peptide synthesis

Peptides corresponding to the human BECN2 BH3D (88-GAMHMLSSIQKAAGDIFDIVSGQA-111) (EZbiolab, Carmel, IN), was chemically synthesized, and then HPLC purified to > 95% purity, with purity confirmed by electrospray mass spectrometry.

4.2.7. ITC for BECN2 interactions with M11 and Bcl-X_L

ITC was performed using a Low Volume Nano ITC (TA Instruments). For the isolated BECN2 BH3D, the peptide was solubilized in ITC buffer comprised of 25 mM Tris pH 8.0, 150 mM NaCl and 2 mM β -mercaptoethanol to a concentration of 1 mM, and rocked at room temperature overnight. However, the commercially synthesized BECN2 BH3D peptide was largely insoluble, even when decrease the peptide concentration to 0.1 mM. The insoluble fraction was then pelleted by centrifugation at 20,000 \times g for 10 min, and peptide concentration in the supernatant assessed and found to be undetectable. Therefore, the binding of BECN2 BH3D-FHD-CCD to M11 or Bcl-X_L was assessed by ITC. Either M11 or Bcl-X_L were co-dialyzed with MBP-BECN1 BH3D-FHD-CCD or MBP-BECN2 BH3D-FHD-CCD against 1L ITC buffer. 0.3-1 μ M M11 or 0.13-0.65 μ M Bcl-X_L was loaded into the syringe, while 0.05-0.12

μM MBP-BECN1 BH3D-FHD-CCD or 0.02-0.06 μM MBP-BECN2 BH3D-FHD-CCD was loaded into the sample cell. ITC was performed at 20 °C with 25 injections of 2 μl each. ITC was performed at 20 °C with 25 injections of 2 μl each. Blank profiles obtained by titrating M11 or Bcl-X_L into buffer were subtracted from the experimental profiles. Data were analyzed with the NanoAnalyze Software (TA Instruments) and fitted with independent interaction model. The data reported are the average of three sets of experiments.

4.3. Results

4.3.1. Domain architecture of BECN2

BECN1 and BECN2 likely have a very similar architecture based on their sequence similarity (56.6% sequence identity) and predicted BECN2 secondary structure. Based on this similarity and secondary structure predictions, BECN2 domain architecture (Figure 4.1) consists of an IDR comprising residues 1-121, a FHD comprising residues 122-152, a CCD comprising residues 158-250 and a BARAD comprising residues 230-431. The most variable region of BECN1 and BECN2 is the IDR. Within the BECN2 IDR, residues 88-111 are equivalent to the Beclin1 BH3D. However, the highly conserved BECN1 BH3D residue, L116, that is critical for binding to various Bcl-2 proteins (Oberstein *et al.*, 2007, Sinha *et al.*, 2008, Su *et al.*, 2014), is not conserved in BECN2. Another BECN1 BH3D residue T119, which is phosphorylated by DAPK to promote dissociation of BECN1 from Bcl-2 (Zalckvar *et al.*, 2009), is also not conserved in BECN2. The FHD-CCD-BARAD region of BECN1 and BECN2 is highly conserved, sharing 60.3 % identity, with the CCD sharing 53.8 % sequence identity.

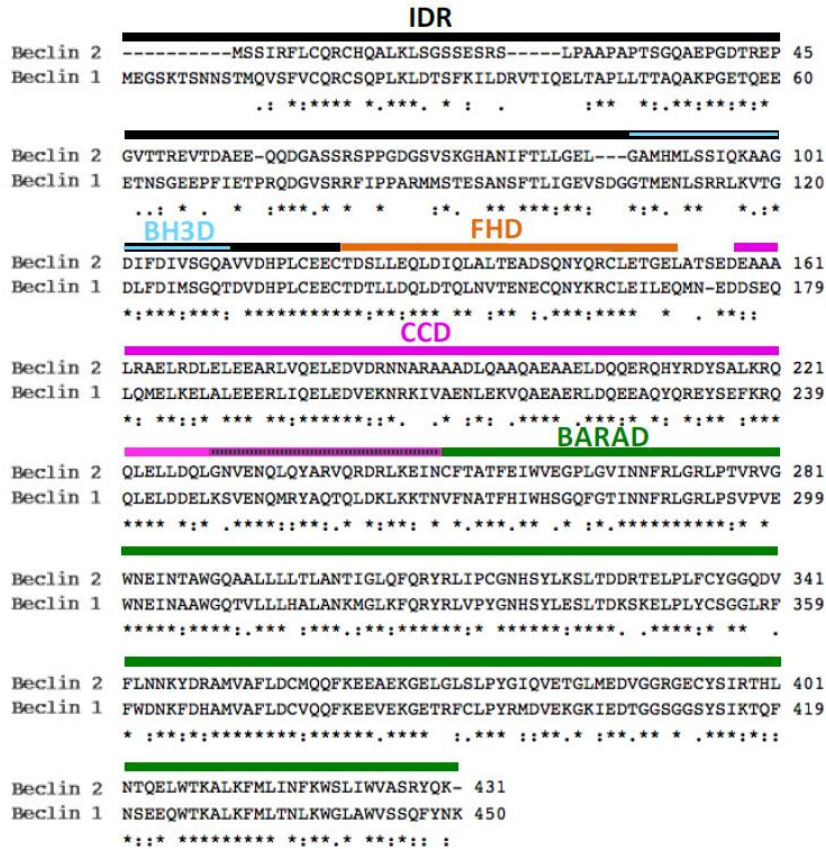


Figure 4.1. Sequence alignment of human BECN1 and BECN2. Asterisks represent identical residues, while double and single dots represent decreasing sequence conservation. Domain boundaries are displayed above the alignment with the black, cyan, orange, violet and green lines representing the IDR, BH3D, FHD, CCD and BARAD, respectively.

4.3.2. Purification of BECN2 fragments

BECN2 CCD E173L and R243L were expressed in *E. coli* BL21(DE3)-pLysS cells, and soluble protein in the cell lysate purified to homogeneity using amylose-affinity chromatography with on-column cleavage with GST-TEV protease, followed by anion-exchange chromatography and SEC. Together, the single peak on SEC and single band on SDS-PAGE indicate each BECN2 CCD mutant preparation was pure and homogenous (Figure 4.2A,B).

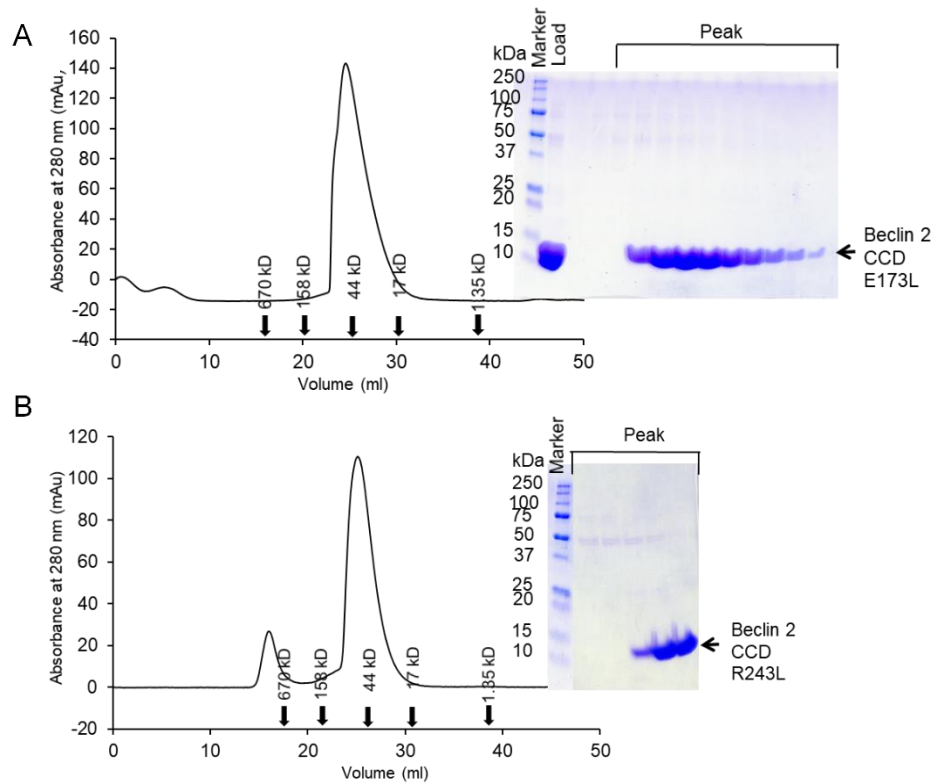


Figure 4.2. Size exclusion chromatogram and the corresponding SDS-PAGE of BECN2 CCD mutants. (A) BECN2 CCD E173L. (B) BECN2 CCD R243L. The elution positions of SEC standards are indicated by arrows.

The apparent molecular mass of BECN2 CCD E173L calculated based on the elution volume from SEC is 63.1 kD, which is 2.8-times greater than the theoretical molecular mass of 22.3 kD for the CCD dimer calculated from the amino acid sequence. The apparent molecular mass of BECN2 CCD R243L calculated based on the elution volume from SEC is 57.5 kD, which is 2.6-times greater than the theoretical molecular mass of 22.3 kD for the CCD dimer calculated from the amino acid sequence. This is consistent with each CCD forming elongated dimers. Notably, the SEC peak of the BECN2 CCD E173L has a steeper slope at the leading edge, relative to the trailing edge, suggesting that BECN2 CCD E173L forms weak homodimers, with the leading edge representing dimeric states and trailing edge representing monomeric state. Although the SEC peak of the BECN2 CCD R243L mutant is more symmetric than that of BECN2 CCD E173L, the leading edge is still steeper than the trailing edge. This suggests that

R2432L CCD mutant is a weak homodimer, albeit stronger than the E173L mutant. The final yield of the purified E173L and R243L CCD mutants are 0.8 mg and 0.6 mg respectively, from one liter of bacterial culture.

MBP-BECN2 BH3D-FHD-CCD was expressed in *E. coli* BL21(DE3)·pLysS cells, and soluble protein in the cell lysate purified to homogeneity using amylose-affinity chromatography with on-column cleavage with GST-TEV protease, followed by SEC. Together, the single SEC peak and single band on SDS-PAGE indicate MBP-BECN2 BH3D-FHD-CCD was pure and homogenous (Figure 4.3). The apparent molecular mass of MBP-BECN2 BH3D-FHD-CCD calculated based on the SEC elution volume is 154.9 kD, which is slightly greater than the theoretical molecular mass of 123.4 kD for the homodimer calculated from the amino acid sequence. This is consistent with the BH3D-FHD-CCD forming an elongated dimer. 20 mg of purified MBP-BECN2 BH3D-FHD-CCD was obtained from one liter of bacterial culture.

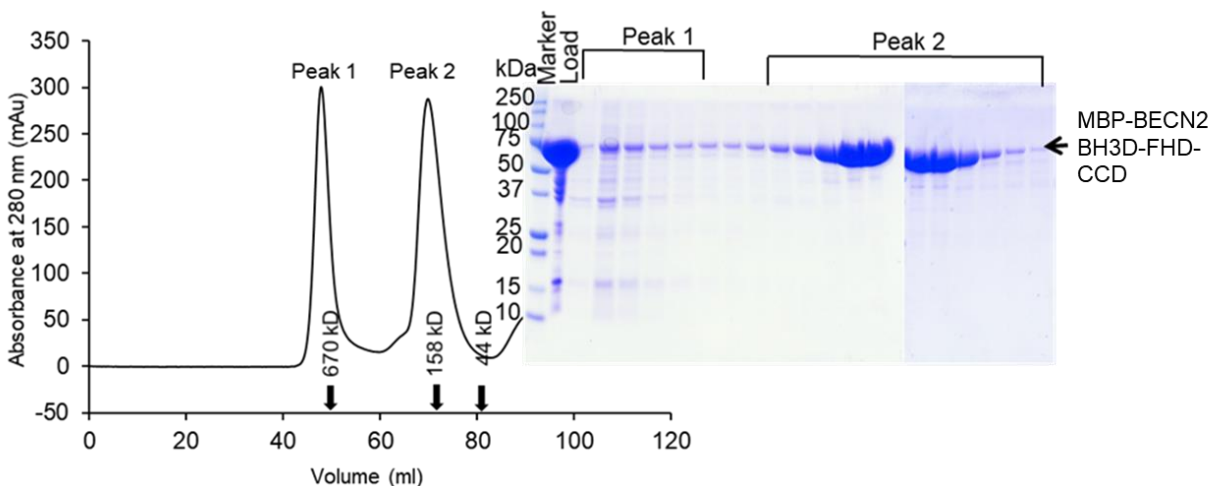


Figure 4.3. Size exclusion chromatogram and the corresponding SDS-PAGE of MBP-BECN2 BH3D-FHD-CCD. The elution positions of SEC standards are indicated by arrows.

4.3.3. ITC for MBP-BECN2 BH3D-FHD-CCD interactions with M11 and Bcl-X_L

We were unable to quantify binding of the BECN2 BH3D to M11 and Bcl-X_L as the commercially synthesized BECN2 BH3D did not dissolve in ITC-appropriate buffers. Therefore,

we purified MBP-tagged BECN2 BH3D-CCD-BARAD for use in ITC experiments to quantify and compare binding affinities and reaction thermodynamics to M11 and Bcl-X_L(Figure 4.4A,B).

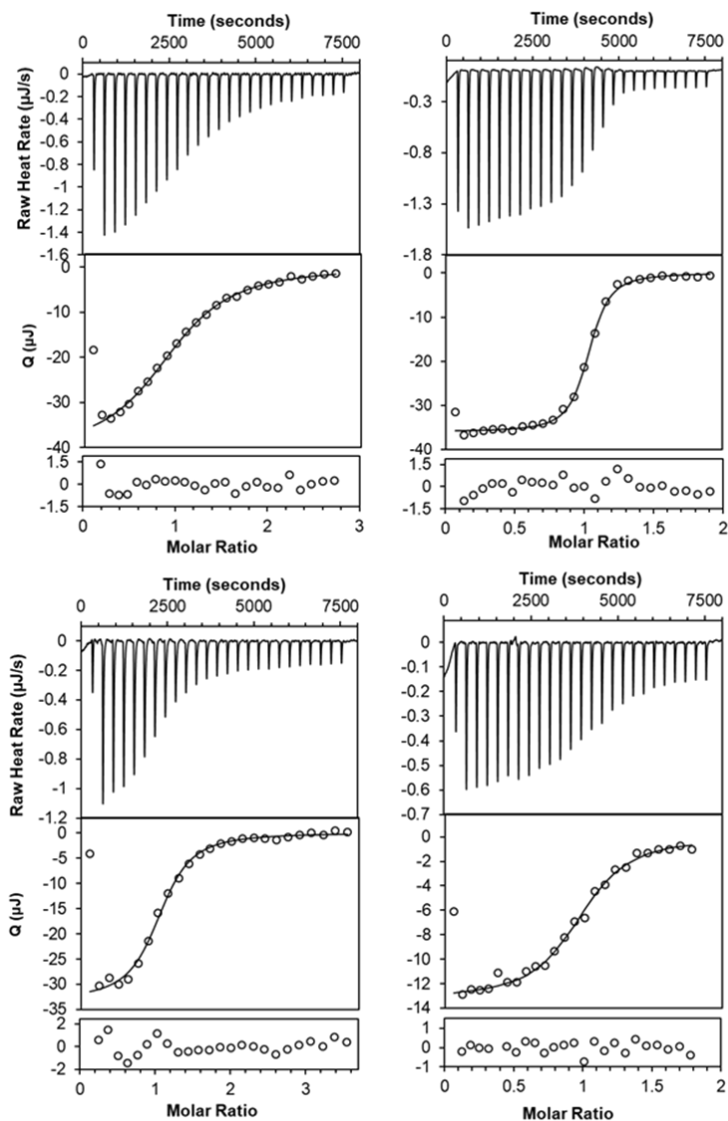


Figure 4.4. Representative ITC profiles of BCL2 homologs binding to BECN2 and BECN1 BH3D-FHD-CCD. Upper panel: raw data; lower panel: integrated heat and theoretical fit by independent interaction model from TA Analysis. (A) 1 mM M11 titrated into 0.12 mM MBP-BECN2 BH3D-FHD-CCD. (B) 0.3 mM M11 titrated into 0.05 mM MBP-BECN1 BH3D-FHD-CCD. (C) 0.65 mM Bcl-X_L titrated into 0.06 mM MBP-BECN2 BH3D-FHD-CCD. (D) 0.125 mM Bcl-X_L titrated into 0.023 mM MBP-BECN1 BH3D-FHD-CCD.

Table 4.6. Thermodynamics of binding of M11 or Bcl-X_L to MBP-tagged BH3D-FHD-CCD fragments of BECN2 and BECN1.

BECN homolog	M11				Bcl-X _L			
	K _d (μM)	ΔH (kJ/mol)	ΔS (J/K·mol)	ΔG (kJ/mol)	K _d (μM)	ΔH (kJ/mol)	ΔS (J/K·mol)	ΔG (kJ/mol)
BECN2	18.67 ± 0.9	-23.39 ± 3.13	18.63 ± 0.03	-26.54 ± 0.13	2.7	-25.9	18.1	-31.2
BECN1	0.44 ± 0.23	-60.70 ± 0.71	-86.85 ± 0.44	-35.64 ± 0.90	1.17 ± 0.61	-52.38 ± 2.09	-67.20 ± 3.25	-33.01 ± 1.15

The ITC results show that M11 binds to MBP-BECN2 BH3D-FHD-CCD ~42-fold more weakly than to MBP-BECN1 BH3D-FHD-CCD (Table 4.5). This is not surprising since two of the BECN1 BH3D residues involved in interaction with M11, R115 and L116, are not conserved in the BECN2 BH3D; and mutation of L116A of BECN1 BH3D decreases the binding affinity of BECN1 BH3D:M11 interaction by ~ 100-fold (Su *et al.* 2014). Surprisingly however, Bcl-X_L binds only slightly more weakly to MBP-BECN2 BH3D-FHD-CCD than to MBP-BECN1 BH3D-FHD-CCD, even though BECN1 BH3D L116A mutation abrogates binding to Bcl-X_L.

The ΔG of M11:BECN2 interaction is smaller than that of the M11:BECN1 interaction, while the ΔG of Bcl-X_L:BECN1 interaction is similar to that of the Bcl-X_L:BECN1 interaction. In addition, the magnitudes of the enthalpic and entropic contributions to the interactions are different (Table 4.6). Binding of the BECN2 BH3D-FHD-CCD to either M11 or Bcl-X_L has similar positive ΔS (Table 4.5), while the binding of the BECN1 BH3D-FHD-CCD to M11 and Bcl-X_L has negative ΔS. While the ΔH of binding of either BECN2 or BECN1 BH3D-FHD-CCD to either M11 or Bcl-X_L is negative, the magnitude of ΔH contributions to binding is ~4 and 3-times smaller respectively, for BECN2 BH3D-FHD-CCD relative to the BECN1 BH3D-FHD-CCD. Therefore, binding of these BCL2 homologs to the BECN1 BH3D-FHD-CCD is driven by enthalpy, while the binding to the BECN2 BH3D-FHD-CCD is favored by both enthalpy and entropy, but has a significantly smaller enthalpy contribution. Thus, the difference

in the BECN2 BH3D-FHD-CCD and BECN1 BH3D-FHD-CCD residues involved in binding to either with M11 or Bcl-X_L result in different thermodynamic drivers for each interaction.

4.4. Conclusions and Discussion

In this study, we created constructs comprising of different BECN2 domains and attempted to purify them. The BECN2 CCD was successfully purified and crystallized, and its structure was solved to 2.3 Å by Dr. Minfei Su. The atomic structure of the BECN2 CCD has been published (Su *et al.*, 2017) and in Dr. Su's dissertation. To summarize, unlike the BECN1 CCD which is straight, the BECN2 CCD forms a curved anti-parallel homodimer, which may imply an ability to interact with membranes of similar curvature or to induce curvature in membranes. Similar to the BECN1 CCD, the BECN2 CCD also contains 7 pairs of non-ideal interface residues, which may make it a weak homodimer. The weak association of the BECN2 homodimer is important for binding to the CCDs of binding partners, such as Atg14 and UVRAG.

Dr. Su also performed and published detailed mutational, biophysical and structural analyses of BECN2 CCD homodimerization and heterodimerization with Atg14, which suggests that these BECN homologs are designed to associate and dissociate in the context of subtle cellular signals. To summarize, the non-ideal pairings of polar and hydrophobic interface residues make BECN2 CCD a meta-stable homodimer, which may represent an autophagy-inactive cellular reservoir of BECN2. This homodimer may be further stabilized by interactions with other proteins in the cell. The weak homodimerization of BECN2 likely facilitates the dissociation of these homodimers upon induction of autophagy, to allow them to form heterodimers with the CCDs of other autophagy proteins like Atg14 and UVRAG.

We also investigated BECN2 interactions with anti-apoptotic proteins, M11 and Bcl-X_L. MBP-BECN2 BH3D-FHD-CCD were purified and its interactions with M11 and Bcl-X_L were quantified by ITC. Notably, despite differences in the sequences of BECN2 and BECN1, including residues that have been shown to be critical for binding to both M11 and Bcl-X_L, such as BECN1 L116 (Su *et al.*, 2014), which corresponds to BECN2 Q97; the BECN2 BH3D-FHD-CCD binds to both M11 and Bcl-X_L. Not surprisingly, however the binding of M11 to the BECN2 BH3D-FHD-CCD is 42-fold weaker than to the BECN1 BH3D-FHD-CCD. Strikingly however, Bcl-X_L binds with similar affinity to the BH3D-FHD-CCD fragments of both BECN2 and BECN1. However, the thermodynamic contributions to the overall binding affinity are different, indicating that the different residues of the BECN proteins result in different thermodynamic drivers for each interaction. Thus, there are clear differences between the binding of BCL2 homologs to different BECN paralogs, suggesting that there may be important differences in the mechanisms by which the different paralogs are regulated by BCL2 homologs. Therefore, it is important to investigate both BECN paralogs found in humans.

CHAPTER 5. STRUCTURAL INSIGHTS INTO THE INTERACTION OF CONSERVED MAMMALIAN PROTEINS GAPR-1 AND BECN1

5.1. Introduction

5.1.1. GAPR-1 belongs to CAP superfamily, the members of which play diverse roles via diverse mechanisms in organisms

Golgi-Associated Plant Pathogenesis Related protein (GAPR-1), also known as GLIPR-2 or C9orf19, is a mammalian protein that belongs to the Cysteine-rich secretory proteins, Antigen 5, and Pathogenesis-related protein (CAP) superfamily (Eberle *et al.*, 2002). CAP superfamily proteins are found in diverse organisms ranging from bacteria to humans (Gibbs *et al.*, 2008). Mammals have multiple CAP domain-containing proteins. Most CAP domain proteins are secreted outside the cell where they have endocrine and paracrine functions (Gibbs *et al.*, 2008). CAP proteins are implicated in diverse biological functions such as reproduction, immune regulation and tumor suppression.

The CAP domain is characterized by a molecular mass of 17-21 kDa and a conserved α - β - α sandwich fold, wherein the central β -sheet is flanked by three helices on one side and by the fourth helix on the other side with the sandwich fold stabilized by the hydrophobic packing, hydrogen bonds and disulfide bonds (Fernandez *et al.*, 1997, Henriksen *et al.*, 2001, Serrano *et al.*, 2004, Asojo *et al.*, 2005, Suzuki *et al.*, 2008, Asojo *et al.*, 2011, Asojo, 2011, Osman *et al.*, 2012, Mason *et al.*, 2014, Darwiche *et al.*, 2016, Orlachs & Helms, 2016). Most members of this superfamily have a signal peptide at the N-terminus and various additional C-terminal domains that likely assign the CAP domain to a specific biological function (Gibbs *et al.*, 2008). Based on sequence similarity, four conserved sequence motifs named CAP1 – CAP4 have been identified in CAP domains (Gibbs *et al.*, 2008).

Multiple, diverse molecular mechanisms have been attributed to different CAP domains (Table 5.1). CAP domains have been shown to bind metals (Henriksen *et al.*, 2001, Suzuki *et al.*, 2008, Wang *et al.*, 2010, Asojo *et al.*, 2011, Osman *et al.*, 2012, Mason *et al.*, 2014, Darwiche *et al.*, 2016); cholesterol (Choudhary & Schneiter, 2012, Choudhary *et al.*, 2014, Kelleher *et al.*, 2014, Darwiche *et al.*, 2016); other lipids or lipid-like molecules (van Galen *et al.*, 2012, Xu *et al.*, 2012, Darwiche *et al.*, 2016); peptides (Milne *et al.*, 2003, Mason *et al.*, 2014) and also predicted to bind glycan (Osman *et al.*, 2012). Most CAP domains have an equatorial surface groove, which, at its center, often includes a deeper cavity lined by conserved residues. This equatorial surface groove was shown to bind metal ions, often within the deeper central cavity (Henriksen *et al.*, 2001, Suzuki *et al.*, 2008, Wang *et al.*, 2010, Asojo *et al.*, 2011, Mason *et al.*, 2014, Darwiche *et al.*, 2016). The equatorial surface groove is also predicted to bind peptides (Milne *et al.*, 2003, Osman *et al.*, 2012, Mason *et al.*, 2014) or other large molecules such as glycan (Osman *et al.*, 2012). Notably, the cone snail venom Tex31 CAP domain has protease activity and can efficiently bind to and cleave the conotoxin propeptide (Milne *et al.*, 2003). In contrast, the yeast Pry1 CAP domain is required and sufficient for binding and transporting cholesterol (Choudhary & Schneiter, 2012, Choudhary *et al.*, 2014). A pocket on the Pry1 CAP domain, distinct from the equatorial groove and named the caveolin-binding motif (CBM), binds 1,4-dioxane from the crystallization solution (Darwiche *et al.*, 2016). The CBM is also required for cholesterol binding, as mutagenesis of these residues abrogates *in vivo* sterol export (Choudhary *et al.*, 2014). However, none of these molecular mechanisms are observed in a wide range of CAP domains, nor have they been characterized in detail. Thus, the molecular mechanism(s) of CAP domains is still not well understood.

Table 5.1. Summary of proteins containing CAP domains and their interaction with metal, lipids, or peptides.

Protein	Binding partners	Binding site	Evidence	References
Ves v5	Hg ²⁺	central cavity in equatorial groove	Seen in structure	Henriksen 2001
Pseudecin	Zn ²⁺	central cavity in equatorial groove	Seen in structure	Suzuki 2008
Natrin	Zn ²⁺	central cavity in equatorial groove	Seen in structure	Wang 2010
Na-ASP-1	Zn ²⁺	central cavity in equatorial groove	Superimposition of the structures of Na-ASP-1 and Natrin:Zn ²⁺ indicates that Na-ASP-1 may also bind Zn ²⁺ at the central cavity	Asojo 2011 a
GLIPR1	Zn ²⁺	central cavity in equatorial groove	Seen in structure	Asojo 2011 b
Ac-ASP-7	Ca ²⁺ and Mn ²⁺	C-terminal hinge-like moiety	Seen in structure	Osman 2012
Na-ASP-2	Zn ²⁺	Central cavity of the equatorial groove	Seen in structure	Mason 2014
Pry1	Mg ²⁺	central cavity in equatorial groove	Seen in structure	Darwiche 2016
Pry1 and Pry2	Cholesterol and Cholesteryl acetate	C279 (not at the equatorial groove)	Cells lack Pry1 and Pry2 do not have cholesterol export ability. Pry1 and Pry2 bind free cholesterol and cholesteryl acetate <i>in vitro</i> (saturable binding of radio-labelled cholesterol and cholesteryl acetate observed). A Pry1 C279S mutant does not bind and export cholesterol <i>in vivo</i> and has 3-fold lower binding affinity <i>in vitro</i> .	Choudhary 2012
Pry1	Cholesterol	caveolin-binding motif (Not in equatorial groove)	Mutation of caveolin-binding motif abrogates the <i>in vivo</i> sterol-export function (F239L; F244L; P242L; and A292L)	Choudhary 2014
SmVAL4	Cholesterol	Not indicated	SmVAL4 expression rescues the cholesterol export ability of cells lacking Pry1 and Pry2; Binds to radiolabelled cholesterol <i>in vitro</i> .	Kelleher 2014
Pry1	Cholesterol	Indicated to bind the caveolin-binding motif	Binds to radiolabelled cholesterol <i>in vitro</i>	Darwiche 2016
Pry1	Dioxane	caveolin-binding motif	Dioxane bound to caveolin-binding motif seen in structure	Darwiche 2016
GAPR-1	Lipids and IP6	Not indicated	Liposome binding assay and gel filtration	Van Galen et al. 2012
tablysin-15	fatty acid	hydrophobic groove formed by helix 1,3, and 4 (different from the equatorial groove)	Tubular shape electron density not accounted for by the protein was observed in a hydrophobic groove formed by helix 1,3, and 4	Xu 2012
tablysin-15	cysteinyl leukotrienes LTC ₄ , LTD ₄ , and LTE ₄	hydrophobic groove formed by helix 1,3, and 4 (different from the equatorial groove)	ITC; and structure of Tablysin-15:LTE ₄ complex	Xu 2012
Tex31	Peptide	central cavity in equatorial groove	Protease activity, the active site is predicted to locate at the equatorial groove	Milne 2003
Ac-ASP-7	Peptide or glycan	equatorial groove	shape and extent of the equatorial groove is predicted to be suitable for binding peptide or glycan	Osman 2012
Na-ASP-2	Peptide	equatorial groove	peptides that bind to Na-ASP-2 are identified by a phage display-12 peptide library kit with lambda bacteriophage M13KE; Na-ASP-2:SK3 (residues 244-255) was modelled, and MD simulation was performed	Mason 2014

5.1.2. Structure and functions of GAPR-1

GAPR-1 is highly expressed in heart, lung and peripheral blood leukocytes, and at lower levels in skeletal muscle, prostate and uterus (Baxter *et al.*, 2007). GAPR-1 is unique amongst mammalian CAP domain-containing proteins in that it consists of only the CAP domain and lacks a signal peptide (Eberle *et al.*, 2002, Serrano *et al.*, 2004). Consistent with the absence of a signal peptide and unlike other CAP domain proteins, GAPR-1 lacks disulphide bonds and is not secreted by canonical pathways, although some reports indicate that it might be secreted into the lumen of small vesicles in seminal fluid by a non-canonical secretory pathway (Van Loon & Van Strien, 1999, Eberle *et al.*, 2002, Aalberts *et al.*, 2012). Further, GAPR-1 localizes to lipid-rich microdomains of the cytosolic leaflet of the Golgi complex. It binds tightly to negatively charged lipid head-groups such as inositol phosphate (IP₆) (van Galen *et al.*, 2012). The crystal structure of GAPR-1 (Figure 5.1, PDB ID: 4AIW) shows that, like other CAP domains, it has a wide and long equatorial groove, but the function of this groove is not established. GAPR-1 was crystallized as a dimer, but appears to equilibrate between monomeric and dimeric states in solution (Serrano *et al.*, 2004). Yeast two hybrid assays suggest that GAPR-1 may exist as a dimer in cells (Serrano *et al.*, 2004). However, another study suggests that GAPR-1 is a monomer in the absence of lipid (van Galen *et al.*, 2012). The presence of negatively charged lipids appears to alter the GAPR-1 dimer, with one GAPR-1 subunit rotated 5° relative to the other (van Galen *et al.*, 2012). Moreover, incubation with liposomes composed of negatively charged lipids stabilizes GAPR-1 dimers, and prolonged incubation causes formation of amyloid-like fibrils via β -sheet extension (Olrichs *et al.*, 2014). Thus, the oligomeric state of GAPR-1 has not been unambiguously established and may change in different cellular contexts.

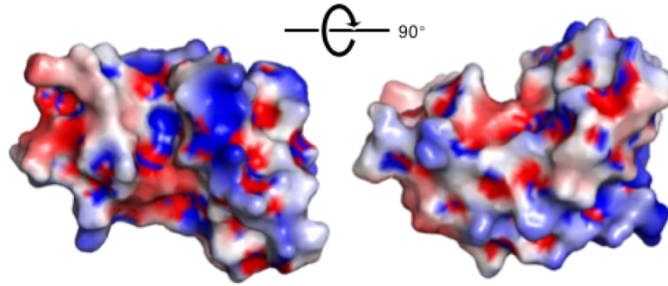


Figure 5.1. Electrostatic surface of WT GAPR-1 generated by APBS (Baker *et al.*, 2001). Blue: positively charged surface; red: negatively charged surface; white: uncharged surface. The range of electrostatic potential displayed is -5 to 5 kT.

5.1.3. GAPR-1 down-regulates autophagy by interaction with BECN1

GAPR-1 was shown to bind to BECN1 and down-regulate autophagy (Shoji-Kawata *et al.*, 2013). BECN1 co-immunoprecipitates (CoIPs) GAPR-1, and deletion of BECN1 residues 267-284, which map to the BARAD, diminishes GAPR-1 CoIP (Shoji-Kawata *et al.*, 2013). Further, a cell-permeable peptide derived from BECN1 residues 267-284 is sufficient to pull-down GAPR-1 and has been shown to induce autophagy, possibly by competitively preventing GAPR-1 binding to BECN1. Peptides with BECN1 F270S or F274S mutations fail to bind to GAPR-1 and fail to induce autophagy (Shoji-Kawata *et al.*, 2013). A cell-permeable peptide, Tat-BECN1, derived from BECN1 residues 267-284 (Figure 5.2), was shown to be a potent autophagy inducer that triggers autophagy to prevent replication of West Nile and Chikungunya viruses and may also target HIV-1 (Shoji-Kawata *et al.*, 2013). Thus, Tat-BECN1 serves as a template for the development of autophagy inducers that may be translated into human therapeutics. Tat-BECN1 is predicted to activate BECN1 and the core autophagy initiation complex by competitively binding to the autophagy down-regulator GAPR-1 (Shoji-Kawata *et al.*, 2013). Thus, besides a therapeutic role, Tat-BECN1 may help explore the mechanism of autophagy initiation and its role in disease. Hence, it is important to understand the molecular mechanism of BECN1-GAPR-1 interaction and how the interaction down-regulates autophagy.



Figure 5.2. BECN1 residues 269-284 (green) in BECN1 BARAD structure (grey) (PDB ID: 4DDP).

5.1.4. The goal of this study

The mechanism by which GAPR-1 binds to BECN1 to down-regulate autophagy is unknown. We hypothesized that the GAPR-1 equatorial surface groove, which is lined with five conserved residues may be responsible for binding BECN1. Our attempts to use isothermal titration calorimetry (ITC) to detect interactions between Tat-BECN1 and GAPR-1, were hampered by the poor solubility of the peptide. Further, no binding heat was detected by ITC, which may be due to the low peptide concentration. Therefore, in order to better understand the interaction of GAPR-1 and BECN1, we constructed a model of the GAPR-1:BECN1 (residues 267-284) complex to identify potential GAPR-1 residues involved in the GAPR-1:BECN1 interaction and used pull-down assays to test the impact of mutating these residues on binding of GAPR-1 to BECN1. We solved the high-resolution three-dimensional structure of a mutant GAPR-1 that does not bind to BECN1 to elucidate structural changes likely to disrupt binding, and used ITC to quantify self-dissociation constants of WT and mutant GAPR-1. Lastly, we used size-exclusion chromatography together with small angle X-ray scattering (SEC-SAXS) to verify the oligomeric states of wild-type (WT) and mutant GAPR-1 in solution.

5.2. Materials and Methods

5.2.1. Constructing a model of the complex of GAPR-1:BEEN1 residues 267-284

Sequence alignments were performed using Clustal W2. The docking server CABS-dock (Kurcinski *et al.*, 2015) was used to model the binding of BEEN1 residues 267-284 to the "receptor molecule", i.e. WT GAPR-1 (PDB ID: 1SMB). Docking involved three discrete steps: 1) Random structures of a peptide comprising BEEN1 residues 267-284 were generated and placed on the surface of the receptor; 2) Replica Exchange Monte Carlo dynamics was used in docking, yielding a total of 10,000 models of the GAPR-1:BEEN1 residues 267-284 complex; and 3) The final representative models were selected in two sub-steps: a. All unbound states were excluded and 100 lowest binding energy models of the GAPR-1:BEEN1 residues 267-284 complex were selected for the next step; b. Selected models were clustered based on the root mean square deviation (RMSD) of the entire complex for model refinement; the clusters were ranked according to size from largest to the tenth largest and the ten top-ranked models (representatives of the 10 most populated clusters) were selected.

5.2.2. Creation of cellular protein expression constructs

WT GAPR-1 residues 1-154 were subcloned from GAPR-1-Myc (Shoji-Kawata *et al.*, 2013) using primers 5'-GAAGATCTATGGGCAAGTCAGCTTCCA and 5'-TTGCGGCCGCTTACTTCTTCGGCGGCAGGA, into a pGEX-6P-1 vector between BamHI and NotI restriction enzyme sites. GAPR-1 mutants E86A, G102K/H103A, H54A/G102K/H103A/N138G, E86A/G102k/H102A/N138G, and H54A/E86A/G102K/H103A/N138G (named the pentad mutant GAPR-1) were generated by PCR mutagenesis using QuikChange II Site-Directed Mutagenesis Kit (Agilent Technologies).

WT BECN1 residues 1-450 were subcloned from FLAG-BECN1 (Shoji-Kawata *et al.*, 2013) using primers 5'- CGGGATCCATGGAAGGGTCT and 5'- TTGCGGCCGCTCATTTGTTATAAAATTGTG between *Bam*HI and *Not*I restriction enzyme sites of a pGEX-4T-1 vector.

MBP-BECN1 CCD-BARAD construct was identical to that used in Chapter 3. MBP-BECN1^{Δ31-104} was created by deleting residues 31-104 from MBP-BECN1 FL construct (see Chapter 2) using the QuikChange II Site-Directed Mutagenesis Kit (Agilent Technologies).

5.2.3. Pull-down assays and western blot

For GST pull-down assays, the GST fusion proteins described above were expressed in *E. coli* strain BL21-CodonPlus(DE3)-RP and purified using glutathione Sepharose 4B (GE Healthcare). GST-tagged GAPR-1 was treated with PreScission protease to remove the GST tag. GAPR-1 variants were incubated with GST-BECN1 or GST conjugated to glutathione Sepharose 4B beads in binding buffer (PBS with 0.5% Triton X-100). After a 2-hour incubation at 4°C, beads were washed three times with binding buffer. The input and bound GAPR-1 proteins were analyzed by western blotting using an anti-GAPR-1 antibody (Eberle *et al.*, 2002). The amount of GST or GST-BECN1 in pull-downs was analyzed by staining the same polyvinylidene fluoride membrane with Ponceau S stain.

5.2.4. Large-scale expression and purification of WT and pentad mutant GAPR-1

For large scale protein purification, the plasmids described above, encoding either GST-PreScission-WT GAPR-1 or H54A/E86A/G102K/H103A/N138G pentad GAPR-1 mutant (herein called the pentad mutant), were used to transform *E. coli* BL21(DE3) pLysS cells which were grown at 37 °C on agar plates supplemented with 50 µg/ml ampicillin and 35 µg/ml chloramphenicol. A single colony from an agar plate was picked and grown in 50 ml LB medium

supplemented with 50 µg/ml ampicillin and 35 µg/ml chloramphenicol overnight. Then the 50 ml overnight culture was dispensed into 6L LB medium supplemented with 50 µg/ml ampicillin and 35 µg/ml chloramphenicol. The 6L medium was grown to $OD_{600} = 0.8$ (log phase) prior to induction of protein expression with 0.5 mM IPTG at 20 °C while shaking at 220 rpm for 18 hours. The cells were harvested via centrifugation at 4,000 g for 20 minutes and the cell pellets were frozen at -80 °C.

Frozen pellets were thawed and resuspended in 300 ml lysis buffer (25 mM HEPES pH 7.5, 300 mM NaCl, 10% glycerol, 2 mM DTT) with 0.2 mM AEBSF, and resuspended cells were lysed in a NanoDeBEE emulsifier (BEE International). The lysate was centrifuged at 20,000 g for 40 minutes to pellet cell debris. The resulting supernatant was passed through a gravity column containing 10 ml GST resin (GE Healthcare). The column was washed by 150 ml lysis buffer to wash off the unbound contaminant proteins. 12 mg of GST PreScission protease was then added to the resin for on-column cleavage of the GST-tag. The GST resin was then resuspended so the protease mixed well with the bound protein and incubated overnight at 4 °C. This cleavage leaves a G-P-L-G-S peptide linker on the protein. The cleaved protein was washed off the column with 20 ml lysis buffer, then the NaCl concentration in the protein solution was diluted to 100 mM with MonoS Buffer A (25 mM HEPES pH 7.5; 2 mM DTT) for further purification by cation exchange chromatography using an 8 ml HR10/10 MonoS column (GE Healthcare). After the diluted protein was loaded, the column was washed with 150 ml of 10% MonoS Buffer B (25 mM HEPES pH 7.5; 1 M NaCl; 2 mM DTT) followed by a 200 mL gradient of 10%-50% Buffer B. GAPR-1 eluted at 27% Buffer B (i.e. at 270 mM NaCl). Lastly, the protein was purified by size exclusion chromatography (SEC) using a HiLoad 16/60 Superdex 200 column (GE Healthcare) equilibrated in SEC buffer comprised of 50 mM Tris pH

8.0, 300 mM NaCl and 2mM DTT. 10 mg/ml GAPR-1 was loaded onto the column in 2.5 ml aliquots, eluted with SEC buffer at 0.5ml/min, and 2 ml fractions were collected. The purity of the protein eluted from SEC was evaluated using SDS-PAGE, and fractions from the single peak corresponding to highly poor and homogenous WT or pentad mutant GAPR-1 were pooled and concentrated to 1 mM (17.2 mg/ml) in SEC buffer using a 10 kD Amicon Ultra-0.5 centrifugal concentrator (EMD Millipore) and stored at -80 °C.

5.2.5. Large-scale expression and purification of MBP-BECN1 CCD-BARAD and BECN1^{Δ31-104}

Recombinant plasmids to over-express either MBP-BECN1 CCD-BARAD or MBP-BECN1^{Δ31-104} was used to transform *E. coli* Arctic Express cells for large scale protein purification. The transformed cells were grown at 37 °C on agar plates supplemented with 50 µg/ml ampicillin and 20 µg/ml gentamycin. A single colony from the agar plate was picked and grown in 50 ml LB medium supplemented with 50 µg/ml ampicillin and 20 µg/ml gentamycin overnight. Then the 50 ml overnight culture was used to inoculate 3L LB medium supplemented with 50 µg/ml ampicillin, and grown at 37 °C to OD₆₀₀ = 0.8 (log phase) while shaking at 220 rpm. The temperature of the cultures was then equilibrated to 13 °C and protein expression was induced by adding 0.5 mM IPTG and growing the cultures for 18 hours. Cells were harvested via centrifugation at 4,000 g for 20 minutes and the cell pellets frozen at -80 °C.

Frozen pellets were thawed and resuspended in 150 ml of lysis buffer (50 mM Tris pH 8.0, 300 mM NaCl, 10% glycerol, 2 mM DTT) with 0.2 mM AEBSF, and resuspended cells were lysed in a NanoDeBEE emulsifier (BEE International). The lysate was centrifuged at 20,000 g for 40 minutes to pellet cell debris. The resulting supernatant was passed through a gravity column containing 10 ml amylose resin (GE Healthcare). The column was then washed

with 150 ml of lysis buffer to wash off the unbound contaminant proteins. The protein bound to the resin was eluted with elution buffer comprised of 50 mM Tris pH 8.0, 300 mM NaCl, 10% glycerol, 2 mM BME. The eluted protein was purified further by SEC using a HiLoad Superdex 200 16/60 GL column (GE Healthcare) equilibrated in a buffer (SEC buffer) comprised of 50 mM Tris pH 8.0, 300 mM NaCl 5% glycerol, and 2mM BME. SEC was performed at a flow rate of 0.5ml/min, and 2 ml fractions were collected. Three SEC runs were performed for the MBP-BECN1 CCD-BARAD protein. For each run, 2.5 ml of 14.2 mg/ml MBP-BECN1 CCD-BARAD was loaded onto the column. Three SEC runs were performed for the MBP-BECN1^{Δ31-104} protein. For each run 2.3 ml of 20 mg/ml MBP-BECN1^{Δ31-104} was loaded onto the SEC column. However, for MBP-BECN1^{Δ31-104}, the SEC column were overloaded, so we pooled the peak fractions and reran it on a Superdex 200 10/300 GL column (GE Healthcare) to confirm that the protein elutes as a single SEC peak. At each stage of purification, protein purity was evaluated using SDS-PAGE. Fractions from the single SEC peak corresponding to either highly pure MBP-BECN1 CCD-BARAD or MBP-BECN1^{Δ31-104} were pooled, and concentrated in SEC buffer to 7 mg/ml or 10 mg/ml respectively, and stored at -80 °C.

5.2.6. Tat-BECN1 peptide

The Tat-BECN1 peptide comprising the amino acid sequence: YGRKKRRQRRRGGTNVFNATFEIWHDGEFGT, was provided by our collaborator Dr. Beth Levine at UT Southwestern Medical Center. The N-terminal 11 amino acids of the peptide are derived from the HIV Tat protein transduction domain, and the remaining from BECN1 residues 267-284. The peptide was synthesized as previously described (Shoji-Kawata *et al.*, 2013).

5.2.7. ITC for GAPR-1-BECN1 interactions

ITC was performed using a Low Volume Nano ITC (TA Instruments). For the MBP-BECN1 CCD-BARAD:GAPR-1 or MBP-BECN1^{Δ31-104}:GAPR-1 interaction, either MBP-BECN1 CCD-BARAD or MBP-BECN1^{Δ31-104} were co-dialyzed with WT GAPR-1 against 1L ITC buffer comprised of 25 mM HEPES, pH 7.5, 150 mM NaCl and 2 mM β-mercaptoethanol. 1 mM WT GAPR-1 was loaded into the syringe, while 0.1 μM of either MBP-BECN1 CCD-BARAD or MBP-BECN1^{Δ31-104} was loaded into the sample cell. ITC was performed at 20 °C with 25 injections of 2 μl each. For the Tat-BECN1-GAPR-1 interaction, the peptide was mixed with ITC buffer to a concentration of 1 mM, and rocked at room temperature overnight to dissolve the peptide into the ITC buffer. However, a significant fraction of the peptide remained insoluble. This insoluble fraction was pelleted by centrifugation at 20,000 × g for 10 min. The supernatant was co-dialyzed with WT GAPR-1 against the ITC buffer overnight at 4 °C, the concentration of the dialyzed peptide and protein was determined by OD₂₈₀. 1 mM Tat-BECN1 was loaded into the syringe, while 0.1 μM WT GAPR-1 was loaded into the sample cell. ITC was performed at 20 °C with 25 injections of 2 μl each.

5.2.8. Crystallization, data collection and structure solution

The pentad GAPR-1 mutant was crystallized at 20 °C by hanging-drop vapor-diffusion, wherein the drop comprised of 1.5 μl protein stock (17 mg/ml protein in 50 mM Tris pH 8.0, 300 mM NaCl, and 2mM DTT) and 0.5 μl reservoir solution (0.1 M Bis-Tris pH 5.5, 35% (w/v) PEG 3350, 50 mM Li₂SO₄). Crystals grew within a week and were harvested in LV CryoOil (MiTeGen) before being flash-cooled in liquid nitrogen.

Diffraction data were collected at 100 K at a wavelength of 0.97918 Å in one 360° sweep from a single crystal at NE-CAT beamline 24ID-C at the Advanced Photon Source (APS),

Argonne National Laboratory (ANL), Argonne, IL. Diffraction intensities were recorded on a 4×4 tiled MAR mosaic CCD detector (Rayonix) at a crystal to detector distance of 250 mm, over a 0.5° crystal rotation for 1 second exposure per image. Diffraction data were processed using the RAPD automated processing web server (<https://rapd.nec.aps.anl.gov/rapd/>). Data statistics are shown in Table 2.1. The structure was solved by molecular replacement using PHASER (McCoy *et al.*, 2007) in the PHENIX suite (Adams *et al.*, 2010), with the WT GAPR-1 structure (PDB ID: 1SMB) as a model. The structure was refined to 1.27 Å using the PHENIX Refinement pipeline (Adams *et al.*, 2010) combined with iterations of manual model building using COOT (Emsley *et al.*, 2010). Final model statistics are reported in Table 5.2.

Table 5.2. X-ray data collection and structure refinement statistics.

Data Collection statistics	
Space group	C222 ₁
Unit Cell Dimension (Å)	62.31, 84.67, 51.43
Resolution (Å)	51.43-1.27
Wilson B-factor (Å ²)	9.94
Unique reflections	35987 (3588)
Completeness	93.8 (99.5)
Multiplicity	3.4 (3.3)
I/σ ₁	11 (2.1)
CC (1/2)	0.986 (0.742)
Refinement Statistics	
PDB ID	5VHG
Resolution range	25.71-1.27 (1.32-1.27)
Completeness (%)	99 (98)
¹ R _{work} (%)	14.5 (20.8)
^{1,2} R _{free} (%)	17.4 (24.6)
Number of protein residues	151
Number of waters	222
RMSD (bonds) (Å)	0.009
RMSD (angles) (°)	0.97
Ramachandran outliers (%)	0
Average B-factor (Å ²)	16.03
Macromolecules	13.75
Solvent	29.18

Values in parentheses are for the highest resolution shell.

¹R factor = $\sum_h |F_{\text{obs}} - |F_{\text{calc}}|| / \sum_h |F_{\text{obs}}|$.

²Test set for R_{free} consisted of 5% of data

5.2.9. Protein structure analysis

Pairwise superimposition of structures was performed using PyMOL (v.1.5.0.2; Schrödinger) (Schrodinger, 2015). Electrostatic properties were calculated with APBS (Baker *et al.*, 2001) using the PARSE force field, and the electrostatic potentials were compared using the web PIPSA server (Richter *et al.*, 2008). Molecular figures were created using PyMOL (v.1.5.0.2; Schrödinger) (Schrodinger, 2015). Dimer interfaces in each crystal structure were analyzed in detail using PISA (Krissinel & Henrick, 2007). Shape complementarity (Sc) at the WT and pentad mutant dimer interface was calculated using the program SC program in the CCP4 suite (Lawrence & Colman, 1993, Winn *et al.*, 2011).

5.2.10. Analytical SEC

Analytical SEC was performed to estimate and compare the molecular mass of WT and pentad mutant GAPR-1. 0.2 ml of 2 mM, 1 mM, 0.5 mM and 0.25 mM purified WT or pentad mutant GAPR-1 in 50 mM Tris pH 8.0, 300 mM NaCl, and 2 mM DTT was injected onto a Superdex 200 10/300 GL SEC column (GE Healthcare) and the molecular masses and hydrodynamic radii (R_s) were calculated by comparison to the elution profile of SEC standards (Bio-Rad Laboratory).

5.2.11. ITC for GAPR-1 homodimer dissociation

ITC experiments were performed using a Low Volume Nano ITC (TA Instruments). WT and pentad mutant GAPR-1 samples were dialyzed against ITC buffer comprising 50 mM Tris pH 8.0, 300 mM NaCl, and 2 mM β -mercaptoethanol. All ITC experiments were performed at 20°C with 25 injections of 2 μ l each, by titrating 0.26 mM protein into ITC buffer. Blank profiles obtained by titrating buffer into buffer were subtracted from the experimental profiles of self-dissociation experiments. Data were analyzed with the NanoAnalyze Software (TA Instruments)

and fitted with dimer dissociation models. The data reported are the average of three sets of experiments.

5.2.12. SEC-SAXS data collection and analysis

SAXS data were collected at beamline 18-ID (Bio-CAT) at APS, ANL, Argonne, IL, using a Pilatus 3 1M detector with X-rays of wavelength 1.033 Å. 17.2 mg/ml WT GAPR-1 or pentad mutant GAPR-1 was injected onto a Superdex 200 10/300 GL SEC column (GE Healthcare) at a flow rate of 0.75 ml/minute and the eluate from the SEC column was immediately exposed to the X-ray beam for one second, with a two second delay between each exposure. The SAXS data were recorded at a sample-to-detector distance of 3.5 meters that covers a momentum transfer range from 0.0036 to 0.4 Å⁻¹ [$q = (4\pi\sin\theta)/\lambda$, where 2θ is the scattering angle]. Scattering data were normalized to the incident X-ray beam intensity, prior to further analysis. Singular value decomposition (SVD) analysis was performed on the normalized scattering data using the program DELA (Lambright *et al.*, 2013, Malaby *et al.*, 2015). The scattering from buffer was subtracted using the BioCAT beamline pipeline based on the ATSAS suite of programs. A q range of $q < 0.3$ Å⁻¹ was used for all SAXS analyses using the ATSAS program suite (Petoukhov *et al.*, 2012). Within the ATSAS program suite, PRIMUS (Konarev *et al.*, 2003) was used to scale and average data for further analysis, and also for Guinier extrapolation. The radius of gyration (R_g) of the averaged data was calculated from the Guinier approximation. The particle pairwise distance distribution function ($P(r)$ plot) and Kratky plot were calculated using GNOM (Semenyuk & Svergun, 1991). The $P(r)$ plot was used to estimate R_g and D_{max} , which were used to constrain the dimensions of the ten independent *ab initio* bead models calculated using DAMMIF (Franke & Svergun, 2009). P1 symmetry was imposed to generate these models. A total of 10 *ab initio* reconstructed models were further averaged and

filtered by DAMSEL, DAMSUP, DAMAVER and DAMFILT (Volkov & Svergun, 2003). CRY SOL (Svergun *et al.*, 1995) was used to calculate and compare theoretical scattering curves from either WT (PDB ID: 1SMB) or pentad mutant GAPR-1 structures. Superimposition of the crystal structures to the ab initio bead models was performed using SUPCOMB (Kozin & Svergun, 2001).

5.3. Results

5.3.1. Expression and purification results of GAPR-1 and BECN1

WT GAPR-1 was expressed in *E. coli* BL21(DE3)-pLysS cells, and soluble protein in the cell lysate was purified to homogeneity by Glutathione affinity chromatography followed by on-column cleavage of the GST tag using TEV protease, followed anion-exchange chromatography, and finally by SEC. The single peak on SEC and single band on SDS-PAGE indicates the WT GAPR-1 was pure and homogenous (Figure 5.3) The apparent molecular mass of WT GAPR-1 calculated based on the SEC elution volume of 98.0 ml from SEC is 16.9 kD, which is similar to the theoretical molecular mass of 17.2 kD for the WT GAPR-1 monomer calculated from the amino acid sequence. The final yield of the purified WT GAPR-1 was 5.16 mg / L cell culture

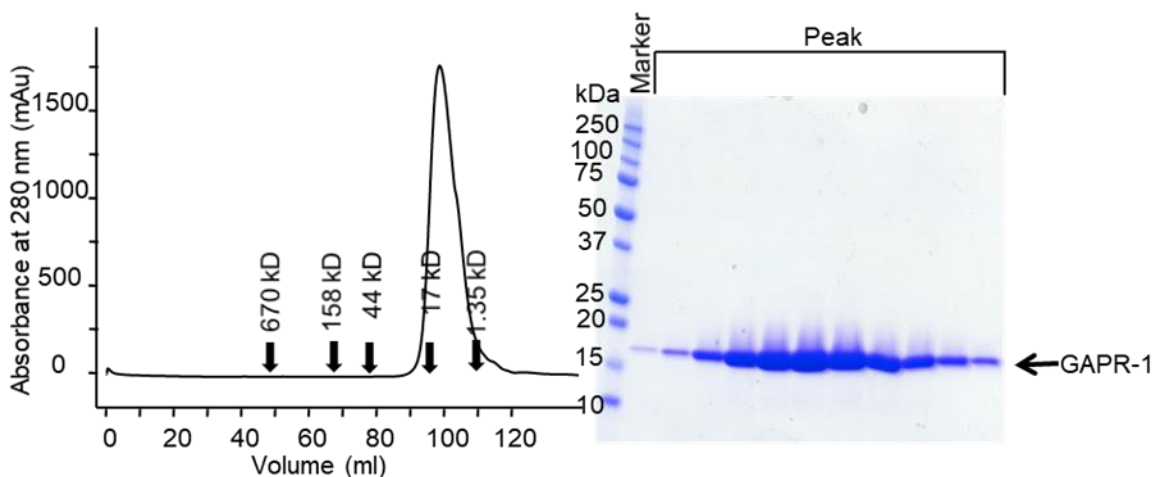


Figure 5.3. Size exclusion chromatogram and the corresponding SDS-PAGE of WT GAPR-1. The elution positions of SEC standards are indicated by arrows.

Pentad mutant GAPR-1 was expressed in *E. coli* BL21(DE3)·pLysS cells, and soluble protein in the cell lysate was purified to homogeneity by glutathione affinity chromatography followed by on-column cleavage of the GST tag using TEV protease, and finally by SEC. The single peak on SEC and single band on SDS-PAGE indicates the pentad mutant GAPR-1 was pure and homogenous. (Figure 5.4) The apparent molecular mass of pentad mutant GAPR-1 calculated based on the SEC elution volume of 87.4 is 31.6 kD, which is 1.84 times larger than the theoretical molecular mass of 17.2 kD for the pentad mutant GAPR-1 monomer calculated from the amino acid sequence, and slightly smaller than the theoretical molecular mass of 34.4 kD expected for the pentad mutant GAPR-1 dimer. The final yield of the purified pentad mutant GAPR-1 was 3.15 mg / L cell culture

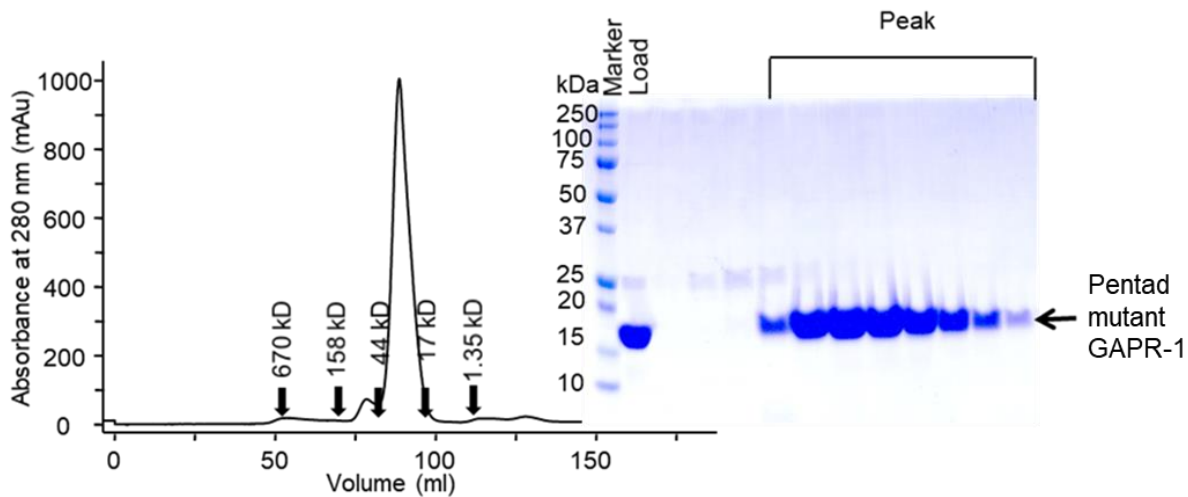


Figure 5.4. Size exclusion chromatogram and the corresponding SDS-PAGE of pentad mutant GAPR-1. The elution positions of SEC standards are indicated by arrows.

MBP-BECN1^{Δ31-104} was expressed in *E. coli* Arctic Express cells, and soluble protein in the cell lysate from a 3 L expression was purified to homogeneity by using an amylose affinity chromatography and SEC. The single peak on SEC and single band on SDS-PAGE indicates the MBP-BECN1^{Δ31-104} was pure and homogenous (Figure 5.5). The apparent molecular weight of MBP-BECN1^{Δ31-104} calculated based on the elution volume from SEC is 501.20 kD, which is

2.88-fold greater than the theoretical molecular weight of 174.22 kD for the MBP-BECN1^{Δ31-104} homodimer calculated from the amino acid sequence, suggesting MBP-BECN1^{Δ31-104} forms an elongated homodimer. The final yield of purified MBP-BECN1^{Δ31-104} was 8 mg / L cell culture.

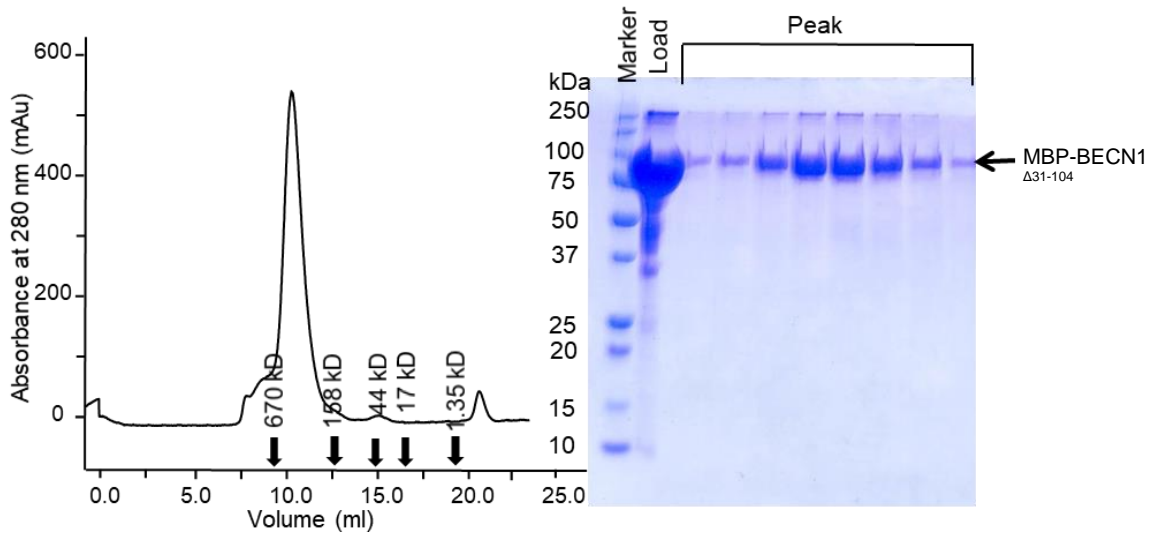


Figure 5.5. Size exclusion chromatogram and the corresponding SDS-PAGE of MBP-BECN1^{Δ31-104}. The elution positions of SEC standards are indicated by arrows.

5.3.2. GPR-1 BECN1 interaction was not detected by ITC

ITC was used to assess interactions between GPR-1 and Tat-BECN1 (residues 267-284) or BECN1 constructs containing BARAD. However, no heat signal was detected between GPR-1 and either Tat-BECN1 (Figure 5.6A) or MBP-BECN1 CCD-BARAD (Figure 5.6B) or MBP-BECN1^{Δ31-104} (Figure 5.6C), therefore we could not quantify the thermodynamics of binding.

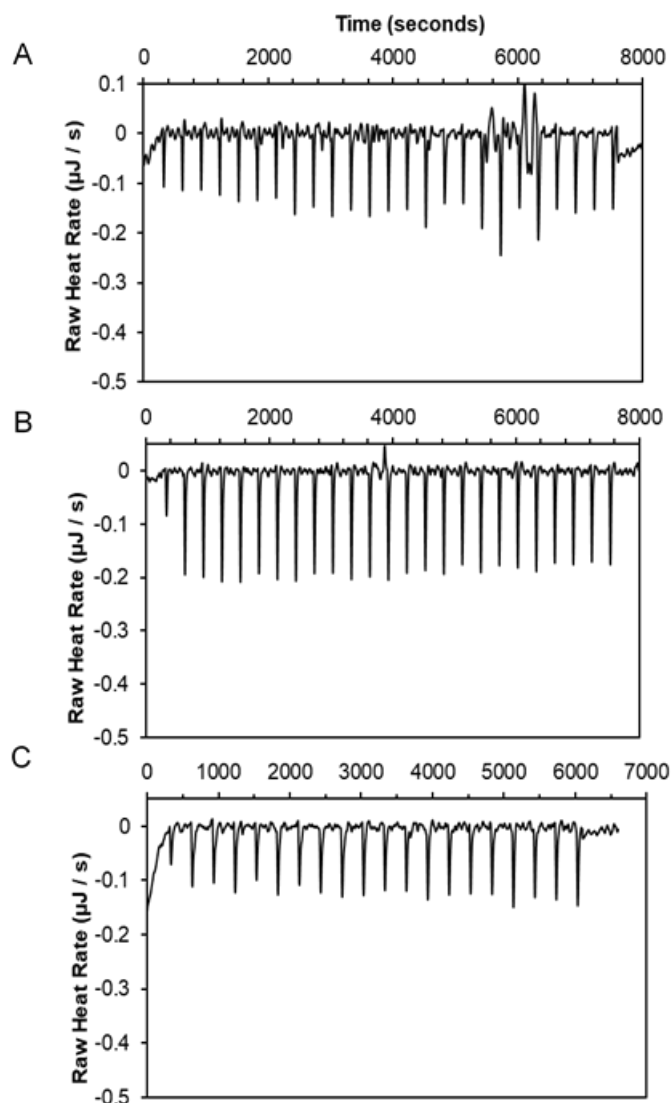


Figure 5.6. ITC profiles of (A) Tat-BECN1 titrated into WT GAPR-1, (B) WT GAPR-1 titrated into MBP-BECN1 CCD-BARAD, and (C) WT GAPR-1 titrated into MBP BECN1^{Δ31-104}.

5.3.3. BECN1 residues 267-284 are predicted to bind to the conserved equatorial groove of the GAPR-1 CAP domain

Several conserved GAPR-1 residues were identified from an alignment of six CAP protein sequences from different species: GLIPR-1 from human, Pseudechetoxin from king brown snake, CRVP from common wasp, VAL4 from blood fluke, P14a from tomato, and Pry1 from yeast (Figure 5.7). The equatorial surface groove on the GAPR-1 surface is the only groove large enough to accommodate a peptide. This groove is lined by eleven residues, six of which,

(H54, E65, E86, G102, H103, and N138,) are conserved amongst various GAPR-1 orthologs (Figure 5.7 and 5.8). The E65 main chain atoms are surface exposed, but the side chain is buried in the core of the protein, with the side chain carboxylate stabilized by a bidentate salt bridge to the R132 guanidinium and by hydrogen bonds to the S55 hydroxyl and main chain amide. Thus, E65 and equivalent residues of homologs are likely essential for structural integrity of CAP domains rather than peptide binding. Side chains of the remaining five residues are solvent exposed, and amongst these, H54 is part of the CAP3 motif, G102 and H103 are part of the CAP1 motif, and N138 is part of the CAP2 motif. Notably, BECN1, including residues 267-284, is also conserved across species from yeast to humans. Thus, we hypothesized that the five conserved, solvent-exposed GAPR-1 residues lining the equatorial groove may play essential roles in binding to a conserved region of BECN1.

Despite the lack of binding observed in ITC, the program CABS-dock (Kurcinski *et al.*, 2015) was successfully used to dock a peptide corresponding to BECN1 residues 267-284 onto the "receptor molecule", i.e. WT GAPR-1 (PDB ID: 1SMB) (Figure 5.8). CABS-dock does not require *a priori* information about the binding site and allows complete peptide flexibility and small fluctuations of the "receptor" backbone during the docking search. The top-ranked model cluster of the WT GAPR-1:BECN1 (residues 267-284) complex (Figure 5.9) has a RMSD value of 6.39 Å over 18 peptide C α atoms. The model from the top ranked model cluster suggests that BECN1 residues 267-284 bind to the equatorial groove on the GAPR-1 CAP domain. The docked peptide superimposes on equivalent residues of the BECN1 BARAD structure (PDB ID: 4DDP) with a RMSD of 4.4 Å over 16 C α atoms.

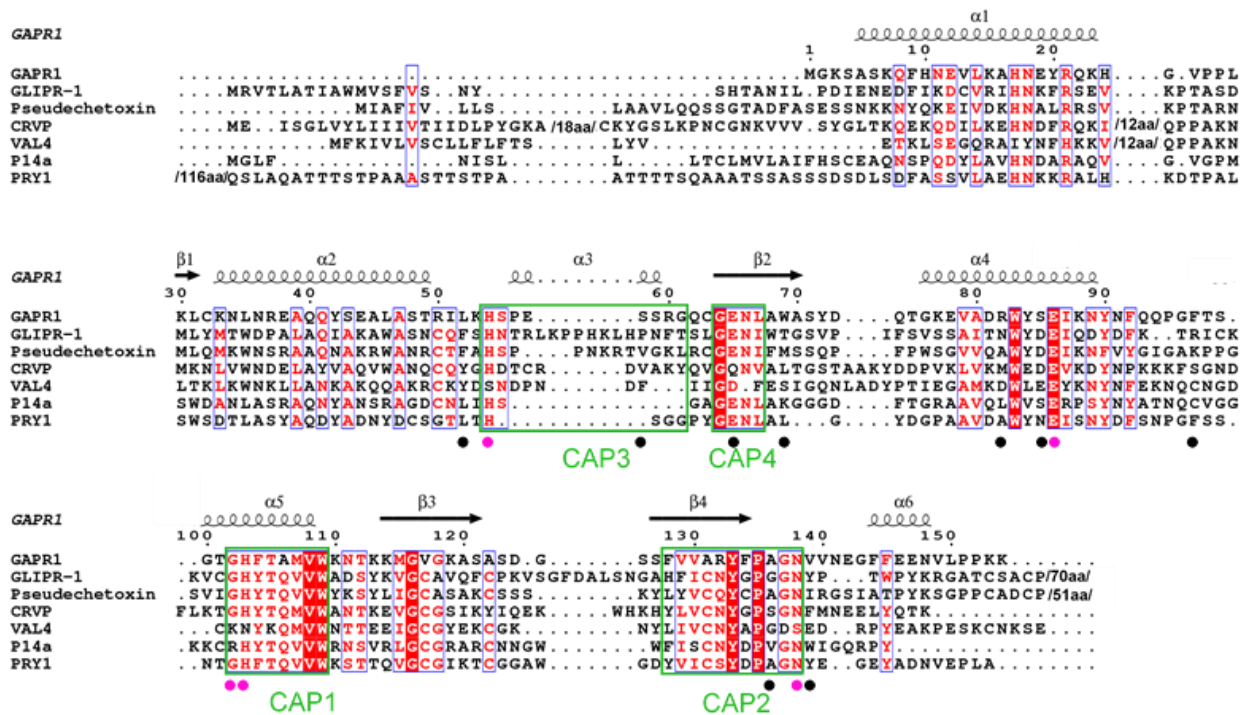


Figure 5.7. GPCR-1 sequence conservation. Alignment of GPCR-1 homolog sequences from different species: GPCR-1, *Homo sapiens*; GliPR-1, *Homo sapiens*; Pseudechetoxin, *Pseudechetopsis australis*; CRVP, *Vespula vulgaris*; VAL4, *Schistosoma mansoni*; P14a, *Solanum lycopersicum*; and PRY1 *Saccharomyces cerevisiae*. Conserved residues are highlighted in red font and invariant residues in white font with red background. Secondary structure elements, i.e. helices and strands, displayed as spirals and arrows respectively above the alignment, correspond to WT GPCR-1. The four conserved CAP sequence motifs are boxed in green. Circles below the sequence alignment indicate residues lining the equatorial binding groove, with magenta circles indicating conserved residues mutated in this study. This figure was made with ESPript (Robert & Gouet, 2014).

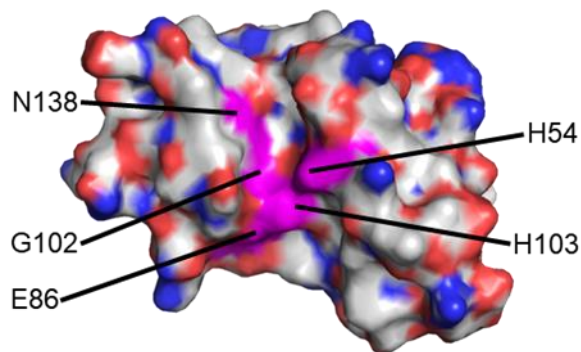


Figure 5.8. Location of mutated, conserved residues within the equatorial GPCR-1 binding groove. The molecular surface of GPCR-1 is colored by atom-type: oxygen, red; nitrogen, blue and carbon, gray; with mutated residues colored magenta.

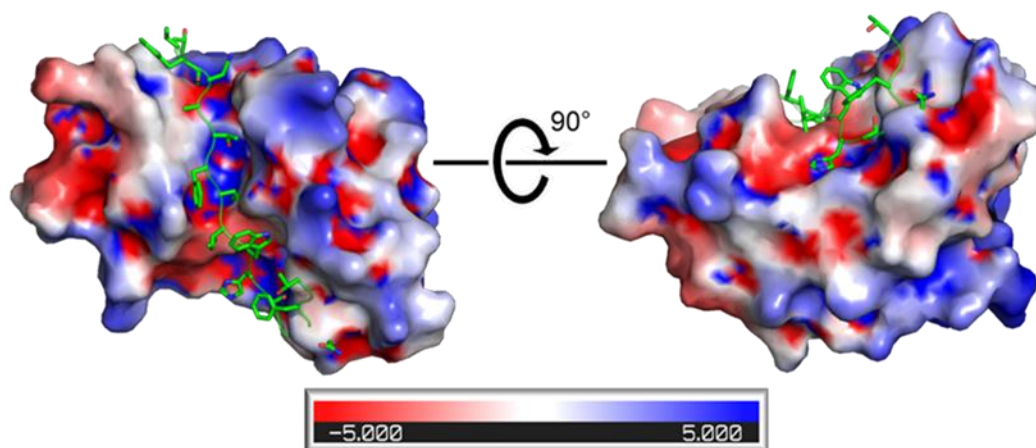


Figure 5.9. Computational model of BECN1 (residues 267-284) docked onto WT GAPR-1 (PDB ID: 1SMB). The electrostatic potential surface of GAPR-1 is shown and the docked peptide comprising BECN1 (residues 167-284) is displayed in green, with side chains shown in stick representation colored by atom type: oxygen, red; nitrogen, blue; carbon, green. The range of electrostatic potential displayed is -5 to 5 kT.

5.3.4. Conserved GAPR-1 residues lining the equatorial binding groove are important for binding to BECN1

The role of the five conserved GAPR-1 residues whose side chains line the equatorial groove was evaluated by assessing the impact of five sets of GAPR-1 mutations (E86A, G102K/H103A double, H54A/G102K/H103A/N138G tetrad, E86A/G102K/H103A/N138G tetrad, and H54A/E86A/G102K/H103A/N138G pentad mutants) on the GAPR-1:BECN1 interaction, as monitored by a GST pull-down assay (Figure 5.10). These assays show that relative to WT GAPR-1, each of these GAPR-1 mutants has substantially decreased binding to BECN1, indicating that residues within each set of mutations likely contribute to the BECN1 interaction interface. Binding to BECN1 is not abolished by either the E86A single mutant, or the G102/H103 double mutant (Figure 5.10) or the N138G single mutant (data not shown), indicating that individually none of these residues is critical for binding. However, the E86A/G102K/H103A/N138G tetrad and H54A/E86A/G102K/H103A/N138G pentad mutations completely abrogate the GAPR-1:BECN1 interaction, suggesting that together the conserved

residues lining the equatorial groove of GAPR-1 proteins, particularly E86, G102, H103, and N138 are important for GAPR-1 binding to BECN1. Therefore, we decided to further investigate the structure of the H54A/E86A/G102K/H103A/N138G pentad mutant GAPR-1.

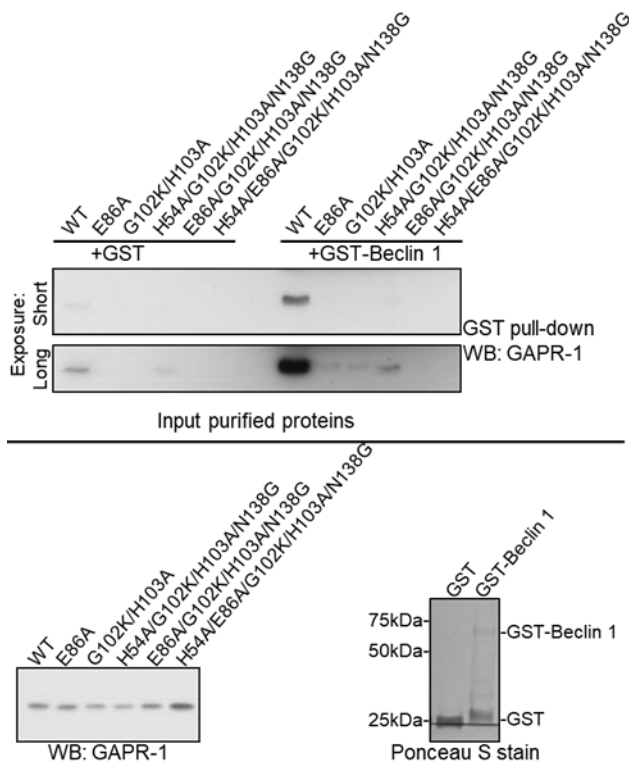


Figure 5.10. GST-BECN1 pull-downs of WT and mutant GAPR-1. GST-tagged BECN1 was used as the bait to pull down WT and mutant GAPR-1. The GAPR-1 bound to BECN1 was detected by anti-GAPR-1 antibodies. WB: Western blot.

5.3.5. The pentad mutation does not impact GAPR-1 tertiary structure

We crystallized the pentad mutant GAPR-1 (Figure 5.11) and determined the 1.27 Å X-ray crystal structure of the pentad mutant GAPR-1 (Figure 5.12A). Pentad mutant GAPR-1 crystals belonged to the space group C2221, with one molecule per asymmetric unit. WT GAPR-1 has previously been crystallized in the ligand-free state (Groves *et al.*, 2004), and in the presence of IP6 (herein called WTinIP6), although IP6 was not visible in the crystal structure (van Galen *et al.*, 2012). Like WT GAPR-1, the pentad mutant GAPR-1 has an α - β - α sandwich fold (Figure 5.12A) and residues packed in the core include a buried E65 that makes bidentate

electrostatic interactions with R132 and hydrogen bonds to S55 (Figure 5.12B). The overall tertiary structure of pentad mutant GAPR-1 is very similar to that of WT and WTinIP6 (Figure 5.13A), with a pairwise RMSD of 1.72 Å over 149 C α atoms of the WT GAPR-1 (PDB ID: 1SMB), and 1.86 Å over 149 C α atoms of WTinIP6 GAPR-1 (PDB ID: 4AIW). The GAPR-1 residues at positions 54, 86, 102, 103, and 138 have well-defined electron density in both the pentad mutant (Figure 5.13A) and WT (Figure 5.13B) GAPR-1 structures.

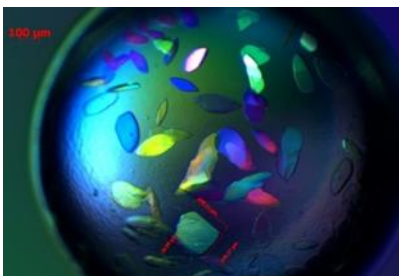


Figure 5.11 Crystals of pentad mutant GAPR-1.

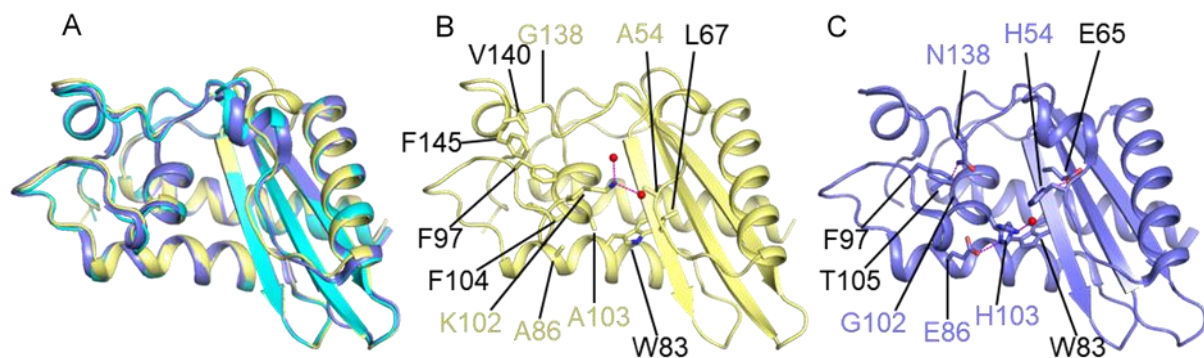


Figure 5.12. GAPR-1 tertiary structure is maintained in the pentad mutant. (A) Superimposed GAPR-1 monomers from different crystal structures: pentad mutant (yellow), ligand-free WT (violet) and WTinIP6 (cyan). (B) Intramolecular interactions of the five mutated residues in pentad mutant GAPR-1. (C) Intramolecular interactions of the WT residues corresponding to those mutated in (B). The side chains of mutated/WT residues and residues that interact with them in (B) and (C) are displayed in stick representation, with atoms colored by type: oxygen, red; nitrogen, blue; carbon, yellow (mutated) or violet (WT). Water molecules are displayed as red spheres. Mutated or WT residues are labeled in yellow or violet, respectively, and interacting residues are labeled in black.

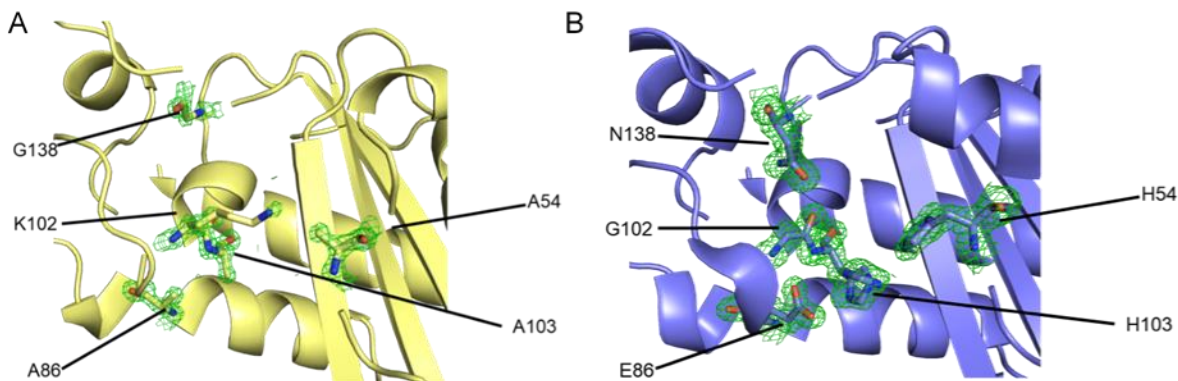


Figure 5.13. $2F_o - F_c$ electron density displayed at contour levels of 1.0σ around the mutated residues of pentad mutant GAPR-1. Mutant residues are shown as sticks, electron density is shown in green mesh. (A) Pentad GAPR-1. (B) WT GAPR-1.

Interactions of residues at positions 54, 86, 102, 103, and 138 are different in the WT and pentad mutant GAPR-1 monomers. In the pentad mutant GAPR-1 structure, A54, A86, K102, A103, and G138 are only involved in hydrophobic interactions (Figure 5.12B). The A54 side-chain packs against the L67 side chain. The A86 side chain packs against side chains of A103 and F104. The aliphatic part of the K102 side chain packs against the aromatic ring of F97 while the charged amino group is solvent exposed and does not make any interactions with protein. In addition to packing with A86, the A103 side chain also interacts with the side chain of W83. Lastly, G138, which lacks a side-chain, enables the packing of F97, V140, and F145 against each other.

In contrast, the equivalent five residues in WT GAPR-1, H54, E86, G102, H103, and N138, also contribute polar interactions (Figure 5.12C). The H54 imidazole NH forms an ionic bond to the E65 side chain carboxylate oxygen. One oxygen of the E86 side chain carboxylate forms ionic bonds to the H103 imidazole NH. In addition to the ionic bond to E86, the H103 imidazole NH hydrogen bonds a water molecule. The H103 C β also packs against the C β of W83. G102 is not involved in any interaction within the subunit. Lastly, the N138 side chain carbonyl oxygen hydrogen bonds the T105 hydroxyl, while the aliphatic part of N138 packs

against the aromatic ring of F97. Thus, the pentad mutations do not disrupt tertiary structure, but do alter interactions of residues within a monomer.

5.3.6. The pentad mutation alters GAPR-1 quaternary structure

Like WT and WTinIP6 GAPR-1, the pentad mutant GAPR-1 forms a crystallographic homodimer, with the subunits related by a 2-fold rotation about the y-axis. However, the dimer interface is significantly different in each of these three structures. Superposition of one subunit of the pentad mutant onto one subunit of the ligand-free WT GAPR-1 dimer reveals that the other subunit of pentad mutant GAPR-1 is rotated 38.1° outward relative to the corresponding ligand-free WT GAPR-1 monomer (Figure 5.14A). In contrast, a similar superposition between pentad mutant and WTinIP6 GAPR-1 shows a rotation of 17.9° inward relative to the other subunit of the WTinIP6 (Figure 5.14B). Notably, neither the conserved residues at positions 54, 86, 102, 103, and 138 of WT GAPR-1, nor the mutated residues at equivalent positions in the pentad mutant GAPR-1, are directly involved in the dimer interface.

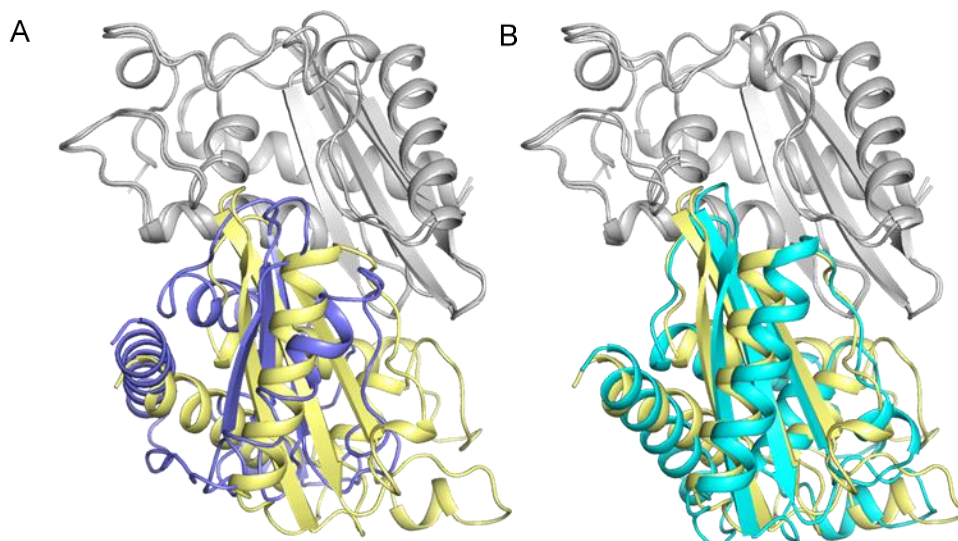


Figure 5.14. The pentad mutation impacts GAPR-1 dimerization. Superimposition of the pentad mutant GAPR-1 dimer (gray and yellow subunits) onto either (A) ligand-free WT GAPR-1 (gray and violet subunits) or (B) WTinIP6 GAPR-1 (gray and cyan subunits). The gray subunits of each dimer are superimposed.

For the pentad mutant, the total surface area buried upon homodimerization is 945 Å², which constitutes about 11.3% of the total surface area of each subunit. The dimer interface involves a total of thirty residues from each subunit and is stabilized by hydrophobic interactions and six intermolecular hydrogen bonds (Figure 5.15A). The three unique, inter-subunit hydrogen bonds are formed between the carbonyl oxygens of L52, R82, and D73; and the R50 guanidinium, the Y72 hydroxyl, and the K88 amino group respectively (Figure 5.15A). Further, we analyzed shape complementarity of the interacting surfaces in the crystallographic dimer, which quantifies the geometric surface complementarity of protein-protein interfaces, where a score of 1.0 denotes perfect geometric complementarity of interacting interfaces (Lawrence & Colman, 1993). Evaluation of protein-protein interaction interfaces identified and obtained by data mining the PDB has shown that the Sc of crystallographically-established interfaces clusters between 0.6-0.8 (De et al., 2005). The pentad mutant GAPR-1 dimer interface has an Sc of 0.70, indicating that the geometrical complementarity at that interface supports dimerization.

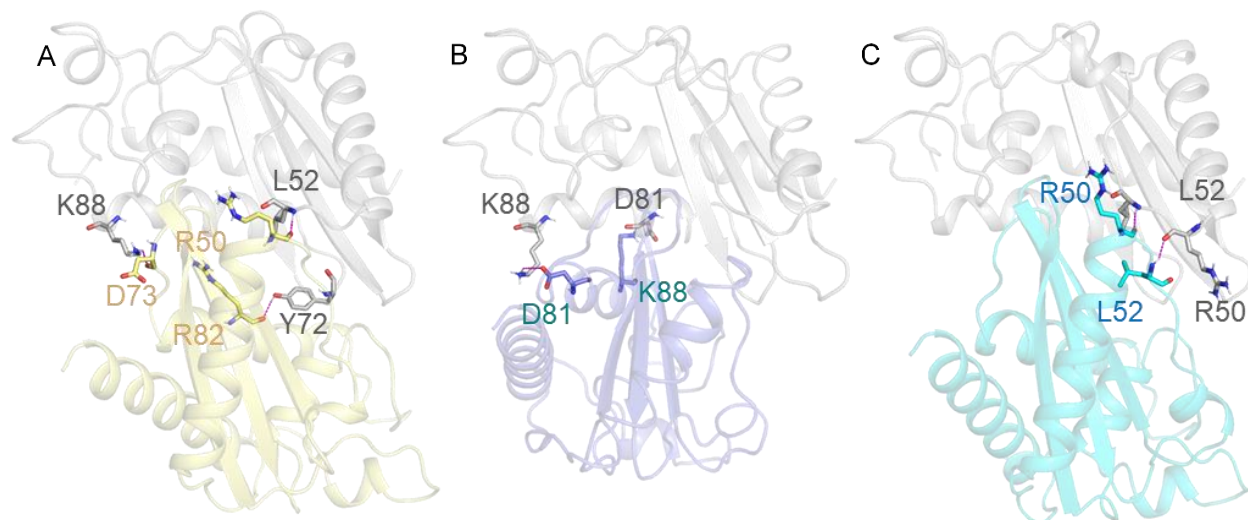


Figure 5.15. The dimer interface varies in the different GAPR-1 dimers. The grey subunit of each dimer is in a superimposable orientation. One set of symmetry-related pairs of hydrogen bonds and salt bridges across the dimer interface are shown for each structure. (A) Pentad mutant. (B) WT. (C) WTinIP6.

Similar to pentad mutant GAPR-1, the total surface area buried upon homodimerization of WT GAPR-1 is 943 Å², constituting approximately 11.7% of the total surface area of each subunit. The dimer interface involves a total of twenty-six residues from each subunit and is stabilized by two pairs of salt bridges, wherein D81 and K88 of one subunit form salt bridges with the K88 and D81 of the other subunit respectively (Figure 5.15B). Despite the similar total surface areas buried upon dimerization of the pentad mutant and WT GAPR-1, the WT GAPR-1 crystallographic dimer interface has an Sc of 0.60, which is less than that of the pentad mutant, indicating that WT GAPR-1 does not dimerize as well due to decreased surface complementarity.

The dimer interface is significantly less extensive for WTinIP6. The total surface area buried upon dimerization is only 717 Å², constituting about 8.6% of the total surface area of each subunit. Twenty-three residues from each subunit contribute to the interface and include a symmetry-related pair of hydrogen bonds. Each symmetry-related hydrogen bond is between the L52 carbonyl oxygen of one subunit and the R50 main chain amide of the other (Figure 5.15C). Unexpectedly though, the WTinIP6 GAPR-1 dimer interface has an Sc of 0.69, comparable to that of pentad mutant GAPR-1, but better than that of WT GAPR-1. Perhaps IP6 induces conformational changes that improve surface complementarity at the GAPR-1 dimer interface.

Neither the five conserved/mutated residues, nor the residues they interact with, are directly involved in the dimer interface interactions (Figure 5.15B, C). However, although the tertiary structures of WT and pentad mutant GAPR-1 monomer superimpose well with a pairwise RMSD of 1.72 Å over 149 C α atoms of the WT GAPR-1 (PDB ID: 1SMB), the C-terminal end of the α 4 helix is distorted in pentad mutant GAPR-1 relative to WT. This helix bears E86 (one of the conserved/mutated residues) and K88 (involved in the dimer interface).

The WT GAPR-1 intramolecular E86 - H103 interaction results in a C α distance of 7.3 Å whereas intramolecular interaction of the corresponding residues, A86 and A103, in the pentad mutant GAPR-1 results in a C α distance of 6.1 Å. This distortion of the α 4 helix likely causes the observed 1.5 Å shift of the K88 C α , and perhaps also impacts the rotamers adopted by the K88 side chain. Therefore, although K88 participates in both dimer interfaces (Figure 5.15A, B), its conformational change in response to the E86A and H103A mutations may result in the different dimer interface observed between the WT and pentad mutant because K88 forms intermolecular interactions with D81 in the WT GAPR-1 and D73 in pentad mutant GAPR-1 dimer.

5.3.7. The pentad mutation impacts characteristics of the equatorial groove

Although the GAPR-1 mutations do not impact global tertiary structure, analysis of the surface electrostatic potential of the WT and the pentad mutant shows that the equatorial binding groove is more positively charged in pentad mutant GAPR-1 (Figure 5.16) than in WT GAPR-1 (Figure 5.9). Further, the G102K mutation reduces the width and depth of the binding groove relative to WT, as the lysine side chain occludes part of the binding groove in the mutant (Figures 5.16 and 5.9). The equatorial surface groove of the pentad mutant GAPR-1 has 15 ordered water molecules, of which two are H-bonded by the mutated K102 side chain amino group. The equatorial surface groove of the WT GAPR-1 has 26 ordered water molecules, of which only one is H-bonded by the H103 imidazole NH. Therefore, the pentad mutations alter the arrangement and number of ordered water molecules bound to the GAPR-1 equatorial groove. Thus, BECN1 binding is also likely to be adversely impacted by the reduction in size, change in shape, and increased positivity of the electrostatic surface of the equatorial binding groove in pentad mutant GAPR-1.

Strikingly, the equatorial groove of each subunit is substantially occluded by the other subunit upon dimerization of pentad mutant GAPR-1 (Figure 5.16, top left and bottom left panels), as well as in WT GAPR-1 (Figure 5.17 top left and bottom left panels) and WTinIP6 GAPR-1 (Figure 5.18, top left and bottom left panels), with maximal occlusion of the groove seen in the pentad mutant GAPR-1. Therefore, binding of BECN1 likely depends on dissociation of the GAPR-1 dimer. At the interface, part of the positively charged equatorial groove of one subunit of pentad mutant GAPR-1 accommodates negatively charged residues of the other subunit (Figure 5.16, top right panel), which stabilizes the pentad mutant dimer. However, at the WT GAPR-1 interface, neutral or negatively charged parts of equatorial groove of one subunit of WT GAPR-1 accommodates both negatively charged and positively charged residues of the other subunit (Figure 5.17, top right panel), which may make it a weaker dimer. Given the increased S_c and electrostatic complementarity of the dimer interface in the pentad mutant, it is likely that the pentad mutant forms more stable dimers relative to the WT. The analysis of GAPR-1 dimerization in solution described below supports this hypothesis.

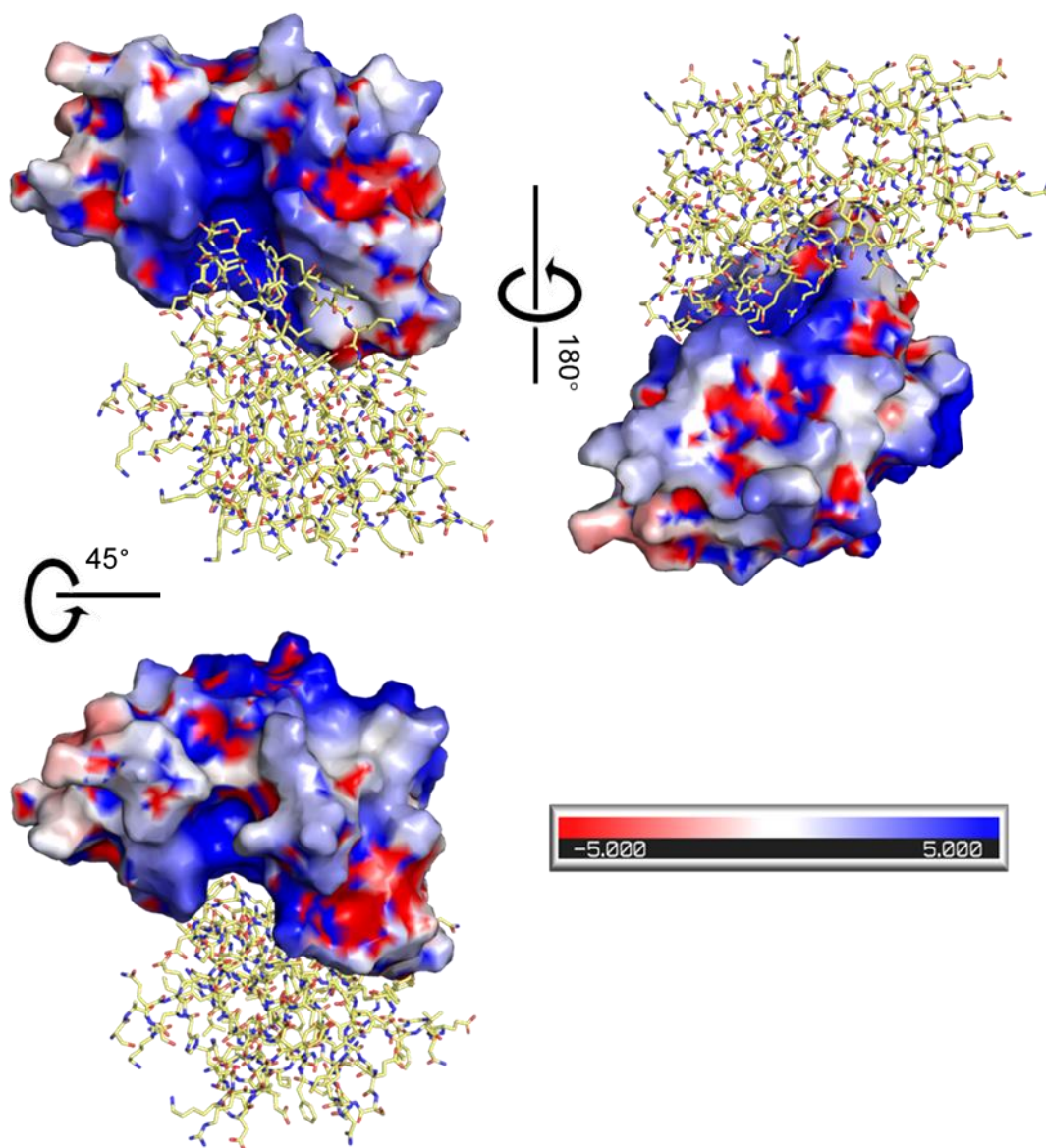


Figure 5.16. Pentad mutant GAPR-1 dimerization occludes the equatorial groove. The electrostatic potential surface of one subunit of the homodimer is shown, while the partner subunit is displayed in stick representation with atoms colored by atom type: oxygen, red; nitrogen, blue; carbon, yellow. The electrostatic potential surface of the same subunit of the homodimer is shown in the top left and bottom panels, while in the right panel the subunit is shown in stick representation, with the partner subunit shown as an electrostatic potential surface. Rotations representing the different views in each panel are indicated.

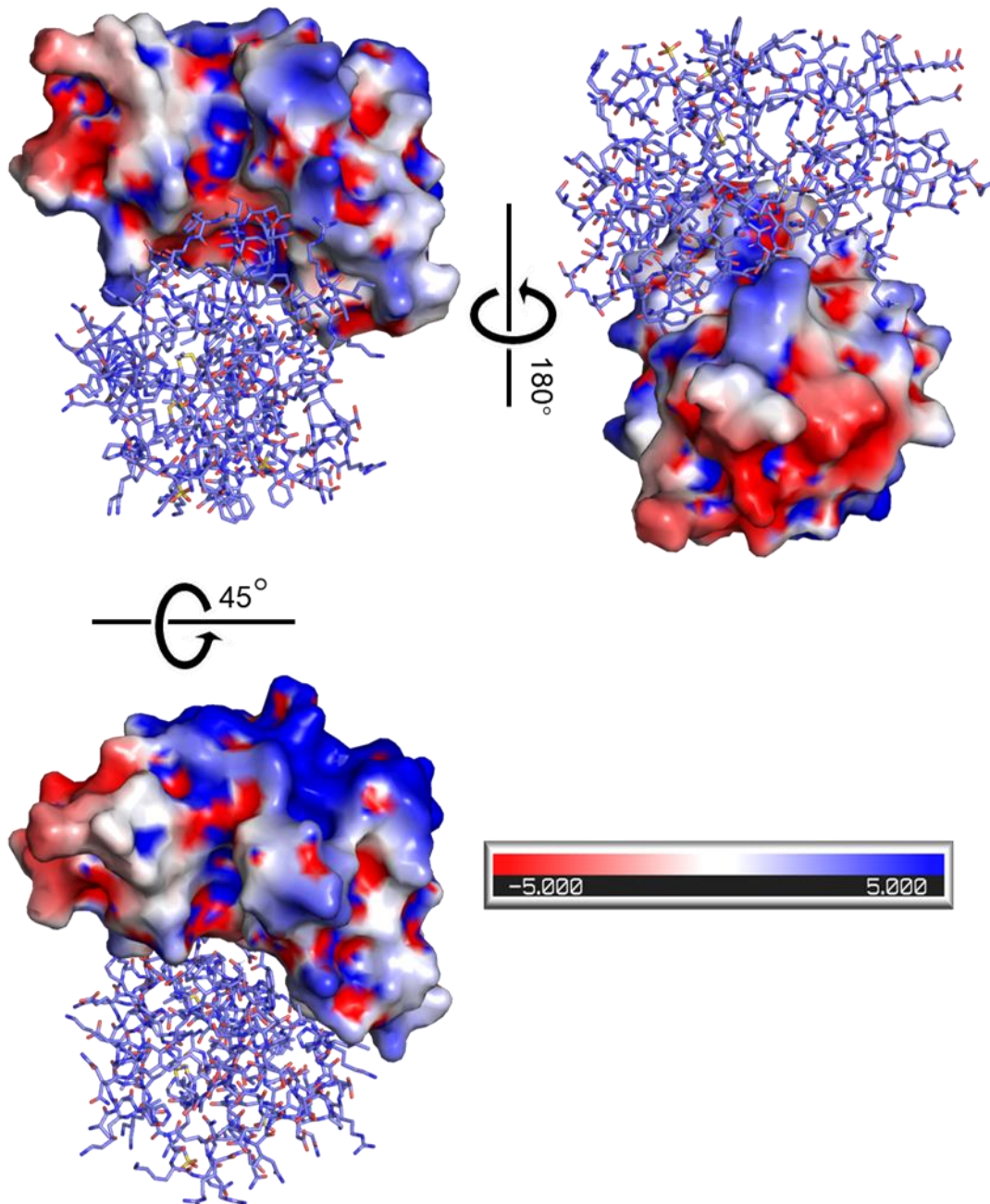


Figure 5.17. WT GAPR-1 dimerization occludes the equatorial groove. The electrostatic potential surface of one subunit of the homodimer is shown, while the partner subunit is displayed in stick representation with atoms colored by atom type: oxygen, red; nitrogen, blue; carbon, violet. The electrostatic potential surface of the same subunit of the homodimer is shown in the top left and bottom panels, while in the right panel the subunit is shown in stick representation, with the partner subunit shown as an electrostatic potential surface. Rotations representing the different views in each panel are indicated.

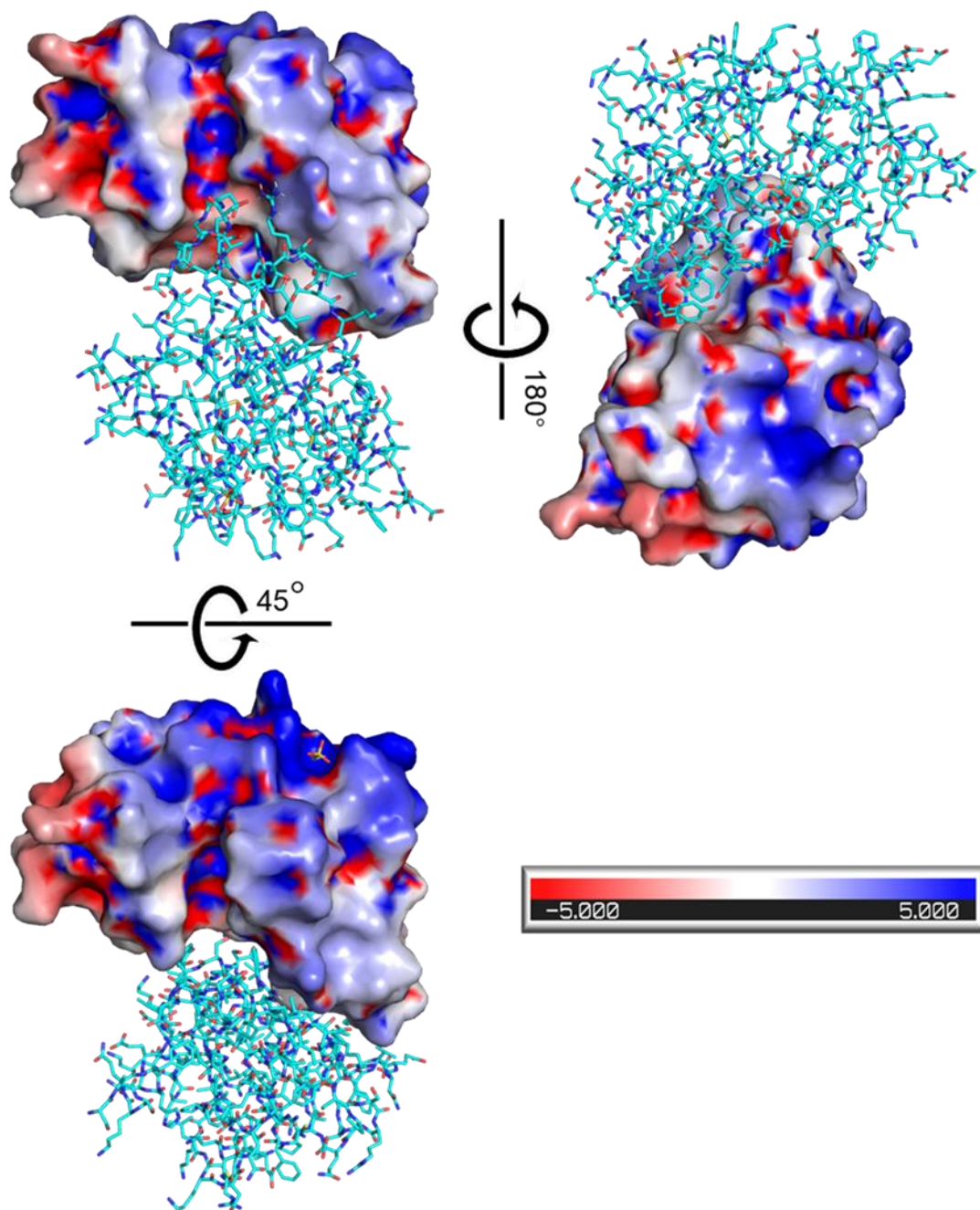


Figure 5.18. WTinIP6 GAPR-1 dimerization occludes the equatorial groove. The electrostatic potential surface of one subunit of the homodimer is shown, while the partner subunit is displayed in stick representation with atoms colored by atom type: oxygen, red; nitrogen, blue; carbon, cyan. The electrostatic potential surface of the same subunit of the homodimer is shown in the top left and bottom panels, while in the right panel the subunit is shown in stick representation, with the partner subunit shown as an electrostatic potential surface. Rotations representing the different views in each panel are indicated.

5.3.8. The pentad mutation shifts the GAPR-1 monomer-dimer equilibrium toward dimerization

The oligomeric state of WT GAPR-1 has not been unambiguously established; therefore, we first used analytical SEC to compare the size of WT and pentad mutant GAPR-1. In our hands, WT GAPR-1 elutes as a monomer for injected sample concentrations ranging from 0.25 – 2 mM (Figure 5.19A), with an estimated molecular mass of 17.7 kDa, which agrees well with the theoretical monomer molecular mass of 17.2 kDa calculated from the GAPR-1 sequence. Consistent with this, the R_s (or R_h , hydrodynamic radius. For protein, the determined R_s reflects the apparent size adopted by the tumbling protein molecule) of WT GAPR-1 calculated from analytical SEC (17 Å) is slightly smaller than the theoretical R_s of 19 Å estimated from the WT GAPR-1 crystal monomer, and much smaller than the R_s of 24 Å estimated from the WT GAPR-1 crystal dimer.

In contrast, the elution profiles of pentad mutant GAPR-1 are dependent on the concentration of sample injected onto the column (Figure 5.19B). When higher concentrations of 1 mM or 2 mM pentad mutant GAPR-1 were injected, the elution peaks were fairly symmetric, but left-shifted relative to WT GAPR-1 (Figure 5.19C). The molecular mass estimated from these profiles is approximately 26 kDa, significantly larger than the 17.2 kDa expected for a monomer, albeit smaller than the molecular mass of 34.4 kDa expected for a dimer (Figure 5.19B). However, when lower concentrations of 0.5 mM or 0.25 mM pentad mutant GAPR-1 were injected, the elution peaks were right-shifted, and were also slightly less symmetric than those at the higher concentrations, with the trailing edge of the 0.25 mM pentad mutant GAPR-1 elution peak overlapping the trailing edge of the peak from elution of WT GAPR-1 (Figure 5.19C), indicating that the pentad mutant dimer dissociates as the concentration decreases and

the elution profile includes both dimeric and monomeric species. The R_s of 21 Å for pentad mutant GAPR-1 estimated from analytical SEC approximates the average of the theoretical R_s of the pentad mutant GAPR-1 crystal dimer (24 Å) and monomer (19 Å).

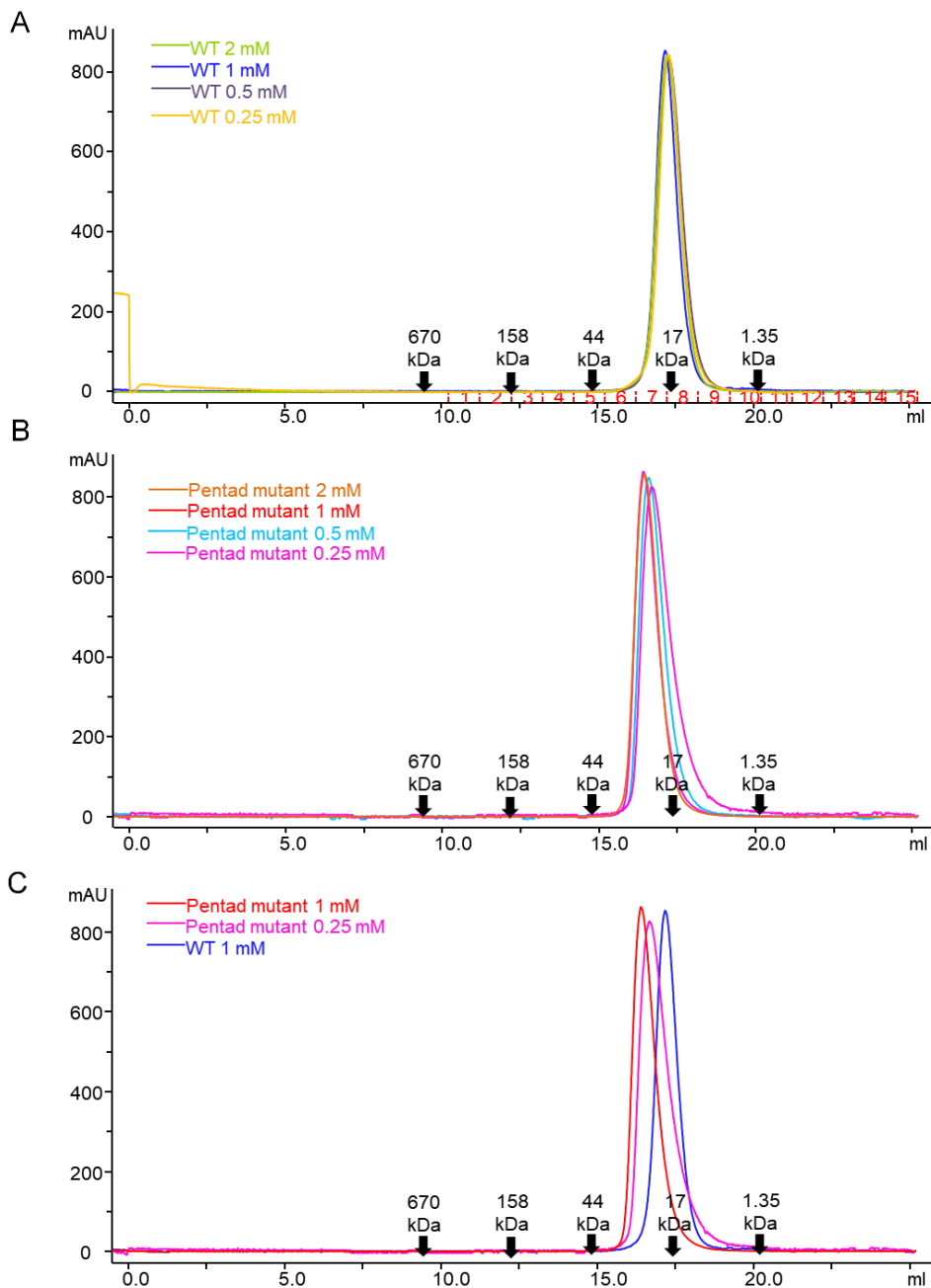


Figure 5.19. Analytical SEC profile of GAPR-1. Different concentration of samples were injected as indicated for (A) WT. (B) Pentad mutant. (C) Superimposed WT and pentad mutant GAPR-1 SEC elution profiles.

ITC was used to quantify self-dissociation constants of WT and pentad mutant GAPR-1. We find that there is no detectable dimer dissociation of WT GAPR-1 (Figure 5.20A). While hypothetically this may be the results of factors such as extremely tight binding or heats of dissociation that are beyond the detection range of this method, the most likely explanation, which is consistent with the SEC analysis reported above, is that WT GAPR-1 does not dimerize at these concentrations. In contrast, the pentad mutant GAPR-1 homodimerizes with an apparent K_d of $29 \pm 7 \mu\text{M}$ (Figure 5.20B). Further, dimerization of the pentad mutant GAPR-1 is favored by both, entropy ($\Delta S = 20 \pm 33 \text{ J/K mol}$) and enthalpy ($\Delta H = -19 \pm 9 \text{ kJ/mol}$). Notably, injection of 1 mM pentad mutant GAPR-1 onto a SEC column results in elution concentrations varying between 2-41 μM (Table 5.3). The leading edge of the SEC elution peak have concentrations above (Table 5.3) the dimer dissociation constant quantified by ITC. However, the concentration of fractions that correspond to the trailing part of the peak range between 2-23 μM , which is lower than the K_d and may result in dimer dissociation. Therefore, the ITC results verify improved homodimerization of pentad mutant GAPR-1 relative to WT GAPR-1, which agrees with the increased shape and electrostatic complementarity of the dimer interface of the pentad mutant relative to WT, as well as the analytical SEC results indicating that WT GAPR-1 is a monomer in solution while the pentad mutant favors forming a dimer.

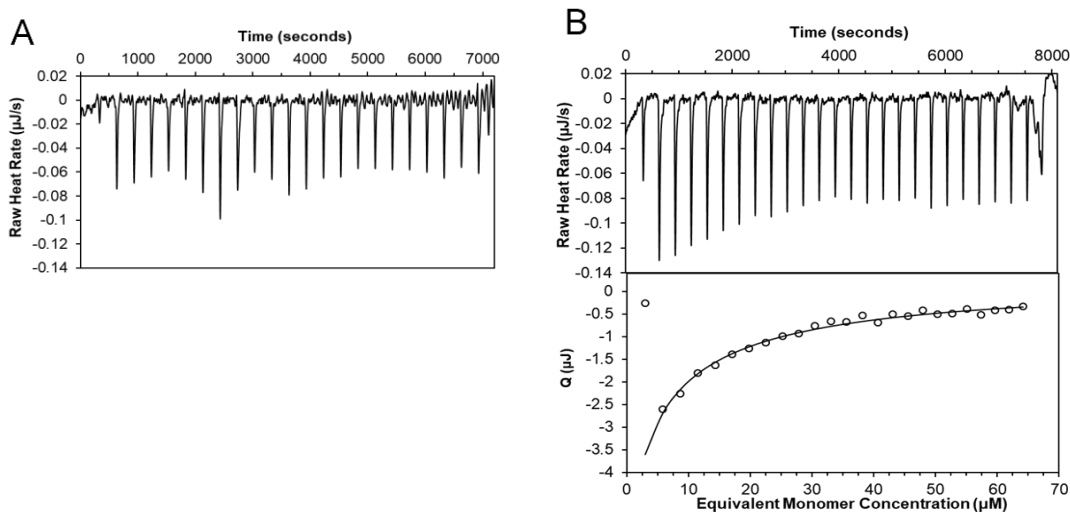


Figure 5.20. ITC quantification of GAPR-1 self-dissociation. (A) WT. (B) Pentad mutant. Upper panel: raw data; lower panel: integrated heat and theoretical fit by independent interaction model from TA Analysis.

Table 5.3. Concentrations of eluate fractions from SEC.

Fraction #	Fraction concentration (μM)	
	WT GAPR-1	Pentad Mutant GAPR-1
6	1	2
7	2	41
8	42	31
9	28	23
10	9	5
11	2	2

Note: 1 mL fractions were collected in each case.

Thus, the reduction in size, change in shape, and increased negativity positivity of the electrostatic surface of the equatorial binding groove, combined with altered dimerization resulting in further occlusion of the equatorial groove in the pentad mutant, increased shape and electrostatic complementarity of the interface, and improved stability of the pentad mutant dimer relative to that of the WT GAPR-1, likely abrogates binding to BECN1. Lastly, in order to confirm the oligomeric state of WT and pentad mutant GAPR-1, we analyzed homogeneous samples of each protein by SEC-SAXS.

5.3.9. SEC-SAXS confirms that WT GAPR-1 is a monomer in solution

$I(0)$ varies across the SEC-SAX peak of WT GAPR-1 (Figure 5.21), consistent with the variation in elution concentration (Table 5.3). The R_g determined from intensity-normalized, buffer-subtracted data is constant across the scattering peak of WT GAPR-1 (Figure 5.22A), indicating that the R_g is not dependent on concentration of WT GAPR-1 in the concentration range tested. SVD analysis was used to determine the minimum number of species required to represent the whole scattering peak. SVD of a matrix containing buffer and WT GAPR-1 scattering data normalized by the incident beam intensity indicated that the sample contained only one dominant species besides the buffer, based on the magnitude of the singular values, autocorrelations of the columns of U and V (Figure 5.22B), and the plots of columns of U (Figure 5.22C).

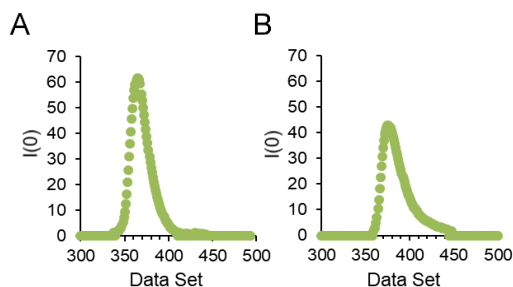


Figure 5.21. I_0 distribution across the GAPR-1 scattering peak. (A) WT. (B) Pentad mutant.

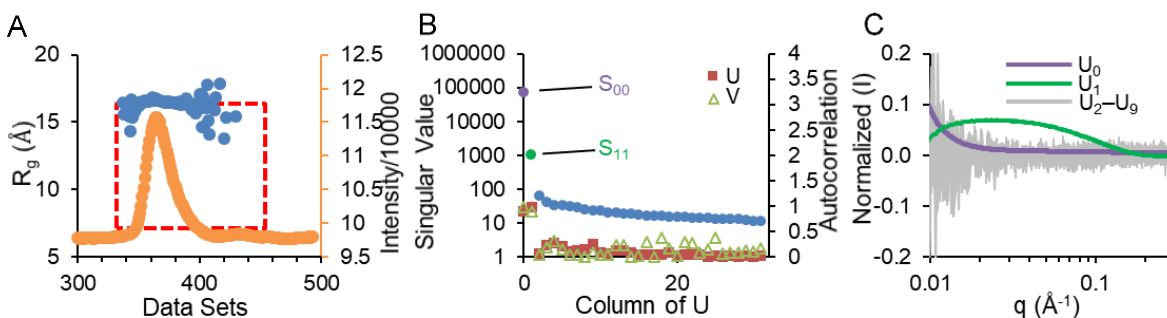


Figure 5.22. WT GAPR-1 SEC-SAXS data showing R_g distribution across the scattering peak and SVD analysis. (A) Raw scattering data (orange) and R_g distribution (blue). (B) Singular values (primary y axis, shown in dots) and autocorrelations of the columns of U (secondary y axis, shown in red squares) and V (secondary y axis, shown in green triangles) of the data from (A). (C) Columns of the orthonormal U matrix multiplied by the corresponding rank-ordered singular values in (B).

Ten data sets with similar R_g were selected, scaled, and averaged for further data analysis. The linear Guinier plots at $qR_g < 1.3$ indicate that the sample does not aggregate (Figure 5.23A). The R_g estimated from the Guinier plot is 16 Å and agrees well with the R_g of 15 Å estimated from the $P(r)$ curve (Figure 5.23B). The R_g of 15 Å calculated from the SAXS data, is consistent with the R_g of 15 Å calculated from the WT GAPR-1 crystal structure monomer, but is substantially smaller than the R_g of 20 Å calculated from the WT GAPR-1 crystal structure dimer. The $P(r)$ curve indicates that WT GAPR-1 is globular, with a maximum molecular dimension (D_{max}) of 58 Å (Figure 5.23B). The dimensionless Kratky plot suggests that WT GAPR-1 has limited disorder (Figure 5.23C). The normalized spatial discrepancy of the 10 generated *ab initio* molecular models is 0.46 ± 0.02 . The envelope confirms the globular shape of WT GAPR-1. Further, the molecular mass estimated from the volume of correlation, V_c (Rambo & Tainer, 2013), is 14.6 kDa, which is a little smaller than the theoretical monomeric molecular mass of 17.2 kDa.

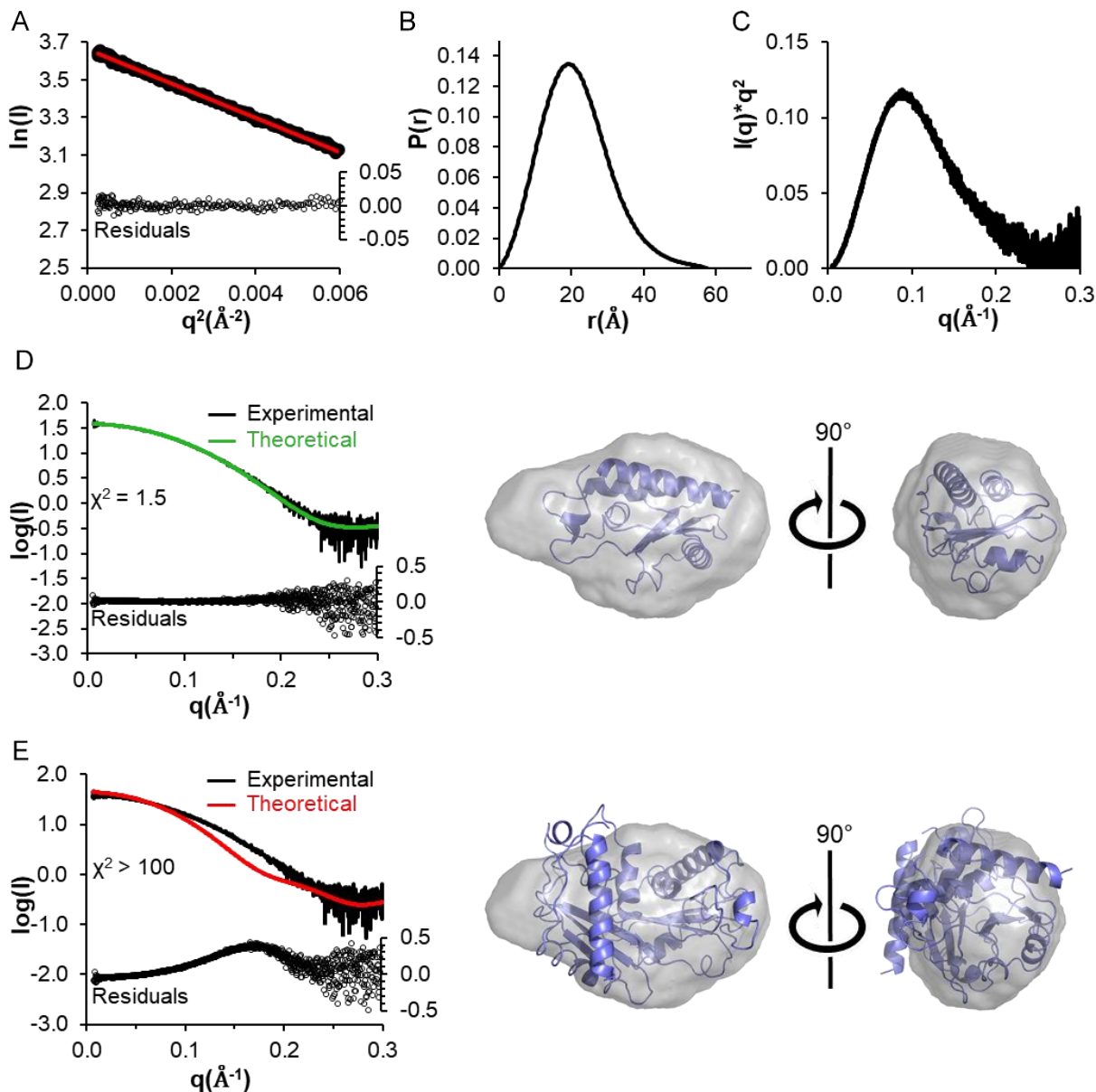


Figure 5.23. SAXS analysis of WT GAPR-1. (A) Guinier plot. (B) $P(r)$ distribution. (C) Krakty plot. (D) Fit of the WT crystal structure monomer to SAXS data. Left panel: The theoretical scattering curve calculated from WT crystal structure monomer (green) fit to experimental scattering data (black). Right panel: WT monomer (violet ribbon) docked into the SAXS molecular envelope (grey surface) shown in two orthogonal orientations. (E) Fit of the WT dimer crystal structure to SAXS data. Left panel: The theoretical scattering curve calculated from the WT dimer crystal structure (red) fit to the experimental scattering data (black). Right panel: WT dimer (violet ribbon) docked into the SAXS envelope (grey surface) shown in two orthogonal orientations.

Theoretical scattering curves, calculated from either the WT GAPR-1 monomer or dimer, were compared to the experimental scattering data (Figure 5.23D,E). The theoretical scattering

curve calculated from the monomer agreed well with the experimental scattering curve as indicated by a χ^2 of 1.5 (Figure 5.23D, left panel), while the theoretical curve calculated from the dimer fit very poorly, indicated by a χ^2 larger than 100 (Figure 5.23E, left panel). The deviation of χ^2 from a perfect value of 1.0 may be because the WT GAPR-1 crystal structure lacks coordinates for a linker (G-P-L-G-S) preceding GAPR-1, as well as for residues 1-3 and 153-154. This good fit indicated by the χ^2 is consistent with our visual observation that the SAXS envelope fits the monomeric WT GAPR-1 crystal structure well (Figure 5.23D, right panel), but is too small to accommodate the WT GAPR-1 dimer (Figure 5.23E, right panel). Therefore, our SEC-SAXS and ITC data consistently confirm that WT GAPR-1 is a monomer in solution at the concentrations tested.

5.3.10. The pentad mutant GAPR-1 transitions between monomer and dimer states in solution

Similar to WT GAPR-1, $I(0)$ also varies across the SEC-SAX peak of pentad mutant GAPR-1 (Figure 5.21B), consistent with the variation in elution concentration (Table 5.3). However, in contrast to WT GAPR-1, the R_g distribution determined from the intensity-normalized, buffer-subtracted SEC-SAXS data of pentad mutant GAPR-1, is inconsistent across the scattering peak (Figure 5.24). The R_g calculated from SAXS datasets at the leading part of the peak is ~ 20 Å (herein called ~ 20 Å R_g peak part), while the R_g calculated from SAXS datasets at the trailing part of the peak is ~ 16 Å (herein called ~ 16 Å R_g peak part), with intervening SAXS data sets having intermediate R_g values between 16-20 Å. The ~ 20 Å peak part corresponds fraction 7-8 of SEC (Table 5.3) and the ~ 16 Å peak part corresponds to fractions 9-11 of SEC (Table 5.3).

The minimum R_g estimated from the pentad mutant GAPR-1 SAXS data is comparable to that calculated from a monomer of the pentad mutant crystal structure and also similar to that observed for WT GAPR-1. The maximum R_g estimated from the pentad mutant GAPR-1 SAXS data is similar to the R_g of 20 Å calculated from the pentad mutant GAPR-1 dimer in the crystal structure. Together, this data indicates that at the concentrations used for these SEC-SAXS experiments, the pentad mutant GAPR-1 may transition between dimeric and monomeric states.

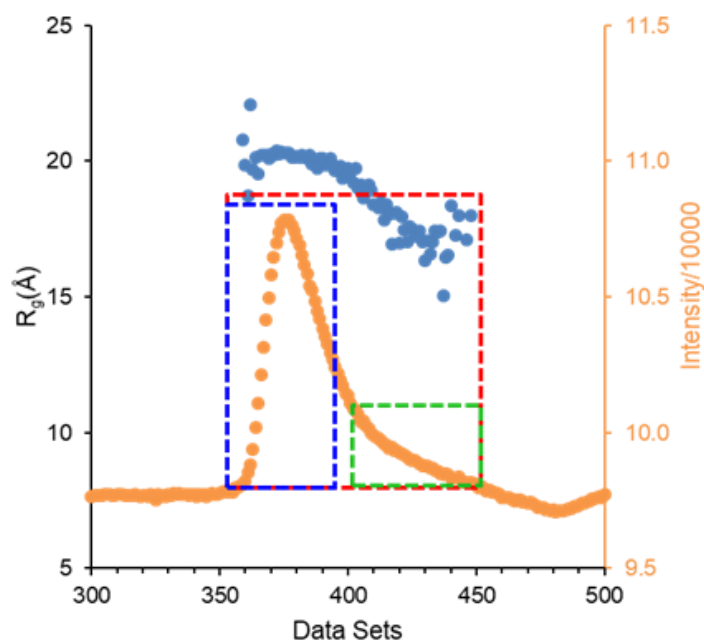


Figure 5.24. R_g distribution across the SEC-SAXS elution peak. Raw scattering data (orange) and R_g distribution (blue) with data selected for SVD analysis of the whole peak (red box), leading part of the peak with $R_g \sim 20$ Å (blue box), and trailing part of the peak with $R_g \sim 16$ Å (green box).

SVD analysis was also performed on SAXS data from the pentad mutant GAPR-1 to determine the minimum number of species required to represent either the whole scattering peak (Figure 5.24 red box and Figure 5.25A,B), the ~ 20 Å R_g peak part (Figure 5.24 blue box and Figure 5.25C,D), or the ~ 16 Å R_g peak part (Figure 5.25 green box and Figure 5.25E,F). Contrary to our expectations based on the observed decrease in R_g across the scattering peak, SVD analysis of the whole scattering peak (Figure 5.25A) indicates that, in addition to the

buffer, S00, the sample contains only one significant component, S11; as the next non-buffer species, S22, cannot be considered significant based on the autocorrelations of the columns of U and V (Figure 5.25A) and the plot of columns of U (Figure 5.25B). Not surprisingly, selection of SAXS datasets only from the $\sim 20 \text{ \AA} R_g$ peak part (Figure 5.25 blue box and Figure 5.25C,D), also indicated the presence of only one species besides the buffer. Likewise, selection of SAXS datasets from the $\sim 16 \text{ \AA} R_g$ peak part (Figure 5.24 green box and Figure 5.25E,F), also identified only one non-buffer component, S11 (Figure 5.24, 5.25H,I). Notably however, this S11 species has a singular value of ~ 100 (Figure 5.25C), which is substantially less than the magnitude of the singular value of the S11 species identified in the analysis of the $\sim 20 \text{ \AA} R_g$ peak part (Figure 5.25B), suggesting that the concentration of the non-buffer component is much lower in $\sim 16 \text{ \AA} R_g$ peak part, relative to that in the $\sim 20 \text{ \AA} R_g$ peak part. Further, the magnitude of the singular value of the S11 species in the $\sim 16 \text{ \AA} R_g$ peak part is comparable to that of the insignificant S22 species in the SVD analysis of the whole peak, raising the possibility that a third species may be present at the trailing part, but at concentrations that are too low for identification as a distinct significant species in the analysis of the whole peak. Another possibility is that the S11 species in the $\sim 16 \text{ \AA} R_g$ peak part simply corresponds to a low concentration of the S11 species in the $\sim 20 \text{ \AA} R_g$ peak part; however, this possibility does not explain the decrease in R_g observed at the trailing part. To further characterize size and shape of the significant species in the two parts of the scattering peak, ten buffer-subtracted data sets were selected from either the $\sim 20 \text{ \AA} R_g$ peak part or from the $\sim 16 \text{ \AA} R_g$ peak part, which were separately scaled and averaged for subsequent data analysis.

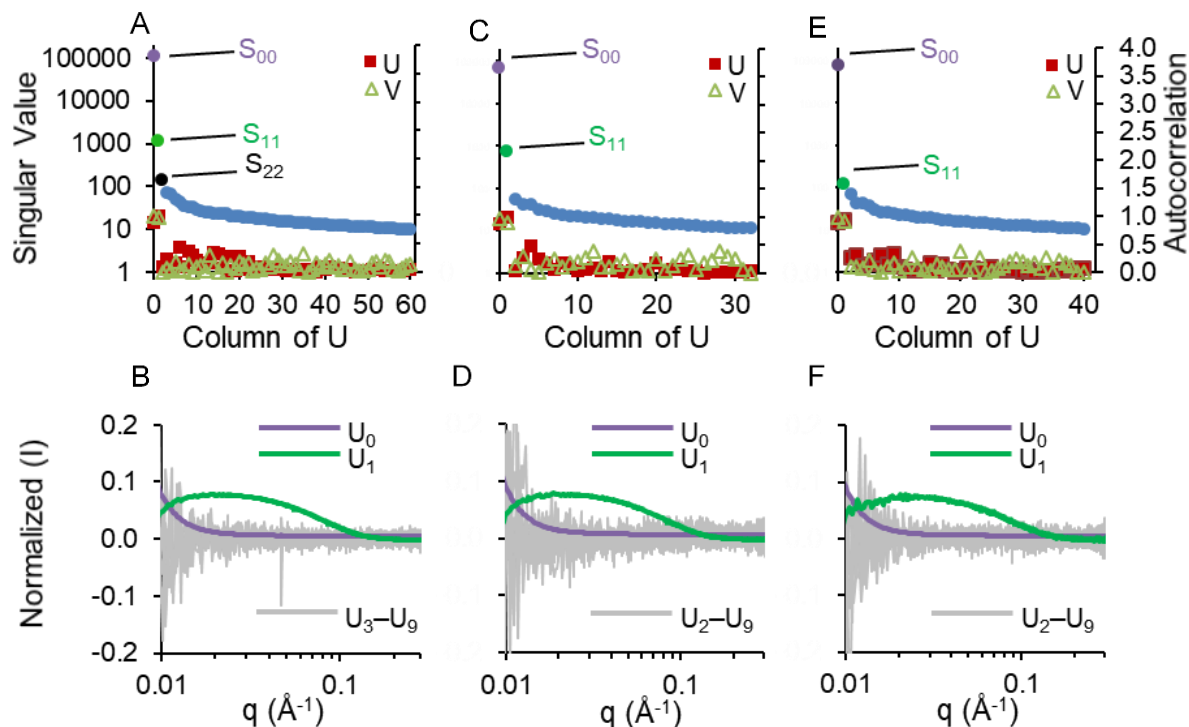


Figure 5.25. SVD analysis of SEC-SAXS from pentad mutant GAPR-1. (A) Singular values (primary y axis, shown in dots) and autocorrelations of the columns of U (secondary y axis, shown in red square) and V (secondary y axis, shown in red square) of the data encompassing the whole peak indicated by red box in Figure 5.25. (B) Columns of the orthonormal U matrix multiplied by the corresponding rank-ordered singular values in (A). (C) Singular values and autocorrelations of the columns of U and V of the data encompassing the leading edge of the peak indicated by blue box in Figure 5.25. (D) Columns of the orthonormal U matrix multiplied by the corresponding rank-ordered singular values in (C). (E) Singular values and autocorrelations of the columns of U and V of the data encompassing the trailing edge of the peak indicated by green box in Figure 10. (F) Columns of the orthonormal U matrix multiplied by the corresponding rank-ordered singular values in (E).

For the averaged pentad mutant GAPR-1 SAXS data derived from the $\sim 20 \text{ \AA}$ R_g peak part, the Guinier plot is linear at $qR_g < 1.3$, indicating this eluted sample does not aggregate (Figure 5.26A). The R_g estimated from Guinier plot analysis and $P(r)$ analysis is 20 \AA (Figure 5.26A,B), substantially larger than the R_g of 16 \AA determined for WT GAPR-1 (16 \AA). The 20 \AA R_g estimated from the pentad mutant GAPR-1 SAXS data agrees with the R_g of 20 \AA calculated from the pentad mutant GAPR-1 crystal structure dimer, but is substantially larger than the R_g of 15 \AA calculated from the pentad mutant GAPR-1 crystal structure monomer. The $P(r)$ plot

indicates that the pentad mutant GAPR-1 in the ~ 20 Å peak part is globular, with a D_{\max} of 66 Å which is larger than the 58 Å D_{\max} of WT GAPR-1 (Figure 5.26B). This 66 Å D_{\max} estimated from the pentad mutant ~ 20 Å R_g peak part is larger than the D_{\max} of 56 Å calculated from the pentad mutant crystal structure monomer, but smaller than D_{\max} of 72 Å calculated from the pentad mutant GAPR-1 crystal structure dimer. The Kratky plot indicates that pentad mutant GAPR-1 is also well folded (Figure 5.26C). The molecular mass of pentad mutant GAPR-1 estimated from the V_c is 24.6 kDa, which is comparable to the mass of 26 kDa estimated from analytical SEC, but smaller than the theoretical molecular mass of 34.4 kDa calculated for a dimer and larger than the theoretical molecular mass of 17.2 kDa for a monomer. The normalized spatial discrepancy of the 10 generated ab initio molecular models calculated from this data is 0.58 ± 0.02 . Lastly, the theoretical scattering curve calculated from the pentad mutant GAPR-1 monomer crystal structure does not fit the experimental scattering curve at all, as indicated by the χ^2 of 96 (Figure 5.26D, left panel), but the theoretical scattering curve calculated from the pentad mutant GAPR-1 dimer agrees well with the experimental scattering curve as indicated by a χ^2 of 2.2 (Figure 5.26E, left panel). Similar to the WT GAPR-1 crystal structure, the pentad mutant GAPR-1 crystal structure used to calculate the theoretical scattering curve lacks coordinates due to missing electron density for linker residues G-P-L-G-S and GAPR-1 residues 1-3, but not GAPR-1 residues 153-154. Therefore, it is unlikely that these missing residues account for the relatively elevated χ^2 of 2.2, rather this is probably indicative of an imperfect fit. Visual observation indicates that the SAXS envelope is much larger than a pentad mutant monomer (Figure 5.26D, right panel), but fits the pentad mutant dimer structure well (Figure 5.26E, right panel). Measurement of SEC eluate concentration indicates a range of 31-41 μ M (Table 5.3) across the ~ 20 Å R_g peak part; which is slightly above the apparent dimer

dissociation K_d ($29 \pm 7 \mu\text{M}$) (Figure 5.20). Thus, our data indicate that the pentad mutant GAPR-1 eluting under the $\sim 20 \text{ \AA}$ R_g peak part is in a dimeric state.

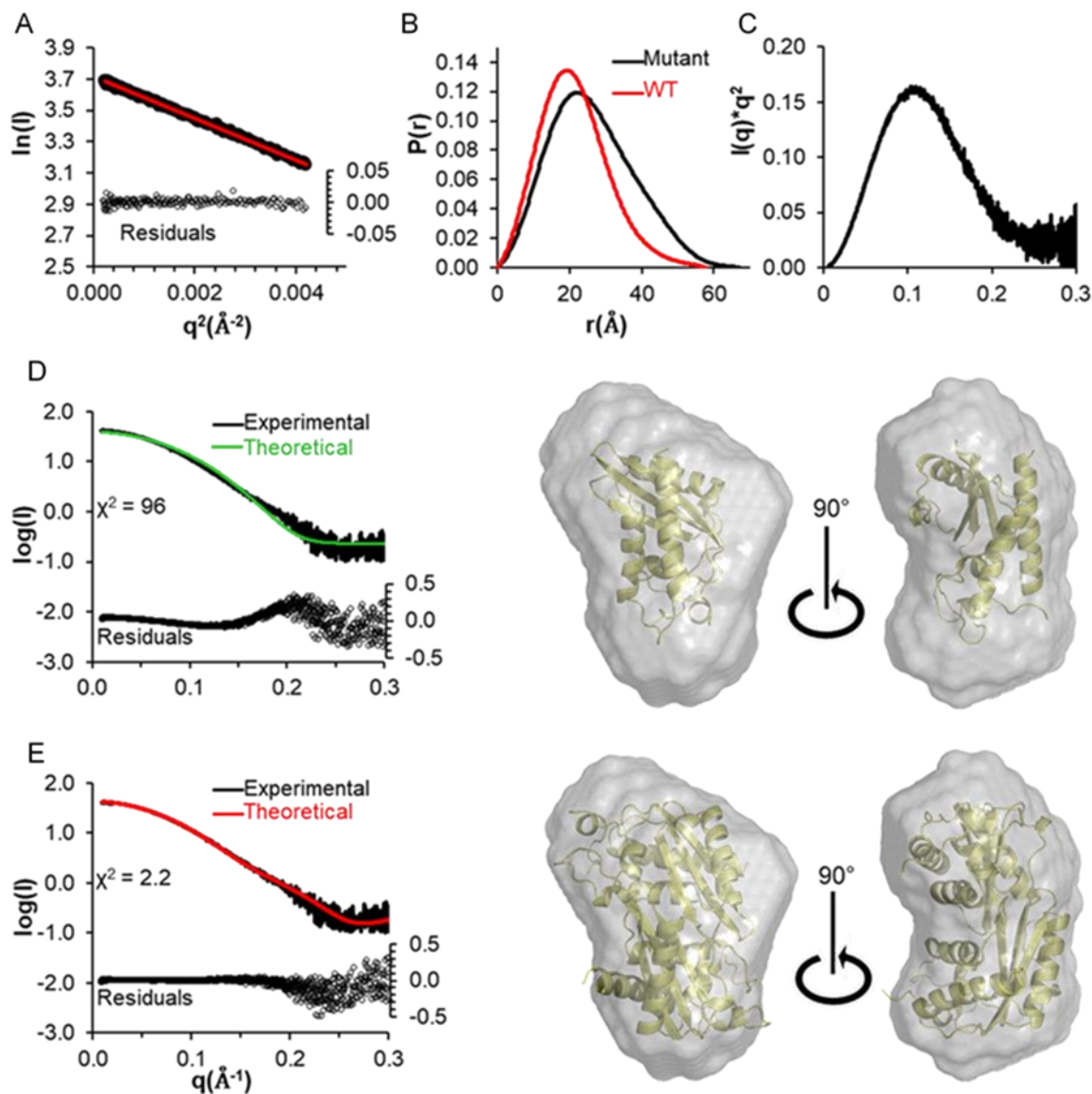


Figure 5.26. Analysis of the $\sim 20 \text{ \AA}$ R_g peak part of pentad mutant GAPR-1 SAXS. (A) Guinier plot. (B) $P(r)$ distribution. (C) Krakty plot. (D) Fit of the pentad mutant crystal structure monomer to the SAXS data. Left panel: The theoretical scattering curve calculated from the pentad mutant monomer (green) fitted to experimental scattering data (black). Right panel: The pentad mutant crystal structure monomer (yellow ribbon) docked into the SAXS molecular envelope (gray surface) shown in two orthogonal orientations. (E) Fit of the pentad mutant crystal structure dimer to the SAXS data. Left panel: The theoretical scattering curve calculated from the pentad mutant monomer (red) fitted to the experimental scattering data (black). Right panel: The pentad mutant crystal structure dimer (yellow ribbon) fitted to the SAXS molecular envelope (gray surface) shown in two orthogonal orientations.

For the averaged pentad mutant GAPR-1 SAXS data derived from the ~ 16 Å R_g peak part, the Guinier plot is linear at $qR_g < 1.3$, indicating this eluted sample does not aggregate (Figure 5.27A). The 17 Å R_g estimated from Guinier and $P(r)$ analysis (Figure 5.27A,B), is similar to the 16 Å R_g estimated for the WT GAPR-1 SAXS data. The R_g of 17 Å estimated from the pentad mutant GAPR-1 SAXS data, is slightly larger than the R_g of 15 Å calculated from the pentad mutant GAPR-1 crystal structure monomer, but is substantially smaller than the R_g of 20 Å calculated from the pentad mutant GAPR-1 crystal structure dimer. The $P(r)$ plot indicated that particles in ~ 16 Å R_g peak part are globular, with a D_{max} of 56 Å (Figure 5.27B), which is similar to the D_{max} of WT GAPR-1. The Kratky plot indicates that these particles are also well folded (Figure 5.27C). The molecular mass estimated from the V_c is 21 kDa, which is larger than the theoretical molecular mass of monomeric pentad mutant GAPR-1 (17.2 kDa), but much smaller than that of dimeric pentad mutant GAPR-1 (34.4 kDa). The normalized spatial discrepancy of the 10 generated ab initio molecular models is 0.50 ± 0.05 . Lastly, the theoretical scattering curve calculated from the pentad mutant GAPR-1 monomer fit the experimental scattering curve well with a χ^2 of 1.9 (Figure 5.27D, left panel), while the theoretical scattering curve calculated from the pentad mutant GAPR-1 dimer did not fit the experimental scattering curve as well as indicated by a χ^2 of 3.0 (Figure 5.28E, left panel). Visual observation indicates that a pentad mutant monomer fits the SAXS envelope calculated from the ~ 16 Å R_g peak part better (Figure 5.27D, right panel) than the pentad mutant dimer structure (Figure 5.27E, right panel). Thus, all of our data suggests that the pentad mutant GAPR-1 eluting under the ~ 16 Å R_g peak part is likely monomeric.

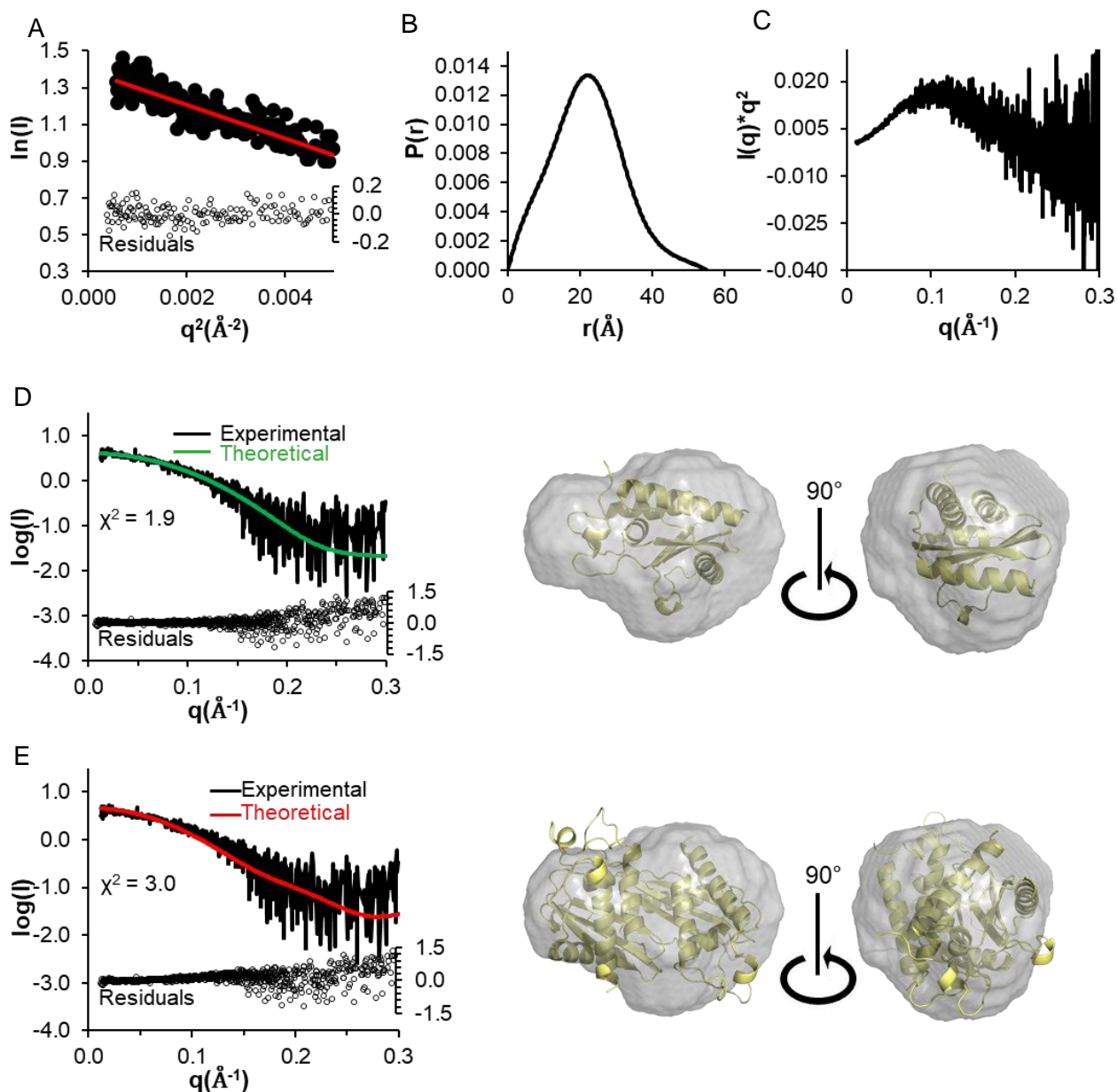


Figure 5.27. Analysis of the $\sim 16 \text{ \AA}$ R_g peak part of pentad mutant GAPR-1 SAXS. (A) Guinier plot. (B) $P(r)$ distribution. (C) Kratky plot. (D) Fit of the pentad mutant crystal structure monomer to the SAXS data. Left panel: The scattering curve calculated from the pentad mutant monomer (green) fit to experimental scattering data (black). Right panel: The pentad mutant crystal structure monomer (yellow ribbon) docked to the SAXS molecular envelope (gray surface) shown in two orthogonal orientations. (E) Fit of the pentad mutant crystal structure dimer to the SAXS data. Left panel: The theoretical scattering curve calculated from the pentad mutant monomer (red) fit to the experimental scattering data (black). Right panel: The pentad mutant crystal structure dimer (yellow ribbon) docked to the SAXS molecular envelope (gray surface) shown in two orthogonal orientations.

Together, our SEC-SAXS analysis of the pentad mutant GAPR-1 indicates that at the concentrations tested in this study, this mutant exists primarily as a dimer, but equilibrates in a

concentration-dependent manner between dimer and monomer oligomeric states that can be detected in SEC-SAXS.

5.4. Conclusions and Discussion

X-ray crystal structures of GAPR-1 and other CAP domain homologs have elucidated the protein fold characteristic of this family (Fernandez *et al.*, 1997, Henriksen *et al.*, 2001, Serrano *et al.*, 2004, Asojo *et al.*, 2005, Suzuki *et al.*, 2008, Asojo, 2011, Asojo *et al.*, 2011, Osman *et al.*, 2012, Mason *et al.*, 2014, Darwiche *et al.*, 2016). These studies also identified an equatorial surface groove present in all homologs of known structure. This groove has been shown to bind metals (Henriksen *et al.*, 2001, Suzuki *et al.*, 2008, Wang *et al.*, 2010, Asojo *et al.*, 2011, Mason *et al.*, 2014, Darwiche *et al.*, 2016), and based on its width, depth, and length, this groove has also been proposed to be a binding site for peptides (Milne *et al.*, 2003, Osman *et al.*, 2012, Mason *et al.*, 2014). However, to date, no direct evidence of peptide binding to this groove has been presented. Our bioinformatics analysis and molecular docking results suggest that this groove is suitable for binding BECN1, and pentad mutation of conserved GAPR-1 residues H54A/E86A/G102K/H103A/N138G lining this groove abrogates binding to BECN1. These mutations do not impact GAPR-1 tertiary structure, rather they alter the size, shape and electrostatic potential of the equatorial groove.

The oligomeric state of WT GAPR-1 has not been unambiguously established because different oligomerization states have been proposed in different studies. A previous study has suggested that GAPR-1 exists as a monomer in solution in the absence of lipid (van Galen *et al.*, 2012), while another suggested that it transitions between monomeric and dimeric states in solution (Serrano *et al.*, 2004). Three different crystal structures of GAPR-1, including that reported in this manuscript, indicate that GAPR-1 dimerizes in selective conditions. Further,

yeast two-hybrid studies suggest that GAPR-1 may exist as a dimer in cells (Serrano *et al.*, 2004). Interestingly, certain CAP proteins have serine protease activity, yet a canonical active site triad is formed only upon homodimerization (Milne *et al.*, 2003), suggesting a functional role for dimerization of certain CAP domains. The results presented here unambiguously indicate that WT GAPR-1 does not homodimerize in the absence of lipids / other proteins, and is a monomer in solution even at 2 mM concentrations. Thus, WT GAPR-1 likely forms a very weak and transient dimer, which is stabilized at high concentrations such as those used for crystallization, and/or in the presence of specific small molecules such as crystallization reagents, selected lipids, or IP₆. The increased concentration of GAPR-1 at lipid-rich microdomains of the Golgi complex may provide similar conditions *in vivo*.

Notably, the dimer interface varies in each of the three different GAPR-1 crystal structures determined to date, either due to mutations, as reported in this study, or the presence of lipid or IP₆ (van Galen *et al.*, 2012). Interestingly, no electron density corresponding to IP₆ was seen in the latter structure, thus it is unclear how IP₆ mediates changes in dimerization. Together, these studies indicate that GAPR-1 likely transitions between monomer and different dimer conformations that are dependent on GAPR-1 concentration as well as upon binding of lipids and/or different ligands or protein partners. It is plausible that these different oligomeric states have different mechanisms and impact different biological functions.

Strikingly, the equatorial surface groove is partially occluded by the partner subunit in all three dimeric states crystallized, suggesting that binding partners such as BECN1 would not bind to the dimeric state of GAPR-1. Indeed, the interaction between GAPR-1 and BECN1 may require co-localization and arrangement of GAPR-1 and BECN1 in suitable orientations, which may be facilitated by membrane association *in vivo*. This may be why the BECN1:GAPR-1

interaction was not detected *in vitro* by ITC, although we also cannot rule out technical explanations such as the heat released during binding being too small to be detected by ITC. Further, various cellular factors such as the presence/binding of specific lipids, protein partners, and/or post-translational modifications may further regulate this interaction via changes in conformation and oligomerization of each partner. Binding of GAPR-1 to BECN1 BARAD residues 267-284 would sterically obstruct binding of autophagy partners such as UVRAG or ATG14, thereby adversely impacting assembly of the autophagosome nucleation complex and reducing cellular autophagy levels.

Our model for binding of GAPR-1 to BECN1 BARAD residues 267-284 suggests a mechanism for the disruption of binding caused by the F270S and F274S mutants (Shoji-Kawata *et al.*, 2013). Our model predicts that BECN1 F270 packs against GAPR-1 hydrophobic residue F144; therefore, the F270S mutation would weaken this hydrophobic packing and the presence of the polar S hydroxyl group may destabilize the interaction further. The aromatic ring of BECN1 F274 packs against the C β of GAPR-1 S99 with a distance of 3.4 Å. An *in silico* mutation of F274 to serine increases this distance to 5.0 Å between BECN1 S274 and GAPR-1 S99, abrogating this packing and likely destabilizing the BECN1 - GAPR-1 interaction.

CHAPTER 6. INVESTIGATING THE INTERACTION BETWEEN THE BECN1 BH3D AND VMP1 ATGD

6.1. Introduction

The BECN1 IDR-FHD (residues 1-171) contains several binding motifs, including five anchor regions: the first three lie within the IDR and consist of residues 13-49, 79-103, and 116-127 (Mei *et al.*, 2014, Lee *et al.*, 2016); the fourth comprises residues 137-145 that overlaps both the IDR and FHD; the last comprises residues 162-169 within the FHD.

The BECN1 IDR-FHD appears to be an interaction hub for various interacting partners, perhaps due to the presence of these Anchors. As discussed in Chapter 1, the BECN1 BH3D, comprising residues 105-130 which includes the third IDR Anchor region, is responsible for binding to various BCL2 proteins and undergoes a binding-induced disorder-to-helix transition (Sinha *et al.*, 2008, Pattingre *et al.*, 2005, Maiuri *et al.*, 2007, Oberstein *et al.*, 2007, Ku *et al.*, 2008). Another protein, VMP1, has also been shown to interact with BECN1 IDR-FHD to up-regulate autophagy (Molejon *et al.*, 2013).

VMP1 is a 406-residue protein, comprised of six *trans*-membrane domains and a C-terminal cytoplasmic domain comprised of the residues 386-406 which has been named the autophagy-related domain (ATGD). VMP1 is highly expressed in the pancreas during acute pancreatitis, promotes intracellular vacuolization and cell death (Duseti *et al.*, 2002, Jiang *et al.*, 2004), and is also required for autophagosome development under both nutrient rich and starvation conditions (Vaccaro *et al.*, 2008, Molejon *et al.*, 2013). Pull-down assays show that the BECN1 residues 1-123 (which contains most part of IDR) are sufficient to bind the VMP1 ATGD, and deletion of BECN1 residues 88-150 (partial IDR + partial FHD) completely disrupts the BECN1:VMP1-ATGD interaction (Molejon *et al.*, 2013). Co-IP assays show that the BECN1

BH3D F123 is required for the BECN1:VMP1 interaction, as the BECN1 F123A mutation completely disrupts the BECN1:VMP1 ATGD interaction (Molejon *et al.*, 2013). The VMP1 ATGD:BECN1 interaction displaces BCL2 from BECN1. BECN1 coimmunoprecipitates with Bcl-2 in absence of VMP1, but coimmunoprecipitates with VMP1 when the cells were transfected by BECN1, Bcl-2, and VMP1; however, the BECN1 coimmunoprecipitates with Bcl-2 when the cells were transfected by BECN1, Bcl-2, and VMP1^{ΔATGD}. The displacement of Bcl-2 by VMP1 ATGD may help BECN1 recruit other proteins such as VPS34 and ATG14L to the BECN1-PI3KC3 complex to up-regulate autophagy (Molejon *et al.*, 2013).

However, the atomic details of the BECN1:VMP1 interaction are unknown. In this study, we hypothesize that the BECN1 IDR (or more specifically BH3D) is responsible for the BECN1:VMP1 ATGD interaction, and the BECN1 BH3D undergoes disorder-to-helix transition upon interaction with VMP1 ATGD. Therefore, we tried to quantify the thermodynamics of VMP1 ATGD binding to the BECN1 BH3D and BECN1 IDR (residues 1-135) using ITC. In addition, we used CD spectra to investigate changes in the secondary structure of the BECN1 BH3D and VMP1 ATGD upon interacting with each other.

6.2. Materials and Methods

6.2.1. Preparation of BECN1 residues 1-135, BECN1 BH3D and VMP1 ATGD

BECN1 residues 1-135 were cloned between *BamHI* and *NotI* restriction enzyme sites of pParallel vectors (Sheffield, Garrard *et al.* 1999) containing an MBP tag to enable amylose affinity (Sinha *et al.*, 2008). Dr. Sangita Sinha completed the subcloning of this construct. The protein was expressed and purified as described for the MBP fusion proteins in Chapter 3 and in (Sinha *et al.*, 2008). Peptides corresponding to the human BECN1 BH3D (105DGGTMENLSRRLKVTGDLFDIMSGQT130) (Protein Chemistry Technology Core,

UTSW; RS synthesis; or EZbiolab), VMP1 ATGD (³⁸⁶SMAQSYAKRIQQRLNSEEKTK⁴⁰⁶) (EZBiolab), and GWG-VMP1 ATGD (GWG-³⁸⁶SMAQSYAKRIQQRLNSEEKTK⁴⁰⁶) (EZBiolab, Carmel, IN) were chemically synthesized, and HPLC purified to > 95% purity as confirmed by electrospray mass spectrometry.

6.2.2. CD Spectroscopy

Dr. Yang Mei from our lab performed the CD spectroscopy experiment and data analysis. VMP1 ATGD (386 SMAQSYAKRIQQRLNSEEKTK406) (EZBiolab) and BECN1 BH3D (105DGGTMENLSRRLKVTGDLFDIMSGQT130) (RS synthesis) were mixed in a 1:1 molar ratio with different resulting concentrations of 7.65 μ M, 30 μ M, 100 μ M and 300 μ M. The mixed sample was loaded into Slide-A-Lyzer G2 dialysis cassettes (ThermoFisher) and dialyzed against 2 L CD buffer of 10 mM potassium phosphate pH 7.6, 100 mM ammonium sulfate overnight, prior to CD spectroscopy analysis. Continuous scanning CD spectra were recorded from 195-250 nm at 4 °C in a 300 μ l, 1mm quartz cell on a Jasco J-815 spectrometer equipped with a PFD-425S Peltier thermoelectric temperature control to determine the secondary structure content. The secondary structural content was analyzed using SELCON3 of the CDpro program suite (Sreerama & Woody, 2000).

6.2.3. ITC

Interactions between BECN1 BH3D and VMP1 ATGD were initially investigated by Dr. Yang Mei from our lab. BECN1 BH3D peptide (RS synthesis) and VMP1 ATGD peptide (EZBiolab) were loaded into separate Slide-A-Lyzer G2 dialysis cassettes (ThermoFisher), and simultaneously dialyzed against 2 L buffer comprised of 50 mM HEPES, pH 7.5, 150 mM NaCl, and 2 mM BME. ITC experiments were performed at 25°C with a stir rate of 250 rpm in the Low Volume Nano ITC (TA Instruments). 400 μ l of 40 μ M VMP1 ATGD was added into the ITC

cell, and 50 μl of 400 μM WT BECN1 BH3D peptide was titrated into the cell using 25 injections of 2 μl each with 300-second intervals at 25°C with a stirring rate of 250 rpm. Data were plotted and analyzed using NanoAnalyze software with an independent binding model to calculate binding affinities.

I continued these studies. First, I repeated Dr. Mei's ITC experiment using the same peptides (BH3D peptide from RS Synthesis, and VMP1 ATGD peptide from EZBiolab) as Dr. Mei used. Subsequently, in order to obtain a more accurate measure of the concentration of the VMP1 ATGD used for ITC, the extinction coefficient of the VMP1 ATGD at 280 nm was increased by the addition of three residues, GWG, prior to the N terminus of VMP1 ATG. These peptides were obtained from EZBiolab. The peptides were initially dissolved in dialysis buffer, comprising 25 mM HEPES pH 8.0, 150 mM NaCl, and 2 mM BME, with a final concentration of 5 mM for GWG-VMP1 ATGD and 1.68 mM for BECN1 BH3D. The VMP1 GWG-ATG, BECN1 BH3D, and MBP-BECN1 1-135 were simultaneously dialyzed in separate cassettes against 1 L of dialysis buffer for 24 h to ensure buffer match. ITC was performed at 20 °C with a stir rate of 250 rpm. 350 μl of 100 μM GWG-VMP1 ATGD was placed in the ITC cell, and 50 μl of 1 mM BECN1 BH3D was titrated into the cell at 300-second intervals using 20 injections of 2.5 μl . Likewise, 350 μl of 100 μM MBP-BECN1 1-135 was placed in the ITC cell, and 50 μl of 1 mM GWG-VMP1 ATGD peptide was titrated into the cell at 300-second intervals using 20 injections of 2.5 μl . Data were plotted and analyzed using NanoAnalyze software with an independent binding model to calculate binding affinities.

6.3. Results

6.3.1. ITC for BECN1 BH3D and VMP1 ATGD interaction

We investigated the interaction between the VMP1 ATGD and BECN1 BH3D using ITC. Initially, Dr. Yang Mei from our lab performed the ITC and ITC analysis, which suggested that the VMP1 ATGD (EZBiolab, Carmel, IN) and BECN1 BH3D (RS synthesis, Louisville, KY) interact weakly, with a K_d of 11.4 μM (Figure 6.1A). Subsequently, I repeated these experiments, and measured a higher binding affinity, with $K_d = 1.3 \mu\text{M}$ for binding of VMP1 ATD (EZBiolab, Carmel, IN) and BECN1 BH3D (RS synthesis, Louisville, KY) (Figure 6.1B). However, this dissociation constant may be inaccurate because the titration started to saturate after the first injection, indicating that the concentration of the VMP1 ATGD in calorimeter cell was too low. Subsequently, when the ITC experiment was repeated using newly purchased BECN1 BH3D from another supplier (EZbiolab), no interaction was detected between BECN1 BH3D and VMP1 ATGD (Figure 6.1C).

Meanwhile, in order to enable more accurate quantification of concentration of the VMP1 ATGD used for ITC using absorbance of the peptide solution at A280, we designed a VMP1 ATGD peptide with three extra residues 'GWG' at the N terminus to increase the extinction coefficient, and measured the interaction between BECN1 BH3D and GWG-VMP1 ATGD. Since Co-IP experiments show that BECN1 residues 1-123 interact with the VMP1 ATGD (Molejon, Ropolo et al. 2013), we also measured the interaction between MBP-BECN1 1-135 and the GWG-VMP1 ATGD by ITC. Contrary to our expectation, no interaction was detected either between the BH3D and the GWG-VMP1 ATGD or between the MBP- BECN1 1-135 and GWG-VMP1 ATGD. These inconclusive binding results might result from the inconsistent peptide quality.

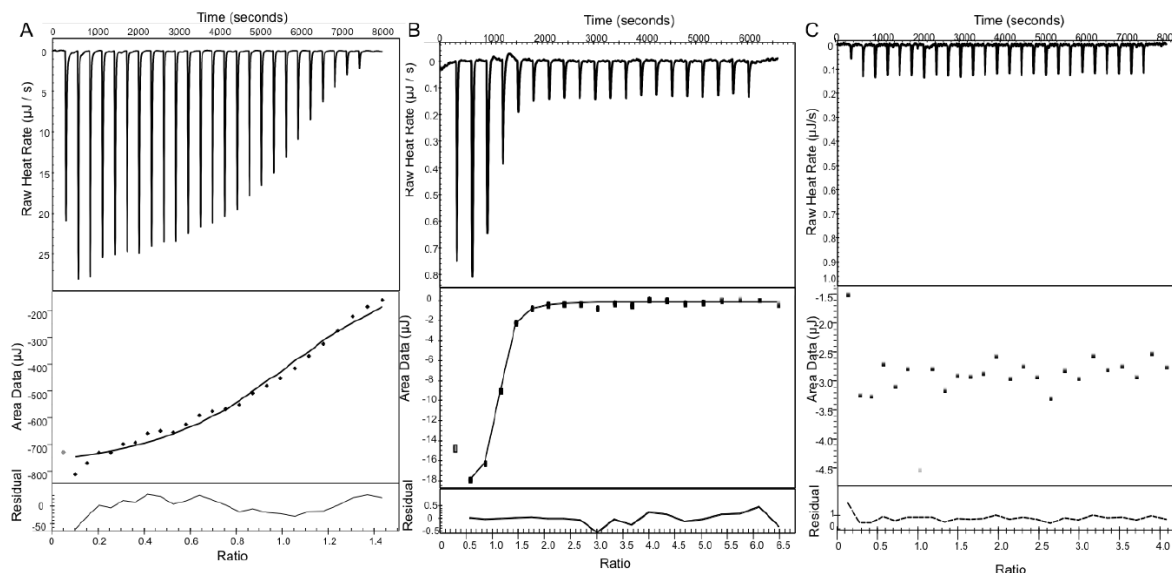


Figure 6.1. ITC data of BECN1 BH3D peptide titrated into VMP1 ATGD peptide. The upper panel shows the raw data and lower panel shows the fitting curve using NanoAnalyze software for (A) WT VMP1 ATGD with BECN1 BH3D, (B) WT VMP1 ATGD with BECN1 BH3D repeated by Yue Li, and (C) GWG-ATGD with BECN1 BH3D.

Table 6.1 Thermodynamics of binding of BECN1 and VMP1 ATGD.

	BECN1 BH3D					MBP-BECN1 1-135				
	Kd (μM)	ΔH (kJ/mol)	ΔS (J/K \cdot mol)	ΔG (kJ/mol)	n	Kd	ΔH	ΔS	ΔG	n
ATGD (Dr. Mei)	11.4 ± 3.2	-181 ± 49.8	511 ± 170	-28.4 ± 0.66	1.0 ± 0.01					
ATGD	1.3	-3.8	99.8	-18.9	1	No binding				
GWG-ATGD	No binding									

6.3.2. Secondary structure of BECN1 BH3D, VMP1 ATGD, and their 1:1 mixture were investigated by CD spectra

Dr. Yang Mei from our lab performed the CD spectra and secondary structure analysis (Figure 6.2, Table 6.1). Analysis of the CD spectrum recorded from VMP1 ATGD indicates that it contains 4 residues α -helical conformation, 1 residue in β -strand and 16 residues in coil (Table 6.1). As previously reported (Mei *et al.*, 2014), the BH3D has 1 residue in α -helix and β -strand, and 24 residues in coil (Table 6.1). Since formation of a stable α -helix or β -strand requires at least 6 residues (Kabsch and Sander 1983, Frishman and Argos 1995), both the BECN1 BH3D and VMP1 ATGD appear to be completely disordered in solution (Figure 6.2 and Table 6.1). Next, we mixed the BH3D and ATGD in a 1:1 molar ratio at concentrations of either 7.65 μM ,

30 μ M, 100 μ M or 300 μ M of each peptide and recorded CD spectra from each mixture (Figure 6.2). The CD results show that proteins in these mixtures remain disordered (Figure 6.2). The secondary structure content estimated using SELCON3 (Sreerama & Woody, 2000), shows that the 100 μ M mixture has the highest helical content (14 residues) and the lowest random coil content (29 residues) (Table 6.1). These results suggest that the weak interaction between the disordered VMP1 ATGD and BECN BH3D may slightly increase the helical content at the expense of coil content. However, at all concentrations the mixture is largely disordered, with more than 61% of the residues being in coil conformation.

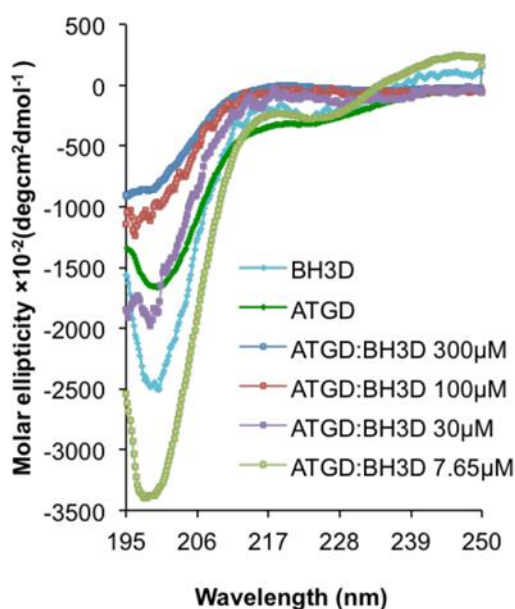


Figure 6.2. CD spectra of VMP1 ATGD, BECN1 BH3D, and their complexes.

Table 6.2. Secondary structure contents analysis of CD spectra for VMP1 ATGD, BECN1 BH3D, and their complexes of Table.

Peptides	# of residues	Percentage of the secondary content (%)		
		Helix	Strand	Coil
BECN1 BH3D	26	4.0	3.8	91.9
VMP1 ATGD	21	20.1	4.8	79.1
BH3D:ATGD (7.65 μ M)	47	6.7	12	81.4
BH3D:ATGD (30 μ M)	47	17.1	7.7	77.6
BH3D:ATGD (100 μ M)	47	30.3	7.4	61.5
BH3D:ATGD (300 μ M)	47	27.8	12.1	63.2

6.4. Conclusions and Discussion

In Chapter 1, we stated that the BECN1 BH3D is an α -MoRF, as it transitions from coil to helix upon binding to BCL2 homologs. Since published Co-IP results suggest that the BECN1 BH3D also interacts with VMP1 ATGD, we hypothesized that the BH3D may undergo a coil-to-helix transition upon binding to the VMP1 ATGD as well. However, our inconsistent ITC results do not unambiguously prove that BECN1 BH3D interacts with VMP1 ATGD *in vitro*. Further, the CD results do not show an obvious coil-to-helix transition when the BH3D and ATGD are mixed at different concentrations in a 1:1 ratio. Sequence analysis of the VMP1 ATGD does not identify a potential Anchor region (data not shown here); therefore, currently there is no indication that the ATGD undergoes binding-induced structural transitions. It is possible that the absence of an Anchor region in the VMP1 ATGD prevents a disorder-to-order transition as is observed in other IDRs lacking Anchor regions (Glover *et al.*, 2016). But, our current results are inconclusive.

CHAPTER 7. INVESTIGATING THE MECHANISM BY WHICH THE γ HV68 BCL2, M11, DOWN-REGULATES BECN1-MEDIATED AUTOPHAGY

7.1. Introduction

As introduced in Chapter 1, anti-apoptotic BCL2 homologs down-regulate autophagy by binding to the BECN1 BH3D, and the interactions between various anti-apoptotic BCL2 proteins and BH3Ds of diverse pro-apoptotic BCL2 proteins or BECN1 have been structurally and thermodynamically characterized. However, the mechanism by which these interactions down-regulate autophagy is not. Compared to the isolated BECN1 BH3D; BECN1 residues 1-135 bind to γ HV68 BCL2 homolog, M11, with higher affinity, but bind to human or KSHV Bcl-2 with similar affinity (Sinha *et al.*, 2008). Interestingly, BECN1 residues 90-266, bind to KSHV Bcl-2 with higher affinity, but bind to human Bcl-X_L with similar affinity (Noble *et al.*, 2008). Therefore, in order to understand the mechanism by which BCL2 homologs down-regulate autophagy, it is important to investigate whether the binding of BCL2 homologs to BECN1 impact the conformation, interactions and function of BECN1 domains other than the BH3D; as well as similarities and differences in the binding of diverse BCL2 homologs.

Here we report the results of our research examining BECN1 binding to γ HV68 M11. We first show that the BECN1 BH3D is not conserved in lower eukaryotes. Then then find out that BH3D is not required for starvation-induced upregulation of autophagy. Next, we use isothermal titration calorimetry (ITC) to quantify the thermodynamics of M11 binding to different multi-domain BECN1 fragments to assess the potential role of other BECN1 domains in binding, and to investigate how M11-binding impacts BECN1 homodimerization. Further, we use circular dichroism (CD) to assess the impact of M11 binding on the secondary structure content and thermostability of multi-domain BECN1 fragments. Additionally, we use HDX-MS to examine

the structural dynamics of multi-domain BECN1 fragments and their complexes with M11. Lastly, we examine the overall shape and flexibility of multi-domain BECN1 fragments and their complexes with M11 using size-exclusion chromatography in tandem with small angle X-ray scattering (SEC-SAXS). Our results provide extensive information on the M11:BECN1 interaction, to better elucidate how BCL2:BECN1 interactions down-regulate autophagy.

7.2. Materials and Methods

7.2.1. Sequence alignment

Sequences of BECN1 homologues from eight diverse eukaryotes (*Homo sapiens*, *Mus musculus*, *Gallus gallus*, *Xenopus laevis*, *Drosophila melanogaster*, *Caenorhabditis elegans*, *Arabidopsis thaliana*, and *Saccharomyces cerevisiae*) were identified by BLASTP searches of Genomic RefSeq Protein databases (<http://blast.ncbi.nlm.nih.gov/>) for each organism. Multiple-sequence alignment of these orthologs was performed using Jalview (<http://www.jalview.org/>).

7.2.2. Autophagy assay

Cellular autophagy levels were quantified by monitoring cellular localization of GFP-tagged LC3 protein (Kabeya *et al.*, 2000). Each chamber of an 8-well culture slide (Nunc™ Lab-Tek™ Chambered Coverglass) was seeded with 1×10^5 MCF7 cells and cultured overnight in DMEM (Gibco) with 10% fetal bovine serum (Gibco) until 80–90% confluent. The cells were co-transfected with 200 ng of GFP-LC3 and 300 ng of FLAG-BECN1 WT or 150 ng of FLAG-BECN1^{ΔBH3D} expression plasmids, using Lipofectamine 2000 reagent (Invitrogen) according to the manufacturer's instructions. After transfection and incubation at 37 °C for 24 h, the cells were cultured in either rich (DMEM, 10% FBS, 2 × essential amino acids, and 2 × nonessential amino acids) or starvation (Earle's balanced salt solution) medium for 4 h. Cells were counterstained with DAPI to visualize nuclei and facilitate total cell counts, fixed to slides with

4% (v/v) paraformaldehyde, and then stored in 70% (v/v) glycerol. Cells were washed with PBS between the counterstaining, fixation, and storage stages. GFP-LC3-positive puncta were observed under a Zeiss LSM700 Confocal Laser Scanning Microscope (CLSM) (Zeiss, Thornwood, NY), using excitation at 488 nm and emission set at 590 nm using a Plan-Apochromat 40x/1.4 oil immersion lens. The GFP-LC3 labelled puncta was quantified by counting a minimum of 50 cells for duplicate samples per condition using Imaris software (Bitplan AG, Zurich, Switzerland) in three independent experiments. The significance of alterations in autophagy levels was determined by a two-tailed, heteroscedastic Student's *t* test, wherein $p \leq 0.05$ is considered significant. Expression levels of WT FLAG-BECN1 and FLAG-BECN1^{ΔBH3D} were verified by Western blotting using commercial mouse monoclonal anti-FLAG M2-peroxidase antibody (Sigma). Actin levels in MCF7 cell lysates, detected using mouse anti-actin (EMD-Millipore) served as a loading control. For detection, the membrane was treated with an Irdye 800CW goat anti-mouse secondary antibody and scanned using the 800nm channel of Odyssey® CLx Imager (LI-COR).

7.2.3. Protein overexpression and purification

M11 residues 1-136 was cloned into pET21(d+) vector (Novagen) encoding a C-terminal His₆-tag, and expressed and purified as described (Sinha *et al.*, 2008).

Plasmids for overexpression of human BECN1 fragments were created by cloning the IDR (residues 1-135), BH3D-FHD (residues 90-171), BH3D-FHD-CCD (residues 105-265), FHD-CCD (residues 136-265), BH3D-FHD-CCD-BARAD^{AFM} (residues 105-450), and CCD-BARAD^{AFM} (residues 175-450), and full-length protein (FL; residues 1-450) between the *Bam*HI and *Xho*I restriction enzyme sites of the pMBP-Parallel-1 bacterial expression vector. For constructs containing the BARAD, a triad mutation F359D/F360D/W361D at the aromatic finger

of BARAD was made using QuikChange II Site-Directed Mutagenesis Kit (Agilent Technologies) to prevent protein aggregation during purification.

Table 7.1. Samples used in Chapter 7.

	Label	Description	Theoretical Molecular Mass (kDa)
1	MBP-BECN1 IDR	BECN1 (1-135) fusion protein	59.1
2	BH3D-FHD	BECN1 (90-171)	9.4
3	FHD-CCD	BECN1 (141-265)	15.5
4	CCD-BARAD	BECN1 (175-450, F359D,F360D,W361D)	32.9
5	BH3D-FHD-CCD	BECN1 (105-265)	19.4
6	BH3D-FHD-CCD-BARAD ^{AFM}	BECN1 (105-450, F359D,F360D,W361D)	40.9
7	M11:BH3D-FHD-CCD	BECN1 (105-265) complexed with M11	36.1
8	M11:BH3D-FHD-CCD-BARAD ^{AFM}	BECN1 (105-450, F359D,F360D,W361D) complexed with M11	57.5

Separate 50 μ L aliquots of *E. coli* Arctic Express cells were transformed with 100 ng of the expression plasmid for each BECN1 fragment, and grown at 37 °C overnight in LB medium containing 100 μ g/mL ampicillin. This starter culture was used to inoculate 6 L of LB medium containing 100 μ g/mL ampicillin and grown at 30 °C to OD₆₀₀ = 0.6. Subsequently, the temperature was equilibrated to 13 °C, then protein expression induced by addition of 0.5 mM isopropyl thio- β -D-galactoside and protein expression continued at 13 °C for 18-20 hours. The cells were harvested via centrifugation at 4000 g for 20 min, washed with lysis buffer (50 mM Tris pH 8.0, 300 mM NaCl, 1 mM EDTA, 2 mM DTT), and re-pelleted by centrifugation at 4000 g for 30 min, prior to storing at -80 °C. The frozen pellets were thawed and resuspended in 180 mL lysis buffer containing 12 tablets of protease inhibitor (Bimake). The resuspended cells were lysed in a NanoDeBEE emulsifier (BEE International), and the lysate centrifuged at 20,000 g for 30 min to pellet down cell debris and clarify the lysate. The clarified lysate was passed over 10 mL amylose affinity resin (GE Healthcare) in a gravity column, then the column was washed

with 150 ml lysis buffer. MBP-tagged fusion proteins were eluted from the amylose resin in 50 mM Tris pH 8.0, 300 mM NaCl, 1 mM EDTA, 2 mM DTT, 25 mM maltose and further purified by size-exclusion chromatography (SEC) using either a Superdex 200 10/300 GL column or a Superose 6 Increase 10/300 GL column (GE Healthcare), in SEC buffer consisting of 50 mM Tris pH 8.0, 150 mM NaCl, 2 mM β -Mercaptoethanol.

Untagged protein was obtained by loading and washing the amylose resin as described above, followed by overnight on-column cleavage of the MBP tag by 20 mg of GST-tagged TEV protease. This cleavage leaves a linker comprising residues GAMDP at the N-terminus of the protein. The cleaved protein was washed off with two column volumes of lysis buffer. For all the cleaved proteins except BECN1^{AFM} FL, the proteins washed off from affinity column after cleavage were further purified by anion-exchange chromatography using an 8 ml HR10/10 Mono Q column (GE Healthcare) (MonoQ Buffer A: 50 mM Tris pH 8.0, 2 mM β -Mercaptoethanol; Buffer B: 50 mM Tris pH 8.0, 1 M NaCl, 2 mM β -Mercaptoethanol), the protein was eluted at gradient of 20% - 30% Buffer B. The protein was lastly purified by SEC as described for the tagged protein. For the BECN1^{AFM} FL, the protein washed off from affinity column after cleavage was purified by SEC as described for the tagged protein.

For each protein preparation, SDS-PAGE was used to evaluate protein purity at each stage of purification. The final purified protein was concentrated to 8-12 mg/ml in the SEC buffer, flash-frozen in liquid nitrogen, and stored at -80 °C.

7.2.4. Isolation of complexes of M11 and different BECN fragments

Different M11:BECN1 fragment complexes were obtained by adding pure M11 to each pure BECN1 fragment in a 3:2 molar ratio. The complex was then passed over Ni-NTA affinity resin (GE Healthcare) in a gravity column, and washed with wash buffer consisting of 50 mM

Tris pH 8.0, 150 mM NaCl, 25 mM imidazole, and 2 mM BME. The complex was eluted from the Ni-NTA resin by elution buffer consisting of 50 mM Tris pH 8.0, 150 mM NaCl, 250 mM imidazole, and 2 mM β -Mercaptoethanol, and then, as described above, SEC was performed to remove the excessive M11, concentrated, flash-frozen in liquid nitrogen, and stored at -80 °C.

7.2.5. ITC

A Low Volume Nano ITC (TA Instruments) was used to perform ITC experiments at 20 °C. All samples were dialyzed against ITC buffer comprising 50 mM Tris pH 8.0, 150 mM NaCl and 2 mM β -mercaptoethanol. M11 interaction with BECN1 fragments was assessed by titrating 100 – 500 μ M M11 in 25 injections of 2 μ l each into the sample cell containing 30-100 μ M BECN1 samples. Dimer dissociation experiments were performed by titrating 20-150 μ M protein in 20 injections of 2.5 μ l each, into the sample cell containing ITC buffer. Data were analysed with the NanoAnalyze Software (TA Instruments). Buffer blanks, measured by titrating M11 into buffer, or buffer into buffer for the dimer dissociation experiments, were subtracted from the experimental profiles of interaction experiments, which were then fitted with independent models. The data reported are the average of triplicates.

7.2.6. CD spectroscopy

10 μ M BH3D-FHD-CCD or M11: BH3D-FHD-CCD, or 5 μ M BECN1 BH3D-FHD-CCD-BARAD^{AFM} or M11: BH3D-FHD-CCD-BARAD^{AFM} were dialyzed overnight against 2 L buffer containing 10 mM phosphate pH 7.4, 100 mM ammonium sulfate. Continuous scanning CD spectra from each sample were recorded from 190 to 240 nm at 20 °C in a 300 μ l quartz cell (0.1 cm path length) on a Jasco J-815 spectropolarimeter equipped with a Peltier thermoelectric temperature control. Three programs from the CDpro suite, SECON3, CDSSTR, and CONTIN, and the SP37 reference protein database were used to estimate the secondary structure content of

the samples (Sreerama & Woody, 2000, Sreerama *et al.*, 2000, Sreerama *et al.*, 2001), and the average of secondary structure content estimated by each of the three CD data analysis programs reported in Table 7.3.

Thermal denaturation was monitored by recording variable temperature CD spectra at 222 nm at 1-degree intervals with a ramp rate of 1 °C/min. Variable temperature spectra were recorded from 4-55 °C (or 55-4 °C for reverse measurements) for 5 µM BECN1 constructs in buffer containing 10 mM phosphate pH 7.4, 100 mM ammonium sulfate and for M11 and its complexes with BECN1 constructs from 4-90 °C (or 90-4 °C for reverse measurements). Data were analyzed using OriginPro 9 (OriginLab), where mean residue molar ellipticity was plotted against temperature, and the melting temperature (T_m) calculated by fitting the data to the Boltzmann or Double Boltzmann algorithm included in OriginPro.

7.2.7. HDX sample preparation and deuterium exchange measurement

4 µl of 300 µM proteins in 50 mM Tris pH 8.0, 50 mM NaCl, and 2 mM TCEP were diluted with 36 µl D₂O of ≥ 99.75% isotopic purity, to produce a sample with final D₂O concentration of 90%. Prior to quenching with 40 µl of quenching buffer containing 8.4% formic acid and 5 M guanidine-HCl, D₂O exchange was allowed for five time intervals: 0 s (wherein H₂O was used for dilution instead of D₂O), 10 s, 100 s, 1000 s, and 10000 s.

The quenched protein samples were digested for 5 mins by incubating with 40 µl pepsin beads (G-Biosciences), which were mixed by shaking every 30s. The pepsin beads were pelleted by centrifuging at 14,000 g, and the digested peptides were decanted into the tube used for MS which was loaded onto a Waters, Acquity I-class ultra-performance liquid chromatography (UPLC) system equipped with a BEH C18 1.7 µm, 2.1 mm x 100 mm column. The entire experiment was performed at 20 °C. Mobile phase A was water with 0.1% Formic acid (FA). A

5% to 40 % gradient of mobile phase B (Acetonitrile) was used to separate the peptides. The gradient was followed by 10 min of steeper gradient to clean and prepare the column for the next sample. Waters SYNAPT G2-Si High Resolution Quad Time-of-Flight (HR Q-ToF) mass spectrometer was used to acquire the mass spectra. The HR Q-ToF setting was: mass range 50 - 2000 Da, ES+ sensitivity mode, capillary voltage 3.0 kV, Source T = 80°C, cone voltage 30 V, Desolvation Gas flow 350 L/h, Desolvation T = 170° C. MS_E method was used to ramp trap collision energy 20 V to 48 V.

ProteinLynx Globule Server (Waters) was used to map the digested peptides against the protein sequence. Peptides with confidence lower than 80% were excluded from all further analysis. Centroid values were determined using HD-Examiner software (Sierra Analytics). Peptide coverage was 94.5% and 98.7% for BECN1 BH3D-FHD-CCD and M11: BH3D-FHD-CCD, respectively.

7.2.8. SEC-SAXS data collection and analysis

SAXS data were collected at beamline 18-ID (BioCAT) at APS, ANL, Argonne, Illinois, USA. 8-11 mg/ml of BECN1 fragments or their complexes with M11 were injected onto a Superdex 200 10/300 SEC (GE Healthcare) column at a flow rate of 0.75 ml/min and the SEC eluate was immediately exposed to X-rays of wavelength 1.033 Å for 1 s, with a 2 s delay between each exposure. The SAXS data were recorded using a PILATUS3 1M detector at a sample-to-detector distance of 3.5 m, which covers a momentum-transfer range from 0.0036 to 0.4 Å⁻¹ [$q = (4\pi\sin \theta)/\lambda$, where 2θ is the scattering angle]. Scattering data were normalized to the incident X-ray beam intensity prior to further analysis. The scattering from buffer was subtracted using BioCAT beamline programs based on the ATSAS program suite. A q range of $q < 0.3$ Å⁻¹ was used for all SAXS analyses using the ATSAS program suite (Franke et al., 2017). Within the

ATSAS program suite, PRIMUS (Konarev *et al.*, 2003) was used to scale and average data for further analysis, and also for Guinier extrapolation, which provided an estimate of the radius of gyration (R_g). The particle pairwise distance distribution function [P(r) plot] and Kratky plot were calculated using GNOM (Svergun, 1992). The P(r) plot was used to estimate R_g and maximum dimension (D_{max}), which were used to constrain the dimensions of the ten independent *ab initio* bead models calculated using DAMMIF (Franke & Svergun, 2009). P1 symmetry was imposed to generate these models. A total of ten *ab initio* reconstructed models were further averaged and filtered by DAMSEL, DAMSUP, DAMAVER and DAMFILT (Volkov & Svergun, 2003). EOM 2.1 (Tria *et al.*, 2015) was used to generate a pool of 10,000 independent models based on the sequence and structural information input for each protein, and the models that produced theoretical SAXS curves with the best χ^2 fits to the experimental SAXS data constituted the selected ensemble.

7.3. Results

7.3.1. The BECN1 BH3D is not conserved amongst eukaryotes

The autophagy pathway and BECN1 is conserved in all eukaryotes. However, an alignment of BECN1 sequences from diverse eukaryotes ranging from yeast to human show that the IDR is poorly-conserved (Figure 7.1) (Mei *et al.*, 2014). Notably, the BH3D, which is part of the poorly-conserved IDR, appears to be missing in lower eukaryotes such as worm (Figure 7.1). which suggests that the BH3D may not be required for the core autophagy functions of BECN1. Therefore, we performed cellular autophagy assays to determine if deletion of the BECN1 BH3D impacts cellular autophagy levels.

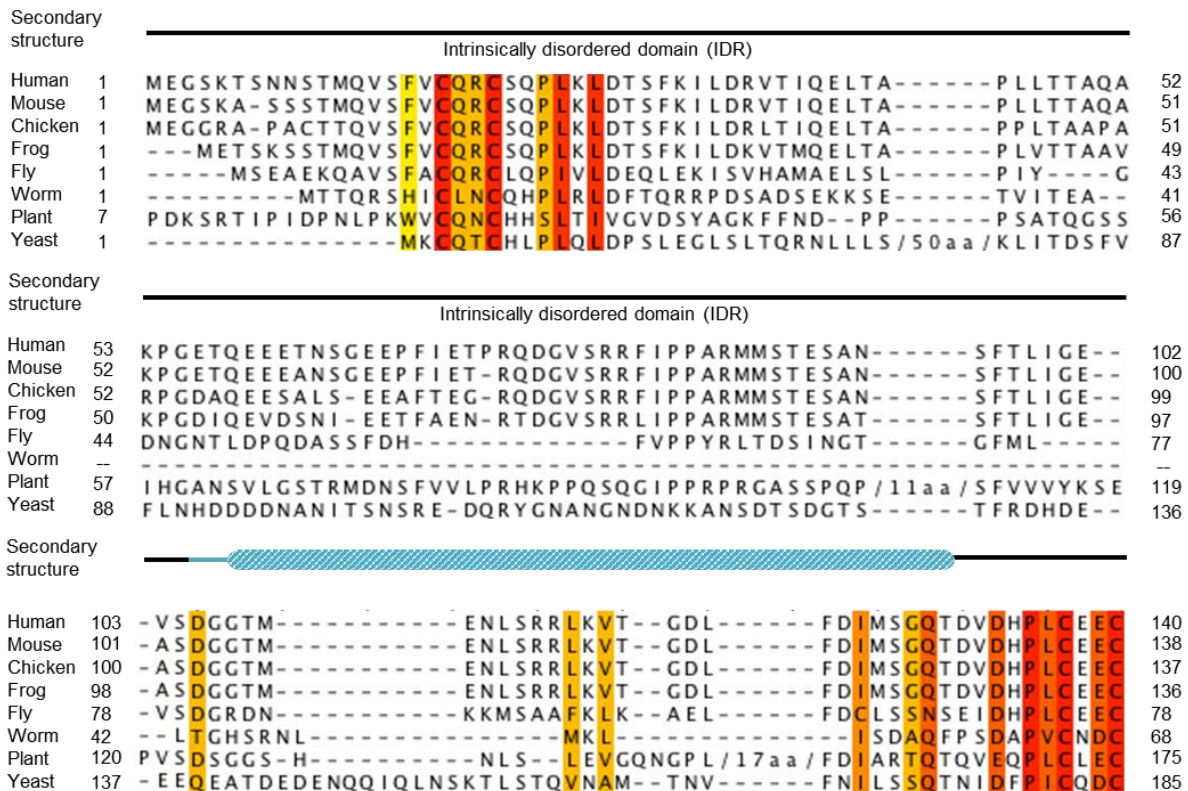


Figure 7.1. The BECN1 BH3D is not conserved. (A) sequence alignment of the IDR of BECN1 orthologs from diverse organisms from yeast to human. Increasing background color intensity corresponds to increasing residue conservation with red corresponding to invariant residues. Experimentally determined secondary structure is displayed above the alignment, with cylinders representing helices and lines representing coil, color-coded by domains as follows: IDR (black) and BH3D (cyan with white diagonal stripes). Diagonal stripes indicate binding-induced secondary structure.

7.3.2. The BECN1 BH3D is not required for starvation-induced autophagy

Cellular autophagy assays were performed by Ms. Shreya Mukhopadhyay, to investigate how deletion of the BECN1 BH3D impacts autophagy levels. Because BECN1 is known to be required for autophagosome nucleation, we evaluated cellular autophagy by monitoring and comparing levels of puncta labeled with GFP-tagged LC3, an autophagosome-specific marker, in cells grown in either nutrient-rich or starvation medium. We used human breast adenocarcinoma MCF7 cells because they lack detectable endogenous expression of BECN1 (Figure 7.2A), resulting in very low basal levels of autophagy (Liang *et al.*, 1999, Pattingre *et al.*, 2005, Sinha *et al.*, 2008) even in starvation conditions unless BECN1 is ectopically expressed (Figure 7.2B,C).

This allows the effect of BECN1 mutants to be assayed in the absence of endogenous BECN1. We first ensured comparable exogenous expression of BECN1 FL and BECN1 Δ BH3D in starvation and nutrient-rich conditions (Figure 7.2A). Transient expression of BECN1 in MCF7 cells did not increase autophagy levels in nutrient-rich conditions ($p = 0.775$ for BECN1 expression *versus* no expression; Figure 7.2B,C) but led to a marked increase in autophagy upon starvation ($p = 0.0102$ for BECN1 expression in starvation condition *versus* nutrient-rich condition) (Figure 7.2B,C). We find that deletion of BH3D does not impact autophagy levels in either nutrient-rich ($p = 0.245$ for BECN1 Δ BH3D *versus* BECN1 FL) or starvation medium ($p = 0.05$ for BECN1 Δ BH3D *versus* BECN1 FL) (Figure 7.2B,C), indicating that the BH3D of BECN1 is not essential for upregulating starvation-induced autophagy. Therefore, binding of BCL2 homologs to the BECN1 BH3D does not by itself explain how BCL2 homologs down-regulate autophagy.

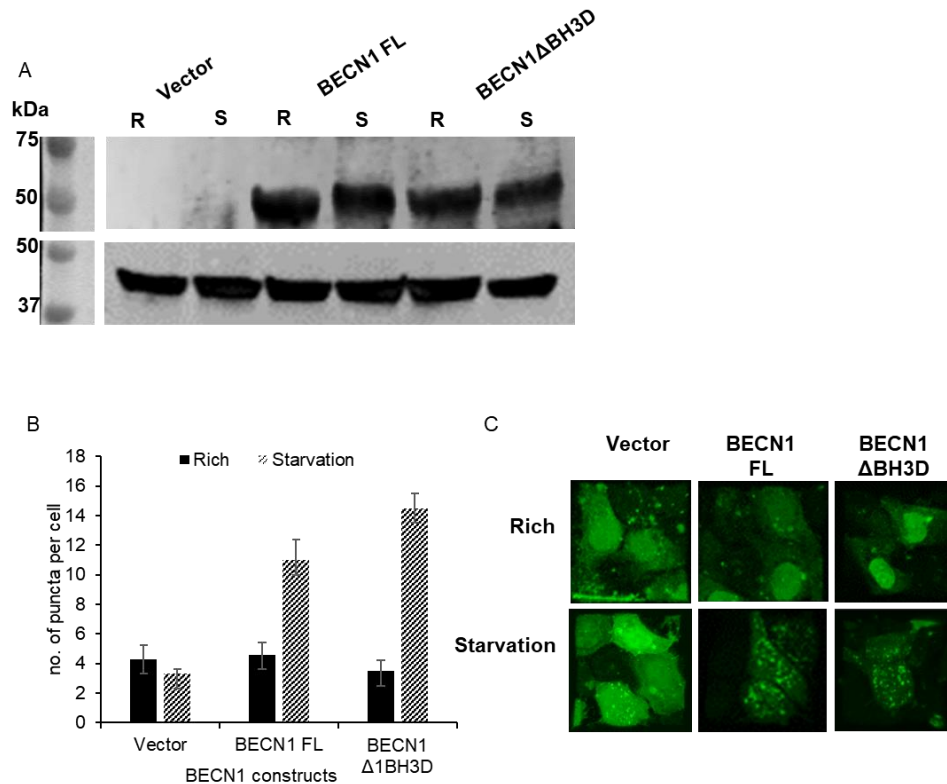


Figure 7.2. The BECN1 BH3D is not required for autophagy. (A) Western blotting of MCF7 cell extracts showing comparable expression levels of FLAG-BECN1 FL and FLAG-BECN1 ^{Δ 31-104} in nutrient-rich (R) and starvation (S) conditions, with actin as a loading control. (B) Light microscopy quantification of discrete GFP-LC3 puncta per cell in GFP-positive MCF7 cells co-transfected with GFP-LC3 and FLAG-BECN1 FL or FLAG-BECN1 ^{Δ 31-104} as indicated below the x-axis. Bars, number of puncta per cell. Error bars, S.D. (C) representative images of GFP-LC3 (green) staining in cells grown in starvation or nutrient-rich medium and transfected with different plasmids as indicated.

7.3.3. Expression and purification results of BECN1 constructs

Various BECN1 fragments (Table 7.1) were purified. For each sample, despite a small aggregation shoulder, the major SEC peak corresponds a single band on SDS-PAGE, indicating that the final SEC sample was pure and homogenous (Figures 7.3, 7.4, 7.5, 7.6, 7.7, and 7.8).

The apparent molecular mass of the MBP-BECN1 IDR, calculated from the elution volume (16.2 ml) of the major SEC peak (Superose 6 Increase, Figure 7.1), is 93.3 kD, which is ~2 times greater than the theoretical molecular mass of the MBP-BECN1 IDR monomer

calculated from the amino acid sequence (Table 7.1). This is consistent with the IDR being disordered. The final yield of purified MBP-BECN1 IDR was 5.2 mg / L of bacterial culture.

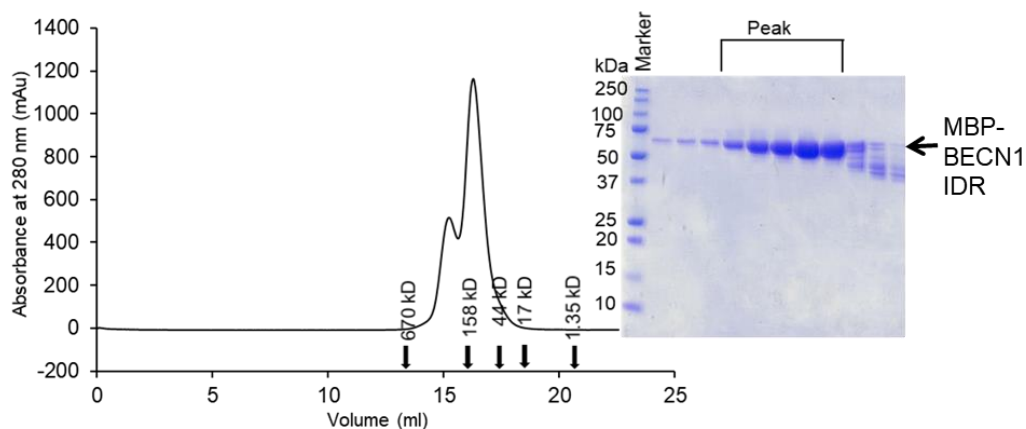


Figure 7.3. Size exclusion chromatogram and the corresponding SDS-PAGE of MBP-BECN1 IDR. The elution positions of SEC standards are indicated by arrows.

The BH3D-FHD was purified by Dr. Karen Glover from our lab. The apparent molecular mass of the BH3D-FHD, calculated from the elution volume (16.0 ml) of the major SEC peak (Superdex 75, Figure 7.4), is 24.2 kD, ~2.6 times greater than the theoretical molecular mass of the BH3D-FHD monomer calculated from the amino acid sequence (Table 7.1), indicating that the BH3D-FHD may form a trimer, or is largely disordered in solution. The final yield of purified BH3D-FHD was 0.3 mg / L of bacterial culture.

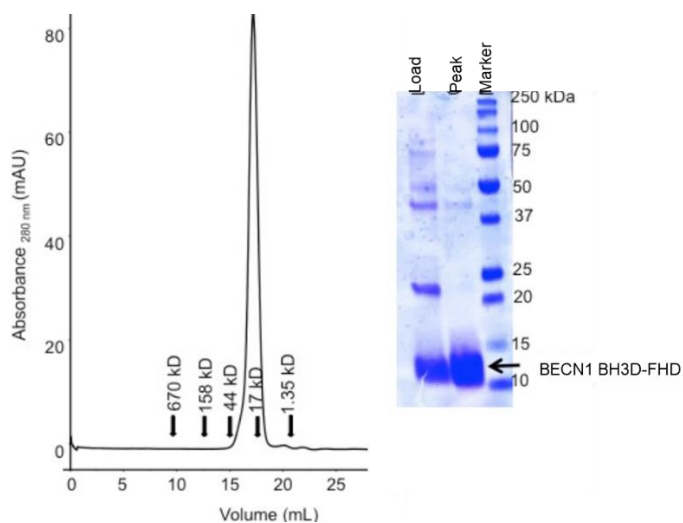


Figure 7.4. Size exclusion chromatogram and the corresponding SDS-PAGE of BECN1 BH3D-FHD. The elution positions of SEC standards are indicated by arrows.

The apparent molecular mass of the FHD-CCD, calculated from the elution volume (14.7 ml) of the major SEC peak (Superdex 200, Figure 7.5), is 53.7 kD, which is ~1.7 times greater than the theoretical molecular mass of the FHD-CCD dimer calculated from the amino acid sequence (Table 7.1). This is consistent with the FHD-CCD being an elongated homodimer. The final yield of purified BH3D-FHD was 0.3 mg / L of bacterial culture.

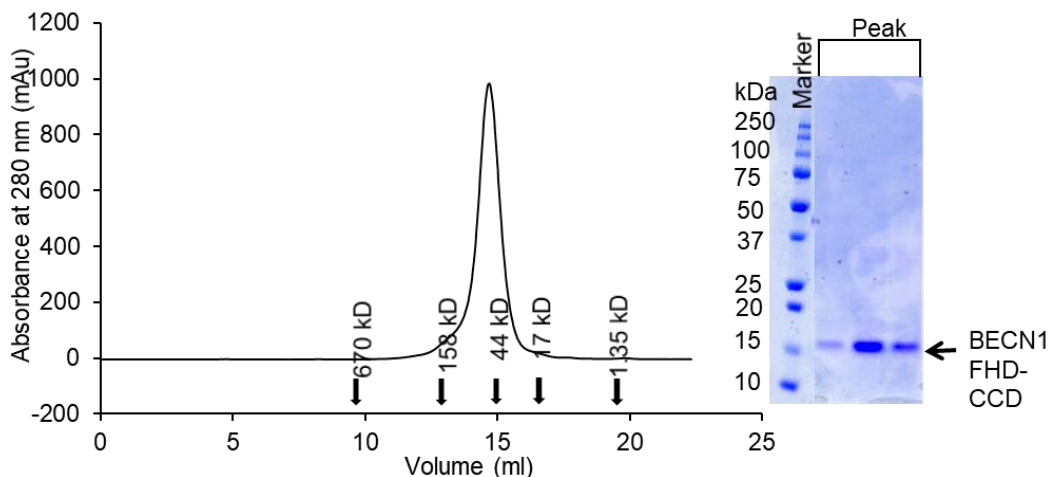


Figure 7.5. Size exclusion chromatogram and the corresponding SDS-PAGE of BECN1 FHD-CCD. The elution positions of SEC standards are indicated by arrows.

The apparent molecular mass of the BH3D-FHD-CCD, calculated from the elution volume (13.3 ml, Superdex 200) of the major SEC peak (Figure 7.6), is 104.7 kD, ~2.7 times greater than the theoretical molecular mass of the BH3D-FHD-CCD homodimer calculated from the amino acid sequence (Table 7.1). This is consistent with the BH3D-FHD-CCD being an elongated homodimer. The final yield of purified BH3D-FHD-CCD was 4.3 mg / L of bacterial culture.

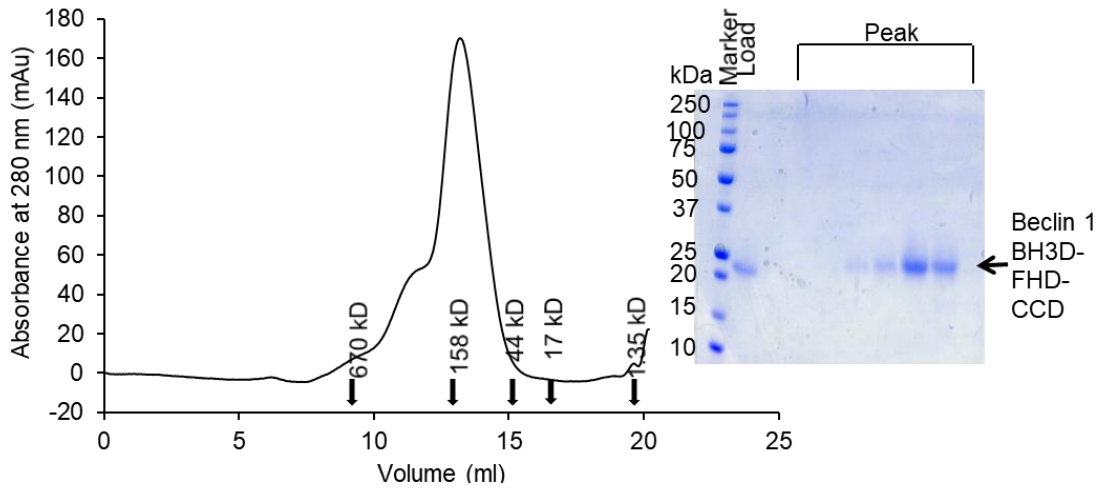


Figure 7.6. Size exclusion chromatogram and the corresponding SDS-PAGE of BECN1 BH3D-FHD-CCD. The elution positions of SEC standards are indicated by arrows.

The apparent molecular mass of the BH3D-FHD-CCD-BARAD^{AFM}, calculated from the elution volume (15.4 ml, Superose 6 Increase) of the major SEC peak (Figure 7.7), is 180.7 kD, which is ~3 times greater than the theoretical molecular mass of the BH3D-FHD-CCD homodimer calculated from the amino acid sequence (Table 7.1). This is consistent with the BH3D-FHD-CCD-BARAD^{AFM} being an elongated homodimer. The final yield of purified BH3D-FHD-CCD-BARAD^{AFM} was 5.6 mg / L of bacterial culture.

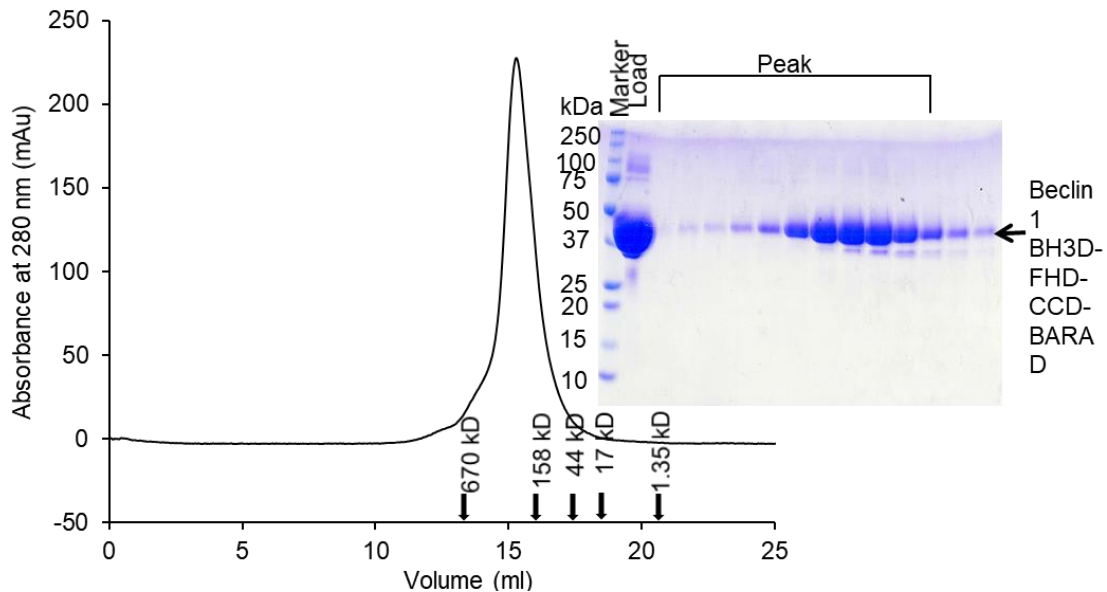


Figure 7.7. Size exclusion chromatogram and the corresponding SDS-PAGE of BECN1 BH3D-FHD-CCD-BARAD^{AFM}. The elution positions of SEC standards are indicated by arrows.

The apparent molecular mass of the BECN1^{AFM} FL, calculated from the elution volume (14.0 ml, Superose 6 Increase) of the major SEC peak (Figure 7.8), is 467.7 kD, which is ~4.5 times greater than the theoretical molecular mass of the BECN1^{AFM} FL homodimer calculated from the amino acid sequence (Table 7.1). This is consistent with the FL BECN1 being an elongated homodimer. The final yield of purified FL BECN1 was 1.8 mg / L of bacterial culture.

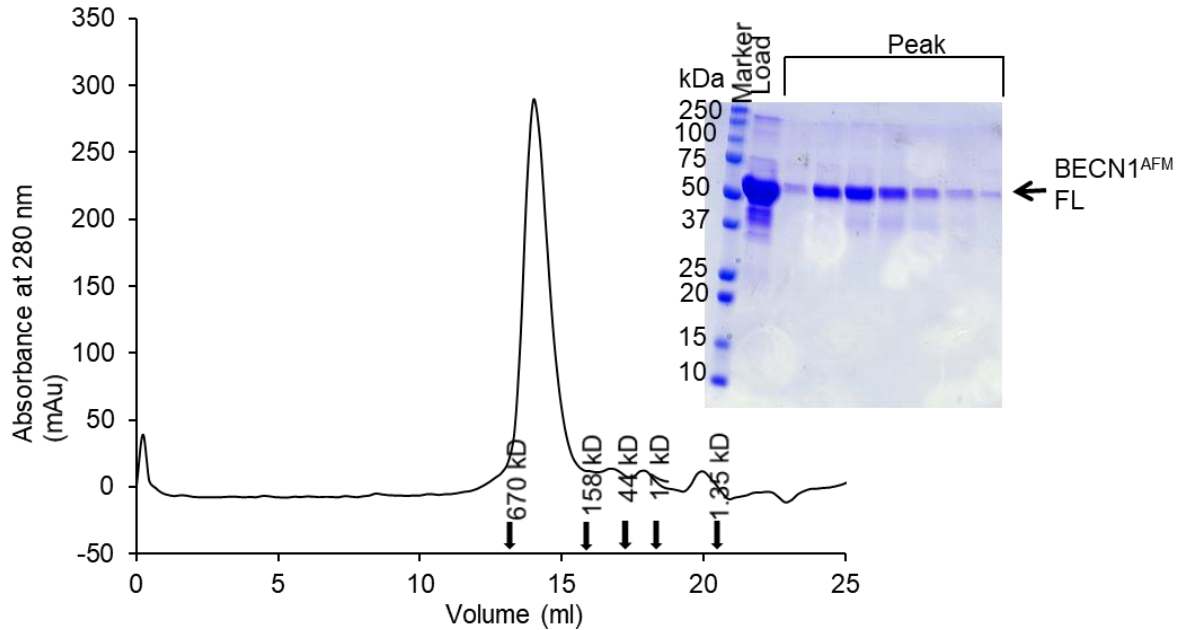


Figure 7.8. Size exclusion chromatogram and the corresponding SDS-PAGE of BECN1^{AFM} FL. The elution positions of SEC standards are indicated by arrows.

The apparent molecular mass of the M11:BH3D-FHD-CCD, calculated from the elution volume (12.3 ml, Superdex 200) of the major SEC peak (Figure 7.9), is 182.6 kD, which is ~2.5 times greater than the theoretical molecular mass of a M11:BH3D-FHD-CCD heterotetramer calculated from the amino acid sequence (Table 7.1). This is consistent with the M11:BH3D-FHD-CCD being an elongated homodimer.

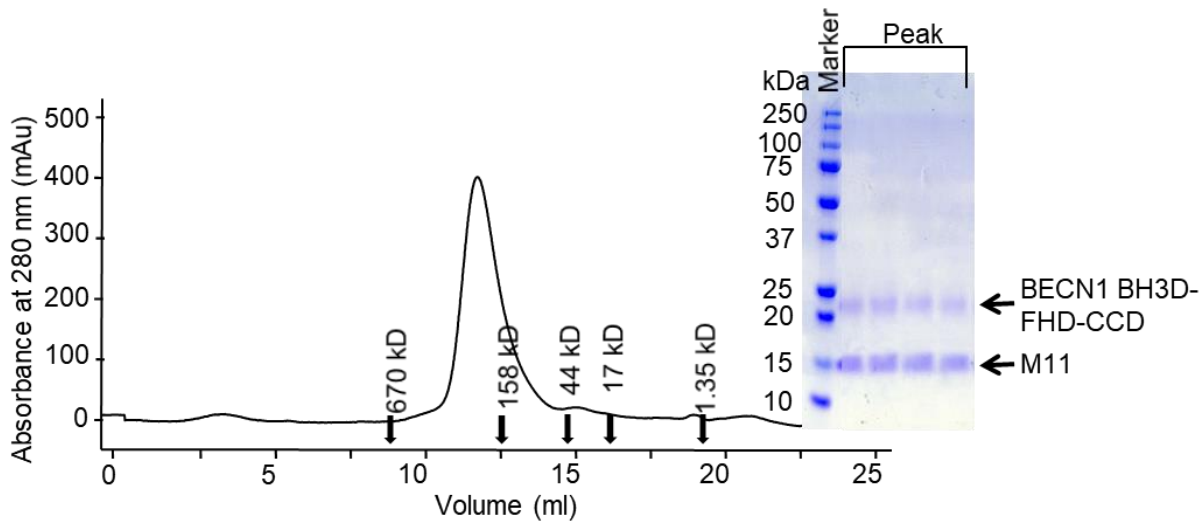


Figure 7.9. Size exclusion chromatogram and the corresponding SDS-PAGE of M11:BH3D-FHD-CCD. The elution positions of SEC standards are indicated by arrows.

The apparent molecular mass of the M11:BH3D-FHD-CCD-BARAD^{AFM}, calculated from the elution volume (15.0 ml, Superose 6 Increase) of the major SEC peak (Figure 7.10), is 239.9 kD, which is ~2 times greater than the theoretical molecular mass of the M11:BH3D-FHD-CCD-BARAD^{AFM} heterotetramer calculated from the amino acid sequence (Table 7.1). This is consistent with the M11:BH3D-FHD-CCD-BARAD^{AFM} is elongated heterotetramer. However, the apparent molecular weight of this complex is small than that of the isolated BECN1 BH3D-FHD-CCD-BARAD^{AFM} protein (297.1), which suggests that the BH3D and possibly other BECN1 regions become ordered upon binding to M11.

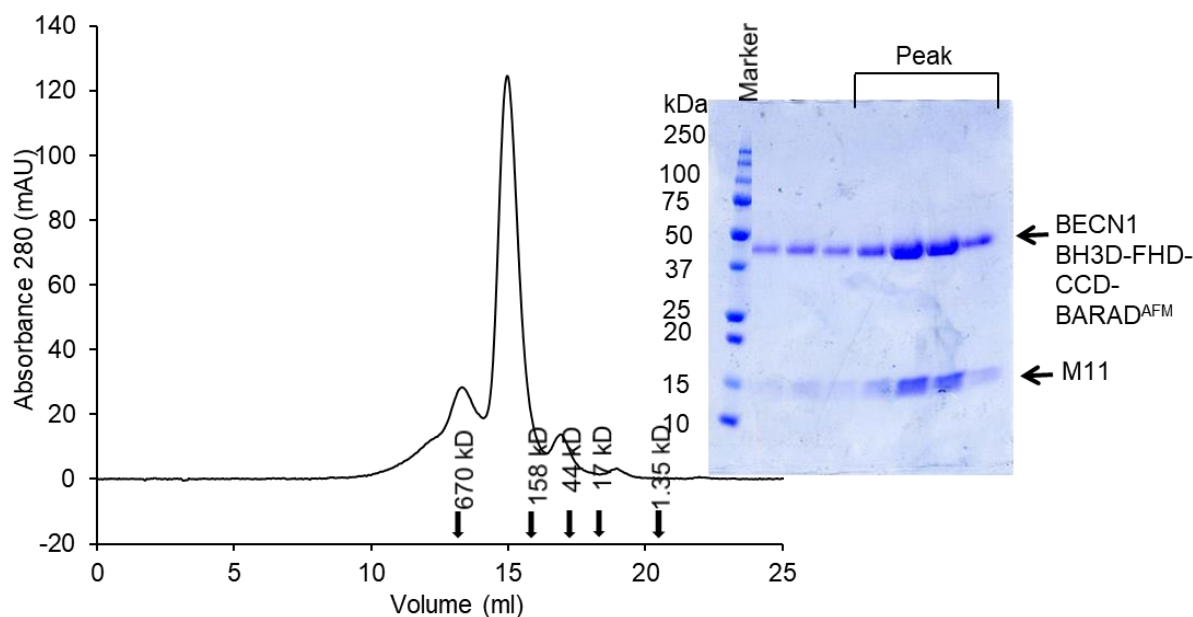


Figure 7.10. Size exclusion chromatogram and the corresponding SDS-PAGE of M11:BH3D-FHD-CCD-BARAD^{AFM}. The elution positions of SEC standards are indicated by arrows.

7.3.4. BECN1 regions outside the BH3D increase binding to M11

We used ITC to quantify and compare binding of M11 to various BECN1 fragments comprised of different domains (Table 7.2, Figure 7.11). As expected, BECN1 fragments that do not contain the BH3D, i.e. the FHD-CCD or CCD-BARAD^{AFM}, do not bind to M11 (data not shown), confirming that the BH3D is required for binding of M11 to BECN1. Therefore, the FHD-CCD and CCD-BARAD^{AFM} were not used for subsequent experiments in this study.

Table 7.2. Thermodynamics of binding of M11 and to BECN1 fragments.

BECN1 Fragments	M11			
	K_d (μ M)	ΔH (kJ/mol)	ΔS (J/K·mol)	ΔG (kJ/mol)
BH3D	1.38 ± 0.41	-70.97 ± 6.39	-125.72 ± 22.50	-33.51 ± 0.71
IDR	0.12 ± 0.04	-69.51 ± 5.13	-108.56 ± 15.91	-39.32 ± 0.54
BH3D-FHD	0.10 ± 0.02	-118.55 ± 2.05	-271.30 ± 6.79	-38.2 ± 0.71
BH3D-FHD-CCD	0.20 ± 0.02	-60.44 ± 1.71	-81.53 ± 6.51	-36.94 ± 0.19
BH3D-FHD-CCD-BARAD ^{AFM}	0.16 ± 0.06	-59.20 ± 0.82	-71.48 ± 1.01	-38.36 ± 1.06
FL	0.18 ± 0.02	-59.43 ± 0.85	-73.79 ± 3.19	-37.03 ± 0.43

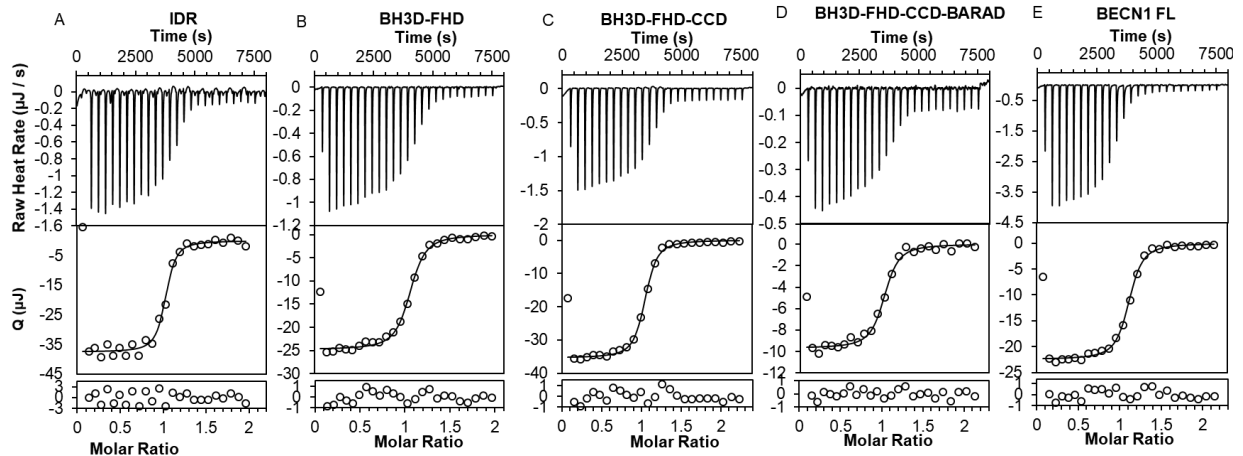


Figure 7.11. Representative ITC results for M11:BEEN1 fragment interactions. Upper panel: raw data; lower panel: integrated heat and theoretical fit by independent interaction model from NanoAnalyze. (A) 300 μM M11 titrated into 50 μM MBP-BEEN1 IDR. (B) 108 μM M11 titrated into 18 μM BH3D-FHD. (C) 300 μM M11 titrated into 44 μM BH3D-FHD-CCD. (D) 78 μM M11 titrated into 13 μM BH3D-FHD-CCD-BARAD^{AFM}. (E) 196 μM M11 titrated into 30 μM BEEN1^{AFM} FL.

The favorable free energy of all the other interactions is due to enthalpic contributions rather than due to entropic contributions. The negative ΔS for all these interactions likely reflects the increased structure of BEEN1 BH3D and M11 upon interaction, which proceeds despite the unfavorable entropic contributions, due to enthalpic compensation. All the BH3D-containing multi-domain BEEN1 fragments bind to M11 with an affinity that is ~ 7 -14-fold tighter than the isolated BH3D (Table 7.2), suggesting that BEEN1 domains besides the BH3D contribute to binding. Further, the BH3D-FHD and the IDR, which includes the BH3D, have the tightest binding (Table 7.2), suggesting that BEEN1 regions adjacent to the BH3D contribute to this improved affinity for M11. Despite the similar ΔG of M11 binding to different BH3D-containing BEEN1 fragments bind to M11, the relative enthalpic and entropic contributions to each interaction are different (Table 7.2). Most strikingly, M11 binds best to the BH3D-FHD, and involves the most favorable enthalpy, about 1.5-2 fold larger than those of the other interactions; but, has the largest entropic cost with ΔS being ~ 2 -4 fold larger than for the other interactions (Table 7.2).

Multiple factors contributed to our decision to use the BH3D-FHD-CCD for most of the subsequent biophysical analyses reported. BECN1 regions adjacent to the BH3D, i.e. the preceding IDR, and the FHD, appear to influence the M11 interaction the most. Therefore, the FHD was included; however, as the high flexibility of the IDR substantially hampers protein purification and biophysical data analyses, we did not include the IDR preceding the BH3D in these studies. The CCD was included to allow investigations into the impact of M11 on BECN1 homodimerization. Lastly, the BARAD does not seem to influence M11:BEEN1 interaction; and including the BARAD in the BECN1 fragment increases the complexity of data analyses, therefore, the BARAD was also not included. Hence, we focused on the M11:BEEN1 BH3D-FHD-CCD interaction for subsequent biophysical studies.

7.3.5. BECN1 domains besides the BH3D undergo significant conformational changes upon M11-binding

HDX-MS was used to identify regions of the BH3D-FHD-CCD that were flexible and solvent-exposed, versus well-ordered and buried, and to assess changes in solvent accessibility upon binding of M11 (Figure 7.12). HDX-MS results for the un-complexed BH3D-FHD-CCD, indicate that some regions of this fragment are highly dynamic; including BH3D residues 108-109 and 110-114 with HDX >90% and 30%-70%, respectively; BH3D-FHD linker residues 132-136 with HDX > 70%; CCD residues 215-218 and 222-224 with HDX of 60% - >90%, and CCD residues 245-265 which include the OH with HDX of 40% - 90%. Other regions are moderately dynamic, such as FHD residues 147-152 and 155-158 with HDX of 10% - 20%, and FHD residues 163-169 with HDX of 20% - 50%; as well as CCD residues 191-214 that follow the NES, with HDX of 10% - 30%, and CCD residues 225-244 with HDX of 20% - 50%.

Unexpectedly, CCD residues 180-190 which comprise the NES have HDX lower than 10%, suggesting this region is least solvent-accessible.

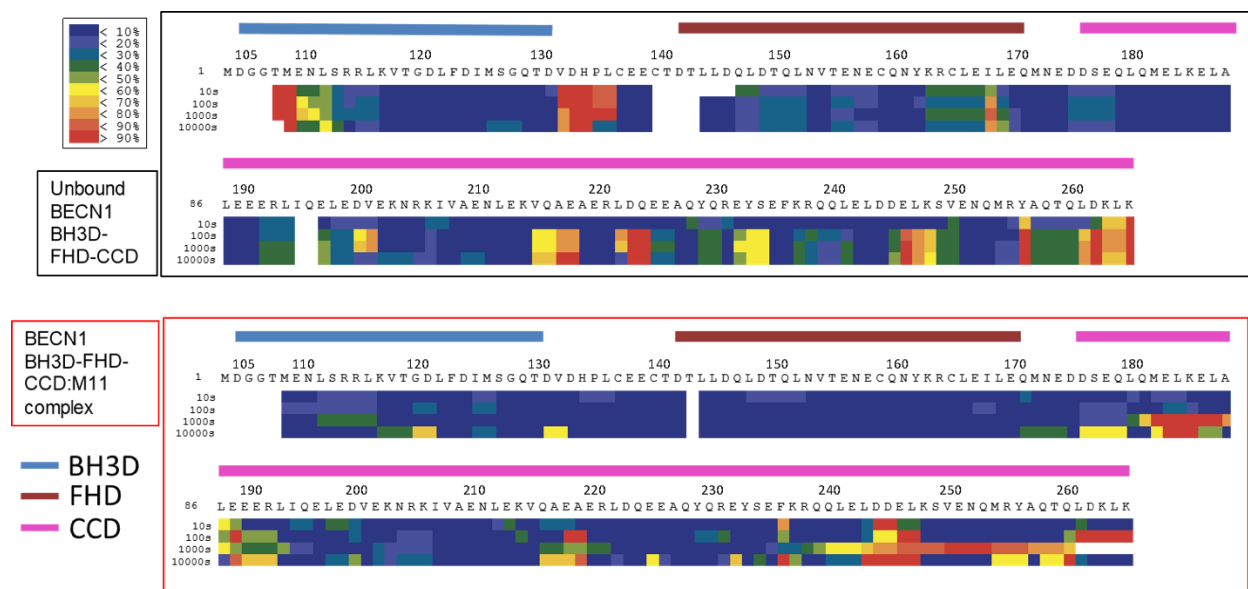


Figure 7.12. HDX heat maps of BECN1 BH3D-FHD-CCD for: (A) Unbound (B) In complex with M11. HDX time points are indicated. Color ramp from blue to red indicates deuterium exchange from <10% to >90%.

As expected, M11 binding to the BH3D-FHD-CCD significantly reduces HDX of almost all BH3D residues to lower than 20% (Figure 7.12), confirming that the BH3D becomes less flexible and solvent-accessible upon binding M11, consistent with previous structural studies (Sinha *et al.*, 2008, Su *et al.*, 2014). Other regions besides the BH3D, including the BH3D-FHD linker, FHD, and CCD residues 215-244, also become less dynamic upon binding M11, with HDX decreasing to <10% (Figure 7.12). M11 binding does not appear to affect HDX of CCD residues 191-214, which follow the NES or residues 245-265 comprising the OH. Strikingly, M11 binding causes an HDX increase to >40% for the NES within the CCD (Figure 7.12), indicating that the NES becomes more dynamic.

While these results are very promising, unfortunately, our HDX-MS results are not completely reliable. Our HDX-MS system does not have a cooling system, hence the UPLC column connected to the MS is at room temperature. Therefore, it is possible that deuterium to

hydrogen back-exchange occurs during separation of the deuterated, digested peptides over the column. As this back-exchange effect is likely more significant for disordered regions of proteins, it may explain why the part of the BH3D expected to be the most flexible displays low HDX.

7.3.6. M11-binding alters secondary structure of BECN1 domains besides BH3D

We used CD to investigate changes in the secondary structure of the BH3D-FHD-CCD upon binding M11 (Figure 7.13, Table 7.3). The CD analysis indicates that, when not in complex with BECN1, M11 has 85, 14, and 42 residues in helical, strand and coil conformations respectively (Table 7.3). The crystal structure of the un-complexed M11 (PDB ID: 2ABO) shows that M11 has 84 and 58 residues in helical and coil conformation respectively, and no β -sheets; therefore, it is likely that the strand content estimated by CD does not represent stable β -sheets or β -strands, but rather, represents disordered regions with transient strand-like structure that are not stabilized by H-bonds characteristic of β -sheets. Therefore, for this and all other proteins for which structures and other biophysical analysis have established a lack of stable β -sheets, we include the β -strand content estimated by CD as part of the coil content. Given this assumption, the secondary structure content determined from the CD analyses of unbound M11 is consistent with that seen in the crystal structure.

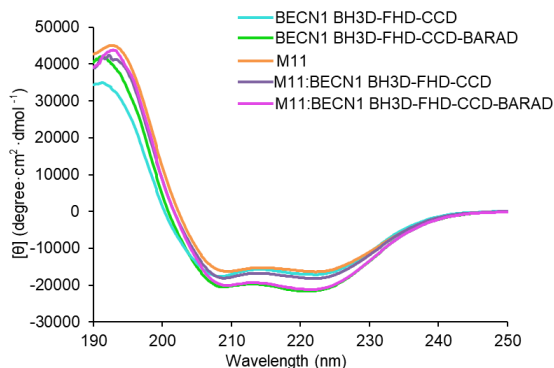


Figure 7.13. CD spectra of BECN1 fragments and their complexes with M11. Cyan: BH3D-FHD-CCD; Green: BH3D-FHD-CCD-BARAD^{AFM}; Orange: M11; Violet: M11:BECN1 BH3D-FHD-CCD; Magenta: M11:BECN1 BH3D-FHD-CCD-BARAD^{AFM}.

Table 7.3. Comparison of secondary structure content of M11, BECN1 fragments and their complexes from protein structure and CD.

Samples	Total # of residues	Experimental 3D Structures				CD		
		PDB ID	Helix	Strand	Coil	Helix	Strand	Coil
M11	142	2ABO	84	0	58	85	14	42
BH3D	26	NA	NA	NA	NA	1	1	24
FHD	31	5EFM	10	0	21	12	6	13
BH3D-FHD	67	NA	NA	NA	NA	Not done	Not done	Not done
CCD	97	5HHE	91	0	7	79	1	20
FHD-CCD*	128	FHD:5EFM CCD:5HHE	FHD:10 CCD:91 Total: 101	0	27	103	0	26
OH+BARAD**	209	4DDP	87	30	92	96	42	71
CCD-BARAD models**						183	15	84
1.OH packed with BARAD, NES flexible	281	CCD: 5HHE BARAD:4DDP	CCD:55 BARAD:87 Total:142	30	109	183	15	84
2. OH & NES flexible	281	CCD: 5HHE BARAD:4DDP	CCD:55 BARAD:70 Total:125	30	126	183	15	84
3. OH packed in CCD	281	CCD: 5HHE BARAD:4DDP	CCD:91 BARAD:70 Total:161	30	90	183	15	84
BH3D-FHD-CCD ^(Yue)	164	NA	NA	NA	NA	89	9	65
BH3D FHD-CCD*	164	NA	NA	NA	NA	106	6	57
BH3D-FHD-CCD-BARAD ^{AFM}	351	NA	NA	NA	NA	210	19	121
M11:BH3D	168	3DVU	M11:92 BH3D:18 Total:110	0	M11:50; BH3D:8 Total:58	Not done	Not done	Not done
M11: BH3D-FHD-CCD	306	NA	NA	NA	NA	180	20	106
M11: BH3D-FHD-CCD-BARAD ^{AFM}	493	NA	NA	NA	NA	307	27	163

*Protein concentrations used for CD = 50-300 μ M (Mei, Ramanathan, *et al.*, 2016).

**Protein concentrations used for CD = 3-20 μ M (Glover *et al.*, 2017).

CD for all remaining samples was recorded by me. Protein concentrations used = 5-10 μ M.

The CD analyses indicate that, when not in complex with M11, the BH3D-FHD-CCD has 89, 9, and 65 residues in helical, strand and coil conformations respectively (Table 7.3) at a concentration of 10 μ M. Interestingly however, at concentrations of 50-300 μ M, the same fragment was reported to have 106, 6, and 57 residues in helical, strand and coil conformations respectively (Mei, Ramanathan, *et al.*, 2016). Based on previously published structures of the FHD (PDB ID: 5EFM) and CCD (PDBs ID: 5HHE), CD analyses of the isolated BH3D

indicating it was completely disordered (Mei *et al.*, 2014), and assuming that the linkers between the three domains are completely disordered, we expected this fragment to have 101, 0, and 63 residues in helical, strand and coil conformations, consistent with that estimated by CD at high concentrations. However, at the lower concentrations of this three-domain construct, the helical content appears to be reduced by approximately three helical turns.

At a concentration of 10 μ M, the M11:BH3D-FHD-CCD complex has 180 and 20 + 106 residues in helical and strand + coil conformations respectively (Table 7.3). Relative to the sum of residues in helical and strand + coil conformation, estimated from CD analyses performed at similar concentrations of the un-complexed M11 and the BH3D-FHD-CCD, the complex has an additional \sim 6 residues in helical conformation and \sim 4 fewer in strand + coil conformation. This marginal increase in helicity is significantly less than expected based on the BH3D undergoing a disorder-to-helix transition. Indeed, the secondary structure content expected for this complex, calculated from crystal structures of the M11:BH3D complex (Loh *et al.*, 2005, Ku *et al.*, 2008, Sinha *et al.*, 2008), the FHD (Mei, Ramanathan, *et al.*, 2016) and the CCD (Mei, Su, *et al.*, 2016), as the sum of residues in helical and coil conformation is 211 and 85 respectively (Table 7.3). Thus, at low concentrations in solution, the M11:BH3D-FHD-CCD complex is significantly less helical and more disordered than expected. Thus, it would appear that a region of the FHD-CCD that is helical in the crystal structures of each domain becomes less helical in the complex. The HDX results reported above suggest that the NES is most likely to have reduced helicity.

We also tested the change in secondary structure content of the BH3D-FHD-CCD-BARAD^{AFM} upon binding M11 (Figure 7.13, Table 7.3). CD indicates that, when not in complex with M11, the BH3D-FHD-CCD-BARAD^{AFM} has \sim 210, 19, and 121 residues in helical, strand and coil conformations respectively. Based on previously published structures of isolated

domains, we expected this fragment to have 152, 30, 169 residues in helical, strand and coil conformations if the OH packs against BARAD and the NES is flexible; 135, 30, 186 residues in helical, strand and coil conformations are expected if the OH and NES are both flexible; and 171, 30, 150 residues in helical, strand and coil conformations are expected if the OH packs against the NES. Thus, a conformation wherein both the OH and NES are helical and part of the CCD agrees best with the CD data.

In comparison, CD indicates that the M11: BH3D-FHD-CCD-BARAD^{AFM} complex has 307, 27, and 163 residues in helical, strand and coil conformations (Table 7.3). Relative to the sum of residues in helical and strand + coil conformation, estimated from CD analyses performed at similar concentrations of the un-complexed M11 and the BH3D-FHD-CCD, the complex has an additional ~12 residues in helical conformation and ~6 fewer in strand + coil conformation. This corresponds to a substantial increase in helicity and decrease in disorder, consistent with the BH3D undergoing a disorder-to-helix transition.

However, the secondary structure content expected for this complex, calculated from crystal structures of the M11: BH3D complex (Loh *et al.*, 2005, Ku *et al.*, 2008, Sinha *et al.*, 2008), the FHD (Mei, Ramanathan, *et al.*, 2016), the CCD including the OH (Mei, Su, *et al.*, 2016) and the BARAD (Huang *et al.*, 2012) excluding the OH, as the sum of residues in helical, strand and coil conformation is 281, 30, and 182 respectively (Table 7.3). This corresponds to maximal helical content amongst the three conformations of the OH we have considered; as the complex would have 183, 15, 84 residues in helical, strand and coil conformations if the NES and OH are helical and packed with each other; have 262, 30, 203 residues in helical, strand and coil conformations if the OH packs against BARAD and the NES is flexible; and 245, 30, 218

residues in helical, strand and coil conformations are expected if the OH and NES are flexible. However, the helical content in each case is still substantially less than that observed by CD.

Further, a previous CD study showed that CCD-BARAD has 183 helical residues (Glover *et al.*, 2017), which is higher than expected based on previously published structure, and ~ 27 fewer than the helical residues in BH3D-FHD-CCD-BARAD^{AFM} measured by CD. Therefore, some region of BH3D or FHD may be more helical than expected in the BH3D-FHD-CCD-BARAD^{AFM} fragment; or the BARAD becomes more helical in the BECN1 homodimer; or both. With all the possibilities mentioned above, it is not possible to draw solid conclusions regarding what region outside BH3D of BH3D-FHD-CCD-BARAD^{AFM} bears conformational change upon binding M11.

Together, the CD results and HDX-MS results indicate that the unexpected lower helicity increase of BH3D-FHD-CCD upon binding to M11 may be attributed to the increased dynamics of the NES within CCD as shown by the HDX-MS results.

7.3.7. Thermostability of BECN1 increases marginally upon binding to M11

CD was also used to assess the impact of M11 binding on the thermal stability of BH3D-FHD-CCD. Since M11, the BH3D-FHD-CCD, and M11:BH3D-FHD-CCD complex are largely helical, we monitored the change of ellipticity during thermal unfolding at 222 nm, as at that wavelength the CD spectra of helices have a minima, while spectra for coils do not. The denaturation curve of M11 fit a single Boltzmann model, as expected for a single globular domain, with a single T_m of 71.7 °C calculated from this fit (Figure 7.14A). The thermal denaturation curve of M11:BH3D also fits a single Boltzmann model, with a single T_m of 73.8 °C (Figure 7.14B), which is slightly higher than that of the unbound M11, indicating binding BH3D marginally increases M11 thermostability.

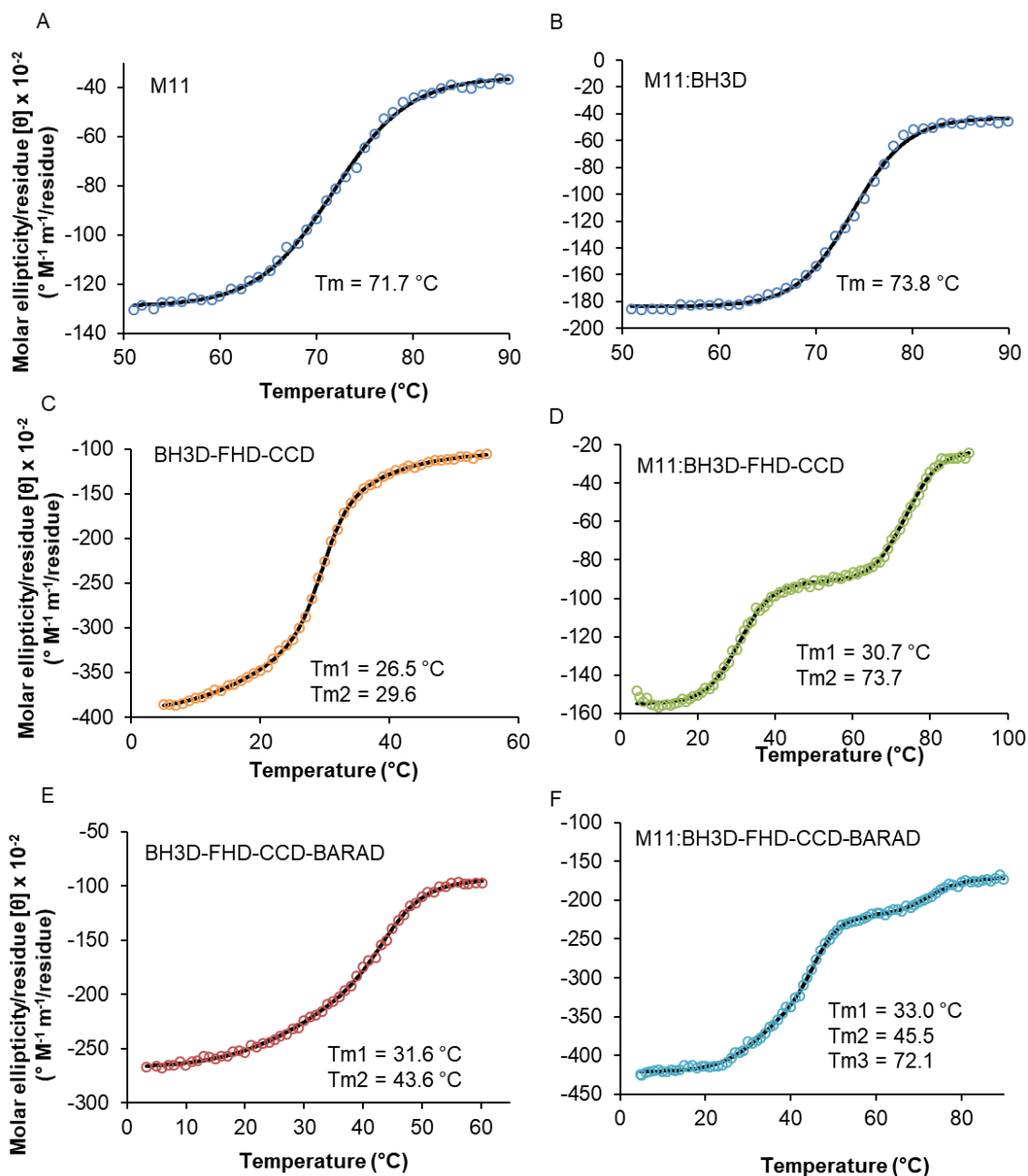


Figure 7.14. Melting curve of BECN1 fragments and their complexes with M11. Boltzmann fits to melting curves are shown in black. (A) M11. (B) M11:BECN1 BH3D. (C) BH3D-FHD-CCD complex. (D) M11:BH3D-FHD-CCD. (E) BH3D-FHD-CCD-BARAD^{AFM}. (F) M11:BH3D-FHD-CCD-BARAD^{AFM}.

The denaturation curve of BH3D-FHD-CCD fit to both single and double Boltzmann models with χ^2 of ~ 1 . The most likely model was identified by a comparison of the Akaike information criterion (AIC), an estimator of the relative quality of statistical models; and the Akaike weight, wherein a value of closer to 1 indicates a higher probability of the model being

true. The fit of the double Boltzmann model has a smaller AIC and Akaike weights closer to 1 relative to the single Boltzmann model (Table 7.4), indicating that the double Boltzmann model is more likely to be the true model. This fit indicates that the BH3D-FHD-CCD undergoes two distinct thermal unfolding transitions with T_m s of 26.5 °C and 29.6 °C (Figure 7.14C), suggesting BH3D-FHD-CCD consists of at least two independently folded domains, most likely the FHD and CCD.

Table 7.4. Comparison of single Boltzmann and double Boltzmann models fitting to the denaturing curve of BECN1 BH3D-FHD-CCD.

	T_m (°C)	X^2	RSS ¹	AIC ²	Akaike Weight ³
Single Boltzmann	28.9	0.9979	1272.6	175.4	6.66E-25
Double Boltzmann	26.5 and 29.6	0.9998	122.4	64.1	1

¹**RSS:** sum of squared residuals.

²**AIC:** the Akaike information criterion, is an estimator of the relative quality of statistical models.

³**Akaike weight:** the probability of model (i) is correct.

The denaturing curve of the M11: BH3D-FHD-CCD complex fit best to a double Boltzmann model, which indicated two well-separated transitions at 30.7 °C and 73.7 °C (Figure 7.14D). Since the BH3D becomes helical upon binding within a hydrophobic groove of M11, it is likely that the M11: BH3D behaves as a globular protein, as the 73.7 °C transition agrees well with the T_m of M11: BH3D (73.8 °C). The transition at 30.7 °C likely reflects a composite T_m for the BECN1 FHD-CCD, indicating that the FHD, and perhaps also the CCD, is marginally stabilized upon M11 binding.

We also used CD to assess the impact of M11 binding on the thermal stability of the BH3D-FHD-CCD-BARAD^{AFM}. The denaturation curve of the BH3D-FHD-CCD-BARAD^{AFM} was also fit to a double Boltzmann model (Figure 7.14E), with two denaturing transitions observed at 31.6 °C and 43.6 °C, indicating the BH3D-FHD-CCD-BARAD^{AFM} contains at least two independently folded regions. The T_m of 43.6 °C likely corresponds to the BARAD (Glover

et al., 2017), while the T_m of 31.6 °C likely corresponds to a composite T_m for the BH3D-FHD-CCD, based on the T_m of 29.6 °C for the BH3D-FHD-CCD fragment.

Three transitions were visible in the denaturing curve of M11: BH3D-FHD-CCD-BARAD. As the Origin software does not have a Boltzmann model for a denaturing curve with three transitions, we fit the denaturing curve to two separate Boltzmann models. The first part of the denaturation curve, corresponding to the temperature range of 4-59 °C, was fit to a double Boltzmann model, with two transitions observed at 33.0 °C, 45.5 °C; while the second part of the desaturation curve, corresponding to the temperature range of 60-90 °C, was fit to a single Boltzmann with a transition observed at 72.1 °C. The three transitions observed at 33.0 °C, 45.5 °C, and 72.1 °C (Figure 7.14F), likely correspond to the denaturation of the FHD-CCD, BARAD and M11: BH3D respectively. Each of these melting transitions is slightly higher than the T_{ms} of the corresponding domains in the un-complexed proteins, suggesting that complex formation increases the thermostability of both, the BH3D-FHD-CCD-BARAD^{AFM} and M11.

The increased thermal stability of BECN1 upon binding M11 agrees with the HDX-MS results showing that several other BECN1 regions besides the BH3D become less dynamic upon binding to M11, including the BH3D-FHD linker, FHD, and the middle region of CCD.

7.3.8. Binding to M11 increases homodimerization of the BECN1 BH3D-FHD-CCD

We used ITC to quantify and compare self-association of the BH3D-FHD-CCD in its free state and when in complex with M11. The BH3D-FHD-CCD homodimerizes with a K_d of ~16 μ M, while M11 binds to the BH3D-FHD-CCD with a ~80-fold higher affinity of ~0.2 μ M. The concentration of the M11: BH3D-FHD-CCD complex in the sample cell is 1.47 μ M, even after the first titration, which is about 7-times higher than the K_d of M11 binding to the BH3D-FHD-CCD, but ~ 10-times lower than the K_d of the BH3D-FHD-FHD-CCD homodimerization. This

indicates that in an ITC experiment wherein the M11:BH3D-FHD-CCD complex was titrated into buffer, the BH3D-FHD-CCD homodimer would preferentially dissociate, rather than the complex with M11.

To verify that M11 dissociation from BECN1 is negligible when titrating M11:BH3D-FHD-CCD complex into buffer within the sample cell, we performed a control experiment using the M11: BECN1 IDR complex. Available data indicates that the IDR does not homodimerize, yet binds to M11 with an affinity comparable to that of the BH3D-FHD-CCD (Table 7.2). Consistent with our expectations, we find no detectable dissociation of the M11:IDR complex upon titrating in the complex at concentrations ranging between 20 μM to 100 μM into buffer (Figure 7.15A,B,C), suggesting that an experiment using similar concentrations of M11:BH3D-FHD-CCD complex would allow us to quantify dissociation of the BH3D-FHD-CCD homodimer without impacting the complex with M11.

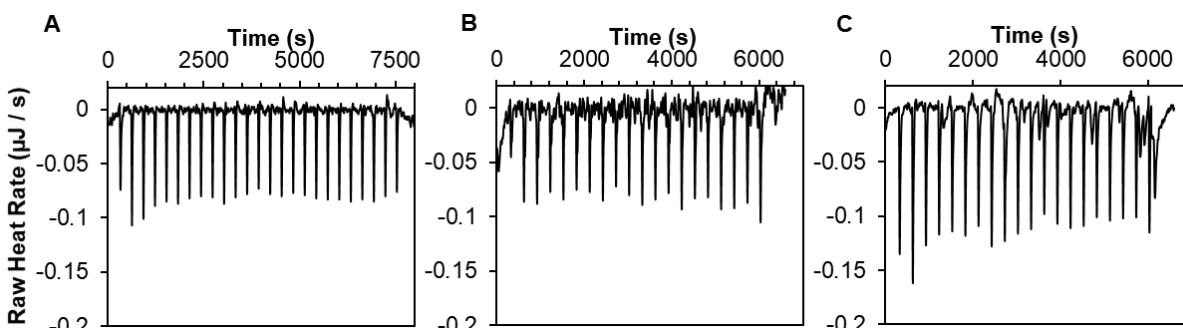


Figure 7.15. Representative ITC raw data of dilution of MBP-BECN1 1-135 into buffer. Concentrations of titrated MBP-BECN1 (1-135) are: (A) 100 μM . (B) 46 μM . (C) 20 μM .

Our ITC results indicate that when M11 is bound, the BH3D-FHD-CCD homodimerizes with a K_d of ~ 4 μM , which is ~ 4 -fold stronger than the homodimerization of the BH3D-FHD-CCD in the absence of M11 (Table 7.5, Figure 7.16A,B). This agrees with the marginal increase in thermostability of the M11:BH3D-FHD-CCD complex relative to the isolated BH3D-FHD-CCD. Further, the improved dimerization of BECN1 upon binding M11 is consistent with the decreased dynamics of the middle region of the CCD shown by HDX-MS.

Table 7.5. Thermodynamics of self-dissociation of BECN1 BH3D-FHD-CCD and its complex with M11.

BECN1 Fragments	Thermodynamic parameters			
	K_d (μM)	ΔH (kJ/mol)	ΔS (J/K·mol)	ΔG (kJ/mol)
BH3D-FHD-CCD	16.36 ± 0.75	99.96 ± 3.03	249.4 ± 10.04	26.86 ± 0.11
BH3D-FHD-CCD:M11	4.03 ± 0.28	114.11 ± 3.39	285.85 ± 11.10	30.28 ± 0.17

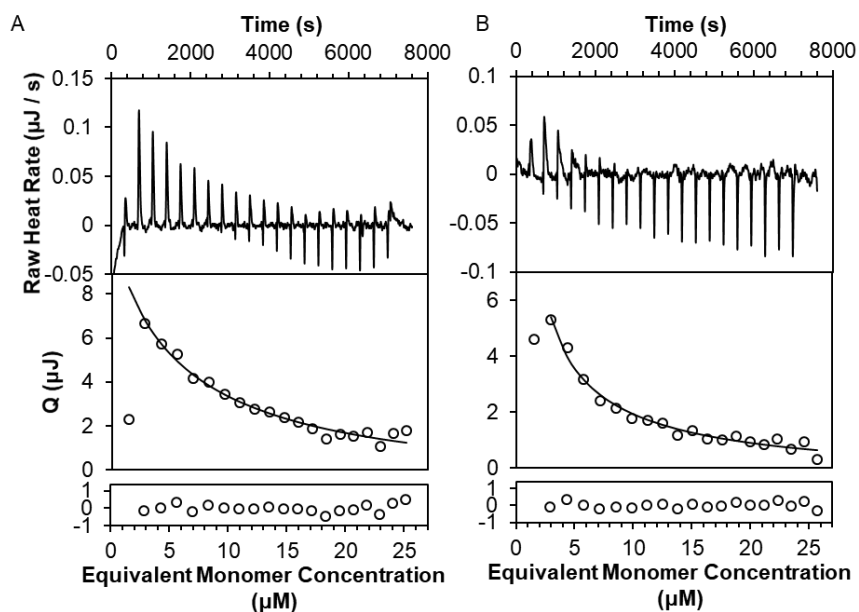


Figure 7.16. Determining K_d of homodimerization for: (A) unbound BECN1 BH3D-FHD-CCD and (B) M11:BH3D-FHD-CCD complex (B). Upper panel: raw ITC data generated by titration of the protein into buffer; lower panel: integrated heat and theoretical fit by dimer dissociation model from TA analysis.

7.3.9. The BECN1 BH3D-FHD-CCD has a flexible, elongated conformation

We used SEC-SAXS to characterize and compare the overall shape and flexibility of BH3D-FHD-CCD and its complex with M11. The variation of $I(0)$ across the BH3D-FHD-CCD SEC-SAXS peak (Figure 7.17A) is consistent with the variation in SEC eluate concentration. The R_g determined from Guinier analyses of the intensity-normalized, buffer-subtracted data ranges between 45 to 55 Å across the scattering peak (Figure 7.17A), indicating that the BH3D-FHD-CCD is flexible. The linear Guinier plot at $qR_g < 1.3$ indicates that the sample does not aggregate (Figure 7.17B). The $P(r)$ curve indicates that BH3D-FHD-CCD is an elongated, multi-domain protein with a D_{max} of 199 Å and an average R_g of 58 Å, similar to that estimated from

the Guinier analyses (Figure 7.17C, Table 7.6). The Kratky plot suggests that BH3D-FHD-CCD is partially disordered (Figure 7.17D). The normalized spatial discrepancy of 10 generated *ab initio* molecular models is 0.64 ± 0.04 . Further, the molecular mass estimated from the volume of correlation, V_c (Rambo & Tainer, 2013), is 32.9 kDa (Table 7.6), which is significantly larger than the molecular mass of 19.6 kDa expected for a BH3D-FHD-CCD monomer, but a little smaller than the theoretical molecular mass expected for a dimer.

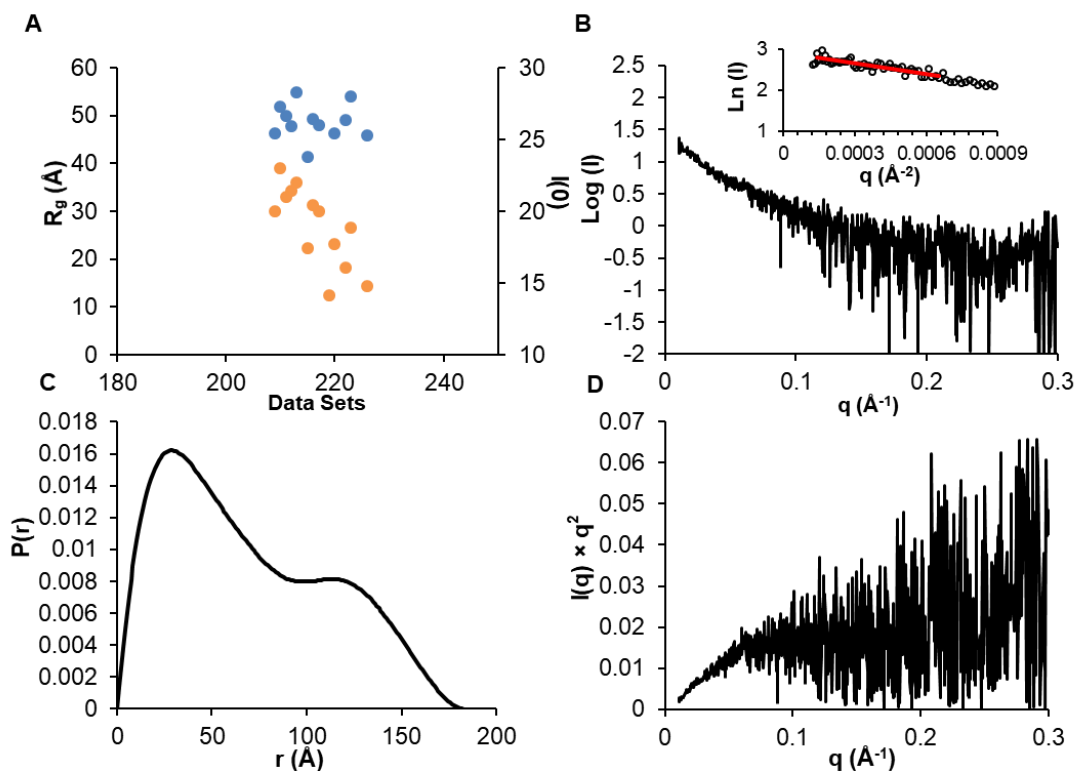


Figure 7.17. SAXS analysis of BECN1 BH3D-FHD-CCD. (A) $I(0)$ (orange) and R_g (blue) as a function of time for the SEC-SAXS run. (B) plot of $\log I(q)$ versus q with inset Guinier plot. (C) $P(r)$ distribution. (D) Kratky plot.

Table 7.6. Structural parameters from data analysis and EOM modeling.

Guinier analysis	BH3D-FHD-CCD	M11:BH3D-FHD-CCD	BH3D-FHD-CCD-BARAD ^{AFM}			M11:BH3D-FHD-CCD-BARAD ^{AFM}			M11	
I(0)	18.7 ± 0.5	51.4 ± 0.1	83.0 ± 1.0			47.4 ± 0.1			92.4 ± 0.2	
q _{min} (Å ⁻¹)	0.0001	0.0001	0.0001			0.0001			0.0001	
qR _g max	1.3	1.3	1.3			1.3			1.3	
R ²	0.76	0.92	0.96			0.83			0.99	
P(r)										
I(0) (cm ⁻¹)	19.8 ± 0.6	53.6 ± 0.6	86.1 ± 0.8			42.3 ± 0.1			92.4 ± 0.2	
R _g (Å)	58 ± 2	75 ± 1	73 ± 1			80 ± 0			16 ± 0	
D _{max} (Å)	199	248	235			288			50	
q range (Å ⁻¹)	0.0118-0.1596	0.0112-0.1191	0.0067-0.1209			0.0052-0.1095			0.0274-0.3896	
χ ² (total estimate from GNOM)	0.996	0.965	0.990			0.940			0.971	
MW from V _c (kDa)	32.9	70.2	61.8			77.3			15.5	
EOM		Pool 1	Pool 2	Pool 1	Pool 2	Pool 3	Pool 1	Pool 2	Pool 3	Did not fit the model
χ ²	0.96	1.6	1.5	1.2	1.6	1.2	1.2	-	1.7	
R _{flex} (selected ensemble, %)	64.7	78.8	79.6	69.9	68.7	66.8	80.0	-	75.1	
R _{flex} (initial pool %)	88.3	88.6	86.6	83.3	81.0	86.3	85.1	-	86.0	
R _{sigma}	0.37	0.86	1.00	0.5	1.47	0.48	0.88	-	0.73	

In order to account for the conformational flexibility of the BH3D-FHD-CCD, EOM was used to generate an initial pool of conformers, based on available structures of the FHD residues 157-171 (PDB ID:5EFM) and the CCD (PDB ID:5HHE), with the remaining residues modelled as flexible. Conformers for which the theoretical scattering curves best fit the experimental SAXS data, with an overall χ^2 of 0.96 (Figure 7.18A), were included in the “selected ensemble”. EOM analyses show that the R_g and D_{max} distribution for the selected ensemble of conformers exhibits a single peak that is narrower than that of the initial pool of conformers (Figure 7.18B,C), indicating that the BH3D-FHD-CCD has restrained, rather than random flexibility. Indeed, the selected ensemble of conformers has a R_{flex} of 64.7%, compared to 88.3% for the

initial pool of conformers (Table 7.6), suggesting that the conformers of the selected ensemble are less flexible than those in the entire pool generated by EOM, as R_{flex} values of 0% and 100% denote completely rigid or flexible conformations respectively. Additionally, a R_{sigma} of 0.37 (Table 7.6) also suggests the selected ensemble of conformers is much less flexible than the pool conformers, as a $R_{sigma} < 1$ indicates the conformers of the selected ensemble are less flexible than those in the entire pool, while a $R_{sigma} = 1$ indicates the selected ensemble of conformers is as flexible as those of the entire pool. Thus, the BH3D-FHD-CCD adopts more restrained and homogenous conformations than models based only on chemical constraints.

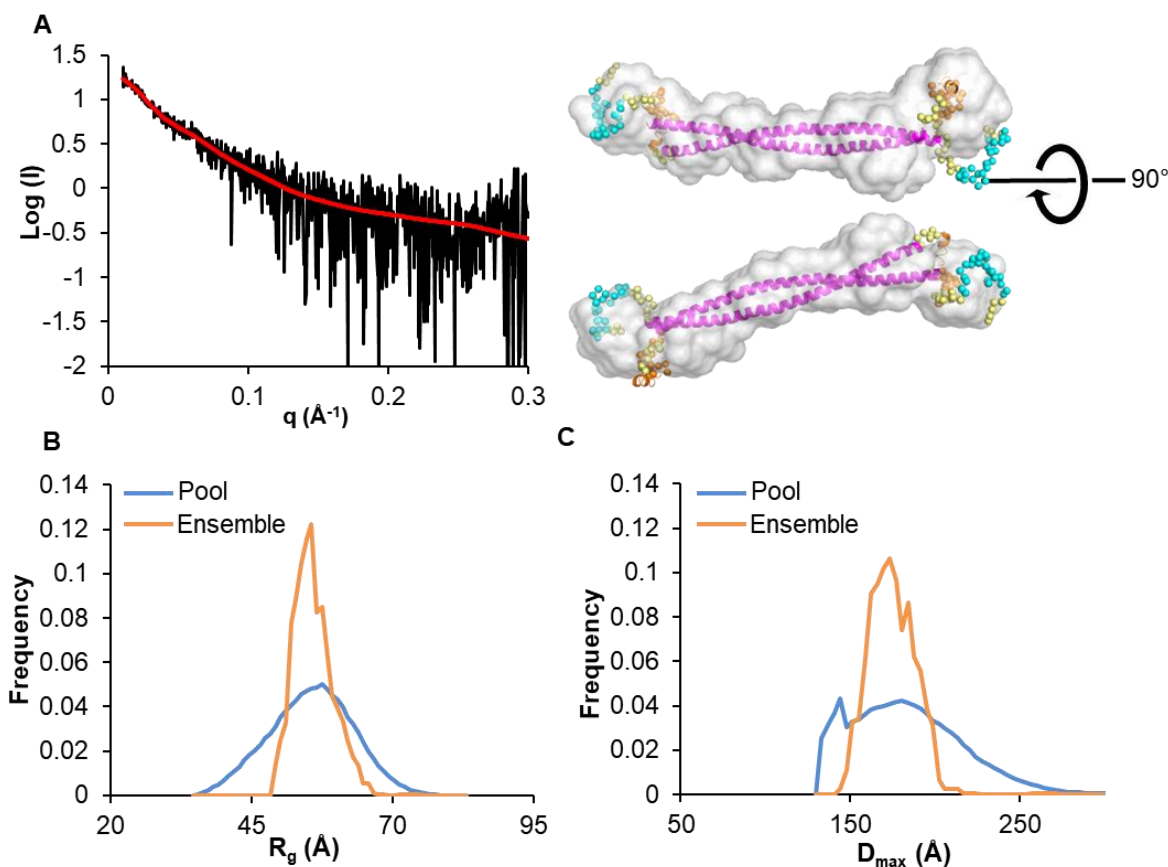


Figure 7.18. EOM fits for BECN1 BH3D-FHD-CCD. (A) Left panel: Experimental SAXS data fit to the theoretical scattering curve calculated from the best fit ensemble of conformers of BH3D-FHD-CCD; Right panel: representative model from the ensemble (Magenta: CCD; orange: FHD; cyan: BH3D; yellow: linker between domains. Structured regions are shown as cartoon; flexible regions as spheres) superimposed into the filtered SAXS envelope (grey surface). (B) R_g distribution and (C) D_{max} distribution of the pool (blue) and selected ensemble (orange) conformers.

7.3.10. The M11:BECN1 BH3D-FHD-CCD transitions between two distinct conformations with a predominant elongated conformation

The variation of $I(0)$ across the SEC-SAX elution peak of the M11:BH3D-FHD-CCD complex (Figure 7.19A) is also consistent with the variation in SEC eluate concentration. The R_g determined from Guinier analyses of the intensity-normalized, buffer-subtracted data ranges between 50 to 75 Å over the scattering peak (Figure 7.19A), indicating that the M11:BH3D-FHD-CCD complex is also flexible. The linear Guinier plot at $qR_g < 1.3$ indicates that the sample does not aggregate (Figure 7.19B). The $P(r)$ curve indicates that M11:BH3D-FHD-CCD is also an elongated, multi-domain protein, with a D_{max} of 248 Å and a R_g of 58 Å which lies within the range of R_g estimated from the Guinier analyses (Figure 7.19C, Table 7.6), which is larger than that of BH3D-FHD-CCD. In contrast to the un-complexed BH3D-FHD-CCD, the Kratky plot suggests that the M11:BH3D-FHD-CCD complex is mostly ordered (Figure 7.19D). The normalized spatial discrepancy of the 10 generated *ab initio* molecular models is 0.63 ± 0.03 . In addition, the molecular mass estimated from the V_c (Rambo & Tainer, 2013) is 70.2 kDa (Table 7.6), similar to the theoretical molecular mass of 72.2 kDa expected for a dimer of the M11:BH3D-FHD-CCD complex.

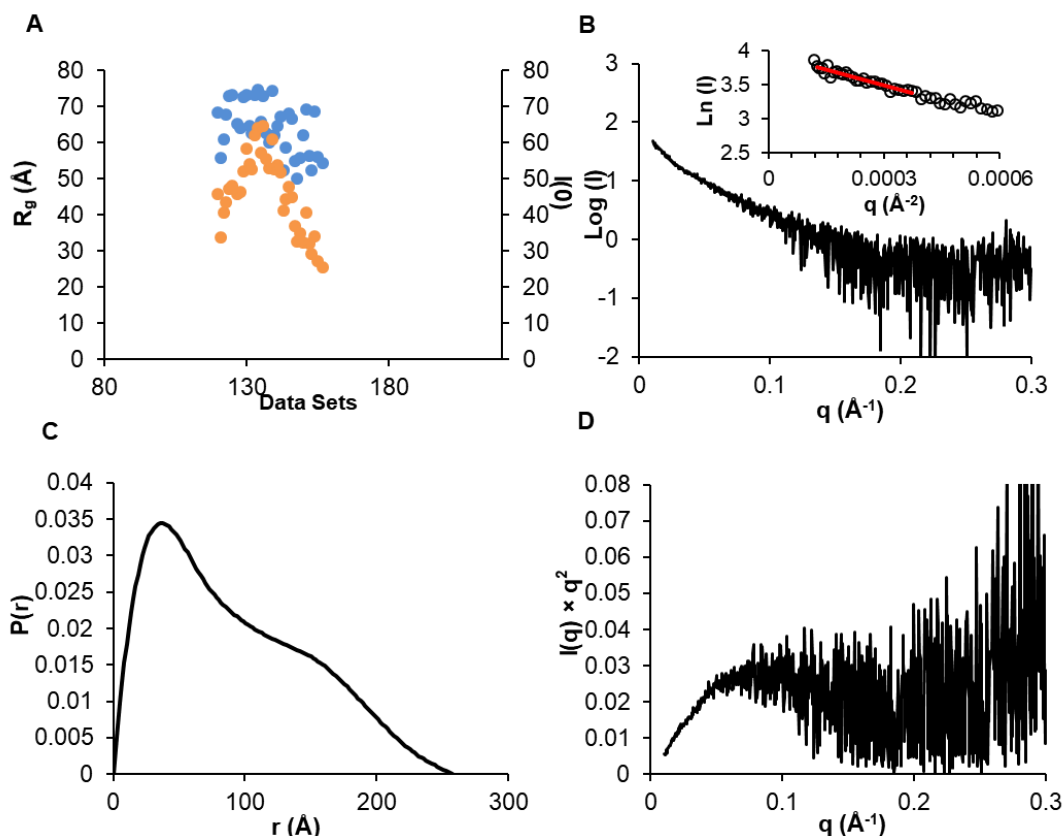


Figure 7.19. SAXS analysis of M11: BH3D-FHD-CCD. (A) $I(0)$ (orange) and R_g (blue) as a function of time for the SEC-SAXS run. (B) plot of $\log I(q)$ versus q with inset Guinier plot. (C) $P(r)$ distribution. (D) Kratky plot.

We also used EOM to generate pools of conformers for the M11: BH3D-FHD-CCD complex. Since the HDX-MS results for the M11: BH3D-FHD-CCD suggest that the NES within the CCD may be flexible, two separate pools of conformers were generated. Both pools were based on available structures of the M11: BH3D complex (PDB ID: 3DVU) and FHD residues 157-171 (PDB ID: 5EFM), but had different structural information input for the CCD; with pool 1 being based on the crystal structure of the CCD (PDB ID: 5HHE) wherein CCD residues 175-265 form a coiled-coil; while pool 2 was based on residues 192-247 modelled as in the CCD structure, but the NES and OH being modelled as flexible.

The ensemble selected from pool 1, for which the theoretical scattering curves best fit the experimental SAXS data had an overall χ^2 of 1.6 (Figure 7.20A). Both R_g and D_{\max} distributions

of this selected ensemble have two distinct peaks corresponding to a R_g of ~ 47 and 70 Å, and a D_{\max} of ~ 145 and 202 Å respectively. The larger R_g and D_{\max} peaks are dominant (Figure 7.20B,C) indicating that the complex fluctuates between two types of conformers with the extended conformer being predominant. The conformers in the selected ensemble of pool 1 have a R_{flex} of 79%, compared to 89% for those from the entire pool 1 (Table 7.6), and have a R_{sigma} of 0.86 (Table 7.6), indicating that conformers in the selected ensemble are slightly less flexible than those in the entire pool 1.

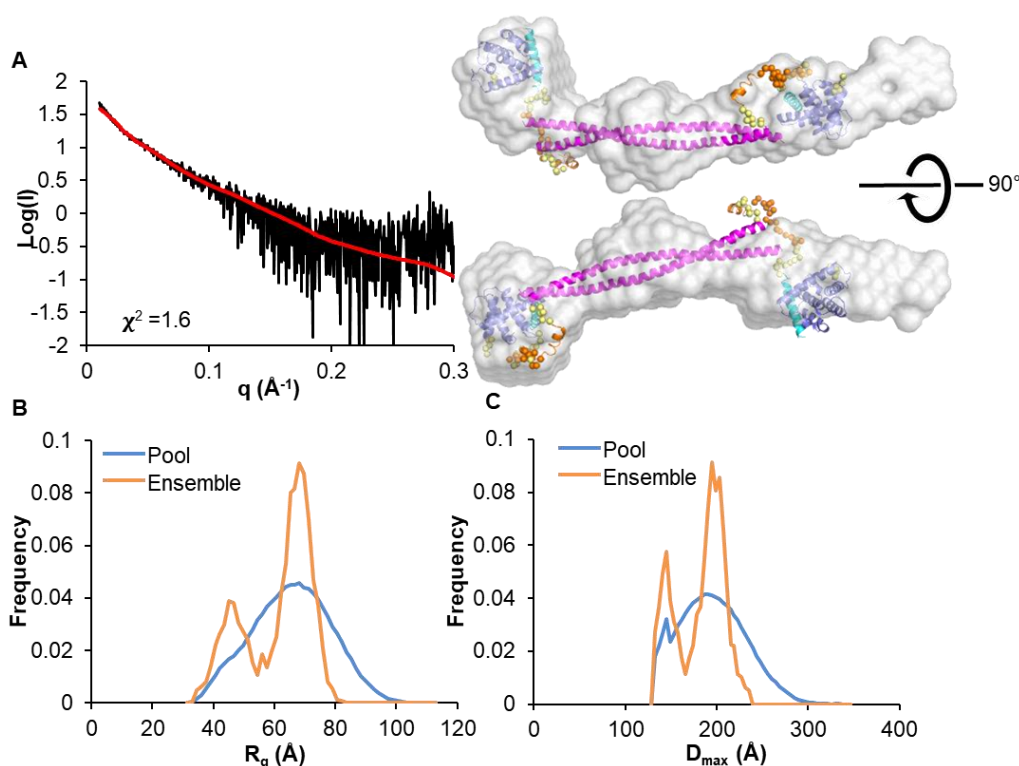


Figure 7.20. EOM fits (1) for M11:BH3D-FHD-CCD complex. (A) Left panel: Experimental SAXS data fit to the theoretical scattering curve calculated from the best fit ensemble of conformers of M11:BH3D-FHD-CCD; Right panel: representative model from the ensemble (M11 is shown in violet; the other color code is the same as that in Figure 6. Structural characters are displayed the same way as in Figure 7) superimposed into the filtered SAXS envelope (grey surface). (B) R_g distribution and (C) D_{\max} distribution of the pool (blue) and selected ensemble (orange) conformers.

The ensemble selected from pool 2, for which the theoretical scattering curves best fit the experimental SAXS data, had an overall χ^2 of 1.5 (Figure 7.21A), which is marginally better than

the ensemble selected from pool 1. Both R_g and D_{max} distributions of this selected ensemble of conformers also have two distinct peaks corresponding to a R_g of ~ 40 and 71 \AA and a D_{max} of ~ 130 and 207 \AA respectively (Figure 7.21B,C), which indicates that the complex fluctuates between two different types of conformations. The conformers in the selected ensemble of pool 2 have a R_{flex} of 80%, compared to 87% to those of the entire pool 2, indicating that the selected ensemble of conformers is only marginally less flexible than those in the entire pool 2, while the R_{sigma} of pool 1 (Table 7.6) suggests that conformers in the selected ensemble are as flexible as those in the entire pool 2.

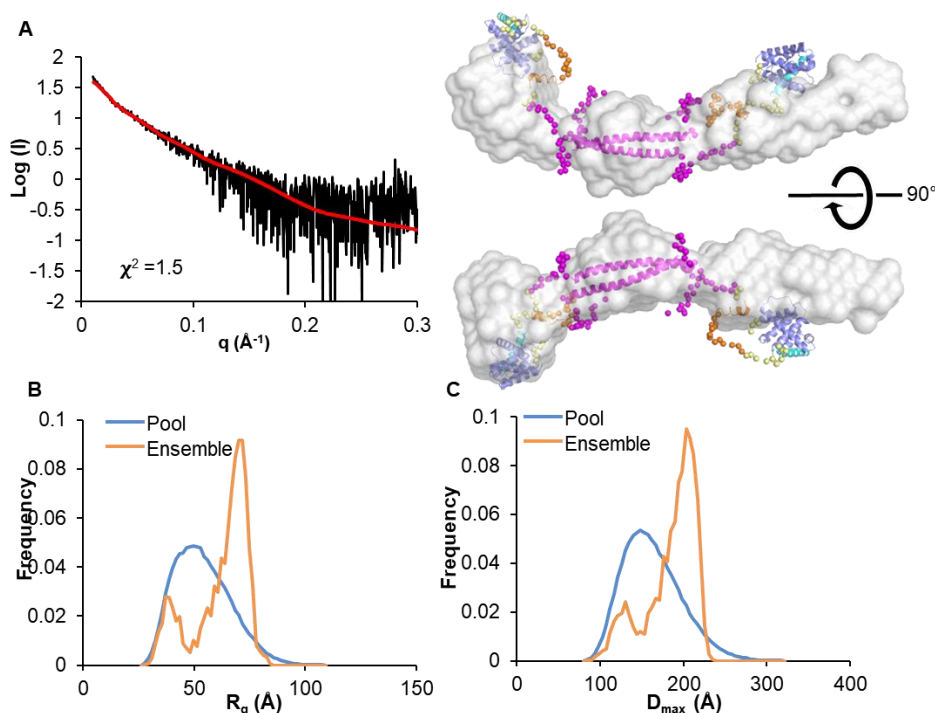


Figure 7.21. EOM fits (2) for M11:BH3D-FHD-CCD complex. (A) Left panel: Experimental SAXS data fit to the theoretical scattering curve calculated from the best fit ensemble of conformers of M11:BH3D-FHD-CCD; Right panel: representative model from the ensemble (the other color code is the same as that in Figure 6. Structural characters are displayed the same way as in Figure 9) superimposed into the filtered SAXS envelope (grey surface). (B) R_g distribution and (C) D_{max} distribution of the pool (blue) and selected ensemble (orange) conformers.

The comparison of SAXS analyses of BH3D-FHD-CCD and its complex with M11 show that the R_g and D_{max} of M11:BH3D-FHD-CCD is ~ 1.3 -times larger than that of the unbound

BH3D-FHD-CCD. The BH3D-FHD-CCD becomes more ordered upon binding M11. In addition, the EOM modeling shows that both the R_g and D_{max} distribution of selected ensemble of conformers for unbound BH3D-FHD-CCD has a single peak that is narrower than that of the entire EOM pool, indicating the flexibility of BH3D-FHD-CCD is restrained; in contrast, for the selected ensemble of conformers for M11:BH3D-FHD-CCD complex the R_g and D_{max} has a bimodal distribution, with an elongated conformation being predominant.

7.3.11. The BECN1 BH3D-FHD-CCD-BARAD^{AFM} adopts a flexible, elongated conformation, with the OH either flexible or preferentially packed against the CCD

We also used SEC-SAXS to characterize the overall shape and flexibility of the BH3D-FHD-CCD-BARAD^{AFM} and its complex with M11. The variation of $I(0)$ across the BH3D-FHD-CCD-BARAD^{AFM} SEC-SAXS peak (Figure 7.22A) is consistent with the variation in eluate concentration. The R_g determined from Guinier analyses of the intensity-normalized, buffer-subtracted data ranges between 60 to 70 Å across the scattering peak (Figure 7.22A), indicating that the BH3D-FHD-CCD-BARAD^{AFM} is flexible. The linear Guinier plot at $qR_g < 1.3$ indicates that the sample does not aggregate (Figure 7.22B). The $P(r)$ curve indicates that BH3D-FHD-CCD-BARAD^{AFM} is an elongated, multi-domain protein with a D_{max} of 235 Å and an average R_g of 72 Å, similar to that estimated from the Guinier plot (Figure 7.22C, Table 7.6). The Kratky plot suggests that BH3D-FHD-CCD-BARAD^{AFM} is partially disordered (Figure 7.22D). The normalized spatial discrepancy of 10 generated *ab initio* molecular models is 0.60 ± 0.02 . Further, the molecular mass estimated from V_c is 58.0 kDa (Table 7.6), which is significantly smaller than the theoretical molecular mass of 81.2 kDa expected for a BH3D-FHD-CCD-BARAD^{AFM} dimer. Molecular masses of the CCD and the CCD-BARAD calculated from V_c

(Rambo & Tainer, 2013) were also smaller than expected, perhaps suggesting that this may be characteristic of well-folded, elongated molecules.

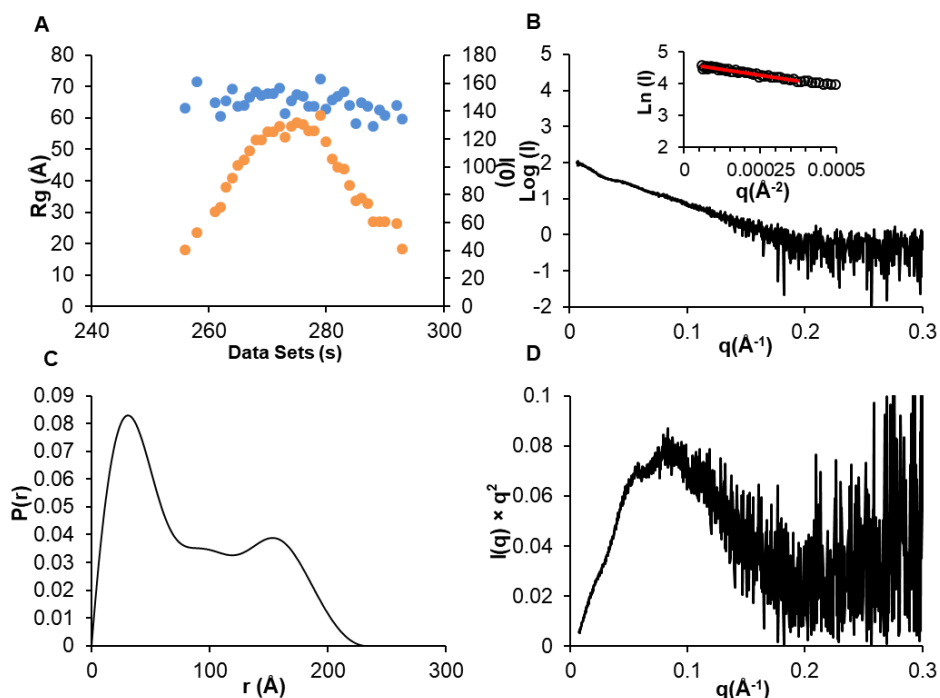


Figure 7.22. SAXS analysis of BECN1 BH3D-FHD-CCD-BARAD^{AFM}. (A) $I(0)$ (orange) and R_g (blue) as a function of time for the SEC-SAXS run. (B) plot of $\log I(q)$ versus q with inset Guinier plot. (C) $P(r)$ distribution. (D) Kratky plot.

We then used EOM to generate pools of conformers for the BH3D-FHD-CCD-BARAD^{AFM}. Since previous studies (Glover *et al.*, 2017) have shown that the OH transitions between CCD and BARAD in the BECN1 CCD-BARAD fragment, three separate pools of conformers were generated. All three pools were based on available structure of FHD residues 157-171 (PDB ID:5EFM), but had different structural information input for the CCD and BARAD; with pool 1 being based on the crystal structure of the CCD (PDB ID: 5HHE) wherein CCD residues 175-265 form a coiled-coil and the structure of BARAD (PDB ID: 4DDP) excluding the OH; pool 2 was based on residues 192-247 modelled as coiled-coil; and residues 248-450 as in the BARAD structure (PDB ID: 4DDP) including the OH, and the NES modelled as flexible; pool 3 was based on residues 192-247 modelled as in the CCD structure, residues

266-450 modelled as per the BARAD structure excluding the OH, and both the NES and OH modelled as flexible.

The selected ensemble of conformers from pool 1 for which the theoretical scattering curves best fit the experimental SAXS data had an overall χ^2 of 1.2 (Figure 7.23A). EOM analyses show that the R_g and D_{max} distribution for conformers in the selected ensemble exhibits a single peak that is narrower than that of the entire pool 1 (Figure 7.23B,C), indicating that the BH3D-FHD-CCD-BARAD^{AFM} has restrained, rather than random flexibility. The ensemble of conformers selected from pool 1 has a R_{flex} of 69.9%, compared to 83.3% for those from the entire pool 1 (Table 7.6), and has a R_{sigma} of 0.86 (Table 7.6), indicating that conformers in the selected ensemble are slightly less flexible than the conformers in the entire pool 1.

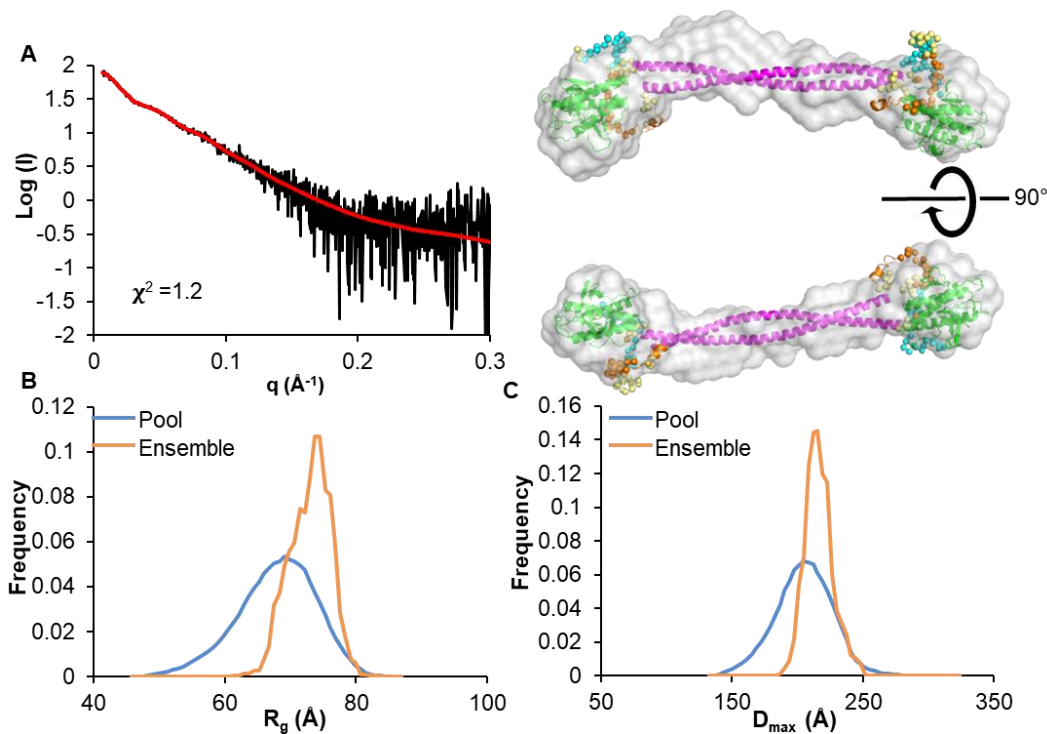


Figure 7.23. EOM fits (1) for BECN1 BH3D-FHD-CCD-BARAD^{AFM}. (A) Left panel: Experimental SAXS data fit to the theoretical scattering curve calculated from the best fit ensemble of conformers of the BH3D-FHD-CCD-BARAD^{AFM}; Right panel: representative model from the ensemble (Green: BARAD; Magenta: CCD; orange: FHD; cyan: BH3D; yellow: linker between domains. Structured regions are shown as cartoon; flexible regions as spheres) superimposed into the filtered SAXS envelope (grey surface). (B) R_g distribution and (C) D_{max} distribution of the pool (blue) and selected ensemble (orange) conformers.

The selected ensemble of conformers from pool 2 for which the theoretical scattering curves best fit the experimental SAXS data had an overall χ^2 of 1.6 (Figure 7.24A), which is worse than the ensemble selected from pool 1. EOM analyses show that the R_g and D_{max} distribution for the selected ensemble of conformers exhibits a single peak that is narrower than that of the entire pool 2 of conformers (Figure 7.24B,C), indicating that BH3D-FHD-CCD-BARAD^{AFM} has restrained, rather than random flexibility. The ensemble of conformers selected from pool 2 has a R_{flex} of 68.7%, compared to 81.0% for those of the entire pool 2 (Table 7.6), indicating that the selected ensemble is less flexible than the conformers in the entire pool 2. However, a R_{sigma} of 1.47 (Table 7.6) suggests that conformers in the selected ensemble are more flexible than those in the entire pool 2, which contradicts with the results of R_g , D_{max} distribution, and R_{flex} . These contradictory results may indicate the assumption that the OH packs with the BARAD is untrue.

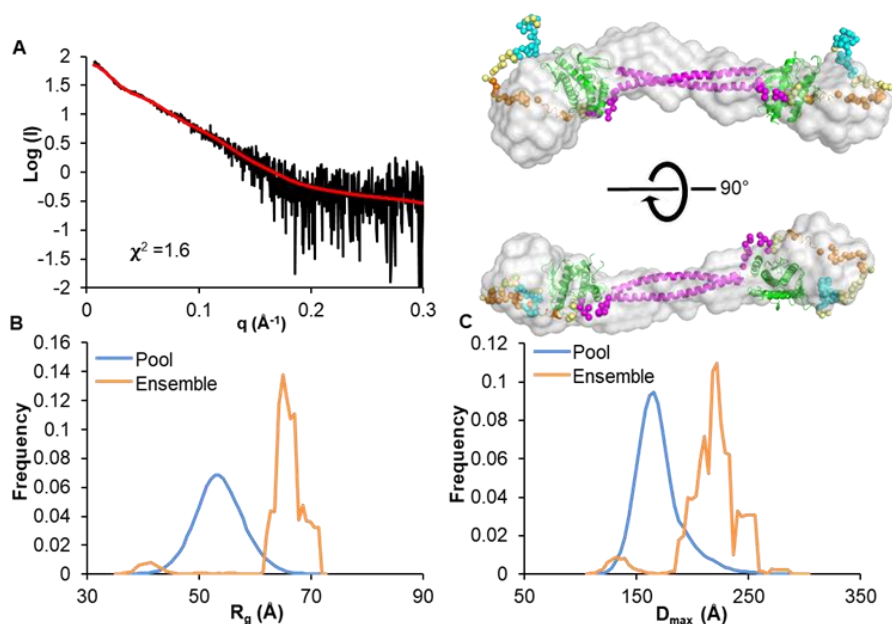


Figure 7.24. EOM fits (2) for BECN1 BH3D-FHD-CCD-BARAD^{AFM}. (A) Left panel: Experimental SAXS data fit to the theoretical scattering curve calculated from the best fit ensemble of conformers of the BH3D-FHD-CCD-BARAD^{AFM}; Right panel: representative model from the ensemble (color code and structure display are the same as that in Figure 12) superimposed into the filtered SAXS envelope (grey surface). (B) R_g distribution and (C) D_{max} distribution of the pool (blue) and selected ensemble (orange) conformers.

The selected ensemble of conformers from pool 3 for which the theoretical scattering curves best fit the experimental SAXS data had an overall χ^2 of 1.2 (Figure 7.25A), which is as good as the ensemble selected from pool 1. EOM analyses show that the R_g and D_{max} distribution for the conformers in the selected ensemble exhibits a single peak that is narrower than that of the entire pool 3 (Figure 7.25B,C), indicating that BH3D-FHD-CCD-BARAD^{AFM} has restrained, rather than random flexibility. The ensemble of conformers selected from pool 3 has a R_{flex} of 66.8%, compared to 86.3% for those from the entire pool 3 (Table 7.6), and a R_{sigma} of 0.48 (Table 7.6), indicating that the selected ensemble is less flexible than those in the entire pool 3.

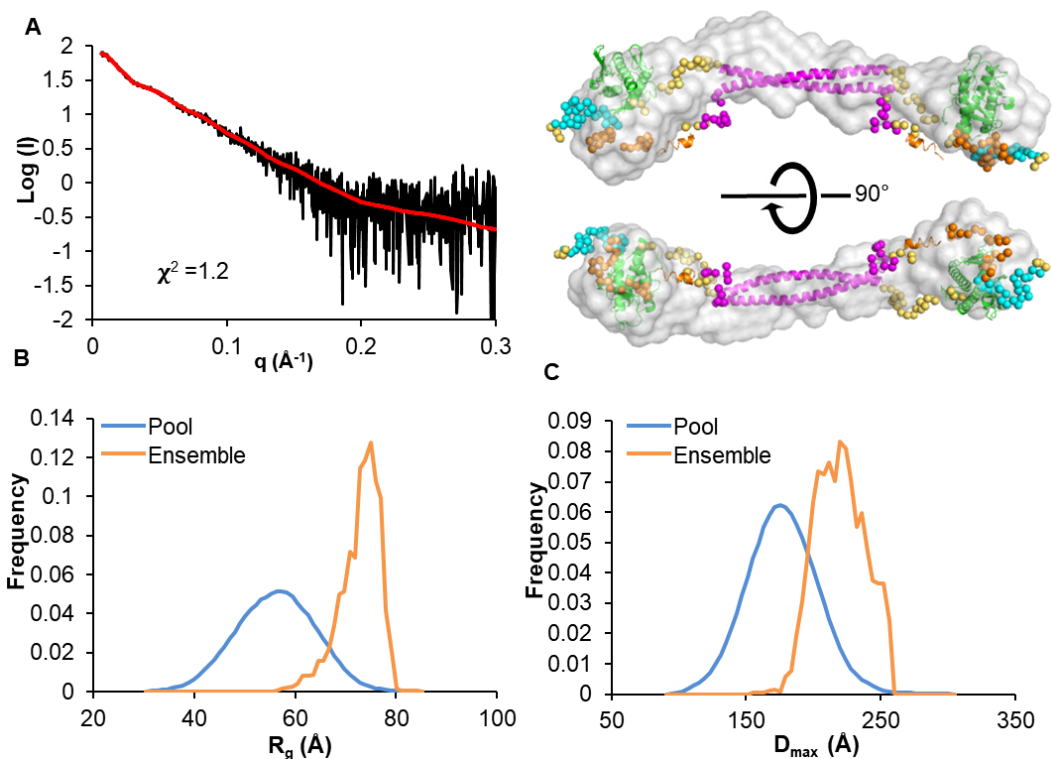


Figure 7.25. EOM fits (3) for BECN1 BH3D-FHD-CCD-BARAD^{AFM}. (A) Left panel: Experimental SAXS data fit to the theoretical scattering curve calculated from the best fit ensemble of conformers of the BH3D-FHD-CCD-BARAD^{AFM}; Right panel: representative model from the ensemble (color code and structure display are the same as that in Figure 12) superimposed into the filtered SAXS envelope (grey surface). (B) R_g distribution and (C) D_{max} distribution of the pool (blue) and selected ensemble (orange) conformers.

7.3.12. The M11:BECN1 BH3D-FHD-CCD-BARAD^{AFM} complex adopts a flexible, elongated conformation, with the OH preferably packing in the CCD or being flexible

The variation of $I(0)$ across the SEC-SAX elution peak of the M11: BH3D-FHD-CCD-BARAD^{AFM} complex (Figure 7.26A) is consistent with the variation in SEC eluate concentration. The R_g determined from intensity-normalized, buffer-subtracted data decreases over elution time, from a range of 70 – 90 Å to a range of 50 – 70 Å (Figure 7.26A), indicating that M11: BH3D-FHD-CCD-BARAD^{AFM} is also flexible. The linear Guinier plot at $qR_g < 1.3$ indicates that the sample does not aggregate (Figure 7.26B). The $P(r)$ curve indicates that M11: BH3D-FHD-CCD-BARAD^{AFM} is an elongated, multi-domain protein, with a D_{max} of 288 Å and a R_g of 82 Å which lies within the range of R_g estimated from the Guinier analyses (Figure 7.26C, Table 7.6). Notably, the Kratky plot suggests that the M11: BH3D-FHD-CCD-BARAD^{AFM} complex is well-folded (Figure 7.26D). The normalized spatial discrepancy of the 10 *ab initio* molecular models generated is 0.62 ± 0.03 . In addition, the molecular mass estimated from the V_c is 73.3 kDa (Table 7.6), which is smaller than the theoretical molecular mass of 114.4 kDa expected for a dimer of the M11: BH3D-FHD-CCD-BARAD^{AFM} complex.

EOM was used to generate pools of conformers for the M11: BH3D-FHD-CCD-BARAD^{AFM} complex. Three separate pools of conformers were generated, analogous to pools generated for the BH3D-FHD-CCD-BARAD^{AFM}. These three pools were based on available structures of the M11: BH3D complex (PDB ID: 3DVU) and FHD residues 157-171 (PDB ID: 5EFM), but had different structural information input for the CCD and BARAD as described for three pools of conformers generated for BH3D-FHD-CCD-BARAD^{AFM}.

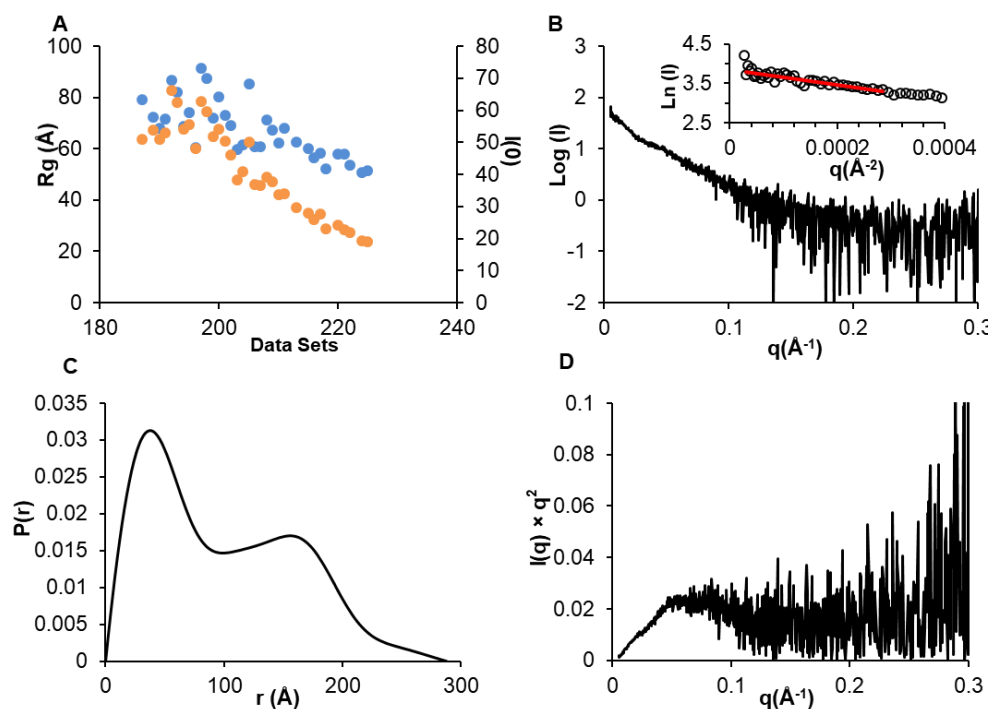


Figure 7.26. SAXS analysis of M11: BH3D-FHD-CCD-BARAD^{AFM}. (A) $I(0)$ (orange) and R_g (blue) as a function of time for the SEC-SAXS run. (B) plot of $\log I(q)$ versus q with inset Guinier plot. (C) $P(r)$ distribution. (D) Kratky plot.

The selected ensemble of conformers from pool 1 for which the theoretical scattering curves best fit the experimental SAXS data had an overall χ^2 of 1.2 (Figure 7.27A). EOM analyses show that the R_g and D_{\max} distribution of the conformers in the selected ensemble exhibits a single peak that is marginally narrower than that of the entire pool 1 (Figure 7.27B,C), suggesting that the selected ensemble is slightly less flexible than the entire pool 1. The ensemble selected from pool 1 has a R_{flex} of 80.0%, compared to 85.1% for those from the entire pool 1 (Table 7.6) and has a R_{sigma} of 0.88 (Table 7.6), which also indicates that the selected ensemble is slightly less flexible than the conformer in the entire pool 1.

Our attempts to use EOM to generate pool 2 failed to output conformers even after computer runtimes of several weeks. Therefore, we are unable to report results for pool 2.

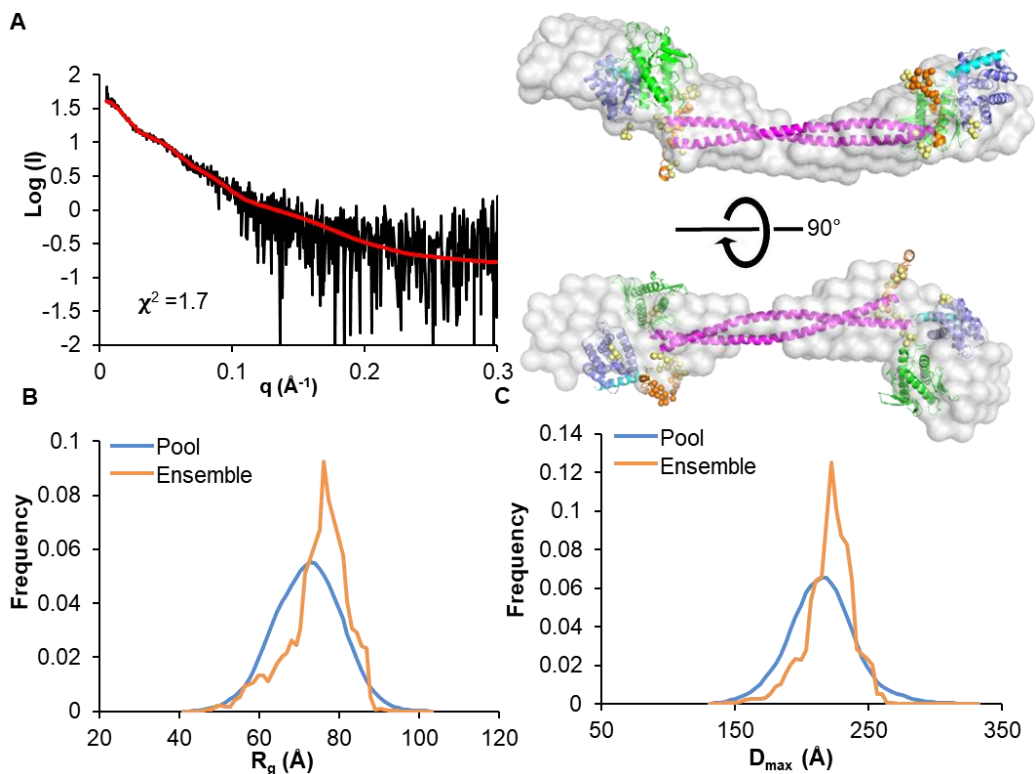


Figure 7.27. EOM fits (1) for M11: BH3D-FHD-CCD-BARAD^{AFM} complex. (A) Left panel: Experimental SAXS data fit to the theoretical scattering curve calculated from the best fit ensemble of conformers of M11: BH3D-FHD-CCD-BARAD^{AFM}; Right panel: representative model from the ensemble (violet: M11; color code and structure display are the same as that in Figure 12) superimposed into the filtered SAXS envelope (grey surface). (B) R_g distribution and (C) D_{max} distribution of the pool (blue) and selected ensemble (orange) conformers.

The selected ensemble of conformers from pool 3 for which the theoretical scattering curves best fit the experimental SAXS data had an overall χ^2 of 1.7 (Figure 7.28A), which is worse than the ensemble selected from pool 1. EOM analyses show that the R_g and D_{max} distribution for the conformers in the selected ensemble exhibits a single peak that is narrower than that of the entire pool 1 (Figure 7.28B,C), suggesting that conformers in the selected ensemble are slightly less flexible than those in the entire pool 3. The ensemble of conformers selected from pool 3 has a R_{flex} of 75.1%, compared to 86.0% for those from the entire pool 3 (Table 7.6), and a R_{sigma} of 0.73 (Table 7.6), which also indicates that the selected ensemble is slightly less flexible than the entire pool 1.

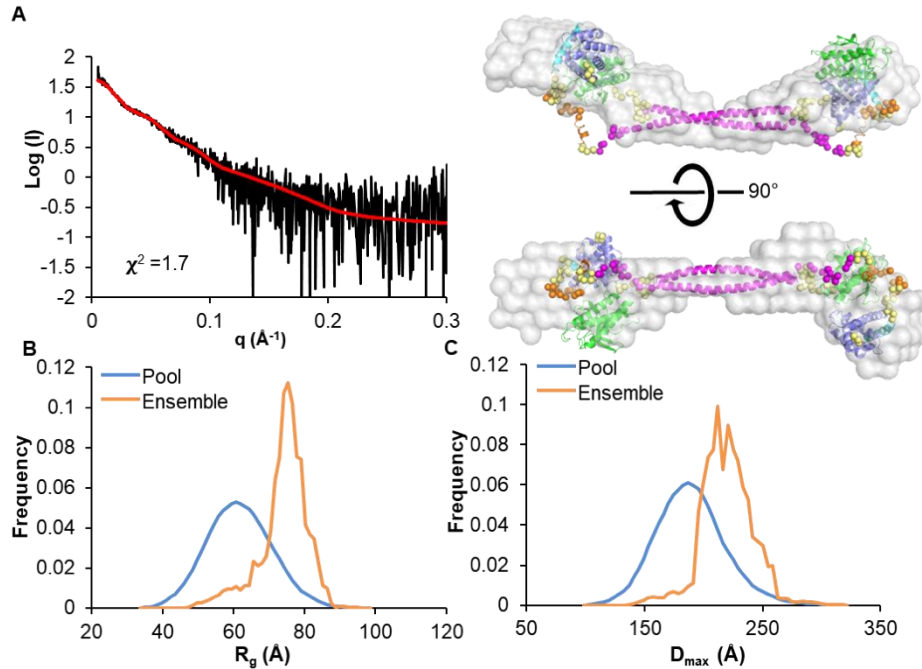


Figure 7.28. EOM fits (3) for M11: BH3D-FHD-CCD-BARAD^{AFM} complex. (A) Left panel: Experimental SAXS data fit to the theoretical scattering curve calculated from the best fit ensemble of conformers of M11: BH3D-FHD-CCD-BARAD^{AFM}; Right panel: representative model from the ensemble (color code and structure display are the same as that in Figure 12) superimposed into the filtered SAXS envelope (grey surface). (B) R_g distribution and (C) D_{max} distribution of the pool (blue) and selected ensemble (orange) conformers.

SAXS analyses of BH3D-FHD-CCD-BARAD^{AFM} and its complex with M11 show that relative to the unbound BH3D-FHD-CCD-BARAD^{AFM}, the M11: BH3D-FHD-CCD-BARAD^{AFM} complex has R_g and D_{max} that are ~ 1.1 - and 1.2 -fold larger respectively. The un-complexed BH3D-FHD-CCD-BARAD^{AFM} is largely ordered, and binding to M11 does not change this. The EOM modeling suggests that the unbound BH3D-FHD-CCD-BARAD^{AFM} adopts flexible conformations, but the flexible region is not completely unrestrained. The OH tends to be either flexible or packed against the CCD, rather than the BARAD, in both unbound protein and M11 complex, which is different from our previous research showing that the OH prefers to pack against BARAD in the BECN1 CCD-BARAD^{AFM} fragment (Glover *et al.*, 2017).

7.4. Conclusions and Discussion

The studies investigating the mechanisms by which BCL2 homology proteins regulate autophagy have chiefly focused on the BECN1 BH3D, which interacts directly with the BCL2 homologs. However, our sequence analysis shows that the BECN1 BH3D is not conserved across eukaryotes, suggesting that it is dispensable for core autophagy functions. Indeed, the BH3D appears to only be present in organisms that express BCL2 homologs, suggesting that this domain was an evolutionary adaptation to facilitate regulation by BCL2 proteins. We used cellular autophagy assays to demonstrate that deletion of the BECN1 BH3D does not down-regulate BECN1-induced autophagy, consistent with the BH3D not being conserved amongst eukaryotes. Therefore, we used a multi-pronged biophysical approach to investigate whether binding of the γ HV68 BCL2 homolog, M11, involves other domains and impacts their structure, function and oligomerization.

Our ITC results indicate that BECN1 regions outside the BH3D, especially the IDR and FHD improve binding to M11. Notably, M11 appears to bind best to the BH3D-FHD fragment, with the most favorable enthalpy, but the largest entropic cost. Further, we use HDX-MS to show that in addition to the BH3D, the BH3D-FHD linker, the FHD, and the center of the CCD become less flexible upon binding M11. This agrees with the increased BECN1 thermostability shown by the thermal denaturation monitored by CD, and improved homodimerization shown by ITC. The NES within the BECN1 CCD becomes more dynamic upon binding M11, which agrees with the unexpected decrease in BH3D-FHD-CCD helicity upon binding M11 indicated by CD.

Our SAXS data analyses and EOM modeling suggests that the BECN1 BH3D-FHD-CCD adopts flexible conformations, but the flexibility of modelled flexible region is restrained in both the un-complexed and M11-bound states. The M11:BECN1 BH3D-FHD-CCD complex appears to

fluctuate between two distinct conformations with a more elongated conformation being dominant. This fluctuation may be mediated by the flexibility of the NES, although it is unclear whether the NES and OH are packed within the CCD or are flexible in the M11 complex.

These results are important for understanding the mechanisms by which BCL2 proteins down-regulate autophagy. M11-binding is enhanced by interactions with the FHD, but decreases FHD flexibility. The FHD is implicated in binding-associated disorder-to-helix transitions (Mei, Ramanathan, *et al.*, 2016). The region equivalent to the FHD in the yeast BECN1 homolog, VPS30, forms a helix and packs against VPS38 (equivalent to human UVRAG) in the yeast VPS34 complex II (Rostislavleva *et al.*, 2015). The FHD is also implicated in interactions with several proteins such as Ambra1, an autophagy up-regulator (Strappazon *et al.*, 2011). Therefore, M11-binding likely adversely impacts BECN1 association with UVRAG, and possibly ATG14, and consequently its subsequent incorporation into VPS34 complexes, as well as interactions with other proteins that up-regulate autophagy such as Ambra1.

Our experimental evidence shows that the human BECN1 NES, which is part of the CCD, becomes more dynamic upon binding M11 may be important for NES interaction with other proteins. The N-terminal region of the CCD in yeast VPS30, which corresponds to the NES in human BECN1, is helical and packs against the N-terminal region of CCD of yeast VPS38 (equivalent to human UVRAG) in the yeast VPS34 complex II (Rostislavleva *et al.*, 2015). The increased flexibility of the NES would likely inhibit interactions of BECN1 CCD with other CCD-containing VPS34 complex components such as Atg14 and UVRAG. Indeed, recently, Wu *et al.* reported that the NES region of BECN1 CCD is the most important region of the CCD for binding to Atg14 and UVRAG (Wu *et al.*, 2018), therefore disordering of this region would likely diminish BECN1 interactions with these two proteins. Further, our results show that

binding to M11 increases the BH3D-FHD-CCD homodimerization. Therefore, binding to M11 decreases BECN1 homodimer self-dissociation as well as disrupts BECN1 interaction with UVRAG or Atg14, leading to down-regulation of autophagy.

The nuclear exporter, CRM1, has been reported to interact with the BECN1 NES for BECN1 export from the nucleus (Liang *et al.*, 2001). Mutation of leucine residues in the BECN1 NES decreases BECN1 export and traps BECN1 in the nucleus (Liang *et al.*, 2001). Numerous cellular and virus BCL2 homologs such as human Bcl-2 and EBV BHRF-1 also localize in the paranuclear space (Portier & Taglialatela, 2006, Chan *et al.*, 1995, Henderson *et al.*, 1993, Krajewski *et al.*, 1993), and M11 has also been found in the cell nucleus, though only in relatively small amounts (Wang *et al.*, 1999). The actual biological relevance of the nuclear localization of BCL2 homologs is not really understood, and has only been investigated in relation to apoptosis. Our results suggest that binding of BCL2 homologs to BECN1 may enhance BECN1 interaction with CRM-1 as the increased flexibility of NES makes NES more accessible for CRM-1 binding. Conversely, binding to BCL2 homologs could also decrease BECN1 interaction with CRM1 if the decreased helicity of the NES inhibits CRM-1 binding, preventing export of BECN1 from the nucleus to the cytosol, thereby down-regulating autophagy. Thus, our study provides potential evidence for a role in autophagy regulation for BCL2 homologs localized to the nucleus.

Our results provide important insights into how binding of BCL-2 homologs may down-regulate autophagy. In the future, it would be invaluable to obtain a better understanding of whether M11-induced conformational changes in the BH3D modulate conformations of the FHD and NES, and the mechanism by which this is accomplished. Further, an important focus of future biophysical and structural studies should be to understand the impact of M11-binding on

various BECN1-interacting proteins. These should include proteins that upregulate autophagy such as VMP1 that binds to the BH3D, AMBRA1 that binds to the FHD, ATG14 and UVRAG that bind to the CCD; CCD-containing proteins that down-regulate autophagy; as well as the nuclear exporter, CRM1. Lastly, it would be important to delineate similarities and differences in these impacts upon binding of different BCL2 homologs. Together, all this information will be invaluable for the rational design of selective therapeutics to modulate autophagy.

CHAPTER 8. INVESTIGATING M11 INTERACTIONS WITH BECN1 FL AND

BECN1^{Δ31-104}

8.1. Introduction

We have investigated the interaction between M11 and BECN1 in Chapter 7, that suggests possible mechanisms by which this interaction down-regulates autophagy. To reduce the complexity of data analysis, we performed most of the biophysical assays using BECN1 BH3D-FHD-CCD instead of BECN1 FL. In this Chapter, we report our investigation of M11 interaction with BECN1 FL and BECN1^{Δ31-104}.

We used isothermal titration calorimetry (ITC) to quantify the binding affinity and thermodynamics of M11 binding to monomeric and dimeric BECN1 fragments, to assess the impacts of BECN1 dimerization on binding M11. Further, we examined the overall shape and flexibility of BECN1 FL and BECN1^{Δ31-104} fragments and their complexes with M11 using size-exclusion chromatography (SEC) in tandem with small angle X-ray scattering (SAXS). Lastly, we attempted to image these samples using negative-stained electron microscopy (EM), in order to assess the feasibility of using cryo-EM for high-resolution structure determination.

8.2. Materials and Methods

8.2.1. Creation of protein expression constructs

Human BECN1 residues 1-450 (FL) was cloned between the *Bam*HI restriction enzyme site of the pET SUMO bacterial expression vector (Figure 8.1) and AFM, a triad mutation F359D/F360D/W361D made at the aromatic finger of BARAD (named Strep-SUMO-BECN1^{AFM} FL) using the QuikChange II Site-Directed Mutagenesis Kit (Agilent Technologies) to prevent protein aggregation during purification. Subsequently, Strep-SUMO-BECN1^{Δ31-104} and Strep-SUMO-BECN1^{Δ31-104,AFM} were created by deleting residues 31-104 from the Strep-SUMO-

BECN1 FL and Strep-SUMO-BECN1^{AFM} FL constructs respectively, using the QuikChange II Site-Directed Mutagenesis Kit (Agilent Technologies). The MBP-BECN1^{AFM} FL construct is identical to that used in Chapter 2. MBP-BECN1^{Δ31-104,AFM} was created by deleting residues 31-104 from MBP-BECN1^{AFM} FL construct using the QuikChange II Site-Directed Mutagenesis Kit (Agilent Technologies). A pentad mutation, L222A/V250A/M254A/L261A/L264A was made at CCD interface of MBP-BECN1^{AFM} FL (named MBP-BECN1^{AFM,CCDPentad} FL) using the QuikChange II Site-Directed Mutagenesis Kit (Agilent Technologies) to disrupt BECN1 homodimerization. The M11 construct is identical to that described in Chapter 4. These BECN1 fragments and their complexes with M11 are summarized in Table 8.1.

Table 8.1. Samples used in this chapter.

	Label	Purpose	Description	Theoretical Molecular Mass (kDa)
1	Strep-SUMO-BECN1 ^{Δ31-104}	SAXS	Strep-SUMO-BECN1(1-30 & 105-450) fusion protein	56.67
2	M11:Strep-SUMO-BECN1 ^{Δ31-104}	SAXS	Strep-SUMO-BECN1(1-30 & 105-450) fusion protein complexed with M11(1-136)	73.34
3	Strep-SUMO-BECN1 ^{Δ31-104,AFM}	SAXS	Strep-SUMO-BECN1(1-30 & 105-450; F359D,F360D, W361D) fusion protein	56.54
4	M11:Strep-SUMO-BECN1 ^{Δ31-104,AFM}	SAXS	Strep-SUMO-BECN1(1-30 & 105-450;F359D,F360D, W361D) fusion protein complexed with M11	73.21
5	Strep-SUMO-BECN1 ^{AFM} FL	SAXS, EM	Strep-SUMO-BECN1 full length (1-450; F359D,F360D, W361D) fusion protein	66.14
6	M11:Strep-SUMO-BECN1 ^{AFM} FL	SAXS, EM	Strep-SUMO-BECN1 full length (1-450; F359D,F360D, W361D) fusion protein complexed with M11	82.76
7	MBP-BECN1 ^{Δ31-104,AFM}	EM	MBP-BECN1(1-30 & 105-450; F359D,F360D, W361D) fusion protein	86.97
8	M11: MBP-BECN1 ^{Δ31-104,AFM}	EM	MBP-BECN1(1-30 & 105-450; F359D,F360D, W361D) fusion protein complexed with M11	103.64
9	MBP-BECN1 ^{AFM,CCDPentad} FL	M11 interaction	MBP-BECN1(1-30 & 105-450; L222A,V250A,M254A, L261A,L264A) fusion protein	96.00

```

NNNATGGGCAGTGCTGGAGCCACCCGCGAGTTCGAAAAAGCAGCGGCCTGGT
GCCGCGCGGCAGCCATATGGCTAGCATGTGGACTCAGAAGTCAATCAAGAAGC
TAAGCCAGAGGTCAAGCCAGAAGTCAAGCCTGAGACTCACATCAATTTAAAGGT
GTCCGATGGATCTTCAGAGATCTTCTTCAAGATCAAAAAGACCACTCCTTTAAGA
AGGCTGATGGAAGCGTTCGCTAAAAGACAGGGTAAGGAAATGGACTCCTTAAGA
TTCTTGTACGACGGTATTAGAATCCAAGCTGATCAGACCCCTGAAGATTTGGACA
TGGAGGATAACGATATTATTGAGGCTCACAGAGAACAGATTGGTGGATCCATGGA
AGGG.....AAATGAAGCTTGCGGCCGCACTCGAGACCACCACCACCACCCT
GAGA

```

ATG: Start codon TGA: Stop codon GGATCC: BamHI site AAGCTT: HindIII site

Red: SUMO Green: BECN1 Orange: His6-tag Blue: Strep-tag

Figure 8.1. Strep-SUMO-BECN1 sequence in pET vector.

8.2.2. Protein expression and purification

Separate aliquots of *E. coli* BL21(DE2)-pLysS cells were transformed with expression plasmids of each Strep-SUMO BECN1 construct (Table 8.1) and grown at 37 °C in LB medium with 15 µg/mL kanamycin to an OD₆₀₀ = 0.6 (log phase). For M11:SUMO-BECN1 complexes, separate aliquots of *E. coli* BL21(DE2)-pLysS cells were co-transformed with expression plasmids of each SUMO-BECN1 and M11 construct and grown at 37 °C in LB medium with 15 µg/mL kanamycin and 100 µg/mL ampicillin to an OD₆₀₀ = 0.6. Then the temperature was equilibrated to 13 °C, protein expression induced by addition of 0.5 mM isopropyl thio-β-D-galactoside, and protein expressed at 13 °C for 18-20 hours. The cells were harvested, lysed, and clarified the same way as the BECN1 fragments described in Chapter 4 with the same lysis buffer. At all subsequent stages of purification, the purity of the protein sample was evaluated using SDS-PAGE. The clarified lysate was passed over 10 mL of Strep-Tactin affinity resin (IBA Lifesciences) in a gravity column, then unbound contaminants were washed off using 100 ml of lysis buffer. The protein-bound Strep-Tactin resin was then incubated in Elution Buffer (50 mM Tris pH 8.0; 300 mM NaCl; 2 mM DTT; 5 mM desthiobiotin (IBA Lifesciences)) for 1h and finally the protein was eluted from the Strep-Tactin resin with 20 ml Elution Buffer. This

protocol was followed for all SUMO-BECN1 and M11:SUMO-BECN1 complex samples. After Strep-Tactin affinity chromatography, the protein was further purified by SEC using a HiLoad 16/600 Superdex 200 or Superdex 200 10/30 GL column (GE Healthcare) in SEC buffer comprising 50 mM Tris pH 8.0; 300 mM NaCl, and the purified protein was concentrated in the SEC buffer, flash-frozen in liquid nitrogen, and stored at -80 °C.

All MBP-BECN1^{AFM} samples were prepared in the same way as MBP-BECN1 CCD-BARAD^{AFM} described in Chapter 4. M11 was expressed and purified as previously described (Sinha *et al.*, 2008). The M11:MBP-BECN1^{Δ31-104,AFM} complex was obtained the same way as the M11:BECN1 complexes described in Chapter 7.

8.2.3. ITC

A Low Volume Nano ITC (TA Instruments) was used to perform ITC experiments at 20 °C. All samples were dialyzed against ITC buffer comprising 50 mM Tris pH 8.0, 150 mM NaCl and 2 mM β-mercaptoethanol. M11 interaction with BECN1 fragments was assessed by titrating 100-200 μM M11 proteins in 25 injections of 2 μl each into the sample cell containing 14-30 μM BECN1 samples. Dimer dissociation experiments were performed by titrating 50 μM protein in 20 injections of 2.5 μl each, into the sample cell containing ITC buffer. Data were analysed with the NanoAnalyze Software (TA Instruments). Buffer blanks, measured by titrating M11 into buffer, were subtracted from the experimental profiles of interaction experiments, which were then fitted with independent models. The data reported are the average of triplicates.

8.2.4. SEC-SAXS data collection and analysis

SAXS data were collected and analyzed as described in Chapter 7. EOM 2.1 (Tria *et al.*, 2015) was used to generate ensemble of models for the M11:SUMO-BECN1^{Δ31-104,AFM} with a pool of 10,000 independent models generated based on the input sequence and structural

information, from which the ensemble of models that produced theoretical SAXS had the best χ^2 fits to the experimental SAXS data were selected. Due to the multiple domains and high conformational flexibility of BECN1 FL, the EOM modeling did not provide reliable information regarding the overall shape and flexibility of either BECN1 or M11:BECN1. Therefore, we did not perform EOM modeling for the other samples.

8.2.5. Cryo-negative staining

Grids were glow discharged for 30 s. For each sample, a 3.5 μ L drop of 0.05-0.5 μ M sample was applied to the grid. Samples were incubated on the grid on the benchtop at room temperature for 30 s. Grids were sequentially washed with 20 μ L of SEC buffer and 20 μ L of 150 mM NaCl for 2-5 sec each, while blotting with filter paper after each wash. Grids were stained with 10 μ L 0.75% uranyl formate (UF) for 2-5 s, blotted, stained with another 10 μ L of 0.75% UF for 2-5 sec, blotted, then allowed to dry in air. Imaging was performed using the T12 microscope located in James L. Sorenson Molecular Biotechnology Building at University of Utah (<https://nanoinstitute.utah.edu/news-events/nanobytes-newsletter/vol-1-iss-2/ustar-center.php>). Search images were taken at 2,700x magnification, exposure images were taken at 30,000x magnification.

8.3. Results

8.3.1. Expression and purification of BECN1 constructs and their complexes with M11

The different constructs (Table 8.1) were over-expressed in *E. coli* Arctic Express cells and purified to homogeneity. The major peak on SEC and corresponding single band for unbound protein, and two distinct bands for complexed protein, on SDS-PAGE indicated that each SEC sample was pure and homogenous (Figure 8.2-8.10)

The apparent molecular mass of SUMO-BECN1^{Δ31-104}, calculated from the elution volume (10.91 ml on Superdex 200) of the major SEC peak (Figure 8.2), is 380.2 kD, which is ~3.4 times larger than the theoretical molecular mass of Strep-SUMO-BECN1^{Δ31-104} dimer (Table 8.2), which suggests that Strep-SUMO-BECN1^{Δ31-104} is an elongated homodimer. The final yield of the purified Strep-SUMO-BECN1^{Δ31-104} was 0.5 mg / L of bacterial culture.

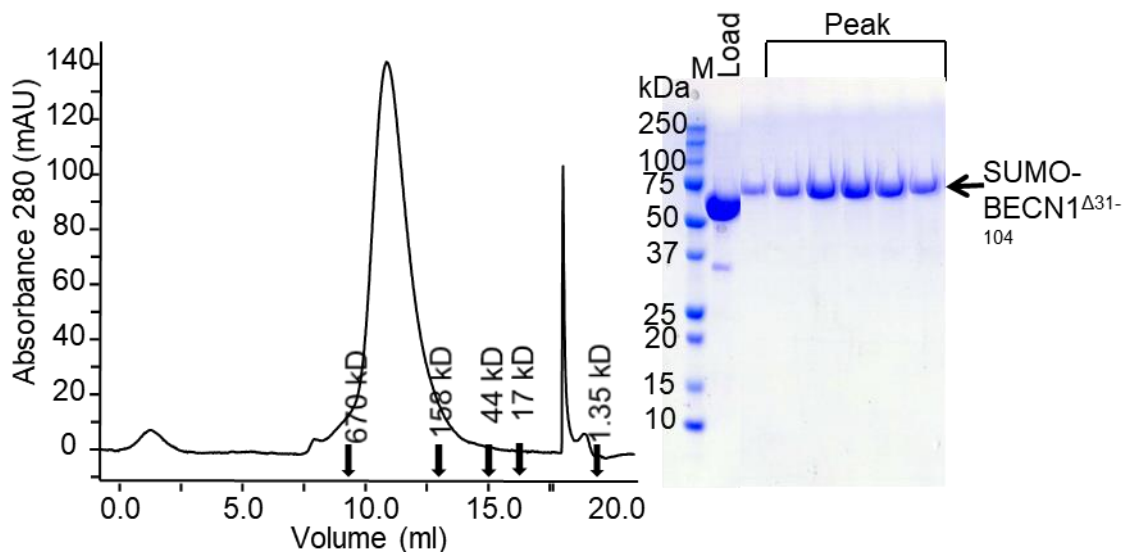


Figure 8.2. SEC and the corresponding SDS-PAGE of SUMO-BECN1^{Δ31-104}. Elution positions of SEC standards are indicated by arrows.

The apparent molecular mass of M11:SUMO-BECN1^{Δ31-104}, calculated from the elution volume (10.7 ml on Superdex 200) of the major SEC peak (Figure 8.3), is 426.6 kD, which is ~2.9 times larger than the theoretical molecular mass of M11:SUMO-BECN1^{Δ31-104}:M11 heterotetramer (Table 8.1), suggesting that M11:SUMO-BECN1^{Δ31-104} is an elongated heterotetramer. The molecular mass of this complex estimated from SEC is ~46 kD larger than that of the unbound SUMO-BECN1^{Δ31-104}, consistent with binding of two-three M11 molecules. Since BECN1 is an elongated homodimer and binds to M11 with a 1:1 ratio, the 46 kD extra MW should correspond two M11 molecules. The final yield of the purified M11:SUMO-BECN1^{Δ31-104} complex was 0.7 mg / L of bacterial culture.

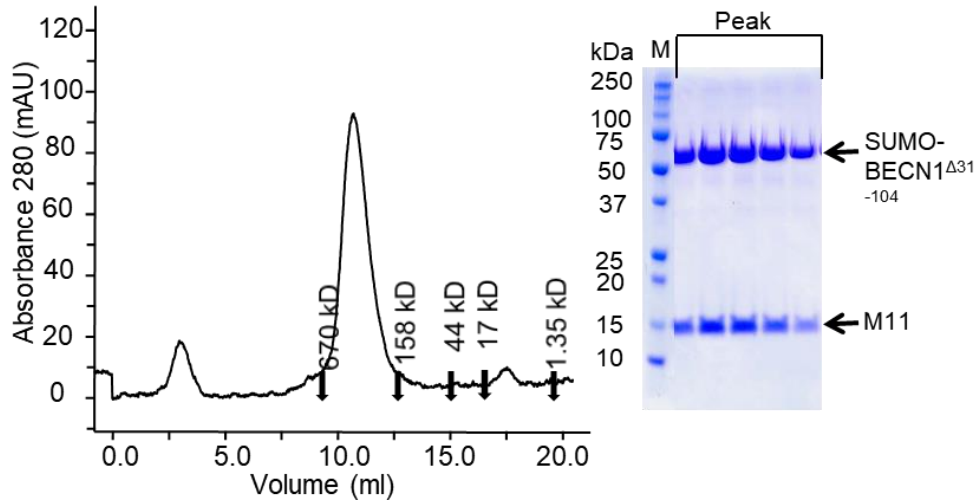


Figure 8.3. SEC and the corresponding SDS-PAGE of M11:SUMO-BECN1 Δ^{31-104} . Elution positions of SEC standards are indicated by arrows.

The apparent molecular mass of SUMO-BECN1 $\Delta^{31-104,AFM}$, calculated from the elution volume (11.71 ml on Superdex 200) of the major SEC peak (Figure 8.4), is 251.2 kD, which is ~2.2 times larger than the theoretical molecular mass of SUMO-BECN1 $\Delta^{31-104,AFM}$ dimer (Table 8.1), which suggests that SUMO-BECN1 $\Delta^{31-104,AFM}$ is an elongated homodimer. The final yield of the purified SUMO-BECN1 $\Delta^{31-104,AFM}$ was 0.8 mg / L of bacterial culture.

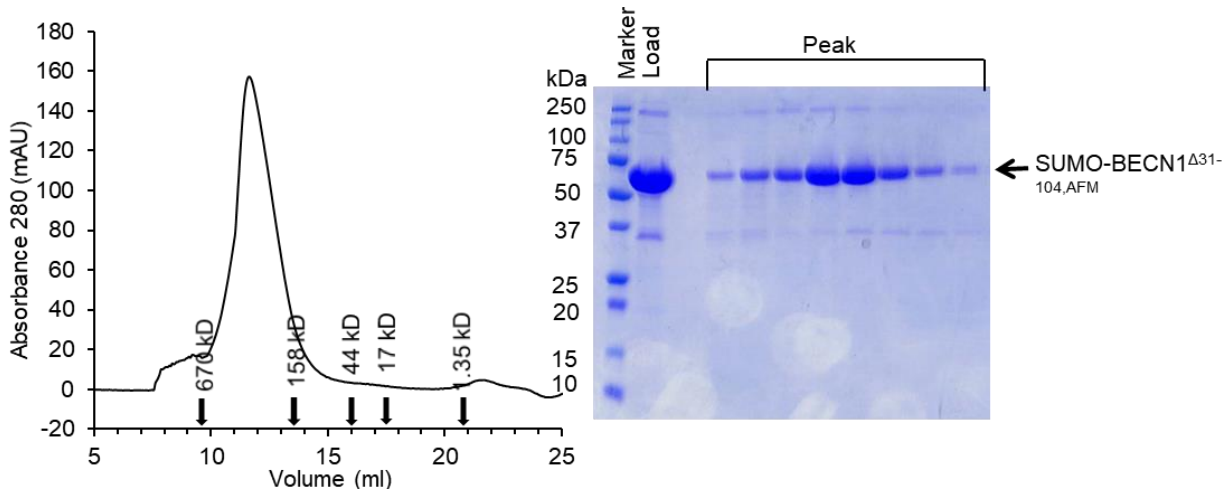


Figure 8.4. SEC and the corresponding SDS-PAGE of SUMO-BECN1 $\Delta^{31-104,AFM}$. Elution positions of SEC standards are indicated by arrows.

The apparent molecular mass of M11:SUMO-BECN1 $\Delta^{31-104,AFM}$, calculated from the elution volume (11.33 ml on Superdex 200) of the major SEC peak (Figure 8.5), is 308.3 kD,

which is ~2.9 times larger than the theoretical molecular mass of M11:SUMO-BECN1^{Δ31-104,AFM} heterotetramer (Table 8.1), which suggests that M11:SUMO-BECN1^{Δ31-104,AFM} is an elongated heterotetramer. The molecular mass of this complex estimated from SEC is about 57 kD larger than that of the unbound SUMO-BECN1^{Δ31-104,AFM}, consistent with binding of two-three M11 molecules. Since BECN1 is an elongated homodimer and binds to M11 with a 1:1 ratio, the 46 kD larger molecular mass estimated from SEC should correspond two M11 molecules. The final yield of the purified Strep-SUMO-BECN1^{Δ31-104,AFM}:M11 complex was 0.8 mg / L of bacterial culture.

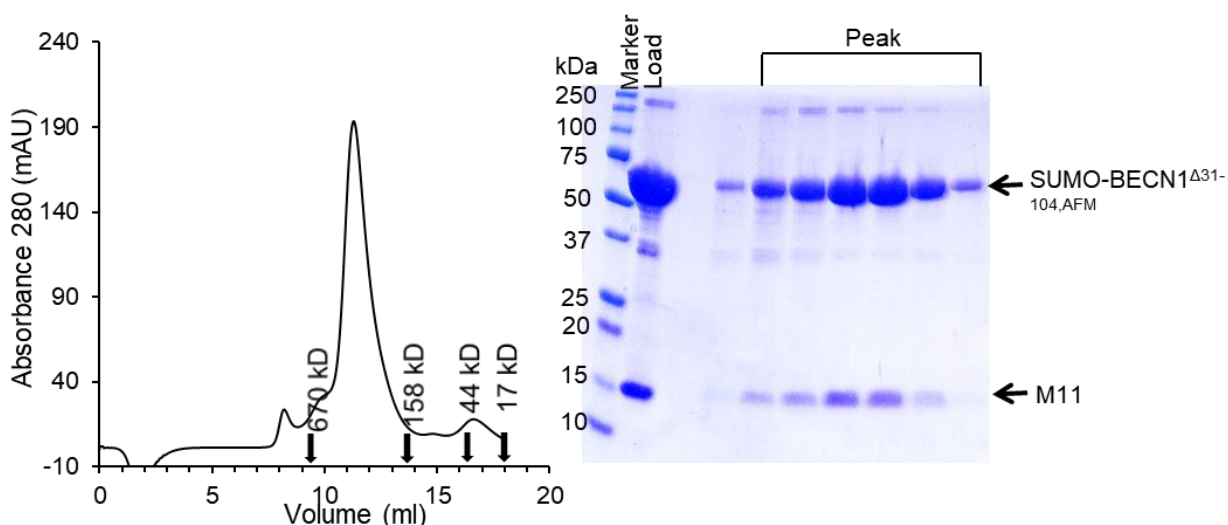


Figure 8.5. SEC and the corresponding SDS-PAGE of M11:SUMO-BECN1^{Δ31-104,AFM}. Elution positions of SEC standards are indicated by arrows.

The apparent molecular mass of SUMO-BECN1^{AFM} FL, calculated from the elution volume (10.19 ml on Superdex 200) of the major SEC peak (Figure 8.6), is 549.5 kD, which is ~4 times larger than the theoretical molecular mass of SUMO-BECN1^{AFM} FL homodimer (Table 8.1), which suggests that SUMO-BECN1^{AFM} FL is an elongated homodimer. The final yield of the purified Strep-SUMO-BECN1^{AFM} FL was 0.7 mg / L of bacterial culture.

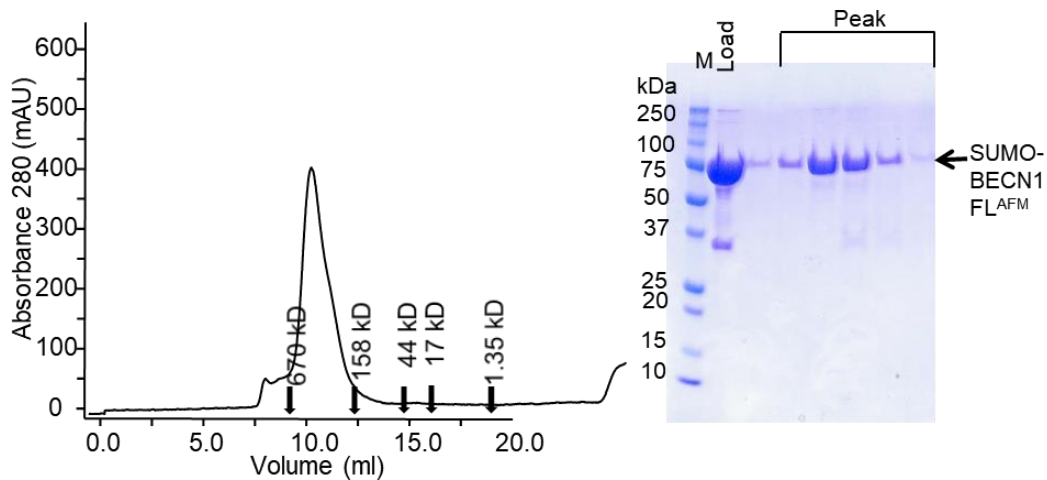


Figure 8.6. SEC and the corresponding SDS-PAGE of SUMO-BECN1^{AFM} FL. Elution positions of SEC standards are indicated by arrows.

The apparent molecular mass of M11:SUMO-BECN1^{AFM} FL, calculated from the elution volume (10.01 ml on Superdex 200) of the major SEC peak (Figure 8.7), is 612.4 kD, which is ~3.7 times larger than the theoretical molecular mass of a M11:SUMO-BECN1^{AFM} FL heterotetramer (Table 8.1), which suggests that M11:SUMO-BECN1^{AFM} FL is an elongated heterotetramer. The molecular mass of this complex estimated from SEC is ~63 kD larger than that of the unbound SUMO-BECN1^{AFM} FL, consistent with binding of four M11 molecules. Since BECN1 is an elongated homodimer and binds to M11 with a 1:1 ratio, the 63 kD larger molecular mass estimated from SEC should correspond two M11 molecules. The final yield of the purified M11:SUMO-BECN1^{AFM} FL complex was 0.7 mg / L of bacterial culture.

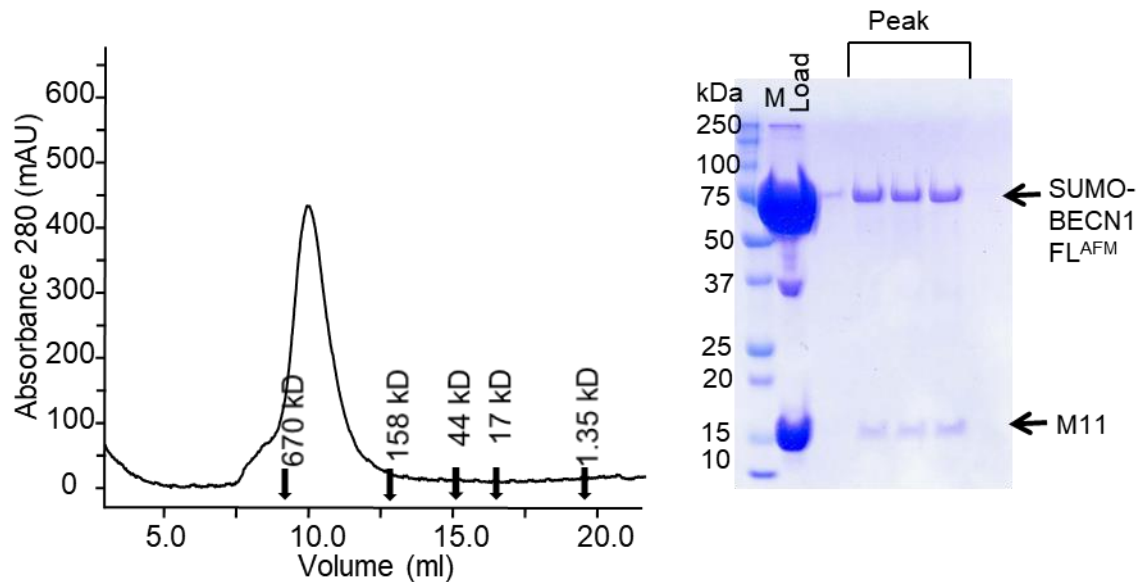


Figure 8.7. SEC and the corresponding SDS-PAGE of M11:SUMO-BECN1^{AFM} FL. Elution positions of SEC standards are indicated by arrows.

The apparent molecular mass of MBP-BECN1^{Δ31-104,AFM}, calculated from the elution volume (10.44 ml on Superdex 200) of the major SEC peak (Figure 8.8), is 480.5 kD, which is ~2.8 times larger than the theoretical molecular mass of 173.9 kD for MBP-BECN1^{Δ31-104,AFM} dimer (Table 8.1), which suggests that MBP-BECN1^{Δ31-104,AFM} is an elongated homodimer. The final yield of the purified MBP-BECN1^{Δ31-104,AFM} was 2.5 mg / L of bacterial culture.

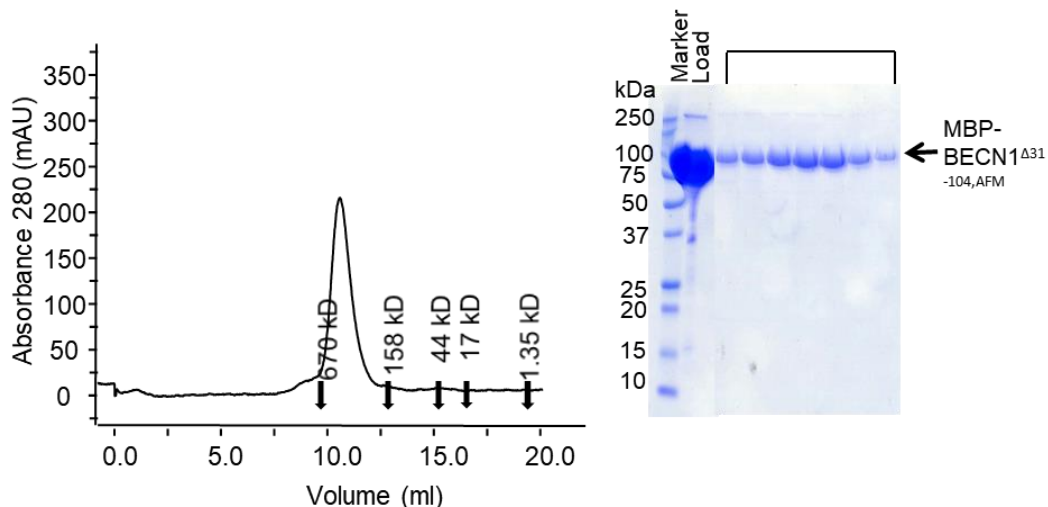


Figure 8.8. SEC and the corresponding SDS-PAGE of MBP-BECN1^{Δ31-104,AFM}. Elution positions of SEC standards are indicated by arrows.

The apparent molecular mass of M11:MBP-BECN1^{Δ31-104,AFM} calculated from the elution volume (10.26 ml on Superdex 200) of the major SEC peak (Figure 8.9), is 535.8 kD, which is ~2.6 times larger than the theoretical molecular mass of 207.3 kD for M11:MBP-BECN1^{Δ31-104,AFM} heterotetramer, suggesting that M11:MBP-BECN1^{Δ31-104,AFM} is an elongated heterotetramer. The molecular mass of this complex estimated from SEC is ~55 kD larger than that of the unbound MBP-BECN1^{Δ31-104,AFM}, consistent with binding of two to three M11 molecules. Since BECN1 is an elongated homodimer and binds to M11 with a 1:1 ratio, the 55 kD larger molecular mass estimated from SEC should correspond two M11 molecules. The final yield of the purified M11:MBP-BECN1^{Δ31-104,AFM} complex was 2.7 mg / L of bacterial culture.

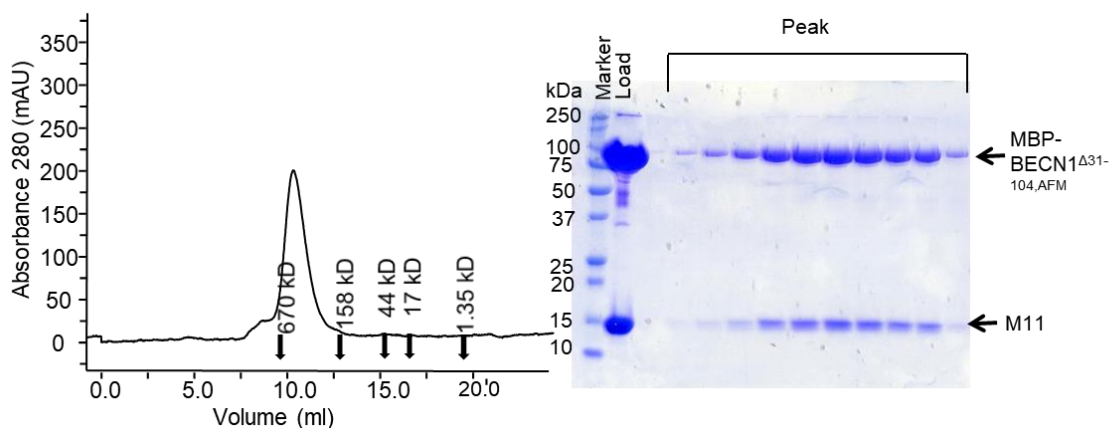


Figure 8.9. SEC and the corresponding SDS-PAGE of M11:MBP-BECN1^{Δ31-104,AFM}. Elution positions of SEC standards are indicated by arrows.

The apparent molecular mass of MBP-BECN1^{AFM,CCDPentad} FL, calculated from the elution volume (14.95 ml on Superose 6 Increase) of the major SEC peak (Figure 8.10, blue curve), is 240.0 kD, which is ~1.25 times larger than the theoretical molecular mass of 192.0 kD for MBP-BECN1^{AFM,CCDPentad} dimer (Table 8.1), but ~1.7 times smaller than the molecular mass of MBP-BECN1^{AFM} FL homodimer calculated from SEC elution volume (Figure 8.10, green curve). This suggests that MBP-BECN1^{AFM,CCDPentad} is possibly an elongated monomer. The final yield of the purified MBP-BECN1^{AFM,CCDPentad} FL was 5.2 mg / L of bacterial culture.

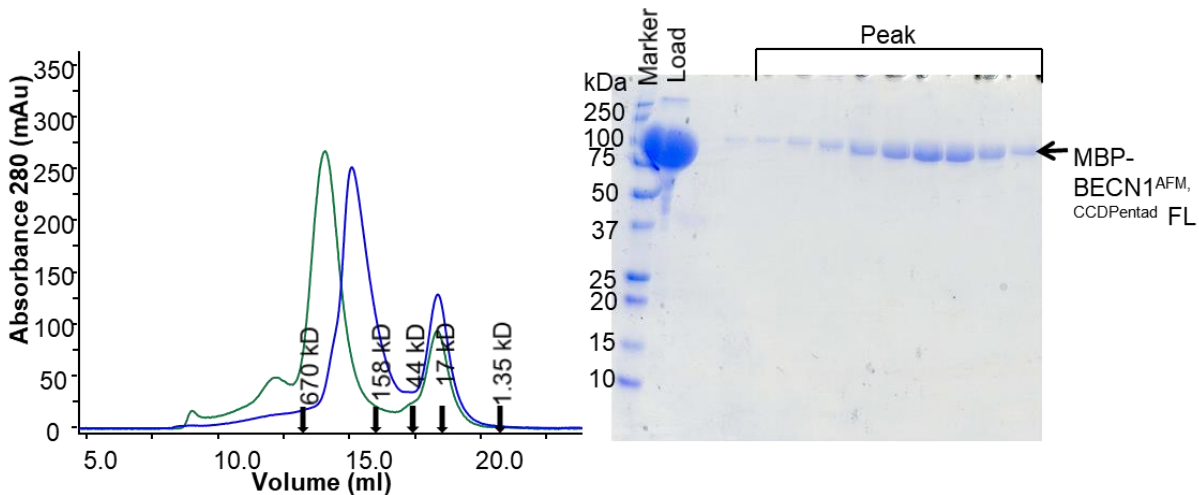


Figure 8.10. SEC and the corresponding SDS-PAGE of SUMO-BECN1^{AFM,CCDPentad}. Elution positions of SEC standards are indicated by arrows.

Since BECN1 FL aggregates severely and cannot be purified without the AFM mutation, to ensure consistency in comparisons, all the BECN1 constructs used for the biophysical experiments in this chapter were AFM mutants. Therefore, though the SUMO-BECN1^{Δ31-104} and its complex with M11 can be purified without making the AFM mutation, they were not used for the following biophysical experiments.

8.3.2. M11-binding affinity is not impacted by BECN1 homodimerization

We used ITC to quantify and compare the affinities of M11 binding to dimeric (MBP-BECN1^{AFM} FL) and monomeric (MBP-BECN1^{AFM,CCDPentad} FL) BECN1 fragments. We first performed a homodimer dissociation test for the pentad mutant by titrating it into the ITC buffer, which did not generate a detectable dissociation signal (Figure 8.11A), verifying that the pentad mutant is a monomer as previously suggested by SEC. The ITC results show that M11 binds with similar affinity to the dimeric and monomeric BECN1 fragments (Table 8.2, Figure 8.11).

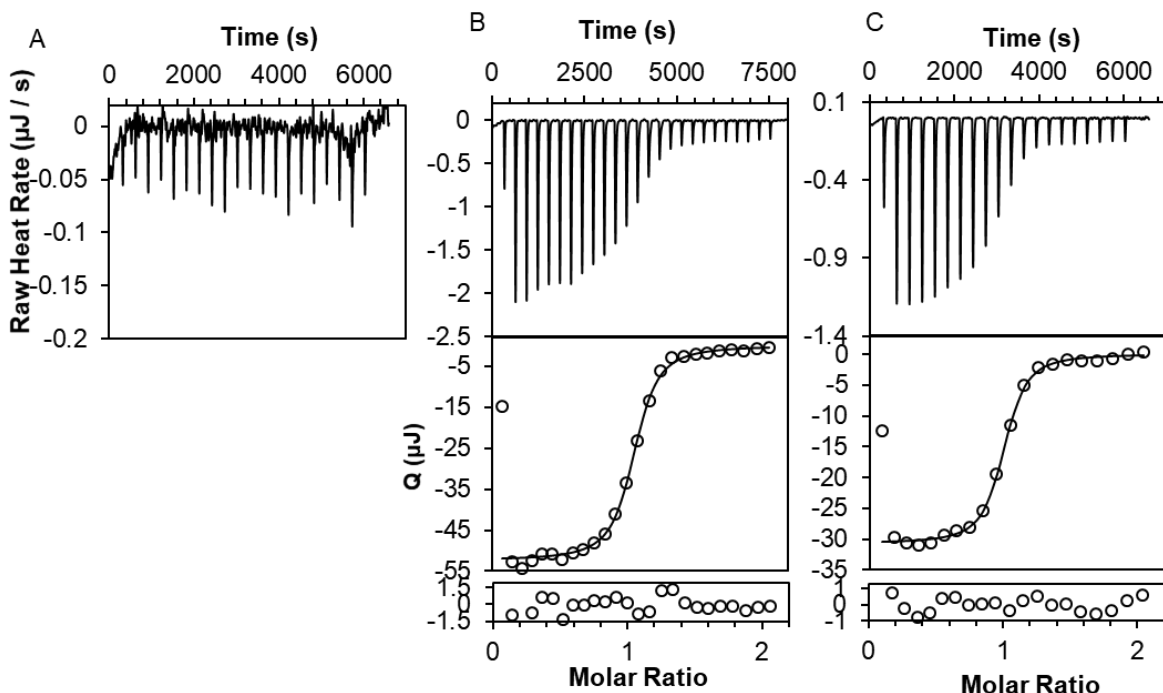


Figure 8.11. Representative plots of ITC for M11:BECN1 interactions. Upper panel: raw data; lower panel: integrated heat and theoretical fit by independent interaction model from TA Analysis. (A) BECN1^{AFM,CCDPentad} titrated into buffer. (B) M11 titrated into BECN1^{AFM}. (C) M11 titrated into BECN1^{AFM,CCDPentad}.

Table 8.2. Thermodynamics of binding of M11 to dimeric and monomeric BECN1 fragments.

BECN1 Fragments	M11			
	K_d (μM)	ΔH (kJ/mol)	ΔS (J/K·mol)	ΔG (kJ/mol)
BECN1 ^{AFM}	0.45 ± 0.10	-55.35 ± 3.80	-70.56 ± 15.13	-35.02 ± 0.57
BECN1 ^{AFM,CCDPentad}	0.25 ± 0.04	-62.09 ± 1.00	-85.45 ± 4.88	-37.04 ± 0.43

8.3.3. BECN1 ^{Δ 31-104} and its complex with M11 adopt a flexible, elongated conformation

The variation of $I(0)$ across the SUMO-BECN1 ^{Δ 31-104,AFM} SEC-SAXS peak (Figure 8.12A) is consistent with the variation in eluate concentration. The R_g determined from Guinier analyses of the intensity-normalized, buffer-subtracted data ranges between 70 to 100 Å across the scattering peak (Figure 8.12B). The linear Guinier plot at $qR_g < 1.3$ indicates that the sample does not aggregate (Figure 8.12B). The $P(r)$ curve indicates that SUMO-BECN1 ^{Δ 31-104,AFM} is an elongated, multi-domain protein with a D_{max} of 279 Å and an average R_g of 87 Å, within the range estimated from the Guinier plot (Figure 8.12C, Table 8.3). The Kratky plot suggests that SUMO-BECN1 ^{Δ 31-104,AFM} is well-folded (Figure 8.12D). The normalized spatial discrepancy of

10 generated *ab initio* molecular models is 0.73 ± 0.05 . Further, the molecular mass estimated from V_c is 135.1 kDa (Table 8.3), which is slightly larger than the theoretical molecular mass of 111.4 kDa expected for a SUMO-BECN1 $^{\Delta 31-104,AFM}$ homodimer.

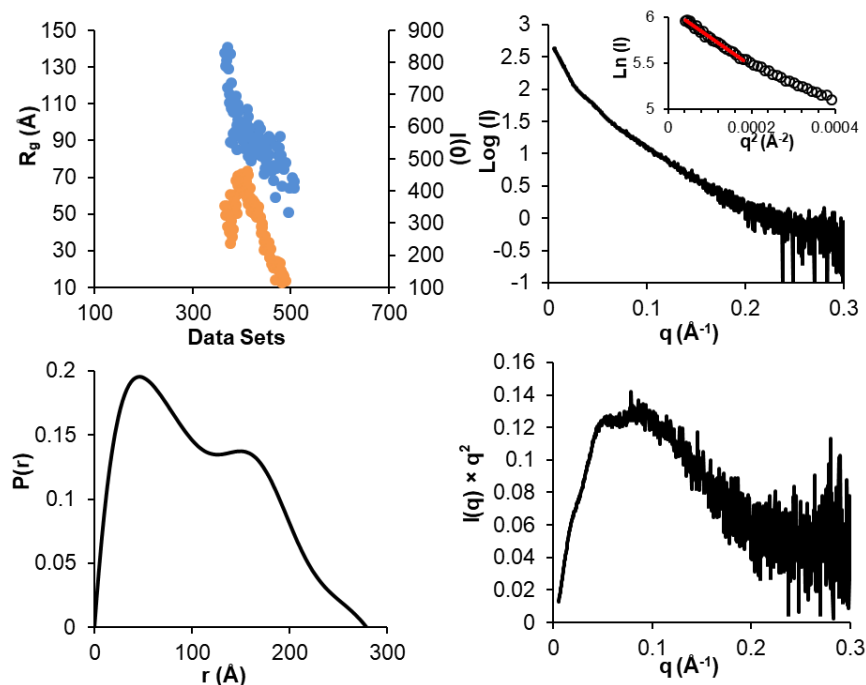


Figure 8.12. SEC-SAXS results for SUMO-BECN1 $^{\Delta 31-104,AFM}$. (A) $I(0)$ (orange) and R_g (blue) as a function of time for the SEC-SAXS run. (B) plot of $\log I(q)$ versus q with the inset showing the Guinier plot. (C) $P(r)$ distribution. (D) Kratky plot.

Table 8.3. Structural parameters from SAXS data analysis.

Guinier analysis	BECN1 $^{\Delta 31-104,AFM}$	M11:BECN1 $^{\Delta 31-104,AFM}$	BECN AFM FL	M11:BECN1 AFM FL
$I(0)$	439.8 ± 3.3	79.6 ± 0.4	183.6 ± 0.6	213.0 ± 0.6
q_{min} (\AA^{-1})	0.00005	0.0001	0.00005	0.00005
qR_g max	1.3	1.3	1.3	1.3
R^2	0.99	0.97	1.00	1.00
P(r) distribution				
$I(0)$ (cm^{-1})	391.1 ± 2.8	82.9 ± 0.4	189.2 ± 0.5	214.5 ± 0.4
R_g (\AA)	87 ± 0	78 ± 1	92 ± 0	93 ± 0
D_{max} (\AA)	279	281	337	342
q range (\AA^{-1})	0.0131-0.0810	0.0088-0.1141	0.0072-0.0935	0.0078-0.0846
MW from V_c (kDa)	135.1	112.4	202.3	205.0

The variation of $I(0)$ across the M11:SUMO-BECN1 $^{\Delta 31-104,AFM}$ SEC-SAXS peak (Figure 8.13A) is consistent with the variation in eluate concentration. The R_g determined from Guinier

analyses of the intensity-normalized, buffer-subtracted data ranges between 65 to 80 Å across the scattering peak (Figure 8.13A). The linear Guinier plot at $qR_g < 1.3$ indicates that the sample does not aggregate (Figure 8.13B). The $P(r)$ curve indicates that M11:SUMO-BECN1 $^{\Delta 31-104,AFM}$ is an elongated, multi-domain protein with a D_{max} of 281 Å and an average R_g of 78 Å, within the range estimated from the Guinier plot (Figure 8.13C, Table 8.3). The Kratky plot suggests that M11:SUMO-BECN1 $^{\Delta 31-104,AFM}$ is well-folded (Figure 8.13D). The normalized spatial discrepancy of 10 generated *ab initio* molecular models is 0.80 ± 0.05 . Further, the molecular mass estimated from V_c is 112.4 kDa (Table 8.3), which is slightly smaller than the theoretical molecular mass of 146.7 kDa expected for a M11:SUMO-BECN1 $^{\Delta 31-104,AFM}$ heterotetramer.

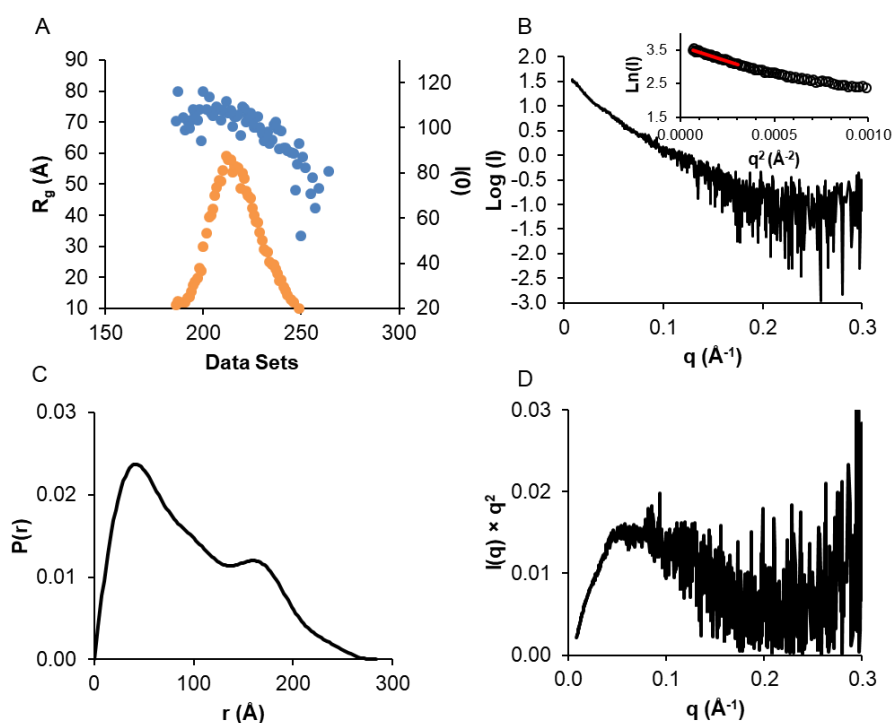


Figure 8.13. SEC-SAXS results for M11:SUMO-BECN1 $^{\Delta 31-104,AFM}$. (A) $I(0)$ (orange) and R_g (blue) as a function of time for the SEC-SAXS run. (B) plot of $\log I(q)$ versus q with the inset showing the Guinier plot. (C) $P(r)$ distribution. (D) Kratky plot.

We then used EOM to generate an initial pool of conformers, based on available structures of the SUMO (PDB ID: 1WM2), the M11:BECN1 BH3D complex (PDB ID:3DVU), the FHD residues 157-171 (PDB ID:5EFM), the CCD (PDB ID:5HHE), and the BARAD (PDB

ID: 4DDP) excluding the OH, with the remaining residues modelled as flexible. Conformers for which the theoretical scattering curves best fit the experimental SAXS data, with an overall χ^2 of 2 (Figure 6A), were included in the “selected ensemble”. EOM analyses show that the R_g and D_{max} distribution for the selected ensemble of conformers exhibits a single peak that is of similar width as that of the initial pool of conformers (Figure 6B,C), indicating that the flexibility of the selected ensemble of conformers of the M11:SUMO-BECN1 $\Delta^{31-104,AFM}$ is similar to that of the conformers in the entire pool. The selected ensemble of conformers has a R_{flex} of 84.0%, compared to 84.2% for the entire pool, and has a R_{sigma} of 1 (Table S3), also indicating that conformers in the selected ensemble are as flexible as the conformers in the entire pool.

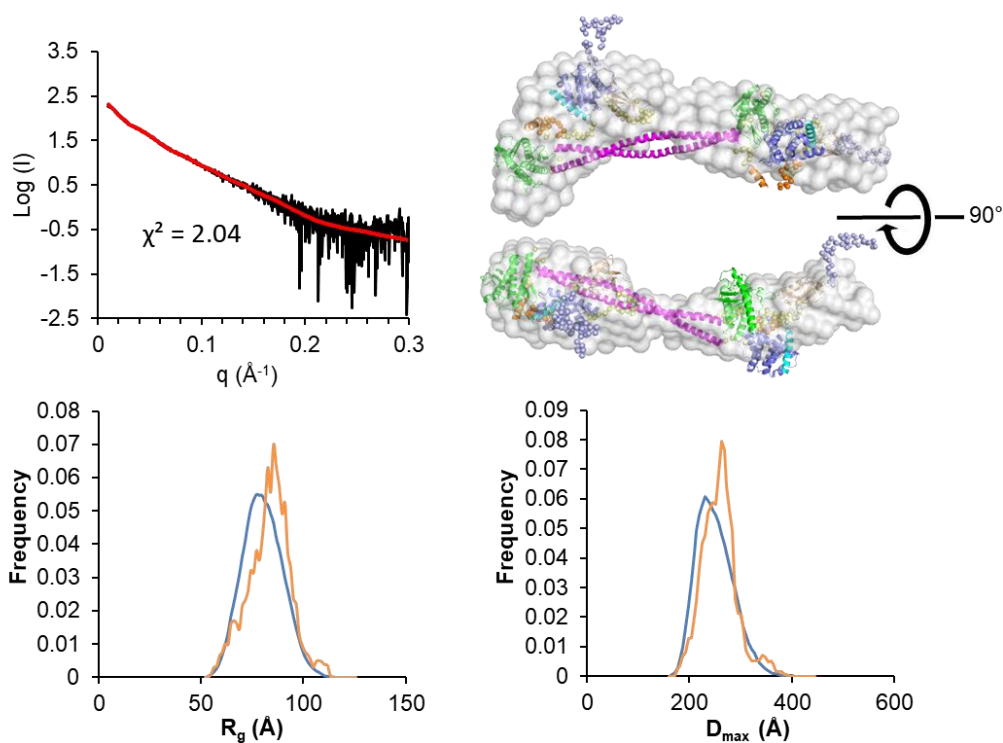


Figure 8.14. EOM modeling for the M11:SUMO-BECN1 $\Delta^{31-104,AFM}$ complex. (A) left panel: Fit of experimental data to theoretical scattering curve calculated from the best fit ensemble of conformers; right panel: representative model from the ensemble (Magenta: CCD; orange: FHD; cyan: BH3D; Green: BARAD; violet:M11; tint: SUMO; light violet: Strep-tag; yellow: linker between domains). Structured regions are shown as cartoon; flexible region as spheres) superimposed into the filtered SAXS envelope (shown as grey surface). (B) R_g distribution and (C) D_{max} distribution of conformers in the pool (blue) and selected ensemble (orange).

The SAXS analysis of SUMO-BECN1^{Δ31-104,AFM} and its complex with M11 suggests that M11:SUMO-BECN1^{Δ31-104,AFM} has a slightly smaller R_g and similar D_{max} compared to the unbound BECN1. The relatively smaller R_g of the complex may be due to the decreased flexibility of BECN1 upon binding to M11.

8.3.4. BECN1 FL and its complex with M11 adopt a flexible, elongated conformation

We used SEC-SAXS to characterize the overall shape and flexibility of SUMO-BECN1 and their complexes with M11. The variation of $I(0)$ across the SUMO-BECN1^{AFM} FL SEC-SAXS peak (Figure 8.15A) is consistent with the variation in eluate concentration. The R_g determined from Guinier analyses of the intensity-normalized, buffer-subtracted data ranges between 80 to 90 Å across the scattering peak (Figure 8.15A), indicating that the SUMO-BECN1^{AFM} FL is flexible. The linear Guinier plot at $qR_g < 1.3$ indicates that the sample does not aggregate (Figure 8.15B). The $P(r)$ curve indicates that SUMO-BECN1^{AFM} FL is an elongated, multi-domain protein with a D_{max} of 337 Å and an average R_g of 92 Å, within the range estimated from the Guinier plots (Figure 8.15C, Table 8.3). The Kratky plot suggests that SUMO-BECN1^{AFM} FL is well-folded (Figure 8.15D). The Kratky plot of SUMO-BECN1^{AFM} FL does not reflect the disorder of the IDR, which may be because a much larger region of this fragment is folded compared to the isolated IDR. The normalized spatial discrepancy of 10 generated *ab initio* molecular models is 0.72 ± 0.07 . Further, the molecular mass estimated from V_c is 202.3 kDa (Table 8.3), which is larger than the theoretical molecular mass of 132.3 kDa expected for a SUMO-BECN1^{AFM} FL dimer. The larger molecular mass estimated from V_c may be due to the large disordered region at the N-terminus of BECN1.

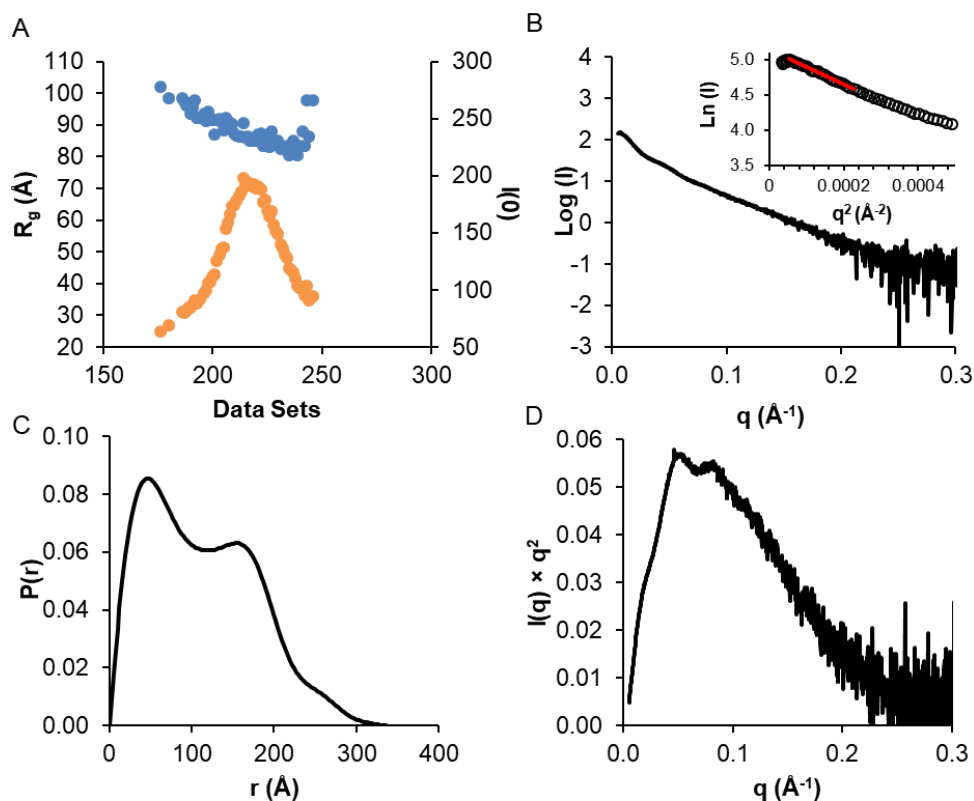


Figure 8.15. SEC-SAXS results for SUMO-BECN1^{AFM} FL. (A) $I(0)$ (orange) and R_g (blue) as a function of time for the SEC-SAXS run. (B) Plot of $\log I(q)$ versus q with the inset showing the Guinier plot. (C) $P(r)$ distribution. (D) Kratky plots.

The variation of $I(0)$ across the M11:SUMO-BECN1^{AFM} FL SEC-SAXS peak (Figure 8.16A) is consistent with the variation in eluate concentration. The R_g determined from Guinier analyses of the intensity-normalized, buffer-subtracted data ranges between 70 to 90 Å across the scattering peak (Figure 8.16A) with a decreasing trend over time. The linear Guinier plot at $qR_g < 1.3$ indicates that the sample does not aggregate (Figure 8.16B). The $P(r)$ curve indicates that SUMO-BECN1^{AFM} FL is an elongated, multi-domain protein with a D_{\max} of 342 Å and an average R_g of 93 Å, close to the high end of the range estimated from the Guinier plot (Figure 8.16C, Table 8.3). The Kratky plot suggests that M11:SUMO-BECN1^{AFM} FL is well-folded (Figure 8.16D). The normalized spatial discrepancy of 10 generated *ab initio* molecular models is 0.73 ± 0.04 . Further, the molecular mass estimated from V_c is 205.0 kDa (Table 8.3), which is

slightly larger than the theoretical molecular mass of 165.5 kDa expected for a M11:SUMO-BECN1^{AFM} FL heterotetramer.

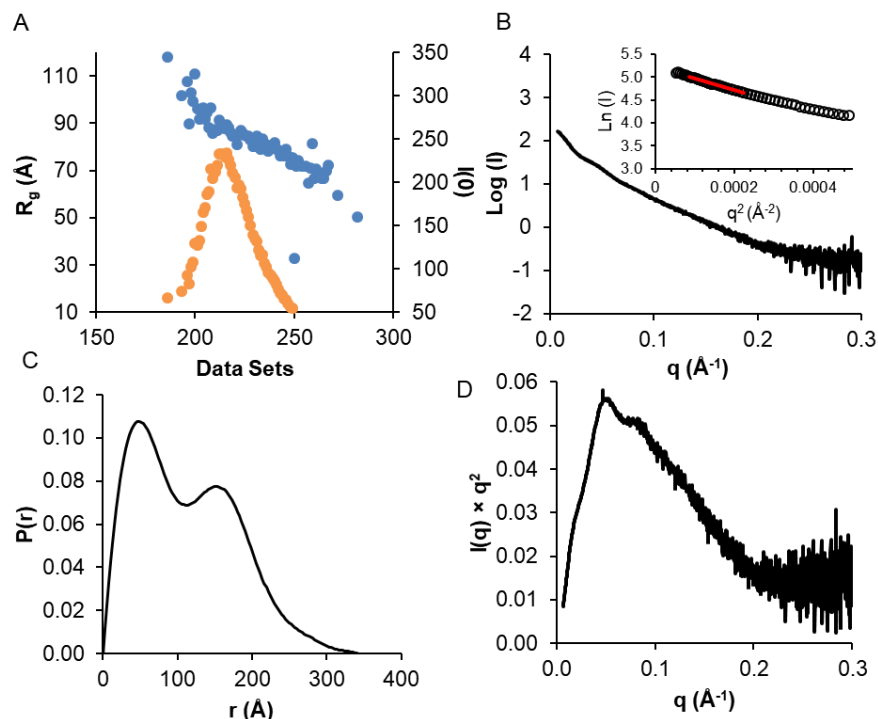


Figure 8.16. SEC-SAXS results for M11:SUMO-BECN1^{AFM} FL. (A) $I(0)$ (orange) and R_g (blue) as a function of time for the SEC-SAXS run. (B) plot of $\log I(q)$ versus q with the inset showing the Guinier plot. (C) $P(r)$ distribution. (D) Kratky plot.

The SAXS analysis of SUMO-BECN1^{AFM} FL and its complex with M11 suggests that M11:SUMO-BECN1^{AFM} FL has a similar R_g but slightly larger D_{max} compared to unbound BECN1.

8.3.5. Our current BECN1 and M11:BECN1 complex samples are not suitable for EM

We attempted to perform negative staining for BECN1 and its complex with M11, initially using SUMO-BECN1^{AFM} FL. The negative-stained EM images displayed substantial sample aggregation, and though single particles were observed, the particles are not clear or sharp enough (Figure 8.17), which may due to the high flexibility and small size of the sample. The quality of the negative-stained images of the samples suggests that these samples are not suitable for collecting cryo-EM data in order to determine the protein structure.

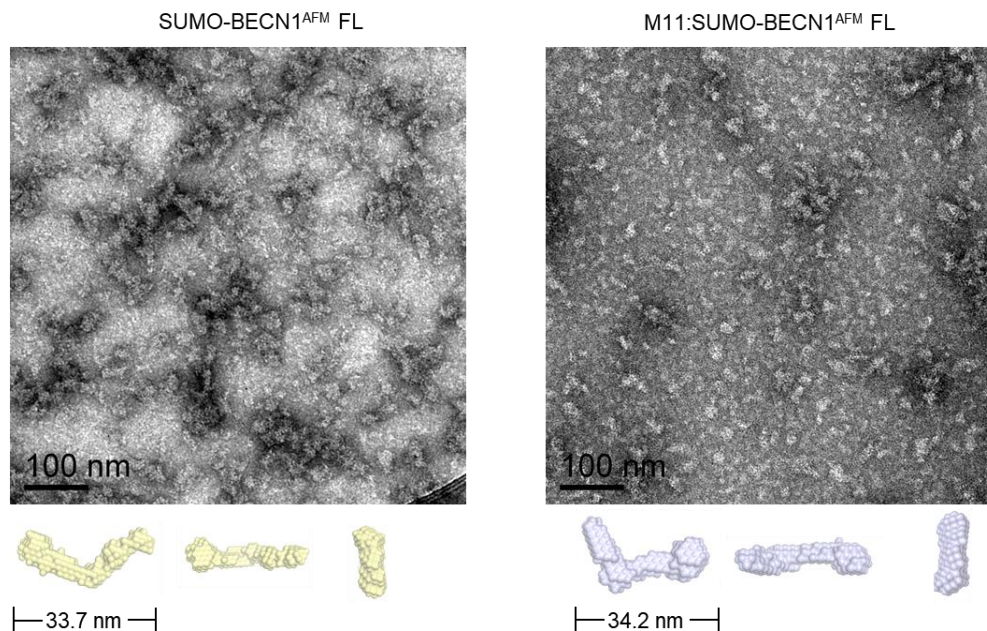


Figure 8.17. Negative-stained images of (A) SUMO-BECN1^{AFM} FL (left panel) and M11:SUMO-BECN1^{AFM} FL (right panel). The SAXS envelopes of each sample are shown below each image. The middle envelope is a rotation of the left envelope about x-axis for 90°, and the right envelope is rotation of the left envelope about y-axis for -90°.

Next, we attempted to obtain negative-stained EM images for the MBP-BECN1^{Δ31-104,AFM} and the M11:MBP-BECN1^{Δ31-104,AFM} complex. The molecular mass of these samples is ~50 kD larger than that of the SUMO-tagged samples we used initially. In addition, most of the BECN1 IDR is truncated in these MBP-tagged samples, which significantly reduces their flexibility. Both the MBP-BECN1^{Δ31-104,AFM} and M11:MBP-BECN1^{Δ31-104,AFM} were tested at initial concentrations of 0.43 μM and 0.29 μM respectively, but this resulted in aggregated particles (Figure 8.18A,C). Then each sample was diluted 5-fold to ~0.086 μM and 0.058 μM, respectively and reimaged. Single particles were observed in the negative-stained images of these diluted samples (Figure 8.18B,D). Unfortunately however, the concentration of the diluted M11:MBP-BECN1^{Δ31-104,AFM} samples is ~3-4 times smaller than the K_d of M11 binding to BECN1^{AFM} FL, suggesting that the imaged particles likely do not correspond to a complex of M11 and MBP-BECN1^{Δ31-104,AFM}.

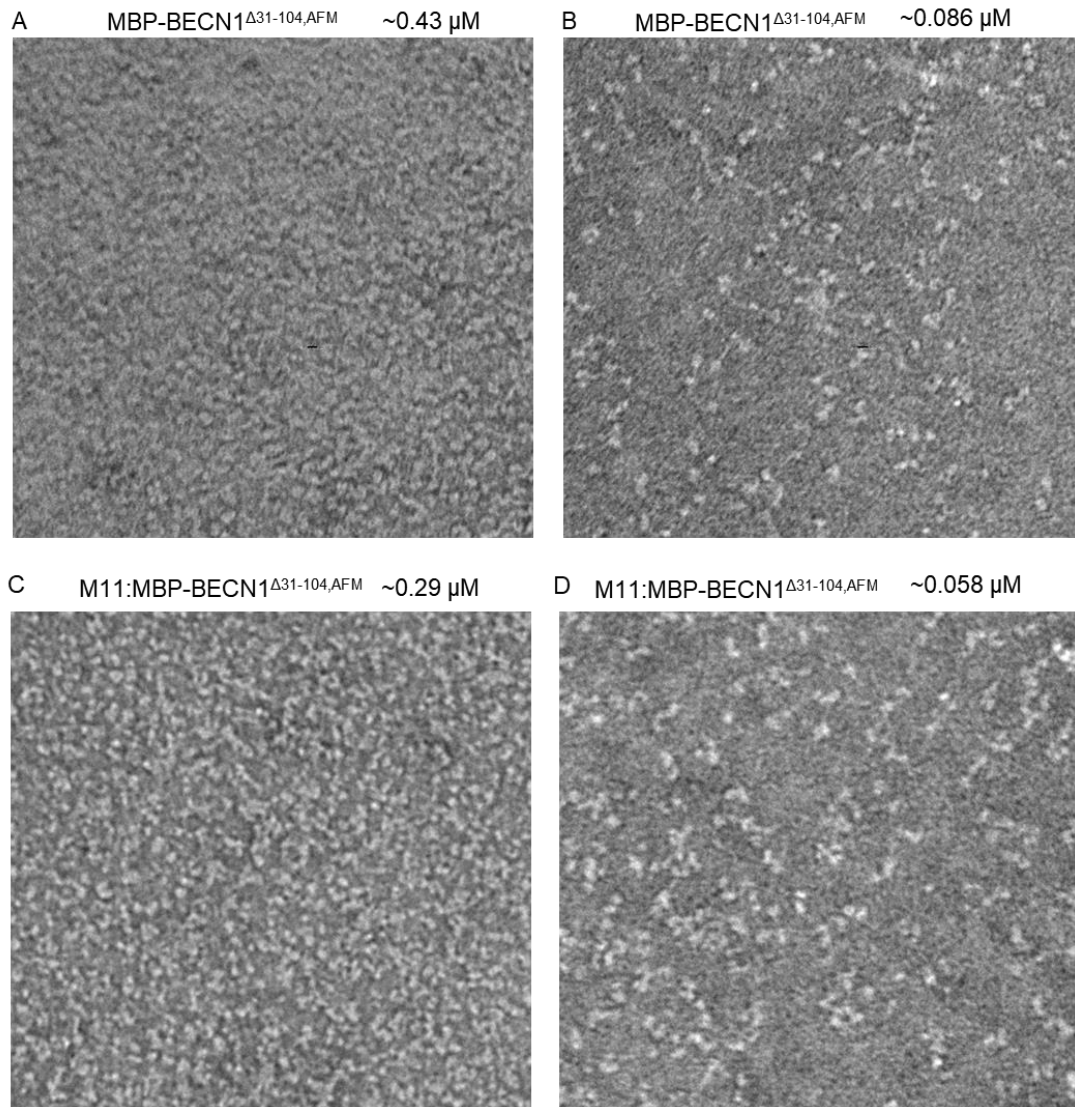


Figure 8.18. Cryo-negatively stained images of (A) and (B) MBP-BECN1^{Δ31-104,AFM} and (C) and (D) M11:MBP-BECN1^{Δ31-104,AFM}. Samples used for (B) and (D) is a 5-time dilution of samples of (A) and (C).

8.4. Conclusions and Discussion

In this Chapter, we used several biophysical methods to investigate the interactions between M11 and BECN1^{Δ31-104} or FL. Our ITC results suggest that BECN1 homodimerization does not impact its interaction with M11. Our SAXS data analyses and EOM modeling suggests that, as expected, both BECN1^{Δ31-104} and FL adopt flexible conformations. BECN1 flexibility

may decrease upon binding M11, but the current SAXS data do not provide unambiguous information regarding the impact of M11 binding on the flexibility and conformation of BECN1.

Lastly, we assessed the potential of using EM to investigate the structures of BECN1^{Δ31-104} or FL and their complexes with M11. Our preliminary negative-stain micrographs suggest that the samples we tested are not suitable for cryo-electron microscopy, due to the high conformational flexibility of BECN1 and the low binding affinity between BECN1 and M11 relative to the sample concentration required for good particle dispersion during EM.

Therefore, we were unable to conclusively determine the overall structure of BECN1 and how M11-binding impacts its conformation using the biophysical methods accessible to us.

CHAPTER 9. INVESTIGATION OF BCL-X_L INTERACTION WITH BECN1

9.1. Introduction

Various BCL2 homologs, including cellular and viral BCL2 homologs, down-regulate autophagy by binding to the BECN1 BH3D. In order to completely understand the regulation of autophagy by BCL2 homologs, it is important to delineate similarities and differences in the interactions of different BCL2 homologs with BECN1. We have investigated the mechanism by which M11, a murine γ HV68 BCL2 homolog, down-regulates BECN1-mediated autophagy in Chapter 7 & 8. Bcl-X_L, a human anti-apoptotic protein, binds to the BECN1 BH3D with affinity comparable to M11. In this chapter, we report our investigation of Bcl-X_L:BECN1 interaction.

We used isothermal titration calorimetry (ITC) to quantify the binding affinity and thermodynamics of Bcl-X_L binding to different multi-domain BECN1 fragments to assess the potential role of other BECN1 domains in binding. Further, we attempted to use circular dichroism (CD) to assess the impact of Bcl-X_L binding on the secondary structure content and thermostability of multi-domain BECN1 fragments. Lastly, we examined the overall shape and flexibility of multi-domain BH3D-containing BECN1 fragments and their complexes with Bcl-X_L using size-exclusion chromatography (SEC) in tandem with small angle X-ray scattering (SAXS). The combined results of this study provide useful information on the Bcl-X_L:BECN1 interaction, enabling us to better understand the differences between Bcl-X_L:BECN1 and M11:BECN1 interactions.

9.2. Materials and Methods

9.2.1. Protein overexpression and purification

The Bcl-X_L (residues 1-208, N52D/N66D) construct was cloned, along with a C-terminal His₆-tag, into the *NdeI* and *NotI* restriction sites of pET29, and expressed and purified as

described (Su *et al.*, 2014). Preparation of all the BECN1 fragments used in this Chapter has been described in Chapter 7.

Different complexes of Bcl-X_L:BECN1 fragments were obtained by co-transforming and co-expressing Bcl-X_L and the BECN1 fragment in *E. coli* Arctic Express cells. Cells were cultured as described for the BECN1 fragments in Chapter 7, except that two antibiotics, 100 µg/ml ampicillin and 15 µg/ml kanamycin were used in the medium. After over-expression, cells were harvested, lysed, and debris clarified as described in Chapter 7. The clarified lysate was flowed over 10 ml amylose affinity resin (GE Healthcare) in a gravity column, followed by on-column cleavage using GST-TEV protease (3 mg TEV protease per L cell culture) to remove the MBP tag from the BECN1 fragments. The cleaved protein was washed off with two column volumes of lysis buffer, and the washed protein was purified further by Ni-NTA affinity chromatography as described for BECN1:M11 complexes in Chapter 7. The eluted protein was purified to homogeneity by SEC using a Superdex 200 10/300 GL or a Superose 6 increase GL column (GE Healthcare), then concentrated in SEC buffer, flash-frozen, and stored at -80 °C.

9.2.2. ITC, CD, and SAXS experiments and analyses were performed as described in Chapter 7

9.3. Results

9.3.1. Expression and purification results of Bcl-X_L:BECN1

Bcl-X_L:BECN1 complexes were over-expressed in *E. coli* Arctic Express cells and purified to homogeneity by amylose and Ni-NTA affinity chromatography, followed by SEC. Despite the small aggregation shoulder, the major SEC peak and distinct bands corresponding to the two proteins on SDS-PAGE indicate that each SEC sample was pure and homogenous (Figure 9.1, 9.2).

The apparent molecular mass of Bcl-X_L:BECN1 BH3D-FHD-CCD, calculated from the elution volume (12.3 ml) of the major SEC peak (Figure 9.2), is 187.0 kD, which is ~2 times larger than the theoretical molecular mass of 87.3 kD expected for the Bcl-X_L:BH3D-FHD-CCD heterotetramer, which suggests that Bcl-X_L:BH3D-FHD-CCD is an elongated heterotetramer. The final yield of the purified Bcl-X_L:BH3D-FHD-CCD was 1.3 mg / L of bacterial culture.

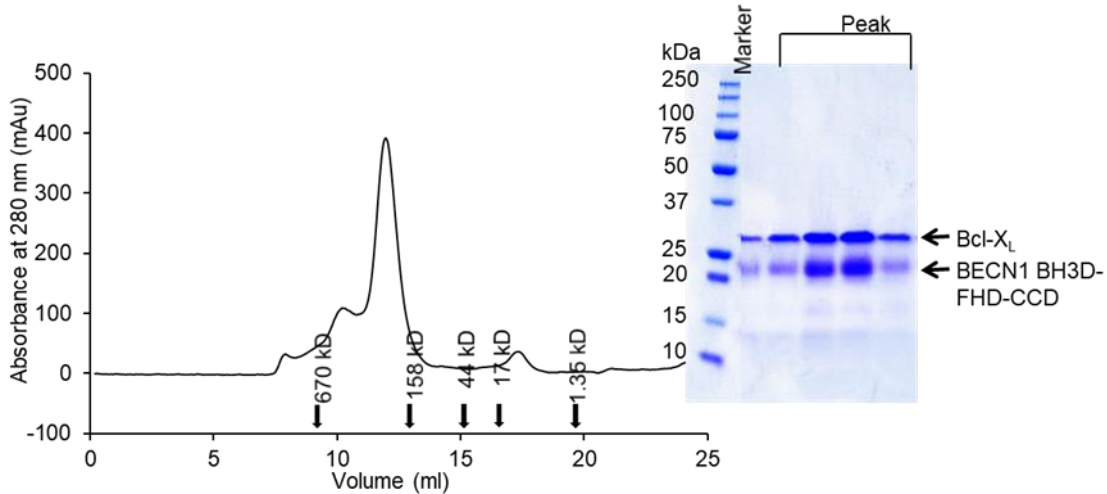


Figure 9.1. Size exclusion chromatogram and the corresponding SDS-PAGE of Bcl-X_L: BH3D-FHD-CCD complex. Elution positions of SEC standards are indicated by arrows.

The apparent molecular mass of Bcl-X_L:BECN1 BH3D-FHD-CCD-BARAD^{AFM}, calculated from the elution volume (15.3 ml) of the major SEC peak (Figure 9.2), is 199.1 kD, which is ~1.5 times larger than the theoretical molecular mass of 129.7 kD expected for the Bcl-X_L: BH3D-FHD-CCD-BARAD^{AFM} heterotetramer, which suggests that the Bcl-X_L:BH3D-FHD-CCD-BARAD^{AFM} is an elongated heterotetramer. The final yield of the purified Bcl-X_L:BH3D-FHD-CCD-BARAD^{AFM} was 1.7 mg / L of bacterial culture.

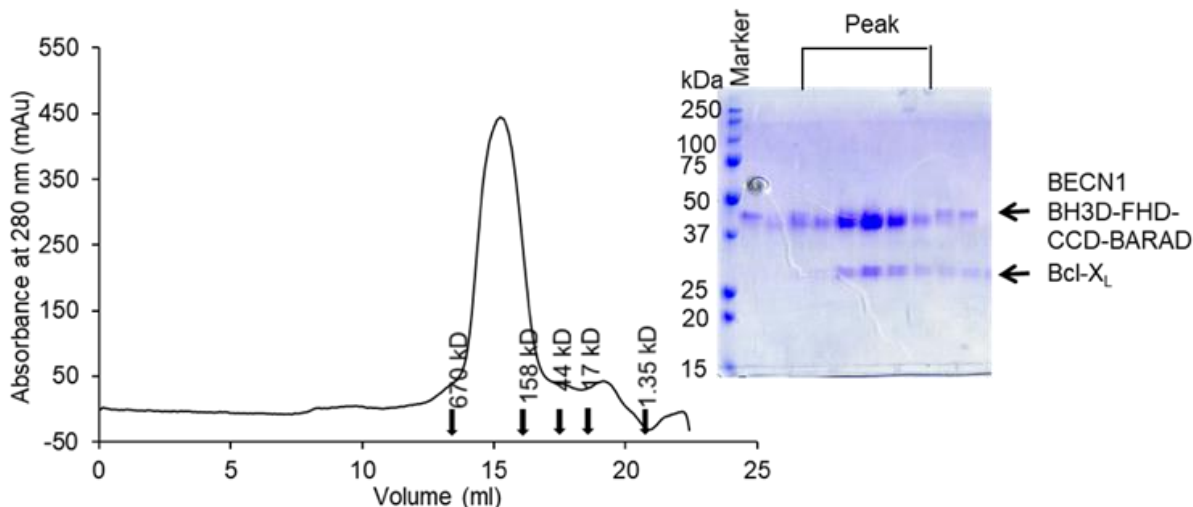


Figure 9.2. Size exclusion chromatogram and the corresponding SDS-PAGE of Bcl-X_L:BEEN1 BH3D-FHD-CCD-BARAD^{AFM} complex. Elution positions of SEC standards are indicated by arrows.

9.3.2. Bcl-X_L-binding affinity is not increased by BEEN1 domains other the BH3D

We used ITC to quantify and compare binding affinities of Bcl-X_L to various BEEN1 fragments comprised of different domains (Table 9.1, Figure 9.3). As expected, BEEN1 fragments that do not contain the BH3D, i.e. the FHD-CCD or CCD-BARAD, do not bind to Bcl-X_L, confirming that the BH3D is required for binding of Bcl-X_L to BEEN1. Therefore, the FHD-CCD and CCD-BARAD were not used for subsequent experiments in this study.

The favorable free energy of all the other interactions is due to enthalpic contributions rather than due to entropic contributions (Table 9.1). For all the BEEN1 fragments, the negative ΔS likely reflects or partially reflects the increased structure of BEEN1 BH3D and Bcl-X_L upon interaction, which proceeds despite the unfavorable enthalpic contributions, due to the enthalpic compensation. The enthalpic contributions to binding are somewhat larger for FHD-containing BEEN1 fragments, but this is compensated by an increased enthalpic penalty, resulting in binding affinities comparable to the other BEEN1 fragments tested.

In contrast to the interactions with M11 described in Chapter 7, Bcl-X_L binds with similar affinity to the isolated BH3D and other BH3D-containing BEEN1 fragments, with the BARAD-

containing BECN1 fragments binding with marginally weaker affinity than the other fragments (Table 9.1). This suggests that BECN1 domains other than the BH3D do not play a significant role in facilitating the interaction with Bcl-X_L. Thus, while the BECN1 BH3D has been shown to be essential for binding the diverse BCL2 homologs, there appear to be differences in how other BECN1 domains interact with diverse BCL2 homologs.

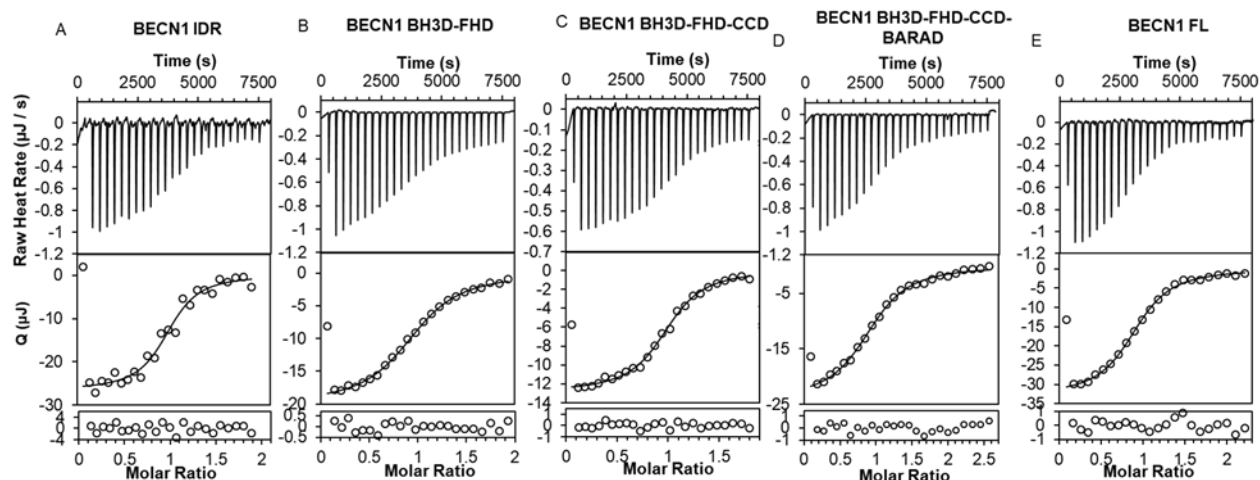


Figure 9.3. Representative plots of ITC for Bcl-X_L:BEcn1 interactions. Upper panel: raw data; lower panel: integrated heat and theoretical fit by independent interaction model from TA Analysis. (A) 300 µM Bcl-X_L titrated into 52 µM MBP-BECN1 IDR. (B) 179 µM Bcl-X_L titrated into 29 µM BECN1 BH3D-FHD. (C) 125 µM Bcl-X_L titrated into 23 µM BECN1 BH3D-FHD-CCD. (D) 236 µM Bcl-X_L titrated into 30 µM BECN1 BH3D-FHD-CCD-BARAD^{AFM}. (E) 490 µM Bcl-X_L titrated into 64 µM BECN1^{AFM} FL.

Table 9.1. Thermodynamics of binding of Bcl-X_L to BEcn1 fragments.

BEcn1 Fragments	Bcl-X _L			
	K _d (µM)	ΔH (kJ/mol)	ΔS (J/K·mol)	ΔG (kJ/mol)
BH3D	1.95 ± 0.19	-43.57 ± 1.44	-36.89 ± 4.53	-32.58 ± 0.23
BH3D-FHD	1.94 ± 0.03	-57.96 ± 2.59	-88.34 ± 8.71	-32.06 ± 0.04
IDR	1.46 ± 0.04	-45.21 ± 0.11	-45.16 ± 0.60	-32.20 ± 0.06
BH3D-FHD-CCD	1.06 ± 0.48	-51.65 ± 2.33	-64.42 ± 4.15	-33.09 ± 1.14
BH3D-FHD-CCD-BARAD ^{AFM}	2.49 ± 0.19	-51.19 ± 0.76	-67.33 ± 3.25	-31.45 ± 0.19
FL	2.36 ± 0.59	-51.00 ± 0.66	-66.17 ± 0.15	-31.50 ± 0.42

9.3.3. CD cannot be used to evaluate changes in secondary structure content upon Bcl-X_L binding to the BECN1 BH3D-FHD-CCD

We attempted to use CD to investigate changes in the secondary structure of the BECN1 BH3D-FHD-CCD upon binding Bcl-X_L (Table 9.2). The CD results show that un-complexed Bcl-X_L has 98, 24, and 92 residues in helical, strand and coil conformations respectively (Table 9.2). According to the NMR structure (PDB ID: 2LPC), Bcl-X_L (residues 1-44 & 86-209) has 128, 0, and 57 (including 12 His-tag and 4 linker residues) in helical, strand, and coil conformations, which has more helical residues than that estimated from CD. Our Bcl-X_L construct used for CD contains the disordered region (residues 45-85), which may destabilize the protein and result in the decreased helical content. As reported in Chapter 7, BH3D-FHD-CCD has 89, 9, and 65 residues in helical, strand and coil conformations respectively. The Bcl-X_L:BECN1 BH3D-FHD-CCD complex has 191, 29 and 159 residues in helical, strand and coil conformations respectively (Table 9.2). As neither of these proteins, nor their complex is expected to have stable β -sheet secondary structure, we will consider the sum of the strand and coil content for each case. Therefore, the Bcl-X_L:BH3D-FHD-CCD has ~4 additional residues in helical conformation and ~ 2 fewer residues in strand + coil conformation, relative to the sum of residues in helical or strand + coil residues in the un-complexed BH3D-FHD-CCD and Bcl-X_L.

Table 9.2. CD analysis: Estimated secondary structure content.

Sample	Total # of residues	Average estimated secondary structure content					
		Helix		Strand		Coil	
		%	#	%	#	%	#
Bcl-X _L	214	45.9 ± 3.5	98 ± 7	11.3 ± 1.5	24 ± 3	42.8 ± 4.6	92 ± 10
BECN1 BH3D-FHD-CCD	164	54.3 ± 2.5	89 ± 4	5.7 ± 2.1	9 ± 4	39.7 ± 4.7	65 ± 8
Bcl-X _L :BECN1 BH3D-FHD-CCD complex	378	50.5 ± 3.2	191 ± 12	7.8 ± 1.7	29 ± 7	42.1 ± 4.6	159 ± 18

However, it should be noted that only 5 μ M Bcl-X_L:BECN1 BH3D-FHD-CCD complex was used for the CD experiments, as higher concentrations would raise the high tension applied

to the photomultiplier tube of the instrument to higher than the acceptable limit of 700 volts. Given that the K_d of $1.06 \pm 0.48 \mu\text{M}$ for the Bcl-X_L: BH3D-FHD-CCD interaction, we expect that more than one third of the Bcl-X_L molecules are dissociated from the BH3D-FHD-CCD at the concentrations used for the CD experiments. Therefore, we cannot draw reliable conclusions from the CD results for Bcl-X_L:BH3D-FHD-CCD complex.

9.3.4. The Bcl-X_L:BECN1 BH3D-FHD-CCD complex has a flexible, elongated conformation

We used SEC-SAXS to characterize the overall shape and flexibility of Bcl-X_L:BH3D-FHD-CCD complex. First, we analyzed the SAXS data for Bcl-X_L (Figure 9.4).

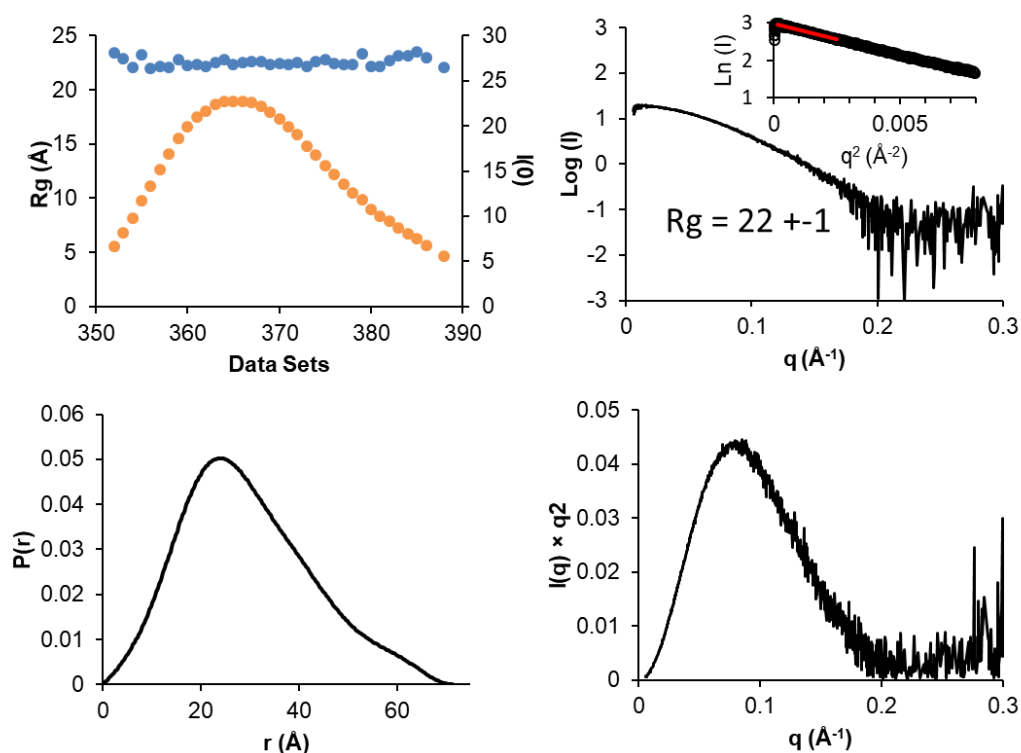


Figure 9.4. SAXS analysis of Bcl-X_L. (A) $I(0)$ (orange) and R_g (blue) as a function of time for the SEC-SAXS run. (B) plot of $\log I(q)$ versus q with the inset showing the Guinier plot. (C) $P(r)$ distribution. (D) Kratky plot.

The variation of $I(0)$ across the Bcl-X_L SEC-SAXS peak (Figure 9.4A) is consistent with the variation in elution concentration. The R_g determined from Guinier analyses of the intensity-

normalized, buffer-subtracted data is uniform across the scattering peak (Figure 9.4A). The linear Guinier plot at $qR_g < 1.3$ indicates that the sample does not aggregate (Figure 8.4B). The $P(r)$ distribution indicates that Bcl-X_L is a globular protein with an average R_g of 23 Å and D_{max} of 75 Å (Figure 9.4C, Table 9.3). The Kratky plot suggests that Bcl-X_L is well-folded (Figure 9.4D). The normalized spatial discrepancy of 10 generated *ab initio* molecular models is 0.46 ± 0.02 . Further, the molecular mass estimated from the V_c is 34.3 kDa (Table 9.3), which is larger than the theoretical molecular mass of 24.0 kDa expected for a Bcl-X_L monomer. The larger molecular mass estimated from V_c may due to disordered regions of Bcl-X_L.

Table 9.3. Structural parameters from data analysis and EOM modeling.

Guinier analysis	BH3D-FHD - CCD*	Bcl-X _L :BH3D-FHD-CCD	BH3D-FHD - CCD-BARAD*	Bcl-X _L :BH3D-FHD-CCD-BARAD ^{AFM}	Bcl-X _L				
I(0)	18.7 ± 0.5	90.3 ± 1.2	83.0 ± 1.0	24.8 ± 1.2	19.9 ± 0.1				
q_{min} (Å ⁻¹)	0.0001	0.0001	0.0001	0.0001	0.0001				
qR_g max	1.3	1.3	1.3	1.3	1.3				
R ²	0.76	0.93	0.96	0.92	0.99				
P(r)									
I(0) (cm ⁻¹)	19.8 ± 0.6	104.1 ± 1.7	86.1 ± 0.8	25.3 ± 2.7	20.0 ± 0				
R_g (Å)	58 ± 2	71 ± 1	73 ± 1	78 ± 3	23 ± 0				
D_{max} (Å)	199	254	235	267	71				
q range (Å ⁻¹)	0.0118-0.1596	0.0172-0.1422	0.0067-0.1209	0.0082-0.1122	0.0126-0.3560				
χ^2 (total from GNOM)	0.996	0.952	0.990	0.975	0.991				
MW from V_c (kDa)	32.9	81.9	61.8	72.3	34.3				
Theoretical MW (kDa)	19.6	43.7	40.8	64.8	24.0				
EOM		Pool	Pool1	Pool2	Pool3	Pool1	Pool2	Pool3	Did not fit the model
χ^2	0.96	1.3	1.2	1.6	1.2	1.0	-	1.0	
R_{flex} (% , selected ensemble)	64.7	85.5	69.9	68.7	66.8	76.9	-	73.1	
R_{flex} (% , initial pool)	88.3	89.1	83.3	81.0	86.3	85.9	-	85.2	
R_{sigma}	0.37	1	0.50	1.47	0.48	0.82	-	0.66	

*The results of these fragments are taken from Chapter 7.

The variations of I(0) across the Bcl-X_L:BECN1 BH3D-FHD-CCD SEC-SAXS peak (Figure 9.5A) and the SEC eluate concentration are consistent. The R_g determined from Guinier

analyses of intensity-normalized, buffer-subtracted data ranges between 50-60 Å across the scattering peak (Figure 8.5A), indicating that the Bcl-X_L:BH3D-FHD-CCD is flexible. The linear Guinier plot at $qR_g < 1.3$ indicates the sample does not aggregate (Figure 9.5B). The $P(r)$ curve indicates that Bcl-X_L:BH3D-FHD-CCD is an elongated, multi-domain protein with an average D_{max} of 254 Å and R_g of 70 Å, which is larger than the R_g range determined from Guinier analyses (Figure 9.5C, Table 9.3). The Kratky plot suggests that Bcl-X_L:BH3D-FHD-CCD is folded (Figure 9.4D). The normalized spatial discrepancy of 10 generated *ab initio* molecular models is 0.58 ± 0.02 . The molecular mass estimated from V_c is 81.9 kDa (Table 9.3), similar to the theoretical molecular mass of 86.8 kDa expected for a Bcl-X_L:BH3D-FHD-CCD heterotetramer.

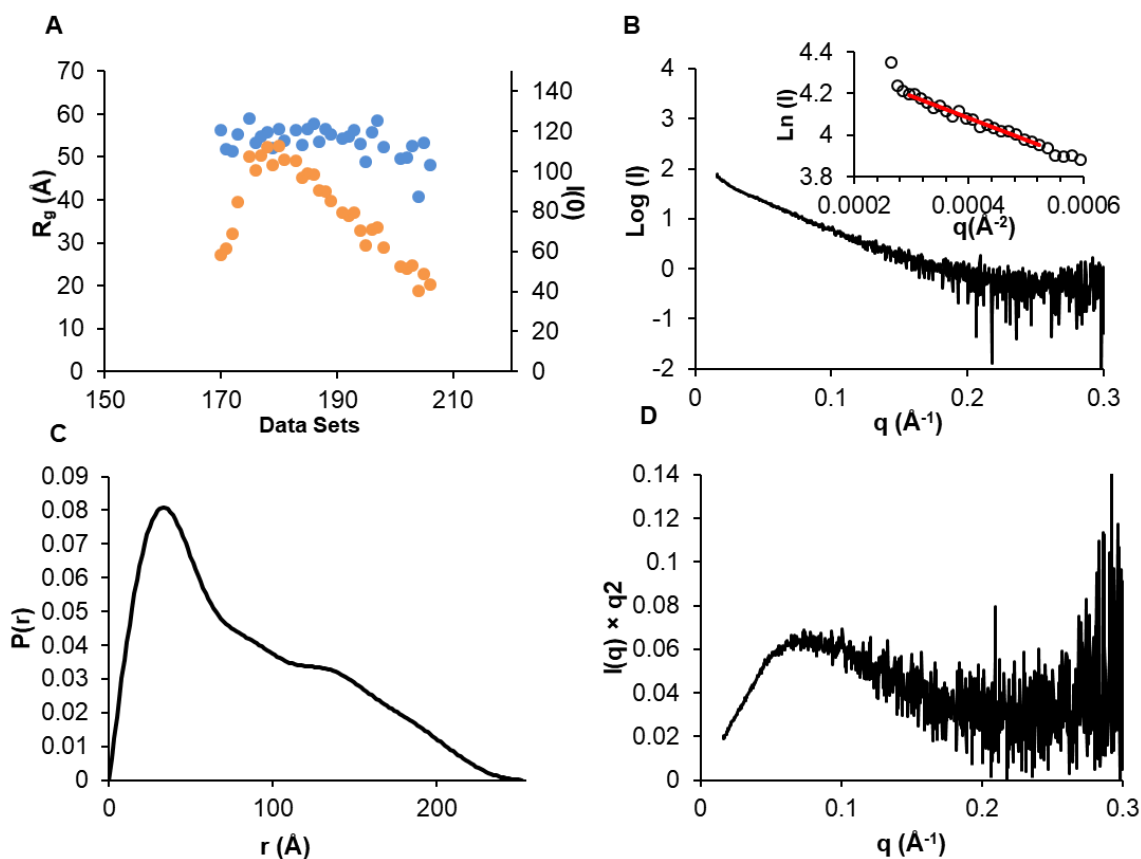


Figure 9.5. SAXS analysis of Bcl-X_L:BEEN1 BH3D-FHD-CCD. (A) $I(0)$ (orange) and R_g (blue) as a function of time for the SEC-SAXS run. (B) plot of $\log I(q)$ versus q with the inset showing the Guinier plot. (C) $P(r)$ distribution. (D) Kratky plot.

In order to account for conformational flexibility of the Bcl-X_L:BH3D-FHD-CCD complex, EOM was used to generate an initial pool of conformers, based on available structures of the Bcl-X_L:BECN1 BH3D complex (PDB ID:2P1L, Bcl-X_L structure covers residues 1-24 & 84-198), CCD (PDB ID:5HHE) and FHD residues 157-171 (PDB ID:5EFM), with the remaining residues modelled as flexible. Conformers for which the theoretical scattering curves best fit the experimental SAXS data, with an overall χ^2 of 1.3 (Figure 9.6A), were included in the “selected ensemble”. EOM analyses show that the R_g and D_{max} distribution for the Bcl-X_L:BH3D-FHD-CCD conformers in the selected ensemble overlaps well with those of the initial pool (Figure 9.6B,C), indicating that the flexibility of conformers in the selected ensemble and the entire pool are comparable. Indeed, the selected ensemble of conformers has a R_{flex} of 85%, similar to 89% for the initial pool (Table 9.3), and a $R_{sigma} = 1$, which also suggests that the selected ensemble of conformers is as flexible as those from the entire pool generated by EOM.

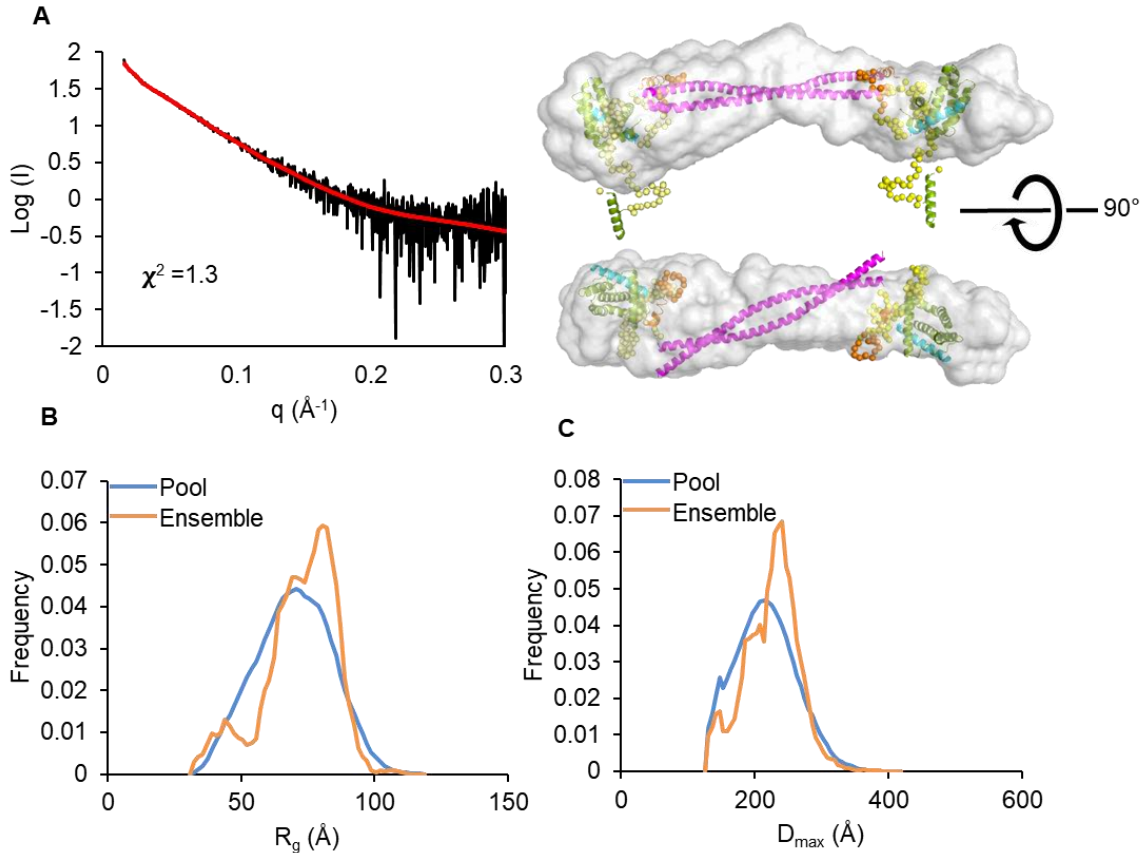


Figure 9.6. EOM modeling for the Bcl-X_L:BECN1 BH3D-FHD-CCD complex. (A) Left panel: Fit of the experimental data to the theoretical scattering curve calculated from the selected best fit ensemble of conformers of BH3D-FHD-CCD; right panel: representative model from the ensemble (Magenta: CCD; orange: FHD; cyan: BH3D; lime: Bcl-X_L; yellow: linker between domains. Structured regions are shown as cartoon; flexible regions as spheres) superimposed into the filtered SAXS envelope (shown as grey surface). (B) R_g distribution and (C) D_{max} distribution of conformers in the pool (blue) and ensemble (orange) plot.

9.3.5. Bcl-X_L:BECN1 BH3D-FHD-CCD-BARAD^{AFM} adopts flexible and elongated conformation, with OH preferably packing against CCD or being flexible

We also used SEC-SAXS to characterize the overall shape and flexibility of the Bcl-X_L:BH3D-FHD-CCD-BARAD^{AFM} complex. The variation of $I(0)$ across the Bcl-X_L:BH3D-FHD-CCD-BARAD^{AFM} SEC-SAXS peak (Figure 9.6A) is consistent with variation in SEC elute concentration. The R_g determined from Guinier analyses of intensity-normalized, buffer-subtracted data ranges between 50-70 Å across the scattering peak (Figure 9.7A), indicating that the Bcl-X_L:BH3D-FHD-CCD-BARAD^{AFM} complex is flexible. The linear Guinier plot at $qR_g <$

1.3 indicates that the sample does not aggregate (Figure 9.7B). The $P(r)$ curve indicates that Bcl-X_L:BH3D-FHD-CCD-BARAD^{AFM} is an elongated, multi-domain protein with an average R_g of 78 Å (Figure 9.7C, Table 9.3). The Kratky plot suggests that Bcl-X_L:BH3D-FHD-CCD-BARAD^{AFM} is folded (Figure 9.7D). The normalized spatial discrepancy of 10 generated *ab initio* molecular models is 0.58 ± 0.02 . The molecular mass estimated from the V_c is 72.3 kDa (Table 9.3), which is smaller than the theoretical mass of 130.4 kDa expected for a Bcl-X_L:BH3D-FHD-CCD-BARAD^{AFM} dimer.

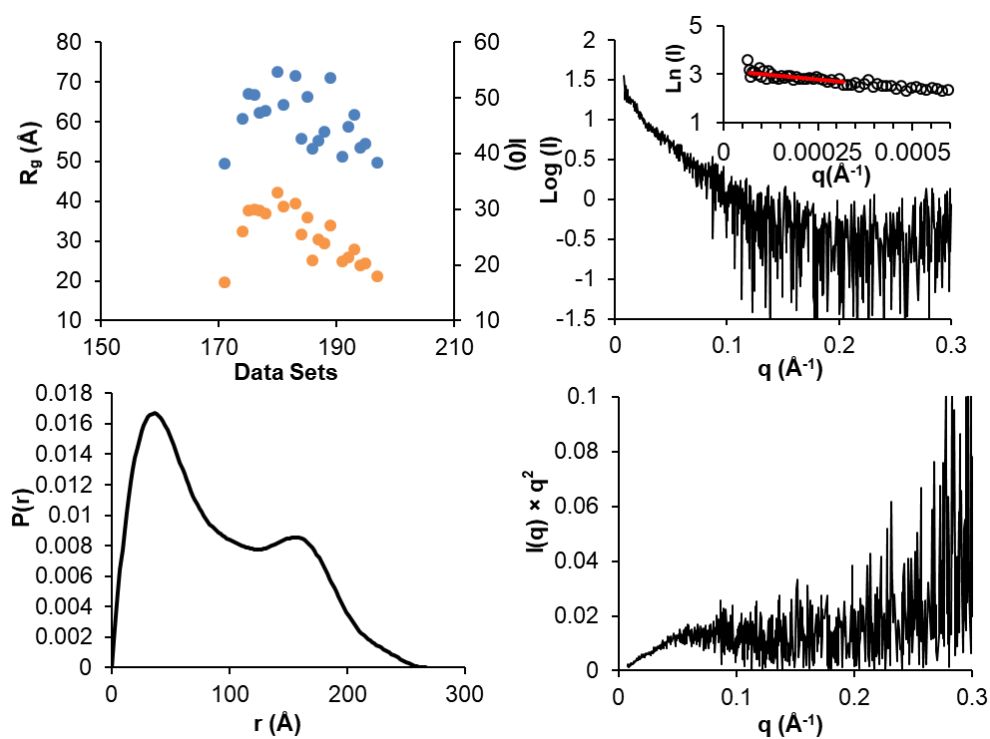


Figure 9.7. SAXS analysis of Bcl-X_L:BEEN1 BH3D-FHD-CCD-BARAD^{AFM}. (A) $I(0)$ (orange) and R_g (blue) as a function of time for the SEC-SAXS run. (B) plot of $\log I(q)$ versus q with the inset showing the Guinier plot. (C) $P(r)$ distribution. (D) Kratky plot.

We then used EOM to generate pools of conformers for the BEEN1 BH3D-FHD-CCD-BARAD^{AFM}. Since previous studies (Glover *et al.*, 2017) have shown that the OH transitions between CCD and BARAD in the CCD-BARAD fragment, three separate pools of conformers were generated. All three pools were based on available structures of the Bcl-X_L:BH3D (PDB

ID:2P1L, Bcl-X_L structure covers residues 1-24 & 84-198), but had different structural information input for the CCD and BARAD; with pool 1 being based on the crystal structure of the CCD (PDB ID: 5HHE) wherein CCD residues 175-265 form a coiled-coil and the structure of BARAD (PDB ID: 4DDP), but excluding the OH; pool 2 was based on residues 192-247 modelled as coiled-coil; and residues 248-450 (including OH) modelled as packed with the BARAD (PDB ID: 4DDP), and the NES modelled as flexible; pool 3 was based on residues 192-247 modelled as in the CCD structure and residues 266-450 being modelled as per the BARAD structure, with both the NES and OH being modelled as flexible.

The ensemble selected from pool 1, for which the theoretical scattering curves best fit the experimental SAXS data had an overall χ^2 of 1.0 (Figure 9.8A). EOM analyses show that R_g and D_{max} distribution for conformers in the selected ensemble has a single peak that is narrower than that of the entire pool 1 (Figure 9.8B,C), indicating that Bcl-X_L:BECN1 BH3D-FHD-CCD-BARAD^{AFM} has restrained flexibility. Conformers in the selected ensemble of pool 1 have a R_{flex} of 77%, compared to 86% for the entire pool 1 (Table 9.3), and have a R_{sigma} of 0.82 (Table 9.3), indicating that the selected ensemble conformers are slightly less flexible than the entire pool 1.

Our attempts to use EOM to generate pool 2 failed to output conformers even after computer runtime of several weeks. Therefore, we are unable to report results for pool 2.

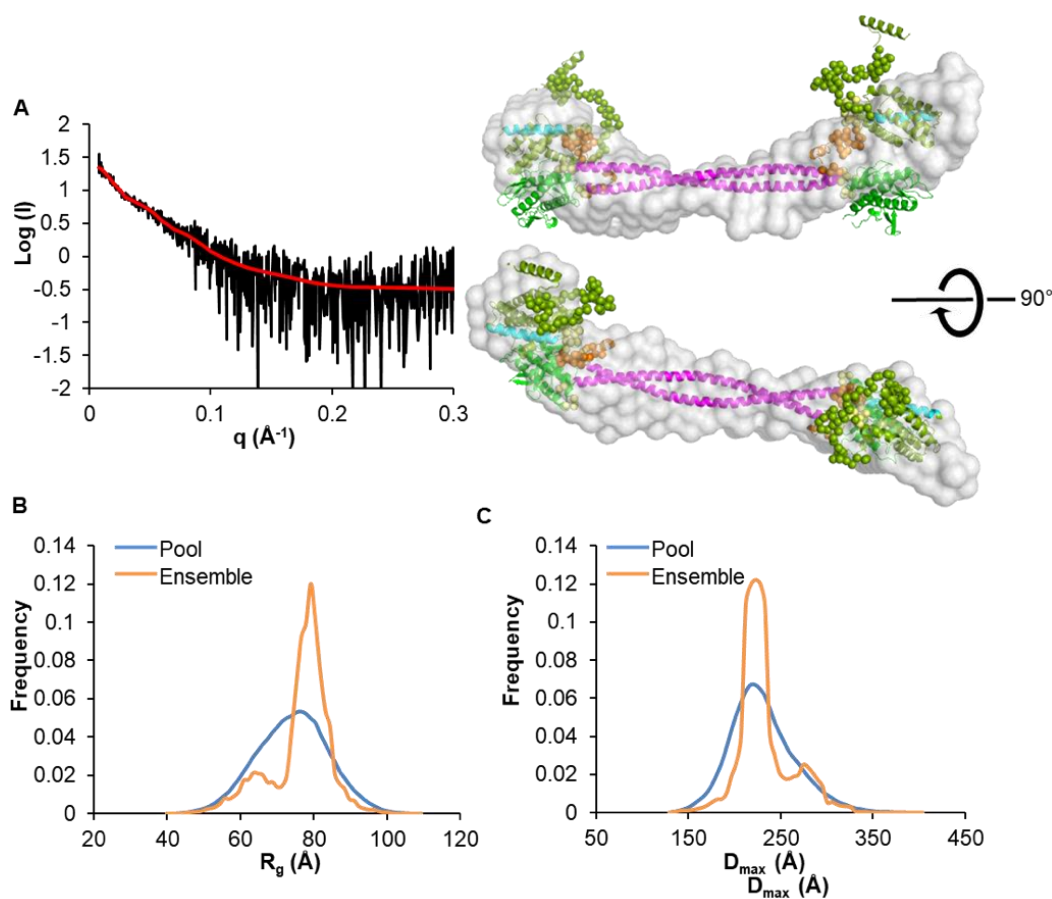


Figure 9.8. EOM modeling (Pool 1) for the Bcl-X_L:BEEN1 BH3D-FHD-CCD-BARAD^{AFM} complex. (A) left panel: Fit of experimental data to theoretical scattering curve calculated from the selected best fit ensemble of conformers of Bcl-X_L:BH3D-FHD-CCD-BARAD^{AFM}; right panel: representative model from the ensemble (Magenta: CCD; orange: FHD; cyan: BH3D; Green: BARAD; lime: Bcl-X_L; yellow: linker between domains. Structured regions are shown as cartoon; flexible region as spheres) superimposed into the filtered SAXS envelope (shown as grey surface). (B) R_g distribution and (C) D_{max} distribution of conformers in the pool (blue) and selected ensemble (orange).

The ensemble selected from pool 3, for which the theoretical scattering curves best fit the experimental SAXS data had an overall χ^2 of 1.0 (Figure 9.9A). EOM analyses show that the R_g and D_{max} distribution for conformers in the selected ensemble exhibits a single peak that is narrower than that of the entire pool 3 (Figure 9.9B,C), indicating that Bcl-X_L:BEEN1 BH3D-FHD-CCD-BARAD^{AFM} has restrained, rather than random flexibility. The conformers in the selected ensemble of pool 1 have a R_{flex} of 73%, compared to 85% for those from the entire pool

1 (Table 9.3), and have a R_{sigma} of 0.86 (Table 9.3), indicating that conformers in the selected ensemble are slightly less flexible than those in the entire pool 3.

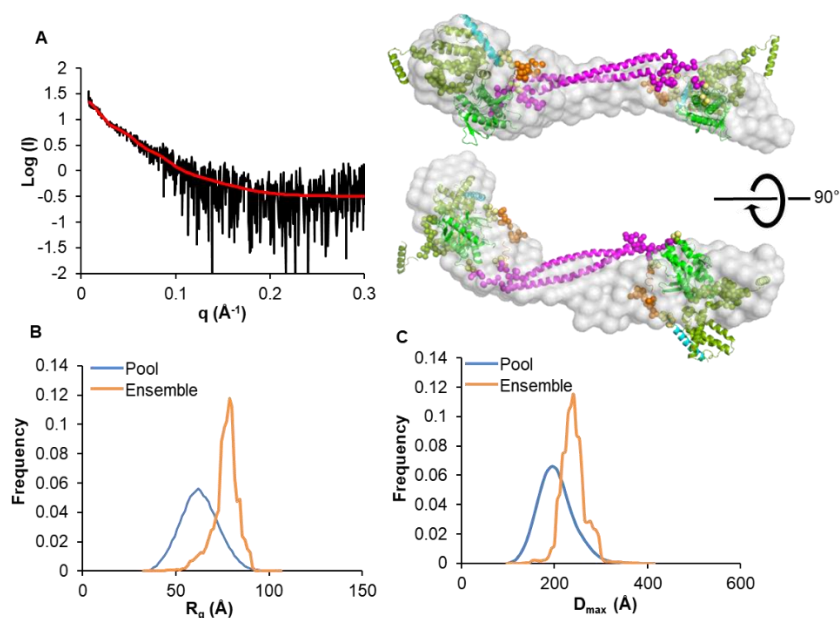


Figure 9.9. EOM modeling (Pool 3) for Bcl- X_L :BEEN1 BH3D-FHD-CCD-BARAD^{AFM} complex. (A) Left panel: Fit of experimental SAXS data to the theoretical scattering curve calculated from the selected best fit ensemble of conformers of Bcl- X_L :FHD-CCD-BARAD; right panel: representative model from the ensemble (Magenta: CCD; orange: FHD; cyan: BH3D; Green: BARAD; lime: Bcl- X_L ; yellow: linker between domains. Structured regions shown as cartoon; flexible region shown as spheres) superimposed into the filtered SAXS envelope (shown as grey surface). (B) R_g distribution of pool (blue) and ensemble (orange) conformations. (C) D_{max} distribution of pool (blue) and ensemble (orange) conformations.

The Bcl- X_L :BH3D-FHD-CCD-BARAD^{AFM} is an elongated, multi-domain protein with an average R_g and D_{max} of 78 Å and 272 Å respectively, which are slightly smaller than the M11:BEEN1-FHD-CCD-BARAD^{AFM} complex R_g and D_{max} of 82 Å and 288 respectively .

9.4. Conclusions and Discussion

In this Chapter, we used several biophysical methods to investigate the interactions between Bcl- X_L and BEEN1. In contrast to the M11:BEEN1 interactions reported in Chapter 7 wherein the BEEN1 IDR and FHD appear to improve binding, our ITC results suggest that BEEN1 regions outside the BH3D do not affect interaction with Bcl- X_L .

We also attempted to use CD to analyze the changes of secondary structure content of BECN1 upon interaction with Bcl-X_L. However, the binding affinity between Bcl-X_L and BECN1 is not high enough to maintain the Bcl-X_L:BECN1 complex during CD. Therefore, we were not able to draw reliable conclusions from the CD experiments. Further, we were also unable to use ITC to quantify the self-association of BH3D-FHD-CCD when in complex with Bcl-X_L, for comparison with the self-association of un-complexed BH3D-FHD-CCD. The BH3D-FHD-CCD homodimerizes with a K_d of ~16 μM, while Bcl-X_L binds to the BH3D-FHD-CCD with an affinity of ~ 1.1 μM. The concentration of the Bcl-X_L: BH3D-FHD-CCD complex in the sample cell is 1.47 μM after the first titration, which is similar to the K_d of Bcl-X_L binding to the BECN1 BH3D-FHD-CCD. Therefore, the total heat change will be a combination of BECN1 homodimer dissociation and Bcl-X_L:BECN1 dissociation, preventing unambiguous interpretation of results.

Our SAXS data analyses and EOM modeling suggests that both Bcl-X_L:BH3D-FHD-CCD and Bcl-X_L:BH3D-FHD-CCD-BARAD^{AFM} complexes are flexible. The flexibility of selected ensemble of models is similar to or slightly smaller than that of the entire computational pool of conformers. Since the Bcl-X_L contains a large flexible loop, it is not possible to draw solid conclusions regarding the contribution of each protein to the overall high flexibility of the Bcl-X_L:BECN1 complexes.

Therefore, we were unable to conclusive determine whether binding to Bcl-X_L involves BECN1 domains besides the BH3D, and whether other BECN1 domains undergo conformational changes. Further biophysical and biochemical studies need to be carried out to test this.

CHAPTER 10. CONCLUSIONS AND FUTURE DIRECTIONS

The work presented in this dissertation aims to understand the conformational flexibility of BECN proteins and how this conformational flexibility enables the BECN1-mediated regulation of autophagy. This is the focus of the research reported in chapters 2 and 3. In chapter 4, we investigate the structure and selected interactions of a human BECN1 paralog, BECN2. Lastly, we also investigate the mechanisms by which selected protein interactions regulate conformational flexibility of BECN1-mediated autophagy. This is the focus of the research reported in chapters 4-9.

In Chapter 2, we show that two invariant CXXC motifs in the BECN1 IDR are responsible for binding Zn^{2+} . Mutation of the cysteines in both CXXC motifs completely abrogates Zn^{2+} -binding by BECN1, while mutation of any one CXXC motif decreases Zn^{2+} binding. My contribution to this project was preparation of BECN1 FL and BECN1 FL Cysteine mutant samples for ICP-MS. Future studies in the lab are now exploring how Zn^{2+} -binding by BECN1 impacts its conformation and cellular autophagy levels.

In Chapter 3, we examine the conformational flexibility of the BECN1 overlap helix (OH) comprising residues 248-265, that has been crystallized in two mutually exclusive packing states, packed within the CCD or against the BARAD. Key to the studies in this project was my finding that the mutation of three residues F359D,F360D,F361D (AFM) would prevent aggregation, enabling us to produce soluble BARAD-containing proteins for our biophysical studies. We show that the OH transitions between these two different packing states, with the predominant state comprising the BARAD. This conformational flexibility significantly impacts BECN1 homodimerization. We also demonstrate that mutation of four of the OH interface residues that mediate OH packing within the CCD as well as against the BARAD, abrogates

starvation-induced up-regulation of autophagy. These results are also reported in (Glover *et al.*, 2017) and Dr. Glover's dissertation.

In Chapter 3, we also attempted to crystallize the BECN1 CCD-BARAD^{AFM} fragment, but the crystallization was not successful. However, a double C353S/C391S mutation facilitated crystallization, suggesting that the C353S/C391S mutation may help stabilize such fragment by forming stronger hydrogen bonds between the hydroxyl of the mutated C353S and the carbonyl oxygen of D361 side chain as well as between the mutated C391S and the carbonyl oxygen of E384, which may help stabilize the structure of loops bearing S353 and S391. Unfortunately, although the BECN1 CCD-BARAD^{AFM,C353S/C391S} mutant crystallized, the crystals did not diffract well, preventing structure solution. Perhaps, the flexibility of the OH as well as the NES within the CCD, results in a non-uniform arrangement and/or packing of the molecules in the crystal lattice, preventing high-quality diffraction from these crystals. Since the OH transitions between packing against the BARAD and the NES within the CCD, but preferentially packs against the BARAD, it may be worth trying to crystallize a BECN1 CCD-BARAD fragment without the NES, which may eliminate conformational flexibility of the OH.

The research reported in Chapter 4, was led by Dr. Minfei Su, who solved the high-resolution crystal structure of the BECN2 CCD and performed detailed mutational, biophysical and structural analyses of BECN2 CCD homodimerization and heterodimerization with Atg14, which has been reported in (Su *et al.*, 2017) as well as in Dr. Su's dissertation. Initially, we created constructs comprising different BECN2 domains and attempted to purify them. We showed that the affinity of M11 binding to the BECN2 BH3D-FHD-CCD is much weaker than to the BECN1 BH3D-FHD-CCD, while the affinity of Bcl-X_L binding to the BECN2 BH3D-FHD-CCD is similar to that of the BECN1 BH3D-FHD-CCD. Despite the differences in the

sequences of BECN2 and BECN1, including BH3D residues shown to be critical for BECN1 binding both M11 and Bcl-X_L, such as BECN1 L116 (Su *et al.*, 2014), which corresponds to BECN2 Q97, the BECN2 BH3D-FHD-CCD binds to both M11 and Bcl-X_L. Not surprisingly, the binding of M11 to the BECN2 BH3D-FHD-CCD is 42-fold weaker than to the BECN1 BH3D-FHD-CCD. Strikingly however, Bcl-X_L binds with similar affinity to the BH3D-FHD-CCD fragments of both BECN2 and BECN1. However, the thermodynamic contributions to the overall binding affinity are different, indicating that the different residues in each BECN paralog result in different thermodynamic drivers for each interaction. Thus, there are clear differences between the binding of BCL2 homologs to different BECN paralogs, suggesting that there are important differences in the mechanisms by which various BCL2 homologs regulate different paralogs. Therefore, it is important to investigate both BECN paralogs found in humans.

The focus of Chapter 5 is to investigate the interaction of GAPR-1 with BECN1, to understand how this interaction down-regulates autophagy. This study led by me is reported in (Li *et al.*, 2017). We demonstrated that the equatorial groove of GAPR-1 may accommodate BECN1 residues 267-284, and the conserved residues lining the equatorial binding groove are important for the BECN1:GAPR-1 interaction. Mutation of five conserved residues lining this groove abrogates BECN1 binding. The 1.27 Å resolution X-ray crystal structure of this pentad mutant GAPR-1 was determined. Comparison with the WT GAPR-1 structure shows that the equatorial groove of the pentad mutant is shallower and more positively charged, and therefore may not efficiently bind BECN1 residues 267–284, which contains many hydrophobic residues.

Further, our results unambiguously indicate that even at solution concentrations of 2 mM, WT GAPR-1 is a monomer, while the pentad mutant homodimerizes with a K_d of ~29 μM. Both WT and pentad mutant GAPR-1 crystallize as homodimers, and notably, the equatorial surface

groove is partially occluded by the partner subunit in the dimeric states crystallized, suggesting that binding partners such as BECN1 would not bind to GAPR-1 dimers. Further, the interaction between GAPR-1 and BECN1 appears to require co-localization and arrangement of GAPR-1 and BECN1 in suitable orientations, which may be facilitated by membrane association *in vivo*. Various cellular factors such as the presence/binding of specific lipids, protein partners, and/or post-translational modifications may also further regulate this interaction via changes in conformation and oligomerization of each partner. Binding of GAPR-1 to BECN1 BARAD residues 267-284 would sterically obstruct binding of autophagy partners such as UVRAG or ATG14, thereby adversely impacting assembly of the autophagy complexes and reducing cellular autophagy levels.

Previous studies showed that F270S and F274S BECN1 mutants disrupt the BECN1:GAPR-1 interaction (Shoji-Kawata *et al.*, 2013), and our model for binding of GAPR-1 to BECN1 BARAD residues 267-284 suggests a mechanism for the disruption of binding caused by these mutations. Our model predicts that BECN1 F270 packs against GAPR-1 hydrophobic residue F144; therefore, the F270S mutation would weaken this hydrophobic packing and the presence of the polar serine hydroxyl group may destabilize the interaction further. The aromatic ring of BECN1 F274 packs against the C β of GAPR-1 S99 with a distance of 3.4 Å. An *in silico* mutation of F274 to serine increases this distance to 5.0 Å between BECN1 S274 and GAPR-1 S99, abrogating this packing and likely destabilizing the BECN1:GAPR-1 interaction.

In Chapter 6, we attempted to investigate the interaction between VMP1 ATGD and BECN1 BH3D. However, our inconsistent ITC results were insufficient for proving that the BECN1 BH3D interacts with VMP1 ATGD *in vitro*. Further, the CD results did not show an obvious coil-to-helix transition when the two peptide domains were mixed in a 1:1 ratio. Indeed,

the VMP1 ATGD is not predicted to contain an Anchor region, suggesting that it may not undergo binding-induced disorder-to-order transitions (Glover *et al.*, 2016).

The focus of chapter 7 was to investigate the mechanism by which BCL2 homologs regulate BECN1-mediated autophagy. While the BECN1 BH3D has been shown to be sufficient for binding various BCL2 homologs, the mechanism by which BCL2 homologs down-regulate autophagy is not well established. Our sequence analysis shows that the BECN1 BH3D is not conserved across eukaryotes, suggesting that it is dispensable for core autophagy functions. Our autophagy assays show that deletion of the BECN1 BH3D does not down-regulate BECN1-induced autophagy, consistent with the BH3D not being conserved amongst eukaryotes. Therefore, we used a multi-pronged biophysical approach to investigate whether binding of the γ HV68 BCL2 homolog, M11, involves other domains and impacts their structure, function and oligomerization. Our biophysical studies indicate that BECN1 regions outside the BH3D, especially the IDR and FHD improve binding to M11, and, in addition to the BH3D, the BH3D-FHD linker, the FHD, and the center of the CCD become less flexible upon binding M11. In addition, BECN1 thermostability and homodimerization increases upon binding M11. We also found that the NES within the BECN1 CCD becomes more dynamic upon binding M11, but the dynamic of OH does not seem to change.

Our studies in Chapter 7 are important for understanding the mechanisms by which BCL2 proteins down-regulate autophagy. M11-binding is enhanced by interactions with the FHD, but decreases FHD flexibility. The FHD is implicated in binding-associated disorder-to-helix transitions (Mei, Ramanathan, *et al.*, 2016). The region equivalent to the FHD in the yeast BECN1 homolog, VPS30, forms a helix that packs against VPS38 (equivalent to human UVRAG) in the yeast VPS34 complex II (Rostislavleva *et al.*, 2015). The FHD is also implicated

in interactions with several other proteins such as Ambra1, an autophagy up-regulator (Strappazzon *et al.*, 2011). Therefore, M11-binding likely adversely impacts BECN1 association with UVRAG, and possibly ATG14, and its subsequent incorporation into VPS34 complexes; as well as interactions with other proteins that up-regulate autophagy such as AMBRA1.

Our results in Chapter 7 showing that the BECN1 NES becomes more dynamic upon binding M11 suggests that the more dynamic NES may impact the NES interaction with other proteins. Indeed, recently, Wu *et al.* reported that the NES region of BECN1 CCD is the most important region of CCD for binding to Atg14 and UVRAG (Wu *et al.*, 2018), therefore disordering of this region would likely diminish BECN1 interactions with these two proteins. Further, our results show that binding to M11 increases BH3D-FHD-CCD homodimerization. Therefore, binding to M11 decreases BECN1 homodimer self-dissociation, and also disrupts BECN1 interaction with UVRAG or Atg14, leading to down-regulation of autophagy. Numerous cellular and viral BCL2 homologs such as human Bcl-2 and EBV BHRF-1 also localize to the parinuclear space (Portier & Tagliatela, 2006, Chan *et al.*, 1995, Henderson *et al.*, 1993, Krajewski *et al.*, 1993), and M11 has also been found in cell nucleus, though only in relatively small amounts (Wang *et al.*, 1999). Increased NES flexibility upon binding M11 may impact BECN1 interaction with CRM1 in the nucleus. Our results suggest that binding of M11 to BECN1 may enhance BECN1 interaction with CRM-1, as the increased flexibility of the NES makes it more accessible for CRM-1 binding. However, binding to M11 may also decrease BECN1 interaction with CRM1 due to the decreased NES helicity, as it is unclear whether CRM-1 binding is sufficient to induce helicity. In that case, that would prevent export of BECN1 from the nucleus to the cytosol, resulting in autophagy down-regulation. The actual biological relevance of the nuclear localization of BCL2 homologs is not really understood, and has only

been investigated in relation to apoptosis. Thus, our study provides potential evidence for a role in autophagy for BCL2 homologs localized to the nucleus.

Thus, our results reported in Chapter 7 provide important insights into how binding of BCL2 homologs down-regulate autophagy. In the future, it would be invaluable to obtain a better understanding whether M11 induced conformational changes in the BH3D modulate conformations of the FHD and NES, and the mechanism by which this is accomplished. Further, an important focus of future biophysical and structural studies should be to understand the impact of M11-binding on various BECN1-interacting proteins using purified proteins. These should include proteins that upregulate autophagy such as VMP1 that binds to the BH3D, AMBRA1 that binds to the FHD, ATG14 and UVRAG that bind to the CCD; CCD-containing proteins that down-regulate autophagy; as well as the nuclear exporter, CRM-1. Lastly, it would be important to delineate similarities and differences in these impacts upon binding of different BCL2 homologs.

In Chapter 8, we extend the research reported in Chapter 7 to investigate the interactions between M11 and BECN1^{Δ31-104} or FL. Our ITC results suggest that BECN1 homodimerization does not impact its interaction with M11. We also attempted to use SAXS to analyze the overall shape and flexibility of BECN1^{Δ31-104} or FL and their complexes with M11, but the complexity and extensive flexibility of BECN1, prevented unambiguous conclusions regarding the change in flexibility or conformation of BECN1 upon binding M11. In this chapter, we also assessed the possibility of using EM to investigate the structure of BECN1^{Δ31-104} or FL and their complexes with M11. Our negative stain EM results suggest that our samples are not suitable for cryo-electron microscopy due to the high flexibility of BECN1 and the lower binding affinity between BECN1 and M11 relative to the sample concentration required for the cryo-electron microscopy.

Therefore, we were unable to conclusively determine the overall structure of BECN1 and how its conformation changes upon binding M11 with the current biophysical method we used in this chapter.

Lastly, in Chapter 9, we attempted to investigate the interactions between Bcl-X_L and BECN1. In contrast to the M11:BECN1 interactions reported in Chapter 7 wherein the BECN1 IDR and FHD appear improve binding, our ITC results suggest that BECN1 regions outside the BH3D do not affect BECN1 interaction with Bcl-X_L. We also attempted to use other biophysical methods to investigate the interactions between Bcl-X_L and M11, however, we were unable to conclusively determine whether binding to Bcl-X_L involves BECN1 domains besides the BH3D, and whether other BECN1 domains undergo conformational change using these methods due to the relative low binding affinity between Bcl-X_L and BECN1 and high flexibility of BECN1. Further biophysical and biochemical studies need to be carried out to investigate this further.

REFERENCES

- Aalberts, M., van Dissel-Emiliani, F. M. F., van Adrichem, N. P. H., van Wijnen, M., Wauben, M. H. M., Stout, T. A. E. & Stoorvogel, W. (2012). *Biol Reprod* **86**.
- Adams, P. D., Afonine, P. V., Bunkoczi, G., Chen, V. B., Davis, I. W., Echols, N., Headd, J. J., Hung, L. W., Kapral, G. J., Grosse-Kunstleve, R. W., McCoy, A. J., Moriarty, N. W., Oeffner, R., Read, R. J., Richardson, D. C., Richardson, J. S., Terwilliger, T. C. & Zwart, P. H. (2010). *Acta Crystallogr D* **66**, 213-221.
- Adi-Harel, S., Erlich, S., Schmukler, E., Cohen-Kedar, S., Segev, O., Mizrachy, L., Hirsch, J. A. & Pinkas-Kramarski, R. (2010). *J Cell Biochem* **110**, 1262-1271.
- Alexander, L., Denekamp, L., Knapp, A., Auerbach, M. R., Damania, B. & Desrosiers, R. C. (2000). *J Virol* **74**, 3388-3398.
- Altenbach, C., Oh, K. J., Trabanino, R. J., Hideg, K. & Hubbell, W. L. (2001). *Biochemistry* **40**, 15471-15482.
- Asojo, O. A. (2011). *Acta Crystallogr D* **67**, 455-462.
- Asojo, O. A., Goud, G., Dhar, K., Loukas, A., Zhan, B., Deumic, V., Liu, S., Borgstahl, G. E. O. & Hotez, P. J. (2005). *J Mol Biol* **346**, 801-814.
- Asojo, O. A., Koski, R. A. & Bonafe, N. (2011). *Acta Crystallogr D* **67**, 847-855.
- Baker, N. A., Sept, D., Joseph, S., Holst, M. J. & McCammon, J. A. (2001). *P Natl Acad Sci USA* **98**, 10037-10041.
- Banham, J. E., Baker, C. M., Ceola, S., Day, I. J., Grant, G. H., Groenen, E. J., Rodgers, C. T., Jeschke, G. & Timmel, C. R. (2008). *J Magn Reson* **191**, 202-218.
- Baskaran, S., Carlson, L. A., Stjepanovic, G., Young, L. N., Kim, D. J., Grob, P., Stanley, R. E., Nogales, E. & Hurley, J. H. (2014). *Elife* **3**.
- Bauchart-Thevret, C., Cui, L., Wu, G. & Burrin, D. G. (2010). *Am J Physiol Endocrinol Metab* **299**, E899-909.
- Baxter, R. M., Crowell, T. P., George, J. A., Getman, M. E. & Gardner, H. (2007). *Matrix Biol* **26**, 20-29.
- Boise, L. H., Gonzalez-Garcia, M., Postema, C. E., Ding, L., Lindsten, T., Turka, L. A., Mao, X., Nunez, G. & Thompson, C. B. (1993). *Cell* **74**, 597-608.
- Brunger, A. T. (1992). *Nature* **355**, 472-475.
- Campobasso, N. & Huddler, D. (2015). *Bioorg Med Chem Lett* **25**, 3771-3776.
- Castagnetto, J. M., Hennessy, S. W., Roberts, V. A., Getzoff, E. D., Tainer, J. A. & Pique, M. E. (2002). *Nucleic Acids Res* **30**, 379-382.
- Chan, W. K., Mole, M. M., Levison, D. A., Ball, R. Y., Lu, Q. L., Patel, K. & Hanby, A. M. (1995). *J Pathol* **177**, 241-246.
- Cheng, E. H., Nicholas, J., Bellows, D. S., Hayward, G. S., Guo, H. G., Reitz, M. S. & Hardwick, J. M. (1997). *Proc Natl Acad Sci U S A* **94**, 690-694.
- Chittenden, T., Flemington, C., Houghton, A. B., Ebb, R. G., Gallo, G. J., Elangovan, B., Chinnadurai, G. & Lutz, R. J. (1995). *Embo J* **14**, 5589-5596.
- Chittenden, T., Harrington, E. A., O'Connor, R., Flemington, C., Lutz, R. J., Evan, G. I. & Guild, B. C. (1995). *Nature* **374**, 733-736.
- Choudhary, V., Darwiche, R., Gfeller, D., Zoete, V., Michielin, O. & Schneider, R. (2014). *J Lipid Res* **55**, 883-894.
- Choudhary, V. & Schneider, R. (2012). *P Natl Acad Sci USA* **109**, 16882-16887.
- Cole, C., Barber, J. D. & Barton, G. J. (2008). *Nucleic Acids Res* **36**, W197-W201.

- Danial, N. N., Gimenez-Cassina, A. & Tondera, D. (2010). *Adv Exp Med Biol* **687**, 1-32.
- Darsow, T., Rieder, S. E. & Emr, S. D. (1997). *J Cell Biol* **138**, 517-529.
- Darwiche, R., Kelleher, A., Hudspeth, E. M., Schneiter, R. & Asojo, O. A. (2016). *Sci Rep-Uk* **6**.
- Doniach, S. (2001). *Chem Rev* **101**, 1763-1778.
- Dosztanyi, Z., Meszaros, B. & Simon, I. (2009). *Bioinformatics* **25**, 2745-2746.
- Duran, R. V., Oppliger, W., Robitaille, A. M., Heiserich, L., Skendaj, R., Gottlieb, E. & Hall, M. N. (2012). *Mol Cell* **47**, 349-358.
- Duseti, N. J., Jiang, Y., Vaccaro, M. I., Tomasini, R., Azizi Samir, A., Calvo, E. L., Ropolo, A., Fiedler, F., Mallo, G. V., Dagorn, J. C. & Iovanna, J. L. (2002). *Biochem Biophys Res Commun* **290**, 641-649.
- Eberle, H. B., Serrano, R. L., Fullekrug, J., Schlosser, A., Lehmann, W. D., Lottspeich, F., Kaloyanova, D., Wieland, F. T. & Helms, J. B. (2002). *J Cell Sci* **115**, 827-838.
- Ehrensberger, K. M. & Bird, A. J. (2011). *Trends Biochem Sci* **36**, 524-531.
- Emsley, P., Lohkamp, B., Scott, W. G. & Cowtan, K. (2010). *Acta Crystallogr D* **66**, 486-501.
- Fernandez, C., Szyperski, T., Bruyere, T., Ramage, P., Mosinger, E. & Wuthrich, K. (1997). *J Mol Biol* **266**, 576-593.
- Fimia, G. M., Stoykova, A., Romagnoli, A., Giunta, L., Di Bartolomeo, S., Nardacci, R., Corazzari, M., Fuoco, C., Ucar, A., Schwartz, P., Gruss, P., Piacentini, M., Chowdhury, K. & Cecconi, F. (2007). *Nature* **447**, 1121-1125.
- Franke, D. & Svergun, D. I. (2009). *J Appl Crystallogr* **42**, 342-346.
- Galluzzi, L., Bravo-San Pedro, J. M., Levine, B., Green, D. R. & Kroemer, G. (2017). *Nat Rev Drug Discov* **16**, 487-511.
- Gibbs, G. M., Roelants, K. & O'Bryan, M. K. (2008). *Endocr Rev* **29**, 865-897.
- Gibson, L., Holmgreen, S. P., Huang, D. C., Bernard, O., Copeland, N. G., Jenkins, N. A., Sutherland, G. R., Baker, E., Adams, J. M. & Cory, S. (1996). *Oncogene* **13**, 665-675.
- Glatter, O. (1977). *J Appl Crystallogr* **10**, 415-421.
- Glover, K., Li, Y., Mukhopadhyay, S., Leuthner, Z., Chakravarthy, S., Colbert, C. L. & Sinha, S. C. (2017). *J Biol Chem* **292**, 16235-16248.
- Glover, K., Mei, Y. & Sinha, S. C. (2016). *Biochim Biophys Acta* **1864**, 1455-1463.
- Greenfield, N. J. (2006a). *Nat Protoc* **1**, 2733-2741.
- Greenfield, N. J. (2006b). *Nat Protoc* **1**, 2876-2890.
- Groves, M. R., Kuhn, A., Hendricks, A., Radke, S., Serrano, R. L., Helms, J. B. & Sinning, I. (2004). *Acta Crystallogr D* **60**, 730-732.
- Han, J., Flemington, C., Houghton, A. B., Gu, Z., Zambetti, G. P., Lutz, R. J., Zhu, L. & Chittenden, T. (2001). *Proc Natl Acad Sci U S A* **98**, 11318-11323.
- Han, J. M., Jeong, S. J., Park, M. C., Kim, G., Kwon, N. H., Kim, H. K., Ha, S. H., Ryu, S. H. & Kim, S. (2012). *Cell* **149**, 410-424.
- He, C. C., Wei, Y. J., Sun, K., Li, B. H., Dong, X. N., Zou, Z. J., Liu, Y., Kinch, L. N., Khan, S., Sinha, S., Xavier, R. J., Grishin, N. V., Xiao, G. H., Eskelinen, E. L., Scherer, P. E., Whistler, J. L. & Levine, B. (2013). *Cell* **154**, 1085-1099.
- Heinz, U., Kiefer, M., Tholey, A. & Adolph, H. W. (2005). *J Biol Chem* **280**, 3197-3207.
- Henderson, S., Huen, D., Rowe, M., Dawson, C., Johnson, G. & Rickinson, A. (1993). *Proc Natl Acad Sci U S A* **90**, 8479-8483.
- Henriksen, A., King, T. P., Mirza, O., Monsalve, R. I., Meno, K., Ipsen, H., Larsen, J. N., Gajhede, M. & Spangfort, M. D. (2001). *Proteins* **45**, 438-448.

- Hsu, S. Y., Kaipia, A., McGee, E., Lomeli, M. & Hsueh, A. J. (1997). *Proc Natl Acad Sci U S A* **94**, 12401-12406.
- Huang, Q., Petros, A. M., Virgin, H. W., Fesik, S. W. & Olejniczak, E. T. (2002). *Proc Natl Acad Sci U S A* **99**, 3428-3433.
- Huang, W., Choi, W., Hu, W., Mi, N., Guo, Q., Ma, M., Liu, M., Tian, Y., Lu, P., Wang, F.-L., Deng, H., Liu, L., Gao, N., Yu, L. & Shi, Y. (2012). *Cell Research* **22**, 473-489.
- Hung, H. H., Huang, W. P. & Pan, C. Y. (2013). *Cell Biol Toxicol* **29**, 415-429.
- Hustedt, E. J. & Beth, A. H. (1999). *Annu Rev Biophys Biomol Struct* **28**, 129-153.
- Hustedt, E. J., Smirnov, A. I., Laub, C. F., Cobb, C. E. & Beth, A. H. (1997). *Biophys J* **72**, 1861-1877.
- Hwang, J. J., Kim, H. N., Kim, J., Cho, D. H., Kim, M. J., Kim, Y. S., Kim, Y., Park, S. J. & Koh, J. Y. (2010). *Biometals* **23**, 997-1013.
- Ichimura, Y., Kirisako, T., Takao, T., Satomi, Y., Shimonishi, Y., Ishihara, N., Mizushima, N., Tanida, I., Kominami, E., Ohsumi, M., Noda, T. & Ohsumi, Y. (2000). *Nature* **408**, 488-492.
- Ilari, A. & Savino, C. (2017). *Methods Mol Biol* **1525**, 47-78.
- Ishida, T. & Kinoshita, K. (2007). *Nucleic Acids Res* **35**, W460-W464.
- Itakura, E., Kishi, C., Inoue, K. & Mizushima, N. (2008). *Mol Biol Cell* **19**, 5360-5372.
- Itakura, E. & Mizushima, N. (2009). *Autophagy* **5**, 534-536.
- Jiang, P. & Mizushima, N. (2014). *Cell Res* **24**, 69-79.
- Jiang, P. H., Motoo, Y., Vaccaro, M. I., Iovanna, J. L., Okada, G. & Sawabu, N. (2004). *Pancreas* **29**, 225-230.
- Kabeya, Y., Mizushima, N., Ueno, T., Yamamoto, A., Kirisako, T., Noda, T., Kominami, E., Ohsumi, Y. & Yoshimori, T. (2000). *Embo J* **19**, 5720-5728.
- Kabsch, W. (2010). *Acta Crystallogr D* **66**, 125-132.
- Kawamata, T., Horie, T., Matsunami, M., Sasaki, M. & Ohsumi, Y. (2017). *J Biol Chem* **292**, 8520-8530.
- Ke, N., Godzik, A. & Reed, J. C. (2001). *J Biol Chem* **276**, 12481-12484.
- Kelleher, A., Darwiche, R., Rezende, W. C., Farias, L. P., Leite, L. C. C., Schneider, R. & Asojo, O. A. (2014). *Acta Crystallogr D* **70**, 2186-2196.
- Kim, J., Kim, Y. C., Fang, C., Russell, R. C., Kim, J. H., Fan, W., Liu, R., Zhong, Q. & Guan, K. L. (2013). *Cell* **152**, 290-303.
- Kim, J., Kundu, M., Viollet, B. & Guan, K. L. (2011). *Nat Cell Biol* **13**, 132-141.
- Kimura, N., Tokunaga, C., Dalal, S., Richardson, C., Yoshino, K., Hara, K., Kemp, B. E., Witters, L. A., Mimura, O. & Yonezawa, K. (2003). *Genes to Cells* **8**, 65-79.
- Kimura, T., Takabatake, Y., Takahashi, A. & Isaka, Y. (2013). *Cancer Res* **73**, 3-7.
- Konarev, P. V., Volkov, V. V., Sokolova, A. V., Koch, M. H. J. & Svergun, D. I. (2003). *J Appl Crystallogr* **36**, 1277-1282.
- Kozin, M. B. & Svergun, D. I. (2001). *J Appl Crystallogr* **34**, 33-41.
- Kozopas, K. M., Yang, T., Buchan, H. L., Zhou, P. & Craig, R. W. (1993). *Proc Natl Acad Sci U S A* **90**, 3516-3520.
- Krajewski, S., Tanaka, S., Takayama, S., Schibler, M. J., Fenton, W. & Reed, J. C. (1993). *Cancer Res* **53**, 4701-4714.
- Krissinel, E. & Henrick, K. (2007). *J Mol Biol* **372**, 774-797.
- Ku, B., Woo, J., Liang, C., Lee, K., Hong, H., Xiaofei, E., Kim, K., Jung, J. & Oh, B. (2008). *PLoS Pathog* **4**.

- Kurcinski, M., Jamroz, M., Blaszczyk, M., Kolinski, A. & Kmiecik, S. (2015). *Nucleic Acids Res* **43**, W419-W424.
- Kvansakul, M. & Hinds, M. G. (2013). *Cell Death Dis* **4**.
- Laderoute, K. R., Amin, K., Calaoagan, J. M., Knapp, M., Le, T., Orduna, J., Foretz, M. & Viollet, B. (2006). *Molecular and Cellular Biology* **26**, 5336-5347.
- Lambright, D. G., Malaby, A. W., Kathuria, S. V., Nobrega, C., Bilsel, O. & Mathews, R. C. (2013). *Trans. Am. Crystallogr. Assoc.* **44**.
- Larkin, M. A., Blackshields, G., Brown, N. P., Chenna, R., McGettigan, P. A., McWilliam, H., Valentin, F., Wallace, I. M., Wilm, A., Lopez, R., Thompson, J. D., Gibson, T. J. & Higgins, D. G. (2007). *Bioinformatics* **23**, 2947-2948.
- Lawrence, M. C. & Colman, P. M. (1993). *J Mol Biol* **234**, 946-950.
- Lee, E. F., Perugini, M. A., Pettikiriarachchi, A., Evangelista, M., Keizer, D. W., Yao, S. G. & Fairlie, W. D. (2016). *Autophagy* **12**, 460-471.
- Lee, S. J. & Koh, J. Y. (2010). *Mol Brain* **3**, 30.
- Levine, B. & Kroemer, G. (2008). *Cell* **132**, 27-42.
- Levine, B., Packer, M. & Codogno, P. (2015). *J Clin Invest* **125**, 14-24.
- Li, X. H., He, L. Q., Che, K. H., Funderburk, S. F., Pan, L. F., Pan, N. N., Zhang, M. J., Yue, Z. Y. & Zhao, Y. X. (2012). *Nat Commun* **3**.
- Li, Y., Zhao, Y. T., Su, M. F., Glover, K., Chakravarthy, S., Colbert, C. L., Levine, B. & Sinha, S. C. (2017). *Acta Crystallographica Section D-Structural Biology* **73**, 775-792.
- Liang, C., Lee, J. S., Inn, K. S., Gack, M. U., Li, Q., Roberts, E. A., Vergne, I., Deretic, V., Feng, P., Akazawa, C. & Jung, J. U. (2008). *Nat Cell Biol* **10**, 776-787.
- Liang, X. H., Jackson, S., Seaman, M., Brown, K., Kempkes, B., Hibshoosh, H. & Levine, B. (1999). *Nature* **402**, 672-676.
- Liang, X. H., Yu, J., Brown, K. & Levine, B. (2001). *Cancer Res* **61**, 3443-3449.
- Lin, E. Y., Orlofsky, A., Berger, M. S. & Prystowsky, M. B. (1993). *J Immunol* **151**, 1979-1988.
- Liu, X., Dai, S., Zhu, Y., Marrack, P. & Kappler, J. W. (2003). *Immunity* **19**, 341-352.
- Liuzzi, J. P. & Yoo, C. (2013). *Biol Trace Elem Res* **156**, 350-356.
- Loh, J., Huang, Q., Petros, A. M., Nettesheim, D., van Dyk, L. F., Labrada, L., Speck, S. H., Levine, B., Olejniczak, E. T. & Virgin, H. W. t. (2005). *PLoS Pathog* **1**, e10.
- Maiuri, M. C., Le Toumelin, G., Criollo, A., Rain, J. C., Gautier, F., Juin, P., Tasmimir, E., Pierron, G., Troulinaki, K., Tavernarakis, N., Hickman, J. A., Geneste, O. & Kroemer, G. (2007). *Embo J* **26**, 2527-2539.
- Malaby, A. W., Chakravarthy, S., Irving, T. C., Kathuria, S. V., Bilsel, O. & Lambright, D. G. (2015). *J Appl Crystallogr* **48**, 1102-1113.
- Malik, S. A., Orhon, I., Morselli, E., Criollo, A., Shen, S., Marino, G., BenYounes, A., Benit, P., Rustin, P., Maiuri, M. C. & Kroemer, G. (2011). *Oncogene* **30**, 3918-3929.
- Maret, W. (2012). *J Inorg Biochem* **111**, 110-116.
- Maret, W. (2013). *Biometals* **26**, 197-204.
- Maret, W., Larsen, K. S. & Vallee, B. L. (1997). *Proc Natl Acad Sci U S A* **94**, 2233-2237.
- Marshall, W. L., Yim, C., Gustafson, E., Graf, T., Sage, D. R., Hanify, K., Williams, L., Fingerroth, J. & Finberg, R. W. (1999). *J Virol* **73**, 5181-5185.
- Mason, L., Tribolet, L., Simon, A., von Gnielinski, N., Nienaber, L., Taylor, P., Willis, C., Jones, M. K., Sternberg, P. W., Gasser, R. B., Loukas, A. & Hofmann, A. (2014). *Int J Biochem Cell Biol* **50**, 146-155.
- Massa, W. (2004). *Crystal Structure Determination*, 2nd ed. Springer-Verlag Berlin Heidelberg.

- Matsunaga, K., Saitoh, T., Tabata, K., Omori, H., Satoh, T., Kurotori, N., Maejima, I., Shirahama-Noda, K., Ichimura, T., Isobe, T., Akira, S., Noda, T. & Yoshimori, T. (2009). *Nat Cell Biol* **11**, 385-U369.
- Mayer, A. & Wickner, W. (1997). *J Cell Biol* **136**, 307-317.
- Mccoy, A. J., Grosse-Kunstleve, R. W., Adams, P. D., Winn, M. D., Storoni, L. C. & Read, R. J. (2007). *J Appl Crystallogr* **40**, 658-674.
- McKee, D. E. (1993). *Practical Protein Crystallography*, 1 ed. Academic Press.
- Mei, Y., Glover, K., Su, M. & Sinha, S. C. (2016). *Protein Sci* **25**, 1767-1785.
- Mei, Y., Ramanathan, A., Glover, K., Stanley, C., Sanishvili, R., Chakravarthy, S., Yang, Z., Colbert, C. L. & Sinha, S. C. (2016). *Biochemistry* **55**, 1945-1958.
- Mei, Y., Su, M., Sanishvili, R., Chakravarthy, S., Colbert, C. L. & Sinha, S. C. (2016). *Biochemistry* **55**, 4239-4253.
- Mei, Y., Su, M. F., Soni, G., Salem, S., Colbert, C. L. & Sinha, S. C. (2014). *Proteins* **82**, 565-578.
- Melendez, A. & Levine, B. (2009). *WormBook*, 1-26.
- Mertens, H. D. T. & Svergun, D. I. (2010). *J Struct Biol* **172**, 128-141.
- Milne, T. J., Abbenante, G., Tyndall, J. D. A., Halliday, J. & Lewis, R. J. (2003). *Journal of Biological Chemistry* **278**, 31105-31110.
- Mizushima, N. (2018). *Nat Cell Biol* **20**, 521-527.
- Mizushima, N., Levine, B., Cuervo, A. M. & Klionsky, D. J. (2008). *Nature* **451**, 1069-1075.
- Molejon, M. I., Ropolo, A., Lo Re, A., Boggio, V. & Vaccaro, M. I. (2013). *Sci Rep-Uk* **3**.
- Nava, V. E., Cheng, E. H., Veluona, M., Zou, S., Clem, R. J., Mayer, M. L. & Hardwick, J. M. (1997). *J Virol* **71**, 4118-4122.
- Noble, C. G., Dong, J. M., Manser, E. & Song, H. W. (2008). *J Biol Chem* **283**, 26274-26282.
- Noda, N. N., Kobayashi, T., Adachi, W., Fujioka, Y., Ohsumi, Y. & Inagaki, F. (2012). *The Journal of Biological Chemistry* **287**, 16256-16266.
- O'Connor, L., Strasser, A., O'Reilly, L. A., Hausmann, G., Adams, J. M., Cory, S. & Huang, D. C. (1998). *Embo J* **17**, 384-395.
- Oberstein, A., Jeffrey, P. D. & Shi, Y. G. (2007). *J Biol Chem* **282**, 13123-13132.
- Obradovic, Z., Peng, K., Vucetic, S., Radivojac, P. & Dunker, A. K. (2005). *Proteins* **61**, 176-182.
- Oda, E., Ohki, R., Murasawa, H., Nemoto, J., Shibue, T., Yamashita, T., Tokino, T., Taniguchi, T. & Tanaka, N. (2000). *Science* **288**, 1053-1058.
- Ohsumi, Y. (2001). *Nat Rev Mol Cell Biol* **2**, 211-216.
- Olrichs, N. K. & Helms, J. B. (2016). *Aims Biophys* **3**, 232-246.
- Olrichs, N. K., Mahalka, A. K., Kaloyanova, D., Kinnunen, P. K. & Helms, J. B. (2014). *Amyloid* **21**, 88-96.
- Oltvai, Z. N., Milliman, C. L. & Korsmeyer, S. J. (1993). *Cell* **74**, 609-619.
- Osman, A., Wang, C. K., Winter, A., Loukas, A., Tribolet, L., Gasser, R. B. & Hofmann, A. (2012). *Biotechnol Adv* **30**, 652-657.
- Pace, N. J. & Weerapana, E. (2014). *Biomolecules*, pp. 419-434.
- Pattingre, S., Tassa, A., Qu, X. P., Garuti, R., Liang, X. H., Mizushima, N., Packer, M., Schneider, M. D. & Levine, B. (2005). *Cell* **122**, 927-939.
- Peng, K., Radivojac, P., Vucetic, S., Dunker, A. K. & Obradovic, Z. (2006). *Bmc Bioinformatics* **7**.

- Petiot, A., Ogier-Denis, E., Blommaert, E. F., Meijer, A. J. & Codogno, P. (2000). *J Biol Chem* **275**, 992-998.
- Petoukhov, M. V., Franke, D., Shkumatov, A. V., Tria, G., Kikhney, A. G., Gajda, M., Gorba, C., Mertens, H. D. T., Konarev, P. V. & Svergun, D. I. (2012). *J Appl Crystallogr* **45**, 342-350.
- Petros, A. M., Nettesheim, D. G., Wang, Y., Olejniczak, E. T., Meadows, R. P., Mack, J., Swift, K., Matayoshi, E. D., Zhang, H., Thompson, C. B. & Fesik, S. W. (2000). *Protein Sci* **9**, 2528-2534.
- Porod, G. (1982). *General theory*. United Kingdom: Academic Press.
- Portier, B. P. & Tagliatalata, G. (2006). *J Biol Chem* **281**, 40493-40502.
- Rambo, R. P. & Tainer, J. A. (2013). *Nature* **496**, 477-+.
- Reed, J. C. (1998). *Oncogene* **17**, 3225-3236.
- Rhodes, G. (2006). *Crystallography made crystal clear* 3rd ed. Academic Press.
- Richter, S., Wenzel, A., Stein, M., Gabdoulline, R. R. & Wade, R. C. (2008). *Nucleic Acids Res* **36**, W276-280.
- Robert, X. & Gouet, P. (2014). *Nucleic Acids Research* **42**, W320-324.
- Rostislavleva, K., Soler, N., Ohashi, Y., Zhang, L. F., Pardon, E., Burke, J. E., Masson, G. R., Johnson, C., Steyaert, J., Ktistakis, N. T. & Williams, R. L. (2015). *Science* **350**, 178-U181.
- Rubinsztein, D. C., Codogno, P. & Levine, B. (2012). *Nat Rev Drug Discov* **11**, 709-U784.
- Sarid, R., Sato, T., Bohenzky, R. A., Russo, J. J. & Chang, Y. (1997). *Nat Med* **3**, 293-298.
- Sato, T. K., Darsow, T. & Emr, S. D. (1998). *Mol Cell Biol* **18**, 5308-5319.
- Sattler, M., Liang, H., Nettesheim, D., Meadows, R. P., Harlan, J. E., Eberstadt, M., Yoon, H. S., Shuker, S. B., Chang, B. S., Minn, A. J., Thompson, C. B. & Fesik, S. W. (1997). *Science* **275**, 983-986.
- Schrodinger, LLC (2015). The PyMOL Molecular Graphics System, Version 1.8.
- Semenyuk, A. V. & Svergun, D. I. (1991). *J Appl Crystallogr* **24**, 537-540.
- Serrano, R. L., Kuhn, A., Hendricks, A., Helms, J. B., Sinning, I. & Groves, M. R. (2004). *Journal of molecular biology* **339**, 173-183.
- Shao, D., Oka, S., Liu, T., Zhai, P., Ago, T., Sciarretta, S., Li, H. & Sadoshima, J. (2014). *Cell Metab* **19**, 232-245.
- Sheffield, P., Garrard, S. & Derewenda, Z. (1999). *Protein Expression and Purification* **15**, 34-39.
- Shoji-Kawata, S., Sumpter, R., Leveno, M., Campbell, G. R., Zou, Z. J., Kinch, L., Wilkins, A. D., Sun, Q. H., Pallauf, K., MacDuff, D., Huerta, C., Virgin, H. W., Helms, J. B., Eerland, R., Tooze, S. A., Xavier, R., Lenschow, D. J., Yamamoto, A., King, D., Lichtarge, O., Grishin, N. V., Spector, S. A., Kaloyanova, D. V. & Levine, B. (2013). *Nature* **494**, 201-206.
- Sinha, S., Colbert, C. L., Becker, N., Wei, Y. & Levine, B. (2008). *Autophagy* **4**, 989-997.
- Smyth, M. S. & Martin, J. H. (2000). *Mol Pathol* **53**, 8-14.
- Song, C., Zhang, S. & Huang, H. (2015). *Front Microbiol* **6**, 1049.
- Sreerama, N., Venyaminov, S. & Woody, R. (2000). *Analytical Biochemistry* **287**, 243-251.
- Sreerama, N., Venyaminov, S. Y. & Woody, R. W. (2001). *Analytical biochemistry* **299**, 271-274.
- Sreerama, N. & Woody, R. (2000). *Analytical Biochemistry* **287**, 252-260.
- Sreerama, N. & Woody, R. W. (2004). *Methods Enzymol* **383**, 318-351.

- Strappazzon, F., Vietri-Rudan, M., Campello, S., Nazio, F., Florenzano, F., Fimia, G. M., Piacentini, M., Levine, B. & Cecconi, F. (2011). *The EMBO journal* **30**, 1195-1208.
- Su, M. F., Li, Y., Wyborny, S., Neau, D., Chakravarthy, S., Levine, B., Colbert, C. L. & Sinha, S. C. (2017). *Protein Science* **26**, 972-984.
- Su, M. F., Mei, Y., Sanishvili, R., Levine, B., Colbert, C. L. & Sinha, S. (2014). *J Biol Chem* **289**, 8029-8040.
- Suzuki, N., Yamazaki, Y., Brown, R. L., Fujimoto, Z., Morita, T. & Mizuno, H. (2008). *Acta Crystallogr D* **64**, 1034-1042.
- Svergun, D., Barberato, C. & Koch, M. H. J. (1995). *J Appl Crystallogr* **28**, 768-773.
- Svergun, D. I. (1992). *J Appl Crystallogr* **25**, 495-503.
- Svergun, D. I. (1999). *Biophys J* **76**, 2879-2886.
- Svergun, D. I. & Koch, M. H. J. (2003). *Reports on Progress in Physics* **66**, 1735-1782.
- Tang, H. & Da, L. A. (2010). *Hepatology* **52**, 1176-1176.
- Tresse, E., Salomons, F. A., Vesa, J., Bott, L. C., Kimonis, V., Yao, T. P., Dantuma, N. P. & Taylor, J. P. (2010). *Autophagy* **6**, 217-227.
- Tria, G., Mertens, H. D. T., Kachala, M. & Svergun, D. I. (2015). *Iucrj* **2**, 207-217.
- Vaccaro, M. I., Ropolo, A., Grasso, D. & Iovanna, J. L. (2008). *Autophagy* **4**, 388-390.
- van Galen, J., Olrichs, N. K., Schouten, A., Serrano, R. L., Nolte-'t Hoen, E. N. M., Eerland, R., Kaloyanova, D., Gros, P. & Helms, J. B. (2012). *Bba-Biomembranes* **1818**, 2175-2183.
- Van Loon, L. C. & Van Strien, E. A. (1999). *Physiol Mol Plant P* **55**, 85-97.
- Virgin, H. W. t., Latreille, P., Wamsley, P., Hallsworth, K., Weck, K. E., Dal Canto, A. J. & Speck, S. H. (1997). *J Virol* **71**, 5894-5904.
- Volkov, V. V. & Svergun, D. I. (2003). *J Appl Crystallogr* **36**, 860-864.
- Wales, T. E., Eggertson, M. J. & Engen, J. R. (2013). *Methods Mol Biol* **1007**, 263-288.
- Wang, G. H., Garvey, T. L. & Cohen, J. I. (1999). *J Gen Virol* **80** (Pt 10), 2737-2740.
- Wang, Y. L., Kuo, J. H., Lee, S. C., Liu, J. S., Hsieh, Y. C., Shih, Y. T., Chen, C. J., Chiu, J. J. & Wu, W. G. (2010). *J Biol Chem* **285**, 37872-37883.
- Williams, A., Sarkar, S., Cuddon, P., Ttofi, E. K., Saiki, S., Siddiqi, F. H., Jahreiss, L., Fleming, A., Pask, D., Goldsmith, P., O'Kane, C. J., Floto, R. A. & Rubinsztein, D. C. (2008). *Nat Chem Biol* **4**, 295-305.
- Winn, M. D., Ballard, C. C., Cowtan, K. D., Dodson, E. J., Emsley, P., Evans, P. R., Keegan, R. M., Krissinel, E. B., Leslie, A. G., McCoy, A., McNicholas, S. J., Murshudov, G. N., Pannu, N. S., Potterton, E. A., Powell, H. R., Read, R. J., Vagin, A. & Wilson, K. S. (2011). *Acta Crystallogr D Biol Crystallogr* **67**, 235-242.
- Wu, S., He, Y., Qiu, X., Yang, W., Liu, W., Li, X., Li, Y., Shen, H. M., Wang, R., Yue, Z. & Zhao, Y. (2018). *Proc Natl Acad Sci U S A*.
- Xu, X. Q., Francischetti, I. M. B., Lai, R., Ribeiro, J. M. C. & Andersen, J. F. (2012). *J Biol Chem* **287**, 10967-10976.
- Yang, E., Zha, J., Jockel, J., Boise, L. H., Thompson, C. B. & Korsmeyer, S. J. (1995). *Cell* **80**, 285-291.
- Yang, J., Liu, X., Bhalla, K., Kim, C. N., Ibrado, A. M., Cai, J., Peng, T. I., Jones, D. P. & Wang, X. (1997). *Science* **275**, 1129-1132.
- Yu, J., Zhang, L., Hwang, P. M., Kinzler, K. W. & Vogelstein, B. (2001). *Mol Cell* **7**, 673-682.
- Yuan, N., Song, L., Zhang, S., Lin, W., Cao, Y., Xu, F., Fang, Y., Wang, Z., Zhang, H., Li, X., Wang, Z., Cai, J., Wang, J., Zhang, Y., Mao, X., Zhao, W., Hu, S., Chen, S. & Wang, J. (2015). *Haematologica* **100**, 345-356.

- Zalckvar, E., Berissi, H., Eisenstein, M. & Kimchi, A. (2009). *Autophagy* **5**, 720-722.
- Zhang, K., Chen, Y., Zhang, Y., Yao, Q. & Zhuo, H. (2014). *Blood* **124**.
- Zhu, Y., Lin, G., Dai, Z., Zhou, T., Li, T., Yuan, T., Wu, Z., Wu, G. & Wang, J. (2015). *Amino Acids* **47**, 2185-2197.